École Doctorale des Sciences de la Matière, du Rayonnement et de
l'Environnement (ED – SMRE)

Manuscrit de la Thèse de Amanda Sfeir

Soutenue le **24/04/2023**

En vue de l'obtention du **Grade de Docteur** de l'Université de Lille en

Chimie Physique et Chimie des Matériaux

Vers le développement de nouveaux catalyseurs à base de Mo pour la synthèse de l'ammoniac

Membres du Jury:

Pr. Wioletta Raróg-Pilecka	Rapporteur	Warsaw University of Technology
Pr. Catherine Pinel	Rapporteur	IRCELYON UMR5256
Pr. Eric Gaigneaux	Examinateur (Président)	Université Catholique de Louvain
Dr. Nicolas Bion	Examinateur	Université de Poitiers
Pr. Sébastien Royer	Directeur de thèse	Université de Lille
Dr. Axel Löfberg	Co-directeur de thèse	Université de Lille
Dr. Jean-Philippe Dacquin	Co-encadrant de thèse	Université de Lille
Dr. Said Laassiri	Co-encadrant de thèse	Mohamed VI Polytechnic University

École Doctorale des Sciences de la Matière, du Rayonnement et de
l'Environnement (ED – SMRE)

Thesis Manuscript

Defended by **Amanda Sfeir** on **24/04/23**

To obtain the **Grade of Doctor** of University of Lille in

Physical Chemistry and Chemistry of Materials

Towards the development of novel Mo based catalysts for ammonia synthesis

Jury committee:

Pr. Wioletta Raróg-Pilecka	Reviewer	Warsaw University of Technology
Pr. Catherine Pinel	Reviewer	IRCELYON UMR5256
Pr. Eric Gaigneaux	Examinator (President)	Université Catholique de Louvain
Dr. Nicolas Bion	Examinator	Université de Poitiers
Pr. Sébastien Royer	Supervisor	Université de Lille
Dr. Axel Löfberg	Co-supervisor	Université de Lille
Dr. Jean-Philippe Dacquin	Co-supervisor	Université de Lille
Dr. Said Laassiri	Co-supervisor	Mohamed VI Polytechnic University

Acknowledgments:

I would like to take this opportunity to express my heartfelt gratitude and appreciation to all those who have contributed to the successful completion of my PhD dissertation. Their unwavering support, encouragement, and guidance have played an invaluable role in my academic and personal growth. First and foremost, I would like to extend my deepest appreciation to the funding organizations that have generously supported my research (Université de Lille, ED SMRE, MOPGA, Campus France, MOBLILEX). Their financial assistance has enabled me to conduct experiments, attend conferences, and access various resources that have significantly contributed to the quality and depth of my work.

I am indebted to the numerous laboratories and research institutions that provided me with the infrastructure, equipment, and resources necessary for my experiments (Institut Chevreul, Drexel University, University of Glasgow). Their collaborative spirit and commitment to advancing scientific knowledge have greatly enriched my research experience.

I am especially grateful to my supervisors and mentors, Sébastien Royer, Jean-Phillipe Dacquin, Axel Löfberg, Said Laassiri, whose expertise, guidance, and patience have been instrumental throughout my doctoral journey. Their insightful feedback, constructive criticism, and encouragement have shaped my research direction and refined my analytical skills. I am truly fortunate to have had the opportunity to work under their mentorship.

I would also like to express my sincere appreciation to all my lab mates, whose camaraderie and intellectual discussions have created a stimulating and supportive research environment.

To my friends and family, I extend my deepest gratitude for their unwavering love, encouragement, and understanding. Their constant support, words of motivation, and belief in my abilities have been a source of inspiration during challenging times. I am truly grateful for the countless sacrifices they have made to ensure my success and well-being.

Lastly, I would like to acknowledge the divine guidance and blessings from God. I am humbled by the opportunities and capabilities I have been granted. I am grateful for the strength and determination that have been instilled in me, and for the blessings that have led me to this significant milestone.

In conclusion, I extend my deepest gratitude to all those who have supported me in various ways during my PhD journey. Each and every individual mentioned above has played a significant role in shaping my academic and personal development. Their contributions have been invaluable, and I am forever grateful for their presence in my life.

Thank you all from the bottom of my heart.

Abstract:

Considered as a major discovery of the 20th century, and now needed to supply nearly 70% of the world population, ammonia and its synthesis process have been and will continue to be a major focus of academic research. Over 150 million tons of ammonia are produced each year, making it the second most manufactured chemical in the world. While 80% of ammonia production is used in the fertilizer industry, many other industries rely on NH_3 for the manufacture of various products (explosives, some plastics and chemicals, some pharmaceuticals). Recent works have highlighted ammonia for energy applications, due to its potential as a carbon-free molecule for hydrogen storage. In order to face the growing worldwide demand of energy and the climate deregulation, the crucial need for efficient low-pressure and decentralized ammonia synthesis is therefore becoming urgent. Many recent studies propose new catalysts operating under mild synthesis conditions, using various approaches such as electrosynthesis, photocatalysis, plasma-assisted catalysis as alternatives to traditional thermal catalysis. Molybdenum-based materials have proven to be particularly effective for this application. The interest for molybdenum lies in the fact that catalysts can be synthesized as carbides or nitrides, in addition to its exceptional chemical versatility with oxidation states ranging from (-II) to (+VI). In this work, we studied the properties of Mo-based catalysts for the synthesis of ammonia at atmospheric pressure. The synthesized materials were characterized by different techniques (XRD, SAXS, N_2 physisorption, CHNS, ICP, TEM, SEM, XPS, EPR, NMR, TGA-DSC, TPR, H_2-TPD), which allowed us to evaluate the impact of particle size and material structure on the catalyst performances.

Résumé:

Considérés comme une découverte majeure du 20ème siècle, et maintenant nécessaire pour alimenter près de 70% de la population mondiale, l'ammoniac et son procédé de synthèse ont été et seront toujours un sujet d’étude majeur de la recherche académique. Environ 150 millions de tonnes d'ammoniac sont produites chaque année, ce qui en fait le deuxième produit chimique le plus fabriqué au monde. Alors que 80 % de la production d'ammoniac est utilisée pour l'industrie des engrais, de nombreuses autres filières industrielles dépendent du NH_3 qui est nécessaire à la fabrication de produits variés (explosifs, certains plastiques et produits chimiques, certains produits pharmaceutiques). Des travaux récents mettent également en avant l'ammoniac pour des applications de stockage d'énergie, en raison de son potentiel en tant que

molécule sans carbone transporteur d’hydrogène. Afin de faire face à la demande mondiale en énergie et à la dérégulation climatique, la recherche d'une synthèse efficace et verte de l'ammoniac à basse pression et décentralisée devient donc cruciale. De nombreuses études récentes proposent de nouveaux catalyseurs fonctionnant dans des conditions douces de synthèse, en utilisant diverses approches telles que l'électrosynthèse, la photocatalyse, la catalyse assistée par plasma comme plusieurs alternatives à la catalyse thermique traditionnelle. Les matériaux à base de molybdène se sont révélés particulièrement efficaces pour cette application. L'attrait pour le molybdène réside dans le fait que les catalyseurs peuvent être synthétisés sous forme de carbures ou de nitrures, sans oublier son exceptionnelle polyvalence chimique avec des états d'oxydation allant de (-II) à (+VI). Dans ce travail, nous avons étudié les propriétés de catalyseurs à base de Mo pour la synthèse de l’ammoniac à pression atmosphérique. Les matériaux synthétisés ont été caractérisés par différentes techniques (XRD, SAXS, physisorption de N_2, CHNS, ICP, TEM, SEM, XPS, EPR, NMR, TGA-DSC, TPR, H_2-TPD), ce qui a permis d’évaluer l’impact de la taille des particules et de la structure des matériaux sur les performances des catalyseurs.

Table of Contents

I. General Introduction:

‘Bread from Air’; the Haber-Bosch process was discovered in response to the economic and social requirement of fixed nitrogen toward the end of the 19th century due to geometric progression of the world population versus arithmetic progression of food where mankind was sought to suffer from shortage of food which in turn would lead to serious casualties. Over the past century, the world’s population has significantly grown, from less than 2 billion people in 1900, to more than 8 billion people in 2023. 100 years later, more than 6 billion people later, the exact same process is still being used to produce NH_3, with a much higher demand, projected to supply 228 Mt of Ammonia in 2023 (IFA).

Ammonia is an indispensable element in many industrial processes (fertilizers, dyes, medicinal drugs, explosives, cleaning supplies, etc.), ranking second most synthesized inorganic compound after sulfuric acid. With the surge for renewable energy, and finding a suitable energy storage possibility, ammonia possesses appropriate characteristics to be considered as green, safe, and sustainable energy carrier making it an optimum candidate for Power to X (P2X) energy storage systems. Some of these properties include high hydrogen gravimetric content (17.6 wt.%), high energy density (5.2 kWh kg^{-1}) based on the low heat value (LHV), facile liquefaction and low flammability. More importantly, there is an existing infrastructure for safe and cost-effective ammonia transportation and distribution worldwide which alas is not the case for hydrogen.

The H-B process is estimated to consume ~ 1-2 % of the world's annual energy production and is responsible for 2-2.5% of global carbon dioxide emissions, making this process in this day and age an environmental and economic matter. With the evolvement of technology and the expansion of human knowledge today in comparison to the 1900’s, it is baffling that the same exact process is still the primary source for ammonia. Thus, the development of a novel generation of catalysts capable of operating at milder conditions is an important milestone to decrease the carbon footprint and energy consumption, and is consequently unavoidable in the deployment of large-scale Power to Ammonia process for energy storage. Research on alternative processes has also been significantly rising, whether it is electrosynthesis, plasma catalysis, photocatalysis, thermocatalysis, and others.

In the last decades, heterogeneous catalysis has been dominated by the use of materials in metallic and metal oxide forms. However, to meet the increasingly challenging economic and environmental targets, attention has been focused on developing alternative catalysts displaying better activity in milder conditions, to in turn enhance the efficiency of chemical processes. With that, the presence of interstitial species such as carbon or nitrogen modifies the electronic structure of corresponding parent metals, as in the case of systems such as molybdenum carbides and nitrides, to reach materials properties similar to precious metals. Similarly, the accessibility of the active sites, their corresponding surface state and their size distribution can have imperative effect on the activity.

In this thesis, we focused towards the development of novel Mo based catalysts (binary and ternary, carbide and nitride, supported and unsupported) for ammonia synthesis. Thus, this manuscript is divided into 6 Chapters:

- Chapter I includes the bibliographic overview from the discovery of the Haber-Bosch process in the end of the 19th century, development of the industrial process, rise of the pollution and in turn the work on alternative processes, such as electrosynthesis, plasma catalysis, photocatalysis, nitrogenase, chemical looping, and heterogeneous catalysis.
- Chapter II summarizes the materials and methods used to accomplish the experimental part of this thesis. This includes the synthesis of all the different catalyst families. Chapter II also describes the detailed information on characterization methods applied.
- Chapter III and Chapter IV: These two chapters are complementary and describe the synthesis and stabilization of Molybdenum nitride NPs on different commercial supports (TiO_2, CeO_2, Al_2O_3, SiO_2) and on mesoporous silica. These catalysts are extensively characterized and their activity was examined for ammonia synthesis and ammonia decomposition. The effect of the support, and the size of NPs on the activity are concluded from these two chapters. Chapter III describes Mo-N NPs on TiO_2 and SBA-15 (published in Faraday Discussions 2023) whereas Chapter IV reports the effect of CeO_2, Al_2O_3, SiO_2, and mesoporous silica as support for Mo-N NPs (submitted to ACS Energy Letters 2023).
- Chapter V: built from the previous chapters, this section is dedicated to ternary nitride nanoparticles, Co_3Mo_3N, encapsulated in SBA-15 pores for ammonia synthesis. Synthesis of the catalysts with appropriate characterization is discussed in this part, including a detailed part on SBA-15 stability under ammonia. The catalysts are tested for ammonia synthesis and post reaction samples are also examined. This work has been published in Applied Catalysis B: Environmental 2023.

- Chapter VI: saving best for last, this chapter reports novel Co decorated Mo-MXene multilayers for ammonia synthesis. This section includes synthesis, characterization, ammonia synthesis at various temperatures to conclude the high potential of this rising family of materials.

Chapter I : Literature Overview

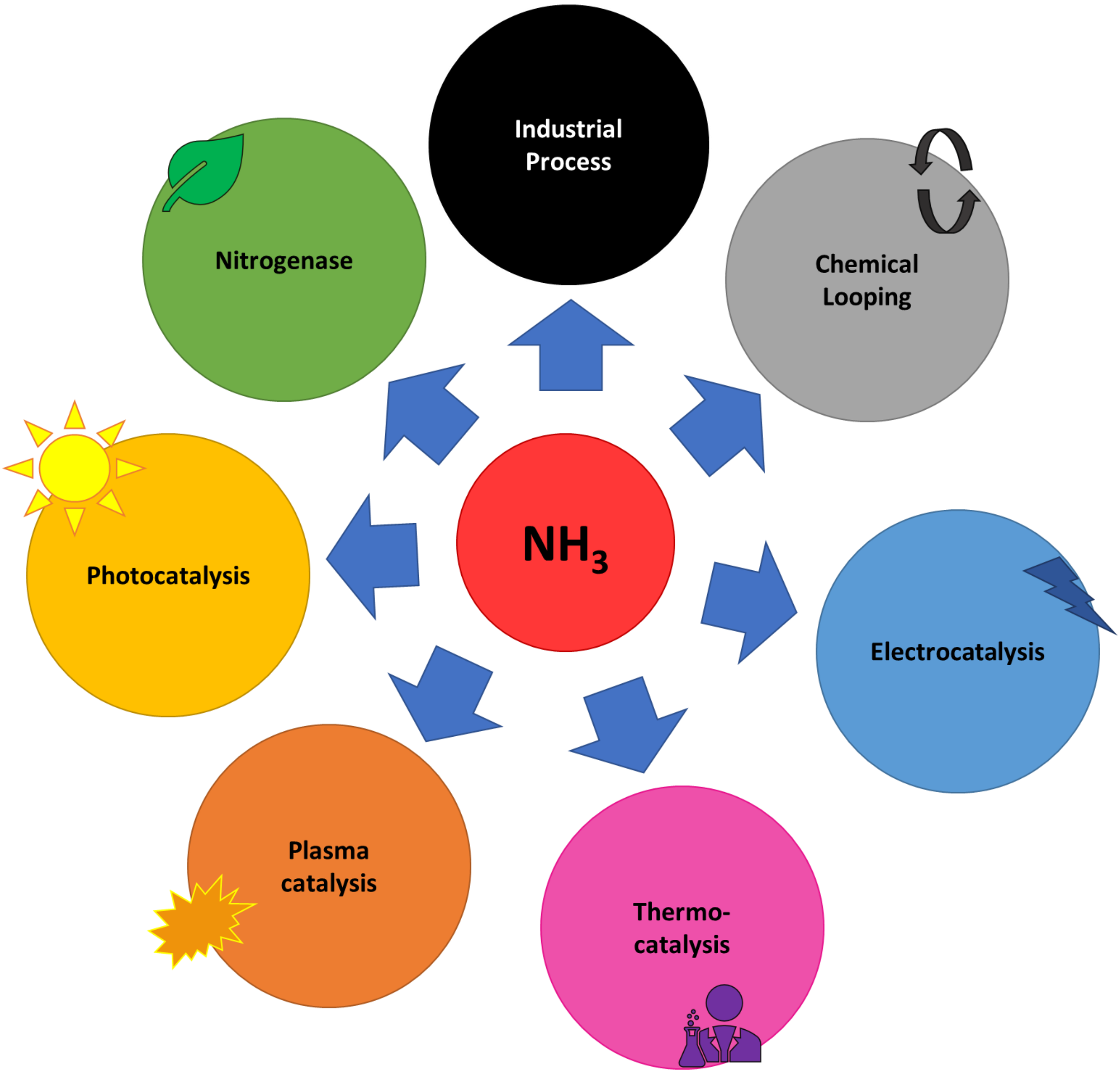

II. Chapter I: Literature Overview

Ammonia synthesis is a never-ending story. Reactive nitrogen is an indispensable element in many industrial processes, where nitrogen containing molecules are essential for the preparation of high value commercial products: fertilizers, dyes, medicinal drugs, and so on. Ammonia synthesis is considered to be one of the most important discoveries in the history of catalysis. This discovery was in response to the economic and social requirement of fixed nitrogen toward the end of the 19th century. Due to geometric progression of the world population and arithmetic progression of food, mankind was sought to suffer from shortage of food which in turn would lead to serious casualties [1]. With fixed-nitrogen being an essential element in fertilizers, the quest for synthetic production of ammonia began in order to save the population from starvation. Among the efforts given in this domain, Haber first proposed the possibility to produce ammonia from naturally abundant nitrogen and hydrogen. The importance of the Haber-Bosch (H-B) process is now recognized both by industrial and scientific communities. Fritz Haber (1868 - 1934) and Carl Bosch (1874 - 1940) were awarded with the Nobel Prize for Chemistry, in 1919 and 1931 [1] respectively, and more recently in 2007, a Noble Prize was given to Gerhard Ertl, for his work on the determination of the mechanisms, at the molecular level, of the catalytic reaction of ammonia on iron surfaces [2]. The H-B process, in its current configuration and after a century of optimization, offers a direct way to convert stable dinitrogen molecule into ammonia, ammonia being a reactive nitrogen compound. Currently, the industrial production of ammonia by the H-B process is estimated to produce around 200 million tons of NH_3 per year, making ammonia the second largest produced inorganic molecule after sulfuric acid [3].

Unfortunately, the H-B process is estimated to consume 3–5% of the global natural gas supply, contributing to the greenhouse gas emission that can reach 1.6 to 2.86 ton of CO_2 emitted per ton of ammonia produced depending on the efficiency of the plant [4]. Due to the operating conditions (high pressure and temperature), the process is also highly energy consuming, requiring an energy input of ~ 485 kJ mol^{-1}, accounting for approximately 1-2% of the global energy exhausted each year [3]. With that being said, alternative approaches for producing local ammonia by sustainable methods have been vastly studied such as, electrosynthesis, plasma synthesis, nitrogenase, chemical looping, and others. These alternative processes can solve some drawbacks associated to the current Haber Bosch process use, but as mentioned above, all these alternatives are far from replacing the conventional H-B and supplying the current NH_3 demand.

The aim of this chapter is to take us back to the end of the 19th century, with the discovery of ammonia synthesis and accompany us on a journey in the 20th century stopping by the important checkpoints from the discovery, development of the industrial process, rise of the pollution and in turn the work on alternative processes, bringing us finally here, to this thesis today, working on alternative catalysts for green ammonia production.

II.1 H-B process

The Haber-Bosch process synthesizes ammonia through the reaction between molecular nitrogen and hydrogen (Eq. 1) with an equilibrium constant directly dependent on the reactant and products partial pressures (Eq. 2):

$$N_{2\,(g)} + 3H_{2\,(g)} \leftrightarrows 2NH_{3\,(g)} \qquad \Delta H_f^{\circ} = -45.9\ kJ.mol^{-1}\ [1] \tag{1}$$

$$K_{eq} = \frac{P_{NH3}}{P_{N2}^{1/2} P_{H2}^{3/2}} \tag{2}$$

Following Le Chatelier's principle, several parameters can be adjusted to shift the reaction in the forward direction. An increase in the reaction pressure with continuous removal of product formed and a low temperature due to the exothermicity of the forward reaction are ideally the optimal parameters in order to obtain the maximum yield of ammonia. From an industrial point of view, a compromise between kinetics and thermodynamics must be considered, to produce with an acceptable yield. Oxygen poisoning reduces the reaction rate and also may reduce the lifetime of the catalyst, thus in order to maintain the levels of production, the increase of pressure with ultra-pure stream and temperature is compulsory. The most efficient industrial parameters to produce ammonia is a pressure of about 200 bar and a temperature ranging between 400°C and 500°C [5]. In order to better understand the relationship between temperature and pressure on the yield and rate of the reaction, especially for low T and low P processes, figure 1 visualizes the optimal working window for ammonia synthesis under thermodynamic and kinetic compromise. The higher the temperature, the higher the rate, yet the lower the equilibrium. Starting with the operating conditions of the H-B process of 200 bar and 500°C (green star), in order to maintain similar equilibrium yields at ambient pressure (as indicated by the green arrow), temperature is required to be lowered ~300 °C, thus a working temperature of ~200 °C.

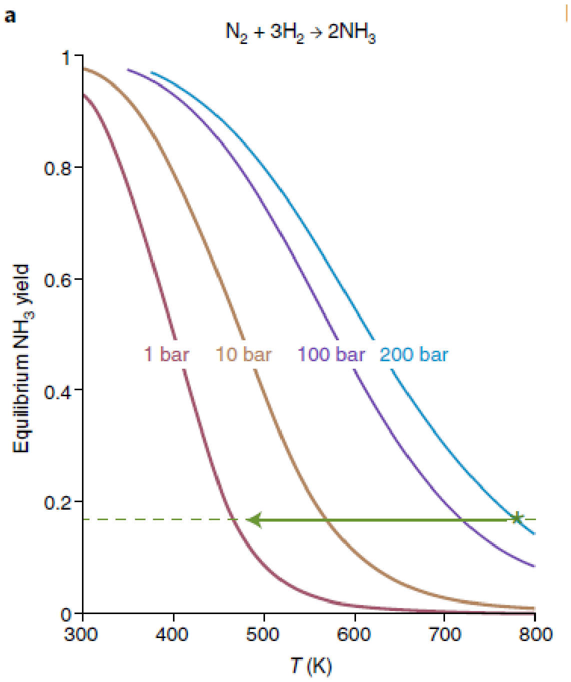

Figure 1: Scheme describing the thermal equilibrium concentrations of ammonia synthesis on versus temperature for different pressures [6]

II.1.1 History and Importance

Ammonia synthesis is considered as one of the most important discoveries in the history of catalysis. As shown in table 1, nitrogen containing molecules are essential building blocks for the preparation of important commercial products. All started in 1904 with the contribution of Haber on the study of ammonia, hydrogen, and nitrogen equilibrium, with measurement at equilibria of ammonia production on an iron catalyst at various temperatures and atmospheric pressure. This was a significant step toward the possibility to synthesize ammonia from its elements at room temperature with a suitable catalyst. Haber studied the arc method in detail, subsequently, with a collaboration with Le Rossignol, Haber performed the reaction with a steel autoclave as a reactor at pressures of up to 200 bar. This intrigued BASF company, sending two highly trained engineers Bosch and Mittasch to Haber in order to start industrial development [1].

Table 1: Main uses of ammonia, adapted from [2][3]

INDUSTRY	APPLICATION
Fertilizer	Production of: urea, $(NH_2)_2CO$; ammonium sulfate, $(NH_4)_2SO_4$; ammonium phosphate, $(NH_4)_3PO_4$ and ammonium nitrate, NH_4NO_3.
Chemicals	Synthesis of: nitric acid, HNO_3; sodium hydrogen carbonate (sodium bicarbonate), $NaHCO_3$; sodium carbonate, Na_2CO_3; hydrogen cyanide (hydrocyanic acid), HCN and hydrazine, N_2H_4 (rocket propulsion systems; reducer).
Explosives	Ammonium nitrate, NH_4NO_3 and TNT (2,4,6-trinitrotoluene),nitroglycerin
Fibers/Plastics	Nylon, $-[(CH_2)_4-CO-NH-(CH_2)_6-NH-CO]-$ and other polyamides.
Refrigeration	Used for making ice, large-scale refrigeration plants, air-conditioning units in buildings and plants.
Pharmaceuticals	Used in the manufacture of drugs such as sulfonamide (inhibition of the growth and multiplication of bacteria), anti-malarias and B vitamin, nicotinamide (niacinamide) and thiamine.
Cleaning	Ammonia in solution is used as a cleaning agent such as in 'cloudy ammonia'.

Bosch later established high-pressure technology in the chemical industry while Mittasch contributed significantly to the development and role understanding of commercial catalysts. Haber was awarded the Nobel Prize in 1919 for his studies on ammonia synthesis. Bosch also received the Nobel Prize in 1931 for his achievement in high-pressure technology development, for bringing the process to economic and technical industrial-scale, jointly with Bergius who also worked with Haber's group in Karlsruhe, which had become a center of excellence in the field of high-pressure technology. This “discovery of the century” was also recently awarded by a third Nobel Prize to Gerhad Ertl in 2007 [2], for studying chemical processes on solid surfaces. He was able to improve the understanding of the reaction mechanism on the industrially relevant iron catalyst. A century has passed after the development of the Haber-Bosch Process for ammonia synthesis in 1913, yet the process for its production has not quite changed over the years. Even though this great breakthrough of synthesizing ammonia from atmospheric nitrogen is genius, winning 3 Nobel prizes, it has many disadvantages that the scientific community hopes to overcome by elaborating greener methods for synthesis.

II.1.2 Mechanism and Catalyst

Gerhard Ertl demonstrated how hydrogen adsorbs in a dissociative manner on iron surfaces and that nitrogen dissociatively chemisorbs forming atomic N leading to the production of ammonia according to a Langmuir-Hinshelwood mechanism [7] .

$$\mathrm{H_2} + * \rightleftharpoons 2\mathrm{H_{ad}} \tag{3}$$

$$\mathrm{N_2} + * \rightleftharpoons \mathrm{N_{2\,ad}} \tag{4}$$

$$\mathrm{N_{2\,ad}} \rightleftharpoons 2\mathrm{N_{ad}} \tag{5}$$

$$\mathrm{N_{ad}} + \mathrm{H_{ad}} \rightleftharpoons \mathrm{NH_{ad}} \tag{6}$$

$$\mathrm{NH_{ad}} + \mathrm{H_{ad}} \rightleftharpoons \mathrm{NH_{2\,ad}} \tag{7}$$

$$\mathrm{NH_{2\,ad}} + \mathrm{H_{ad}} \rightleftharpoons \mathrm{NH_{3\,ad}} \tag{8}$$

$$\mathrm{NH_{3\,ad}} \rightleftharpoons \mathrm{NH_3} + * \tag{9}$$

The rate determining step is the dissociative adsorption of dinitrogen (Eq. 5), with the strong bonding energy of the triple bond making it difficult to cleave. In the Haber-Bosch process, the active catalyst is a doubly promoted iron catalyst that has been optimized throughout the years. The choice of catalyst is crucial and guided by the material being most active to the nitrogen hydrogenation, and least active for ammonia decomposition, not to mention resistant to poisoning. The term "doubly promoted" is given to the H-B catalyst because it is endorsed both structurally and electronically by different promotors. An example of the chemical composition of a double promoted catalyst is: Fe_3O_4, 94.3 wt.%; K_2O, 0.8 wt.%; Al_2O_3, wt.%; Ca, 1.7 wt.%; MgO, 0.5 wt.%; SiO_2, 0.4 wt.%. Structural promoters, such as aluminum, calcium, and silicon are characterized by their ability to partially substitute iron in the magnetite (Fe_3O_4). The structural promoters generate and stabilize the pore structure, leading to a large, unhindered iron surface in the final catalyst. Structural promoters increase the specific surface area of the catalyst from a few $m^2\ g^{-1}$ to a maximum of 18 $m^2\ g^{-1}$ for a 2.5 wt.% loading but slightly decreases for higher loadings [1]. Studies showed that aluminum oxide is the most efficient structural promotor for iron catalyst with a maximum substitution of 3% within the spinel framework. The electronic promoters are potassium cations which have a comparable radius as the oxygen anion, 133 ppm. Thus, the substitution within the spinel structure is excluded, and it segregates on the surface of the catalyst. The addition of potassium oxide increases the specific activity of the catalyst with a maximum enhancement at 0.8 wt.% loading. The electronic promoter's role is firstly electron donation leading to a weakening of the nitrogen triple bond and secondly facilitating the ammonia desorption from the catalyst surface [8]. Further effect of the promoters is the significant increase in long-term stability of the catalyst. Another non-iron catalyst that is commercially found, specifically in the Kellogg's Advanced Ammonia Process, is a ruthenium based catalyst which is particularly efficient for the nitrogen fixation, representing economic benefits previously unachievable [9]. The latter will not be discussed in details in this chapter.

II.1.3 Industrial process (Ammonia Plant)

A huge part of the overall H-B process is closely dependent on the production of the primary raw materials since the ammonia purity depends on the gas production process. There are mainly two types of commercial ammonia processes which are assigned to the method of hydrogen production; i.e. steam reforming of methane and partial oxidation route. Several types of plants are also found such as KAAP (Kellogg's Advanced Ammonia Production), Topsoe, and Braun Purifier systems that undergo different routes under slightly different conditions.

For the steam-reforming route, the feedstock, usually natural gas but can also be liquified petroleum gas or naphtha, first undergoes a hydrodesulfurization step where sulfur is removed in order to avoid any catalyst poisoning. During the primary reforming, reactions (10) and (11) occur:

$$CH_4 + H_2O \longrightarrow CO + 3H_2 \tag{10}$$

$$CO + H_2O \longrightarrow CO_2 + H_2 \tag{11}$$

The role of the second reforming step is to consume the residual methane, making it react with the oxygen present in the air flow added in the process to provide the N_2 reactant:

$$2CH_4 + O_2 \longrightarrow 2\,CO + 4\,H_2 \tag{12}$$

$$CH_4 + 2\,O_2 \longrightarrow CO_2 + 2\,H_2O \tag{13}$$

$$CH_4 + \frac{3}{2}\,O_2 \longrightarrow CO + 2\,H_2O \tag{14}$$

The catalytic column allows to purify the mixture by converting carbon monoxide to carbon dioxide, and the scrubber allows the decarbonation of the reactant feed (elimination of carbon dioxide by absorption in aqueous solution). The final step is the methanation of any remaining carbon oxides lowering the residual carbon oxide content to 5 ppm thus decreasing the risk of poisoning due to oxygen containing compounds. The scheme below shows all the details of the process [1].

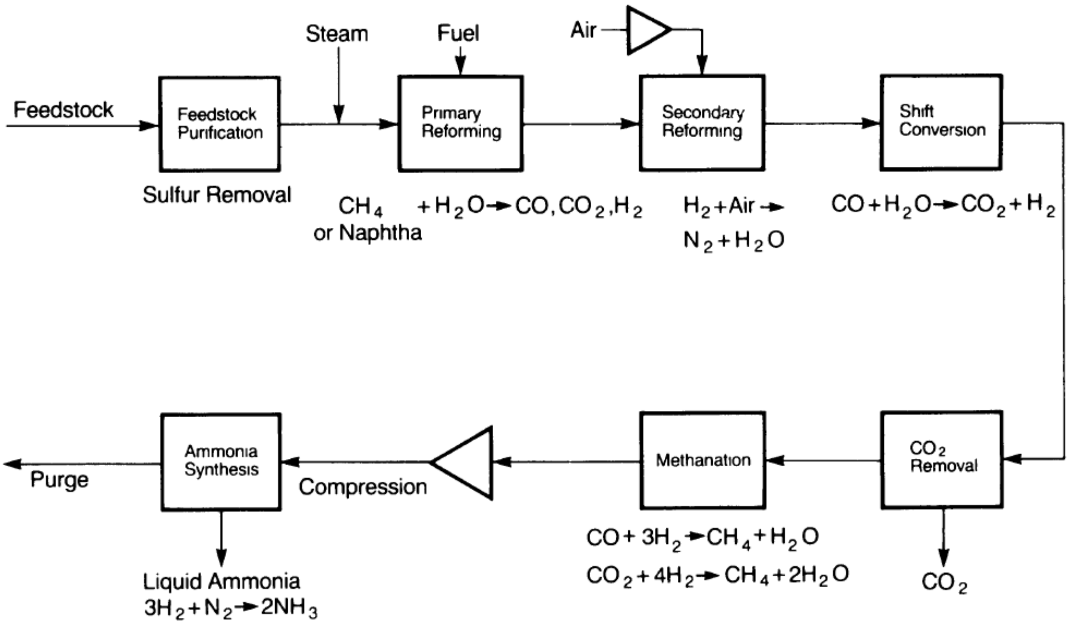

Figure 2: The steam reforming route for ammonia production

The partial oxidation route is used for heavy hydrocarbon feedstocks which are not suitable for steam reforming such as heavy fuel oils, crude oils, asphalt and tar. In the gasifier, the feedstock is burnt with a limited amount of oxygen and steam following the reaction below:

$$C_xH_y + \frac{x}{2}O_2 \rightarrow xCO + \frac{y}{2}H_2 \qquad (15)$$

After this first step, we obtain mainly hydrogen and carbon monoxide, with some carbon dioxide, water, and small amounts of sulfur and methane. The obtained gas is immediately cooled in order to retain a low methane content and then scrubbed to remove any soot remaining. The cool gas is then subjected to a conversion from carbon monoxide to carbon dioxide followed by some purification treatments in order to remove acid gases and hydrogen sulfide. The next step is a nitrogen wash that produces a 3:1 stoichiometric mixture of hydrogen and nitrogen with very low impurities. A diagram of this process is shown below (Figure 3).

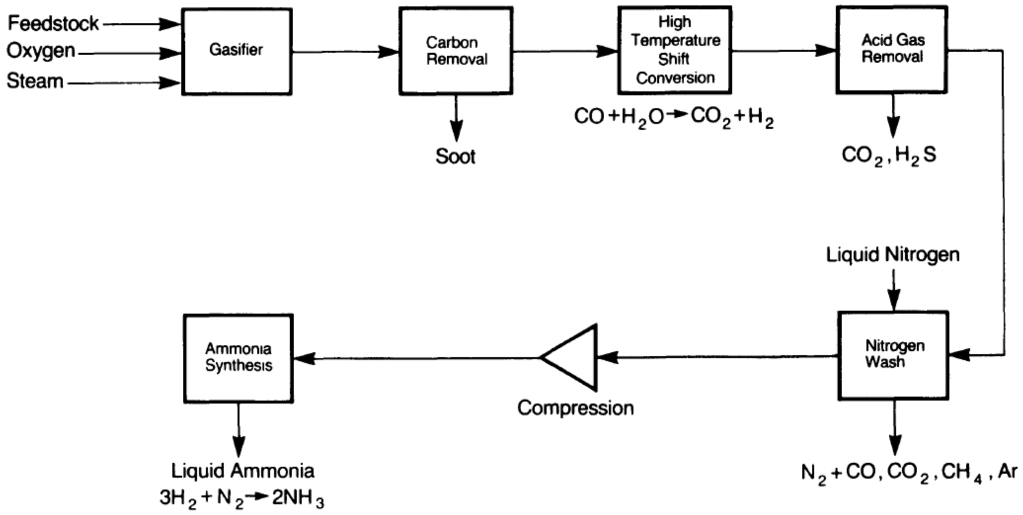

Figure 3: The partial oxidation route for ammonia production

Finally, an ammonia synthesis loop is requested for the final step of the process. An economic loop is a fundamental key in all commercial plants realized in order to recycle unreacted nitrogen and hydrogen after the removal of ammonia from the reactor, since the reactant conversions, under the temperature and pressure of operation, never exceed 15% [3]. The essential features of the loop are as follows:

Table 2: Components of ammonia plant

Component	**Role**
Ammonia Converter	in which lies the catalyst; 530°C temperature and 100 to 350 bars pressure;
Cooler	removes exothermic heat and condense ammonia;
Purge	removes non-reactants;
Synthesis gas addition	addition of fresh reactants into loop;
Ammonia Separator	removes liquid ammonia (also known as catch pot);
Circulator	circulating gas through the loop equipment;

A flow sheet of a high-pressure synthesis loop is shown below in figure 4.

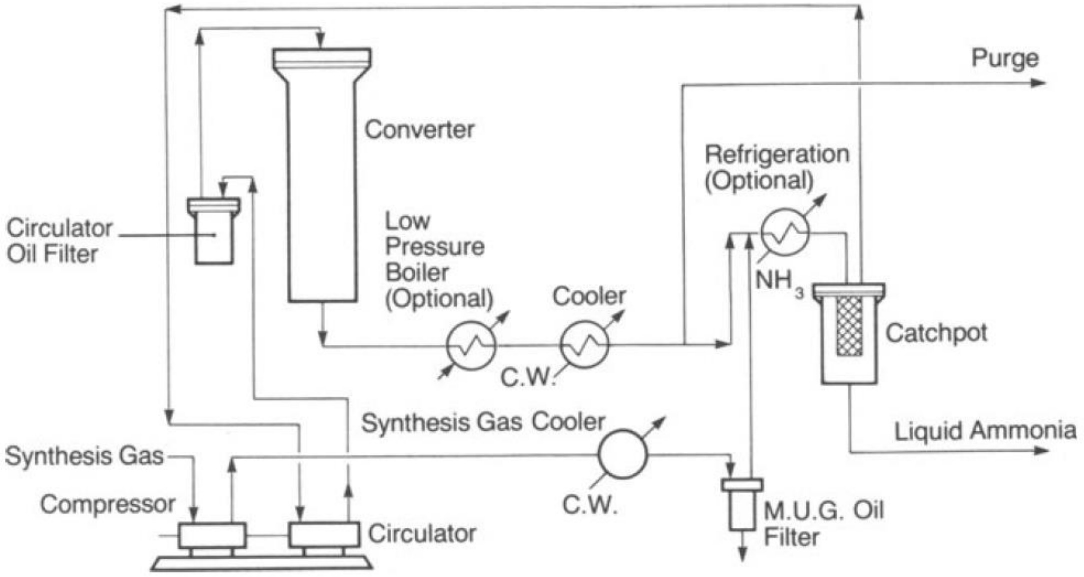

Figure 4: Flowchart for ammonia synthesis loop [1].

II.1.4 Disadvantages of H-B process

During the past century, the Haber-Bosch process was considered vital for the development of the human race. The dependence on fixed nitrogen is growing every year. The medium-term growth rate of nitrogen fertilizer is projected to be 1.4% per year (IFA2019) [10], faster than the world population growth rate of 1.1%. For 2023, global ammonia capacity is expected to reach 228 Mt NH_3. However, this high supply comes with many disadvantages. Among them, the ecological impact arising from the supply chain needed for the process and the production of ammonia itself is tremendous. In this line, associated statistics estimate that 1-2% of the world's manmade energy is consumed by this process and is responsible for a significant proportion (around 2.5%) of global carbon dioxide emissions [11], resulting in a severe environmental impact. Regarding waste management, gases from the primary reformer and steam boilers are released into the atmosphere. The admissible limit values in CO, NO_x, and SO_2 depends on the plant localizations. Wastewater is discharged with or without prior treatment to discharge (depending on their degree of pollution and the limits accepted). Finally, mud residues (cleaning of cooling circuits) must be sent to an appropriate landfill for spreading. Depending on the intended use and the operating mode of the installations, the service life of the catalysts used in ammonia production installations varies between 2 and 8 years. Most catalysts contain significant amounts of Co, Ni, Mo, Cu, Zn, Fe metal oxides and sulfides. The waste partly returns to the manufacturer for reprocessing or is recovered by metallurgical factories [1].

With that being said, alternatives to H-B for nitrogen fixation have been intensively studied.

II.2 Alternative Processes

II.2.1 Electrosynthesis

The current industrially dominating process for ammonia synthesis, the Haber-Bosch process, requires high temperatures and pressures in order to economically produce NH_3. Correspondingly significant amounts of energy, equivalent to 16 ATP moles per 2 mol of ammonia, are required in natural nitrogenase reactions. Interestingly, the need for protons and electrons for the completion of associative nitrogenase reaction (see III.4) indicated that ammonia could be synthesized via an electrochemical process. A few advantages pop into mind when we talk about ammonia production through electrosynthesis. Economically, the hydrogen which is formed from steam reforming of natural gas thus containing carbon monoxide, water vapor, sulfur compounds, usually undergoes a purification step in the traditional industrial process. Since the solid electrolyte is a selective ionic membrane, only H^+ can be transported to the cathode, thus eliminating the hydrogen purification step and therefore saving a significant fraction of the cost for ammonia production. Environmentally, in the electrochemical method, the use of gaseous hydrogen can be by-passed, depending on the temperature of operation, either steam or water in liquid form can be the used as a hydrogen source. This is why various research groups have studied in depth the production of ammonia via the electrochemical route from H_2O and N_2 [12]. One of the first studies was reported by Marnellos et al. [13] in 1998, where ammonia was electrochemically produced at atmospheric pressure (Solid State Ammonia Synthesis) SSAS. The anode was a palladium electrode as seen in figure 5 (**1:** SCY ceramic tube (H^+ conductor); **2:** Quartz tube; **3:** Cathode (Pd); **4:** Anode (Pd); **5:** Galvanostat-potentiostat; and **6:** Voltmeter) on which hydrogen flowed and was oxidized into H^+ protons, which in turn were transported through a perovskite solid electrolyte of the form of $ScCe_{0.95}Yb_{0.05}O_3$ (SCY) to reduce nitrogen at the Pd cathode and produce NH_3. The SCY was used due to its good mechanical strength and high protonic conductivity.

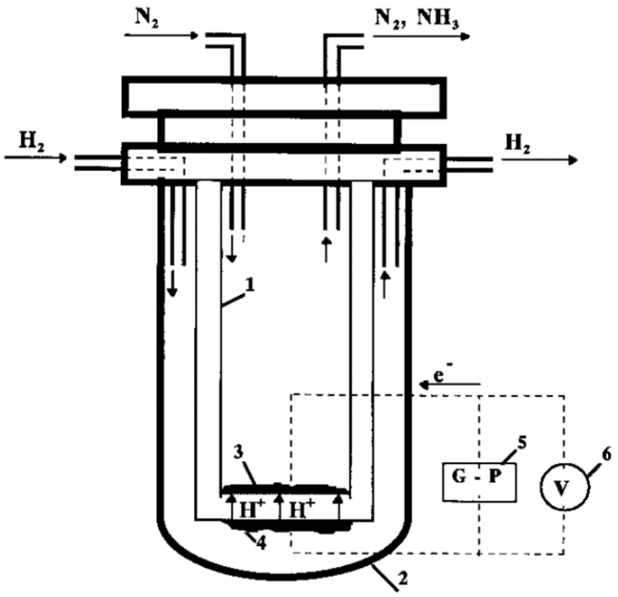

Figure 5: Schematic diagram of first cell reactor for electrosynthesis of ammonia by Marnellos [13]

With the conditions taken (I <2 mA cm^{-2}, T= 570°C; 100% H_2 at anode, He-N_2 mixture at cathode), the authors were able to convert up to 78 % of the hydrogen into ammonia. The limiting reactant was found to be the electrochemically supplied hydrogen, and N_2 partial pressure had no effect on the NH_3 formation rate. The intrinsic kinetics could not be studied at that stage, because a higher current density was not possible at 570 °C because of the ohmic resistance of SCY, and an increase in that temperature would increase the H^+ fluxes, but in turn increase the rate of NH_3 decomposition. Further work was needed in order to propose a valid mechanism for the reaction and for the optimization of the working temperature. Another report described by Wang et al. [14], suggests that a thin, rather than a bulk, electrolyte with large surface area and highly active electrodes will improve the reaction rate performance, not to mention the other advantages it accompanies. A thin electrolyte membrane may have a lower resistance loss, may help in the decrease of the operating temperature and improve current efficiency, etc. Their team prepared a thin, dense, crack free BCY15 electrolyte membrane over an anode substrate (NiO-BCY15) which also works as a catalyst. The $BaCe_{0.85}Y_{0.15}O_{3-\alpha}$ was spin coated on the anode and this following bilayer was sintered in appropriate conditions, followed by another coat of $Ba_{0.5}Sr_{0.5}Co_{0.8}Fe_{0.8}O_{3-\alpha}$. The rate of ammonia formation obtained with the membrane reactor was measured under direct current of 1 mA, and reached its maximum value at 530 °C with a rate of 4.1×10^{-9} mol s^{-1} cm^{-2}, approximately double than what has been previously reported on $BaCe_{0.85}Y_{0.15}O_{3-\alpha}$ [15].

Another notable study by Wang et al. [16], describes the synthesis of ammonia at atmospheric pressures from natural gas and nitrogen with a yttrium doped ceria (YDC) composite electrolyte YDC-$Ca_3(PO_4)_2$-K_3PO_4. The use of natural gas rather than hydrogen gas as a primary component has significant advantage, since it is widely available and relatively abundant, not to mention the difficulties with H_2 storage and additional reforming and purification steps. Ceria-salt composites have great potential as electrolytes since they not only suppress electronic conduction and enhance material stability, but also demonstrate very high ionic conductivity. The yttrium doped ceria (YDC) was prepared via a sol-gel method. The latter was then mixed with appropriate amounts of $Ca_3(PO_4)_2$ K_3PO_4, pressed and sintered to obtain the electrolyte. The cell architecture employed to produce ammonia is:

Natural gas, Ag-Pd | YDC-$Ca_3(PO_4)_2$-K_3PO_4 | Ag-Pd , N_2

The quantity of ammonia produced was observed by the change of pH in a diluted sulfuric acid solution, which was in turn analyzed by spectrophotometry and Nessler's reagent. The evolved rate of ammonia reached a maximum of 6.95×10^{-9} mol s^{-1} cm^{-2} at 650 °C upon imposing a constant potential (U=1.0 V).

A dozen reports in the literature describe electrochemical synthesis of ammonia starting by water in electrolysis rather than hydrogen in order to avoid CO_2 emissions and eliminate reforming and purification; but the formation rate of ammonia is usually several orders lower and the faradic efficiency (FE) drops to less than 1% with such change in reactants. An example on that, one study by Lan et al. [17] used Pt/C electrodes and a Nafion membrane where ammonia was formed at a rate of 0.9×10^{-10} mol s^{-1} cm^{-2} with 0.8% FE. Licht et al. [18], became intrigued by NaOH-KOH eutectic electrolyte, a molten hydroxide found in an ammonia fuel cell. By reversing the latter, they presented an electrochemical pathway to produce ammonia from air and steam and were able to reach at 2 mA cm^{-2} and 200 °C, an ammonia evolution rate of 2.4×10^{-9} mol s^{-1} cm^{-2}. Tremendous work has been done on electrochemical N_2 fixation for ammonia synthesis, all of which can be categorized as seen in the scheme below (Figure 6) by electrolyte type (polymer, aqueous, molten, solid), working temperature, or type of electrocatalyst (metal, nonmetal).

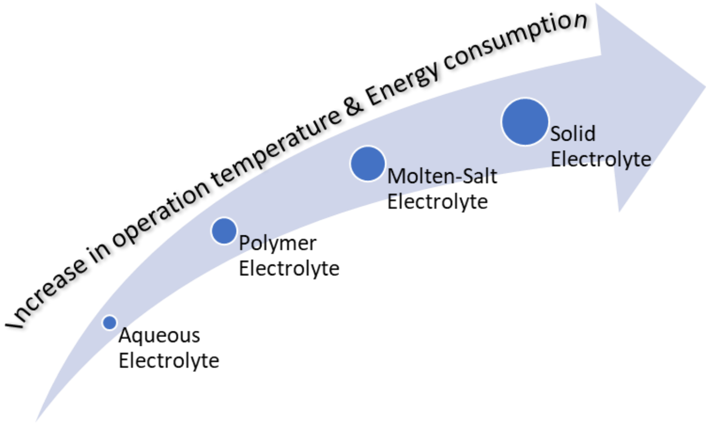

Figure 6: Scheme depicting the relationship between the operation temperature and energy and the different types of electrolytes

II.2.1.1 Solid Electrolyte

Solid State Ammonia Synthesis (SSAS) is usually held at high temperatures, with either O^{2-} conducting materials or proton conducting materials. In the majority of the cases the electrolyte material is a perovskite ($BaCe_{0.8}Gd_{0.1}Sm_{0.1}O_{3-\delta}$ (BCGS) and $BaCe_{0.9}Sm_{0.1}O_{3-\delta}$ (BCS) [19]), or can even be a fluorite or pyrochlore structure ($La_{1.95}Ca_{0.05}Ce_2O_{7-\delta}$ (LCC)[20]). When the electrolyte is a proton conducting material, the electrochemical half reactions are as follows:

$$Anode: 3H_2 \rightarrow 6H^+ + 6e^- \tag{16}$$

$$Cathode: N_2 + 6H^+ + 6e^- \rightarrow 2NH_3 \tag{17}$$

The most common reactants for such cells are gaseous hydrogen and nitrogen at the anode and cathode. The highest rates have been observed over Pd-containing catalysts. The presence of water vapor has been reported to increase the protonic conductivity of perovskite electrolytes, thus various people reported the introduction of humidified, rather than dry hydrogen over the anode [21]. O^{2-} conductor can be used for SSAS where ammonia is synthesized from gaseous nitrogen and steam according to the following:

$$Anode: 3O^{2-} \rightarrow \frac{3}{2}O_2 + 6e^- \tag{18}$$

$$Cathode: N_2 + 3H_2O + 6e^- \rightarrow 2NH_3 + 3O^{2-} \tag{19}$$

Both steam electrolysis and ammonia synthesis occur at the cathode, with reaction rates one third in magnitude of that of proton conducting cells.

II.2.1.2 Molten Salt and Composite Electrolyte

These types of electrolytes fall in the intermediate temperature range, around 300 to 500 °C. Murikami first introduced ammonia synthesis using molten salt electrolytes by establishing a LiCl-KCl-CsCl electrolyte containing 0.5 mol.% Li_3N as a source of nitrogen, and nitrogen and hydrogen gases as reactants [22]. The nitride oxidizes at the Al anode, reacts with gaseous hydrogen to produce ammonia. The nitride ions are then replenished by N_2 at the porous Ni cathode. The production rate was $3.33x10^{-8}$ mol s^{-1} cm^{-2} at 400 °C with FE of 72%. Murikami also studied the same electrolyte with different hydrogen sources such as methane, hydrogen sulfide, and hydrogen chloride [23]. In a similar study [24], hydrogen was replaced by steam on a glassy carbon anode, which resulted in a higher production rate but a lower FE due to the reaction between the carbon electrode and the oxygen ions, by-products of the ammonia synthesis reaction. The carbon anode was replaced by a boron-doped diamond in another study, but gave lower yields possibly due to the inertness of the electrode. In a more recent work, Licht et al. [25] introduced Fe_2O_3 nanopowder as a catalyst in a molten NaOH/KOH mixture (1:1). The reactants were nitrogen and steam and produced ammonia at a rate of $1x10^{-8}$ mol s^{-1} cm^{-2} at 1.45% FE.

A wide interest in composite electrolytes for hydrogen fuel cells at intermediate temperatures has been shown in the last decade [26], [27]. These consist of a mixture of a solid oxide with a second phase that changes the overall properties (thermal, mechanical, electrical). The second phase is usually a molten eutectic mixture of alkali metals (carbonates, halides, sulphates, hydroxides). A eutectic salt mixture $(Li/Ni/K)_2CO_3$ was combined with $LiAlO_2$ and examined on different cathodes that also serve as catalysts (Fe_3Mo_3N, Co_3Mo_3N, $CoFe_2O_4$)[26], [28], [29]. Co_3Mo_3N gave the best results with a maximum rate of $3.28x10^{-8}$ mol s^{-1} cm^{-2} at 450°C with FE 3.83%.

II.2.1.3 Polymer Electrolyte

There is a difference between electrolytic cells using a polymer membrane for separation and electrolytic cells with a polymer electrolyte, having two gas phase reaction chambers, categorized into two conducting polymer cells, proton and anion. The proton conducting electrolytes used in a wide range of studies are Nafion and Sulfonated polysulfone (SPSF).

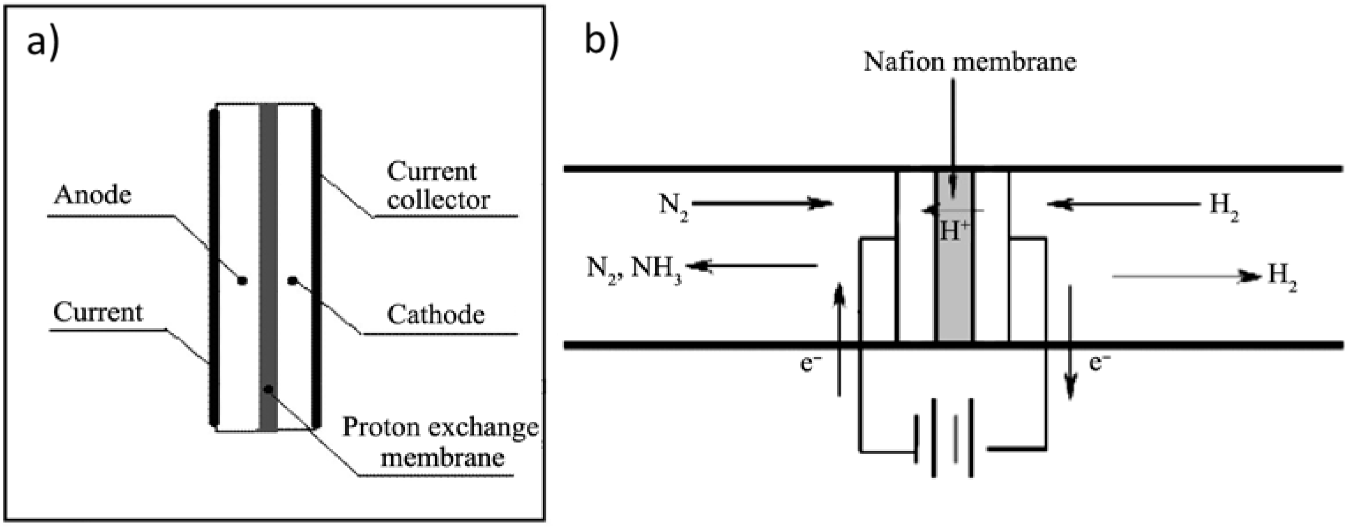

Figure 7: Work by Zhang et al. on polymer electrolytes for ammonia synthesis. a) Sketch of single cell b) sketch of cell reactor for ammonia synthesis

Zhang et al.[30] used a Nafion electrolyte that was directly connected to the cathode ($SmBaCuMO_{5+\delta}$ SBCM where M= Fe, Ni, Co) on one side, and the anode (Ni-$Ce_{0.8}Sm_{0.2}O_{2-\delta}$ SDC) on the other side as seen in figure 7. The reaction was realized at temperatures between 25-95 °C where SBCN showed the highest activity with a rate of $8.70x10^{-9}$ mol s^{-1} cm^{-2}. Many advantages can be mentioned, operation under low temperature (≤100°C), spontaneous reaction with high proton conductivity, but consequently, suffer from quite slow kinetics. Kordali et al. [31], first reported ammonia synthesis in 2000, using a Nafion electrolyte combined in KOH solution that produced ammonia from water and nitrogen. Lan et al. [32] used Nafion 211 as an electrolyte to produce ammonia from nitrogen and humidified H_2/Ar on a Pt/C catalyst. The production rate was $3.1x10^{-7}$ mol s^{-1} cm^{-2} with FE 2% for a potential difference of 0.2 V. Xue et al.[33], reported another study with Nafion as a proton-conducting electrolyte with $SmFe_{0.7}Cu_{0.1}Ni_{0.2}O_3$ as a cathode catalyst and NiO-$Ce_{0.8}Sm_{0.2}O_{2-\delta}$ as an anode catalyst starting from N_2 and H_2 at 80°C. The resulting rate of production $11.3x10^{-9}$ mol s^{-1} cm^{-2} with a faradaic efficiency of 90.4%. Anion conducting polymer has also been interesting for ammonia synthesis. Kong et al. [34],described membrane electrodes with IrO_2 as the anode catalysts and carbon fiber paper sprayed with γ-Fe_2O_3 as the cathode assembled together with an anion exchange membrane as the electrolyte. This cell showed a 3-fold increase in the production rate compared to the conventional electrolytic cell, but the FE drops from 1.9% to 0.0044% possibly due to the lower pH value in the membrane electrode thus enhancing HER (hydrogen evolution reaction) kinetics.

II.2.1.4 Aqueous Electrolyte

In recent years, aqueous electrosynthesis of ammonia has been gaining great interest due to its wide range of advantages. Its simple equipment and production at ambient temperatures and pressures make it a very promising candidate for ammonia synthesis. It is a low cost, eco-friendly process with zero carbon emission and controllable selectivity with change in potential. Another perk that should be mentioned, hydrogen gas can be avoided and substituted with water, making aqueous electrosynthesis a very potent alternative route to H-B. One of the first works was reported by Pickett et al. [35] in 1985, but yielded low amounts of ammonia on trans-$[W(N_2)_2(PMe_2Ph)_4]$ at ambient conditions, value of production rate of 0.25 mol of NH_3 per mol of cation. It was not until the 21st century for this process to properly emerge. Aqueous electrolytes can be categorized into metal based and metal free electrolytes. In 2000, Kordali et al. [31] described NRR (nitrogen reduction reaction) electrocatalytically taking place on a Ru loaded carbon cathode in KOH solution with FE 0.92% and a maximum rate of 1.3 $\mu g.h^{-1}.cm^{-2}$. Even though the rate and FE are low, (50 times lower than at 570 °C), this work is a significant contribution for NRR since it was the first attempt of ammonia synthesis at ambient temperature. A more recent work by Shi et al. [36], with a FE of 8.11% and rate of 21.4 $\mu g \cdot mgcat^{-1} \cdot h^{-1}$, carries out ammonia synthesis on Au nanoclusters dispersed on TiO_2. Finally, Wang et al. [37] described NRR performed on Pd films deposited on Ni foam resulting with an ammonia yield of 18.27 $\mu g\ h^{-1}\ mg_{cat}^{-1}$ in 0.1 M Na_2SO_4 as aqueous electrolyte.

II.2.2 Plasma Catalysis

Another method that has been evolving throughout the years for ammonia synthesis is plasma catalysis. Plasma catalysis is one of the key emerging applications in the field of low temperature plasmas. By definition, plasma catalysis is realized by placing a catalyst in the glow or after-glow region of the discharge leading to an improved processing of the input gas stream. The combination of plasma and catalysis process has brought a great deal of research interest. Ammonia synthesis via plasma catalysis has been extensively studied since the latter shows very promising potential. The presence of reactive plasma species, electrons, ions, and radical; allows efficient catalysis at ambient temperatures and atmospheric pressures. Because of this potential, many large-scale researches have been put to work such as MAPSYN in Europe (Microwave, Ultrasonic and Plasma-assisted Syntheses) and others in USA and Japan to focus on sustainable processes for ammonia production (Renewable Energy to Fuels through

Utilization of Energy-Dense Liquids (REFUEL) Program, and National Institute of Advanced Industrial Science and Technology (AIST) respectively).

The main advantages of plasma catalysis from the conventional thermochemical catalysis can be described: (*i*) plasma has high non-equilibrium characteristics that affect the catalytic process, giving many possible reactions involving the electrons, ions, radicals; (*ii*) the high energy acquired by plasma, not only drives ionization and dissociation processes, but also provides highly efficient excitation of molecules and generation of reactive intermediates which opens additional chemical reaction pathways; (*iii*) with the presence of all these highly energetic species, the gas temperature is relatively low, which is advantageous for an exothermic reaction by minimizing the loss of the product molecules and increasing the life time of the catalyst by decreasing sintering. Another contribution that should be taken into consideration is the interaction between the catalytic material and plasma. Wang et al. [38] have showed that plasma-surface interactions can result in profound differences in the performance of specific catalytic processes. The high surface area of the catalyst, extends the lifetime of short-lived active species, allows them to further react thus producing even more reactive species. These contributions make a chemically enriched and reactive environment without the need for high thermal input. To date, there are four main types of discharges that have been used for ammonia synthesis: **Radio Frequency and Microwave discharges**, **Glow Discharges**, **Dielectric Barrier Discharges,** the most exploited type, and the least explored discharge, **Arc Discharges** which will not be discussed here because there is insufficient literature on the matter.

II.2.2.1 Radio Frequency and Microwave Discharges

This type of discharge is still under development for ammonia synthesis. RF (radiofrequency) and MW (microwaves) have very similar ignition mechanisms and characteristics excluding the bulk gas temperature that is much higher in MW than in RF. In 1989, Matsumoto and his team where the first to use RF and MW discharges for ammonia synthesis with the same reactor tube and catalyst arrangement [39], [40]. They used Fe and Mo as catalysts. The main complication in their work was the quantification technique in which the ammonia adsorbed on a zeolite was followed by titration without taking into consideration its amphoteric nature, not to mention the chemisorption of ammonia on the zeolite and the NH_X radicals trapped on the zeolite surface [41]. Nevertheless, their work did lead to important findings, such as the formation of trace amounts of nitrides, or the formation of both hydrazine and ammonia [42]. Their investigations also revealed that MW plasma generates more N, H, NH_x radicals but fewer ions and yields twice the ammonia of the RF source, suggesting that these radicals are more important than ionic species for ammonia formation. In other work, they also showed that the increase of power led to a decrease in ammonia production rate relating it to high-density atomic hydrogen promoting dissociation reactions [43]. Nakajima et al. [44], explored microwave plasma at atmospheric pressure, giving it a high industrial applicability. Their reaction was plasma assisted with and without a catalyst with a high gas temperature, well above 1000 K. The ammonia yield was low, at a rate of 40 μmol min^{-1} with a concentration of 0.003%. This report showed a correlation between NH_3 concentration and the amount of NH radicals. Argon gas also increase ammonia yield, which is due to the charge transfer of argon ions according to the reactions below:

$$\boldsymbol{Charge\ transfer\ from\ Ar^+}: \quad N_2 + Ar^+ \rightarrow N_2^+ + Ar \qquad (15)$$

$$\boldsymbol{N_2H^+ ion\ formation}: \quad N_2^+ + H_2 \rightarrow N_2H^+ + H \qquad (16)$$

$$\boldsymbol{Dissociative\ recombination}: N_2H^+ + e^- \rightarrow NH + N \qquad (17)$$

Recent research groups have taken great interest in MW for ammonia synthesis[45], [46] and RF as well[47], [48]. Microwave plasma was employed to produce ammonia from methane and nitrogen by Hu and his team on a catalyst that consists of impregnated metals on alumina support. The maximum conversion was in fact low at 0.11% with an energy yield of 0.008 g_{NH3} kW^{-1} h^{-1} , and catalyst poisoning by CNT was observed. On the other hand, Carroen et al. have been lately working on transition metals and alloys with low melting points as catalysts in RF plasma, reaching energy yields as high as 0.31 g_{NH3} kW^{-1} h^{-1} [47], giving a possibility of high conversion under plasma environments. This group is also working on MOFs as catalysts that can outperform pure metals under plasma conditions for ammonia synthesis since they exhibit a dual effect in plasma, by playing the role of a catalyst and an absorber-opening pathway to materials that can store ammonia in situ [49].

II.2.2.2 Glow Discharges

A glow discharge is a plasma formed by the passage of an electric current, direct or alternating, through a gas. This type of plasma was first qualitatively employed for ammonia synthesis in 1873 by Donkin [50], but was not systematically reported until 1929 by Brewer and Westhaver [51][52]. The system consisted of high voltage, vacuum and a magnetic field; the latter did not have a major impact on the ammonia yield. Brewer also showed that AC plasma gave higher ammonia yields than DC (alternating current vs direct current) [53]. In 1968, Eremin et al.[54], [55], introduced transition metals as catalysts in plasma assisted ammonia synthesis and showed that ammonia is formed from surface reactions rather than gas-phase reactions as previously predicted by Brewer. Later on Venugopalan and his research team [56], [57], reached about 8.9% ammonia yields using AC glow discharges with Ag coated quartz electrode/catalyst. This report showed the effect of various electrode materials (Pt > SS (stainless steel) > Ag > Fe > Cu > Al > Zn) on the reaction yield and the catalytic effects in the plasma, the spatial afterglow, and in the quenching or cold-trap stage.

II.2.2.3 Dielectric Barrier Discharges

This is by far the most studied plasma discharge for ammonia synthesis due to its low processing temperature, achievable high production rates, and operation at atmospheric pressure leading to a possibility of industrial scaling. Dielectric barrier discharges (DBDs) are in a self-pulsing operation due to the insulating material between the electrodes. DBDs were initially used for the generation of the ozone. It has opened up many fields of application especially in plasma catalysis [58]. In many plasma catalysis applications, the dielectric barrier has a second role and acts as a catalyst [59]. In 1969, the first article using DBD for ammonia synthesis was published by Eremin et al. [55]. The authors used transition metals as catalysts and internal electrodes simultaneously. Pd catalyst gave the highest conversion of 3.13 %. Later in 2000, Mingdong et al. [60], confirmed that the use of a catalyst increased ammonia concentration in the exit stream by 75% (1467 mmol g^{-1} h^{-1}) by smearing magnesium oxide on the electrode and comparing the generation with and without. Furthermore, authors showed that there exists an inverse quadratic relationship between ammonia yield and the total flow rate, which was also evident in other studies by Mizushima et al. [61], [62]. The latter used metal loaded alumina membranes as catalysts in DBD, proposing that the dissociative adsorption of N_2 takes place on the alumina while ruthenium adsorbs molecular H_2 and stabilizes atomic H species, thus the surface reaction leads to ammonia. In the last decade, several groups have been working on ammonia synthesis by DBD reactors. Gomez-Ramirez et al. [63]–[65], worked on zirconium titanate and barium titanate spheres as dielectric materials and a voltage peak was observed when conversion was maximum. The conversion reached 7%, more than double of usual DBD conversions, and closer to the maximum conversion of H-B process at 15%, thus enabling it to be a potential industrial process in the future.

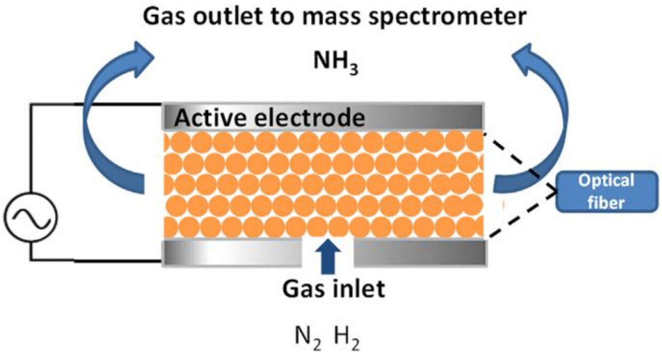

Figure 8: Sketch of reactor set-up from Gomez-Ramirez work [63]

Figure 8 depicts the reactor set-up which consisted of a stainless-steel chamber and plate as active electrodes with the bottom wall of the reactor as grounded electrode. The inter-electrode space was filled with small spherical pellets of PZT (lead zirconate titanate), and the outlet gas stream was connected to a mass spectrometer for analysis. Iwamoto et al. [66] added to Eremin's research, and worked on replacing internal electrodes with a wide range of transition metals. The order of the initial catalytic activity was Au > Pt > Pd > Ag > Cu > Fe > Mo > Ni > W > Ti > Al, demonstrating that the gold thin-wire assembly displayed the highest activity for ammonia synthesis of 73 μmol min^{-1} for a molar ratio of $H_2/N_2 = 1$. In his doctoral thesis [67], Patil carried out ammonia synthesis in DBD with transition metals loaded on alumina (namely W, Mo, Co, Ni, W, Pt, Ru, and Rh) and studied the effect of feed ratio, specific energy input, metal loading, temperature, and flowrate, 2%Rh/Alumina and 2%Ru/Alumina performed best with all changes. Very recently, he studied the addition of a range of materials, usually considered as catalyst supports (α-Al_2O_3, anatase TiO_2, MgO, CaO, γ-Al_2O_3, TiO_2, and $BaTiO_3$), and positioned in the discharge zone of plasma in order to investigate synergetic effects [68]. Size and shape of packed materials did affect the performance but solely because of the packing effect of plasma and not because of a synergetic effect between plasma and the surface. Quartz wool gave the highest ammonia yield at 2900 ppm followed by γ-Al_2O_3 at 2700 ppm. Patil also showed that unlike catalytic ammonia synthesis, plasma synthesis is more efficient at a N_2:H_2 feed ratio ≥ 2 rather than at a stoichiometric ratio of 0.33. The loading of a transition metal to γ-Al_2O_3 can enhance ammonia yield by a factor of 113% in comparison to an empty reactor. A DFT study, done by Mehta et al. [69], showed that the catalytic activity trend is different in thermal catalysis and plasma-catalysis at atmospheric pressure. The rate determining step for thermal catalysis is the dissociative adsorption of nitrogen on the metal surface. This limitation can be avoided if catalysis is coupled with non-thermal plasma. The dissociation barrier decreases for plasma-induced vibrational excitations in N_2 without influencing subsequent reaction steps. A DFT model using N_2 vibrational excitations was used to predict plasma enhancements on metal catalysts. The model shows that the optimal catalysts and active sites in plasma catalysis differ from those in thermal catalysis, and are those who bind to N_2 weakly. This shift in optimal catalyst is validated by kinetic experiments.

II.2.3 Photocatalytic Synthesis

Artificial photosynthesis of ammonia directly from sunlight, N_2, and H_2O via photocatalysis, is the optimal process for ammonia production being energy saving and environmentally friendly [70]. In 1977, Schrauzer et al.[71] firstly reported the conversion of N_2 to NH_3 and the oxidation of H_2O into O_2 simultaneously over a TiO_2 photocatalyst under UV light irradiation. Since then, many attentions have been brought to this field, but it was not until recently with the increasing demand of fixed nitrogen, this research has gathered very high momentum. The overall redox photoreduction reaction is described below:

$$2N_2 + 6H_2O \rightarrow 4NH_3 + 4O_2 \tag{18}$$

The first step, shown in figure 9, is the photoexcitation of photogenerated electrons in the valence band, their migration to the conduction band leaving holes in the valence band (+ in scheme) that will in turn facilitate the oxidation reaction ($H_2O \rightarrow O_2 + H^+$) . The second step is the separation and migration of the photo-induced carriers (H^+), to the active site of the photocatalyst' conduction band; where nitrogen fixation takes place ($N_2 + H^+ \rightarrow NH_3$) [72].

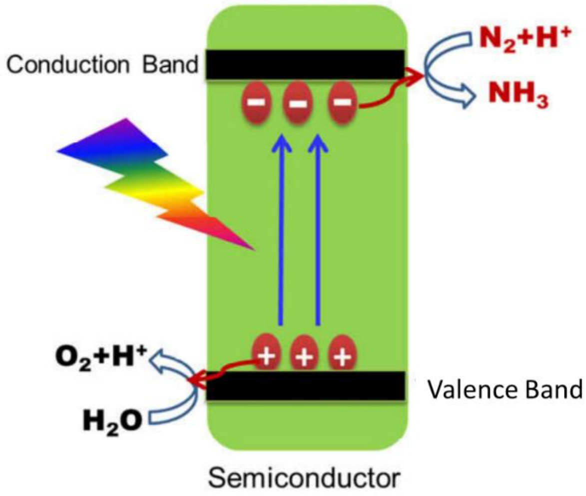

Figure 9: Scheme of photocatalytic N_2 fixation to ammonia [73]

From a thermodynamic point of view, the photocatalytic nitrogen fixation is a nonspontaneous endothermic reaction with a free Gibbs energy of $\Delta G = 339$ kJ mol^{-1} . This reaction is considered much more challenging than water splitting and needs more energy to drive the reaction in the forward. The first half-reaction is H_2O splitting to O_2 and H^+ followed by NH_3 synthesis from N_2 and H^+. Thus, a suitable photocatalyst for artificial photosynthesis must possess water oxidation ability. One of the big challenges in photocatalytic nitrogen fixation is the adsorption and activation of molecular nitrogen (strong triple bond $N \equiv N$) with a dissociation energy of ~ 941 kJ mol^{-1}, making it recognized as the rate-determining step. Another challenge that is encountered, the redox potential of a photocatalyst is determined by its band alignment [73]. The band gap should be kept as small as possible in order to maximize the solar spectrum usage around the UV, visible, and near IR regions; but not too narrow risking the recombination of the photogenerated electron-hole. Suitable band gaps must include the reduction potentials of the NRR and HER [70]. Some ameliorations were done to enhance the activity and stability of the photocatalysts where higher surface area directly relates to higher number of adsorbed nitrogen [74]. Surface modifications such as defect engineering on the surface of the catalyst can promote chemisorption and give access to a larger number of active sites [74]. Incorporation of metal dopants (Fe, Cu) into the photocatalyst structure prevent electron-hole recombination by acting as electron sinks, trapping the electrons in the active sites, this stopping them from recombining with the holes in the valence band. Iron is the mostly used dopant to improve the activity [74]. One of the first studies described on nitrogen fixation in photocatalysis was reported by Schrauzer et al.[71] in 1977, where he studied the effect of nitrogen ratio in gas flow and doping of TiO_2 (0.2% Fe_2O_3) for nitrogen fixation. The tests were conducted upon irradiation with light emitted from Hg-Arc lamp (360 W) at 50 °C and iron-doped titania under pure nitrogen gave the highest yield of 3.475 µmol g^{-1} h^{-1}. A later study by Rao et al. [75] showed that Ru doped TiO_2 is 13.6 times more active than Fe and Os doped photocatalysts (Xe lamp (150 W) at 25 °C). Another noteworthy study by Lashgari et al.[76] used a pH adjustment method on Fe_2O_3 photocatalyst to enhance its activity reaching a maximum yield of 7000 µmol $L^{-1}g^{-1}$ after 4 h of irradiation under Xe Lamp (500 W).

Photoelectrochemical cells are another class of promising setups for solar-driven nitrogen fixation. Hamer et al. [77] reported that solvated electrons on diamond generated by UV could drive the kinetically inert NRR process. In this work, diamonds with H-surface terminations were used to eject electrons into the reactant liquid by UV. These electrons are brought directly to the reactants with no requirement of molecular adsorption, thus circumventing the rate determining step of thermal catalysis. Another valuable conclusion from Hamer’s work is that an inexpensive diamond grit, for polishing, can act as a photocatalyst for N_2 reduction, yielding higher activity than Ru/TiO_2 where a rate of 1.4 µg h^{-1} was established at ambient temperature and pressure. Although H-terminated diamond retains its photocatalytic activity for several days of constant illumination, the activity is gradually reduced due to the increase of O-terminals and also the appearance of traces of nitrogen on the surface. The photoelectrochemical process for N_2 reduction is still considered a new technology with limited number of works and the mechanism of the reaction is still ambiguous with several proposed pathways [78], [79].

II.2.4 Nitrogenase

Nitrogenase is an enzyme system that biologically performs nitrogen fixation by turning dinitrogen into ammonia at ambient temperature and pressure. These proteins are O_2 sensitive and are originally found in the soil in anaerobic conditions [80]. There are three main types of nitrogenases, the most studied Mo-Fe metalloprotein where Mo is said to be the active site, V-Fe protein, and Fe protein. It was later stated that iron is the only essential transition metal in the nitrogenase, and it is in fact the active site in the FeMo cofactor [81].

The overall reaction stoichiometry is still somewhat ambiguous. The uncertainties are expressed in the following equation [82]:

$$\begin{aligned} N_2 + (6+2n)H^+ + p(6+2n)MgATP + (6+2n)e^- \\ \rightarrow 2NH_3 + nH_2 + p(6+2n)MgADP + p(6+2n)PO_4^{3-} \end{aligned} \tag{19}$$

In the ‘standard’ model, one molecule of dihydrogen is coupled to the reduction of one molecule of dinitrogen, and two molecules of ATP are hydrolyzed per electron transferred, so that n = 1 and p = 2. However, there has not been a compelling demonstration of an obligatory mechanistic coupling of dihydrogen evolution and dinitrogen reduction, although ammonia is always accompanied with dihydrogen as a product. High concentrations of Mg^{2+} can inhibit the nitrogen fixation by sequestration of ATP as an inactive Mg-ATP complex. The by-product ADP can also inhibit nitrogenase and its elimination is necessary in order to carry on the reaction [80]. Ammonia, the major product of the enzymatic nitrogen fixation, does not inhibit the reaction but rather represses the synthesis of nitrogenase system.

II.2.4.1 Biological FeMo Factor

We will go into detail on the Mo-Fe protein structure. It is divided into two proteins, homodimeric Fe protein and a heterotetrameric Mo-Fe protein, as seen in figure 10 below. The homodimeric protein is made up of two identical Fe_4S_4 with a M.W. ~ 60 000, and its role is to transfer electrons from the reducing agents to the Mo-Fe protein. The electrons are provided from pyruvate via ferredoxin and flavodoxin. The MoFe protein is an $\alpha_2\beta_2$ -heterotetramer M.W. ~ 220 000 that contains two pairs of metalloclusters, called the P-cluster and the FeMo cofactor. One of each type of metal cluster is contained in an αβ-unit. The P-cluster is made up of 2 Fe proteins, while the Mo-Fe cofactor (Fe_7MoS_9C) $MoFe_3S_3$ and Fe_4S_3 joined by three sulfide bridges.

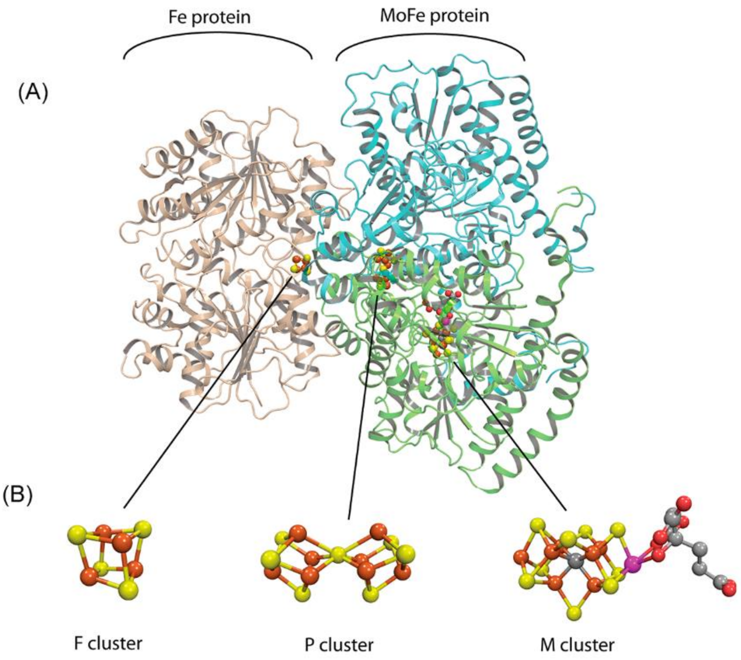

Figure 10:(A) catalytic half of the Fe protein: MoFe protein complex with the Fe protein homodimer in tan, α subunit in green, and β subunit in cyan (B) their corresponding clusters 4Fe-S Cluster (F), P-cluster (P) and FeMo-co (M). Reference of image:[83]

The cluster is bound to the protein by one Cysteine at one Fe end, and by a histidine from the Mo end. Its role is to transform N_2 into NH_3 [84]. Biological nitrogen fixation still contributes to about half of the total nitrogen input to global agriculture, the rest principally coming from nitrogenous fertilizer produced chemically from the Haber-Bosch process [84]. One of the first studies on metal complexes for ammonia generation was proceeded by Leigh et al.[85], who studied a well-defined [**$Fe^0(dmpe)_2N_2$] (dmpe = $Me_2P–CH_2CH_2$-PMe_2)** ($\nu(N_2) = 1975\ cm^{-1}$) complex that formed ammonia at 18% yield and **$Fe^{II}(dmpe)_2Cl_2$** upon the addition of HCl. The iron atom is the only electron source for the reduction, so a maximum yield of 33.3% of ammonia could theoretically be reached if the dinitrogen reaction was paired to the oxidation of Fe^0 to Fe^{II}. By changing the hydrogen concentration, through the addition of $NaBH_4$, they were able to construct a reduction cycle, also known as Leigh Cycle (Figure 11).

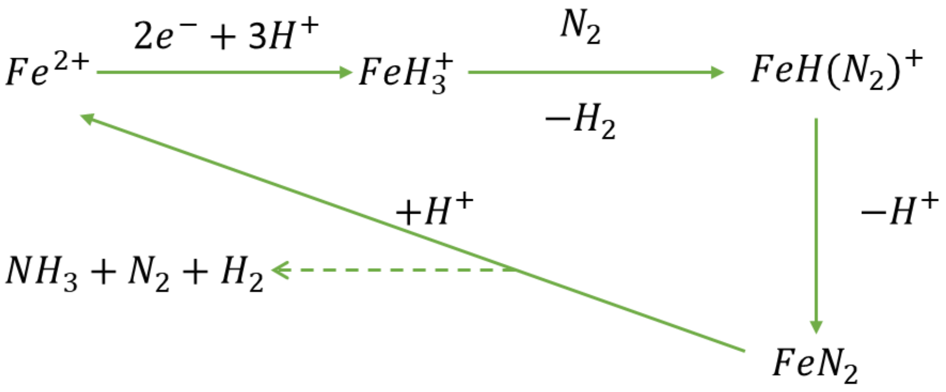

Figure 11: Leigh Cycle [85]

In 2002, Oliver Einsle presented a high-resolution structure model at 1.6 Å of the FeMo cofactor discovering a previously unrecognized interstitial atom coordinated to six iron atoms in the center of the FeMo-cofactor. It was predicted to be nitrogen which is consistent with the Thorneley and Lowe Kinetic model [86]. Recent studies through X-ray emission spectroscopy show that the six iron coordinated ligand is in fact a carbon and not nitrogen atom which drove further studies on its catalytic behavior [87]. In 2014, Hoffman et al. reported the mechanism of nitrogen fixation by nitrogenase and the five catalytic intermediates present, including the “Janus Intermediate”, a key state of N_2 reduction into 2 NH_3 [83].

II.2.4.2 Mimic Studies

Not considering the great differences in reaction conditions, the Haber-Bosch catalyst and the metal ligands in the nitrogenase show several similarities which suggests the possibility of common mechanistic elements in the reduction of dinitrogen to ammonia. Several works focused on fixing nitrogen, developing and improving synthetic catalysts based on biological mechanisms of nitrogenase. The first well-defined homogeneous catalyst for ammonia product was reported by Yandulov et al. in 2003 [88]. This catalyst is the single center Mo(III)triamidoamine complex, Mo[$(HIPTN)_3N$] (will be referred to as **Q**) where [$(HIPTN)_3N]^{3-}$, a tridentate triamidoamine ligand, is used to maximize the steric hindrance of the complex to avoid reaching the unreactive stable bimetallic complexes. **Q**(N_2) is converted into **Q**(NH_3) by a slow addition of electrons (Decamethylchromocene source) into a solution of the molybdenum catalyst containing the proton source. The yield of the reaction is around 66% which is only second to that of Fe/Mo nitrogenase at 75%. Another photoreduction of nitrogen to ammonia was described by Brown et al. [89], which examined N_2 reduction by the MoFe nitrogenase protein after being adsorbed onto CdS nanocrystals. The CdS:MoFe biohybrid protein was optimized in shape and morphology of nanocrystals. An electron donor, HEPES:

4-(2-hydroxyethyl)-1-piperazineethanesulfonic acid), with low background is required for the reaction to take place. The key components of this reaction are HEPES, CdS, light and MoFe protein, where every component is essential in order to achieve the photoexcitation under a 100% N_2 atmosphere resulting in the direct light-driven reduction of N_2 to NH_3. Illumination under ~3.5 mW cm^{-2} of 405 nm light led to NH_3 production rates of 315 ± 55 $nmol_{NH3}.mg_{MoFeprotein}{}^{-1}.min^{-1}$ at a TOF of 75 min^{-1}. N_2 reduction persisted for up to 5 hours under constant illumination with a turnover number (TON) of 1.1×10^4 mol NH_3 (mol MoFe protein)$^{-1}$. This indicates that the MoFe protein in CdS:MoFe protein bio-hybrids can function at rates comparable to physiological TOF by nitrogenase.

II.2.5 Chemical Looping

The adopted chemical looping approach is based upon a novel mechanistic consideration in which the lattice nitrogen itself is the active species. In such a scheme, ammonia generation is separated into two successive non-catalytic sub-reactions.

$M_XN_Z + 3\delta\ H_2 \rightarrow M_XN_{Z-2\delta} + 2\delta\ NH_3$ (eq. 1 discharge reaction)

$M_XN_{Z-2\delta} + \delta\ N_2 \rightarrow M_XN_Z$ (eq. 2 charge reaction)

The linkage between the sub-reactions will be ensured by a metal nitride material acting as a nitrogen transfer medium where the nitride can be reduced using H_2 in a first step to produce ammonia (discharge reaction, eq. 1) and regenerated in a second step using N_2 (charge reaction, eq. 2). The sub-reactions can be conducted in different conditions where thermodynamics are more favorable. Unlike the catalytically activated process, nitrogen chemical looping is a flexible route that allows us to optimize each sub-reaction independently. The mechanism that is followed is of Mars-Van Krevelen type, where the lattice nitrogen reacts to form ammonia, and the catalyst is then regenerated.

With a novel process such as chemical looping for ammonia synthesis, not much literature is found, and the methodology has yet to be set. Wrya et al. [90] reported Mn based nitrides promoted by sodium as a suitable nitrogen agent for chemical looping ammonia synthesis (CLAS). In his work, authors were able to perform three cycles of chemical looping in “stop mode” , and “non-stop mode”. For the stop-mode, the catalyst was removed between every step to be analyzed and then back to the furnace. Figure 12 shows the 3 cycles of “stop-mode”, where the Mn nitride was activated in a first step at 700 °C with a flow of N_2, returned to ambient temperature, where it was grounded under air, and back to 700 °C under a stream of H_2 in order to produce NH_3.

Figure 12: 3 Cycles of chemical looping in stop mode [90]

The production of ammonia was detected by colorimetry in the range of 0.5–4 ppm. The maximum theoretical NH_3 yield based on about 5 g of Mn based nitride containing about 8 wt.% of N is 28 mmol NH_3, assuming that all the lattice nitrogen has reacted to produce ammonia. The best yield achieved for the same mass is about 1.3 and 2.2 mmol NH_3 in the stop mode and non-stop mode, respectively. Wrya et al. also show that Na promoters, not only accelerate the process, but also increase the yield for ammonia formation. Another study by Laassiri et al. [91] studied lithium doped manganese nitrides for CLAS. With lithium used as a dopant, ammonia generation can be observed at a reaction temperature as low as 300 °C. In this work the role of lithium was investigated by in situ neutron diffraction studies and N_2 and H_2 isotopic exchange reactions supplemented by DFT calculations. It showed that the doping of small amounts of lithium results in high reactivity towards hydrogen thus reduces the complications of thermo-chemical stability of manganese nitride and its apparent low selectivity towards ammonia generation when undoped. 15% of the total lattice nitrogen vs 3.1 % was reacted upon the doping of lithium. Hua et al. [92] investigated the thermodynamics of different iron nitride couples that might be suitable for CLAS. In their work they show, by theoretical calculations and comparison of Gibbs free energy, the spontaneity of the reaction of nitrides with hydrogen under different conditions. The feasible Fe-based nitrogen carrier was Fe_2N/Fe_4N with most suitable conditions for the nitridation reaction of temperature of 200–500 °C, 5–20 bar, and a molar ratio of reactants of Fe and N_2 of 8:1. For the amination reaction, the conditions are, 200–400 °C, pressure is under 5 bar, Nitrogen carrier : H_2 is 2:3. According to

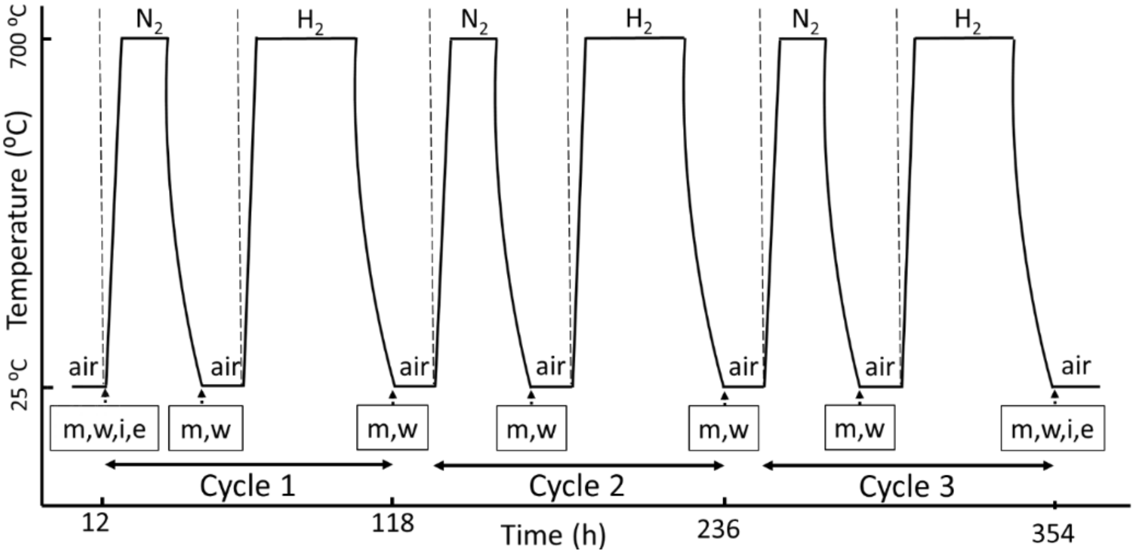

this simulation, 0.392 kmol of NH_3 is produced in one chemical loop cycle. Li et al. [93] studied the reaction for $Ru/3LaN/ZrH_2$, and showed that the doping of LaN not only decreases the activation energy, but also revealed that the $N^{3-}$of LaN reacts with H^- ions to produce NH_3, leaving behind N and H vacancies. The initial state of $Ru/xLaN/ZrH_2$ can be recovered with a full replenishment of the nitride phase under $25\%N_2:75\%H_2$ reaction medium. With a synthesis rate up to 305 $mmol_{NH3}\ g_{Ru}^{-1}\ h^{-1}$ at 350 °C under 1 MPa, this nitrogen/hydrogen carrier has potential for CLAS. Another investigation by Wang et al. [94] reported the N-sorption performance of 18 Mn-/Fe- based nitrogen carriers supported on 2−50% (w/w) Al_2O_3 within the temperature range of 700−900 °C. The objective of this study is to identify feasible nitrogen carriers with high N-sorption capability and strong mechanical properties. The general observation revealed that a lower Al_2O_3 content (≤5 wt %) together with a moderate bed temperature (800 °C) promoted the nitrogen fixation ability and physical structures of nitrogen carriers. The reaction temperature exerted a stronger effect on the performance of N carriers than the support content. Support material could only alleviate the agglomeration phenomenon to some extent at 900 °C, while it could significantly improve the gas−solid contact and well solve the aggregation problem under milder conditions. The best performing nitrogen carriers were Mn95Al4, Fe98Al2, Mn82Fe16Al2, at 800°C where the numbers correspond to the wt.% of the respective elements.

Another interesting work by Gao et al. [95] describes the activity of different transition metals (Fe Co Ni) over BaH_2 for ammonia synthesis. For a classical reaction under N_2/H_2 flow, no activity was seen for BaH_2 under 1 bar and a temperature of 300 °C, while the activity for $20\%Fe\text{-}BaH_2$ $20\%Co\text{-}BaH_2$ $20\%Ni\text{-}BaH_2$ was also modest with a rate of 384, 576, and 48 µmol g^{-1} h^{-1} respectively. Remarkably enough, authors notice an important increase in activity when they switch to a chemical looping process under the same conditions where in a first step the nitridation of the hydride support occurs under a flow of pure nitrogen, followed by the formation of ammonia through the hydrogenation of the nitridated hydride. The activities for all three catalysts increase 1703 µmol g^{-1} h^{-1} for iron, 1866 µmol g^{-1} h^{-1} for Co, and 2033 µmol g^{-1} h^{-1} thus a factor of over 40 for the activity of Ni on BaH_2.

II.2.6 H-B Alternative Catalyst

II.2.6.1 Electrides

An electride is a crystalline ionic salt in which electrons serve as anions. After the discovery of the first stable electride at room temperature, C12A7, by Hosono's team in 2003 [96], these types of materials have been extensively studied for various applications due to their exotic characteristics [97]. Electride-based catalysts, and more specifically ruthenium catalysts with electride supports have been widely studied for ammonia generation. Hosono et al. [98] investigated the inorganic electric $[Ca_{24}Al_{28}O_{64}]^{4+}(e^-)_4$ as an electride support for Ru (Figure 13).

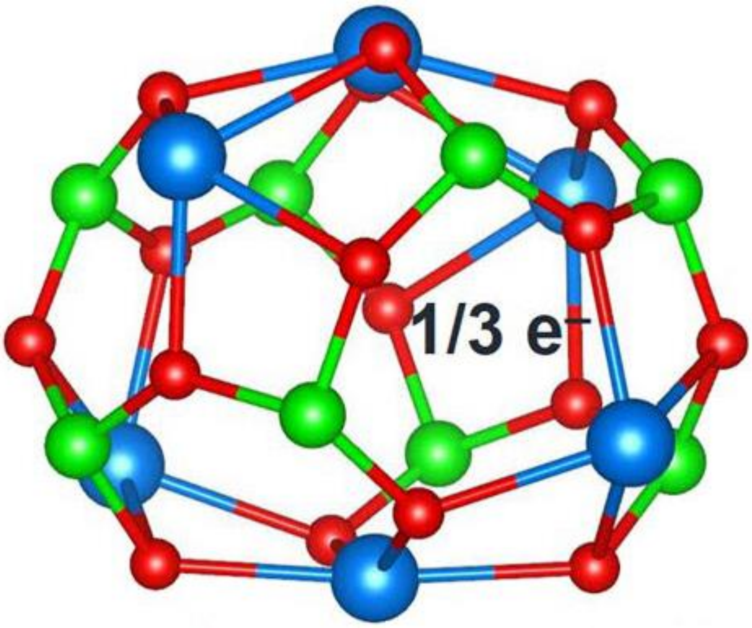

Figure 13: Crystal structure of a relaxed cage containing 1/3 e^- in C12A7:e^- [99]

With 1.2 wt.% of Ru, at 400 °C and 10 bar, the catalyst showed an activity of 8 245 µmol g^{-1} h^{-1} which was attributed to its strong electron donating ability thus facilitating the breaking of the dinitrogen triple bond (the rate determining step in the conventional mechanism) in turn decreasing the activation energy (49 kJ mol^{-1} compared to 120 kJ mol^{-1} for Ru/Cs-MgO) and its hydrogen storage ability. Another noteworthy ruthenium electride catalyst is LaRuSi [100], which after an etching pretreatment with an acidic 5 mM EDTA-2Na solution for 5 h, was able to achieve 5 340 µmol g^{-1} h^{-1} at 400 °C and 0.1 MPa. The purpose of the acidic etch is to modify the surface structure of the intermetallic, by selectively etching La and Si layers to expose more Ru active sites at the surface. An extensive kinetic study was done on Ru/C12A7:e^- (Ruthenium loaded $12CaO.7Al_2O_3$) for ammonia synthesis by Kitano et. al [101], showing the boosting effect of an electride support for the N-N triple bond cleavage thus changing the RDS to NH_x

species formation. In this report, through nitrogen/hydrogen isotopic exchange and hydrogen adsorption/desorption experiments, it is shown that fast cleavage of the triple bond is ensured by efficient electron transfer from the support to the N_2 molecules adsorbed on Ru nanoparticles. This shift in reaction mechanism is also supported by the activation energy which is 49 kJ mol^{-1} [98], unlike conventional Ru catalysts that fall in the 80-120 kJ mol^{-1} range. With 1 wt.% Ru on C12A7:e^-, under ambient pressure and 400 °C, the rate achieved was 2800 µmol g^{-1} h^{-1}. Reaction orders were also calculated [101] where the rate of ammonia synthesis r is given by: $r = k\, P_{N_2}^{\alpha}\, P_{H_2}^{\beta}\, P_{NH_3}^{\gamma}$, where k is the rate constant, and α, β, γ are the reaction orders toward N_2, H_2 and NH_3 respectively. While the reaction order is 0.8-1.0 for conventional heterogenous catalysts for ammonia synthesis, α in this case is 0.46 which is in accordance with the former statement regarding the modification of the RDS. A positive reaction order β = 0.97 on a Ru based catalyst is also not common, since Ru usually exhibits H_2 poisoning due to its high adsorption affinity. With C12A7:e^- , H adatoms can be incorporated into the support structure ($H^0 + e^- \rightarrow H^-$) and later on released ($H^- \rightarrow H^0 + e^-$); this storage-release reaction drastically decreases H_2 poisoning on Ru nanoparticles. Finally, an NH_3 reaction order of γ = -1.0 suggests an activity for ammonia decomposition. Thus, ammonia product must be directly removed from the catalytic bed.

Even with the promising activities obtained, one cannot forget the cost behind such ruthenium rich catalysts, and the energy consuming method of preparation of these electrides, with at least two weeks in arc furnace at temperature as high at 1500 °C.

II.2.6.2 Hydrides

Hydrides have also been extensively studied for ammonia synthesis as promoters/support for several metals such as Ni, Fe, Co, and of course Ru. Some hydrides have been implemented in chemical looping process mentioned earlier; thermal catalysis will be discussed here. A pioneer work by Kobayashi et al. [102] showed the activity of TiH_2 and an oxyhydride $BaTiO_{2.5}H_{0.5}$ for ammonia synthesis with no transition or noble metal addition. These materials showed a modest activity of 1-2 mmol g^{-1} h^{-1} at 400 °C and 50 bar. The authors suggested that a rare Hydrogen-MvK mechanism can be in play. The hydride was shown to partially nitride during the reaction resulting in a hydride/nitride catalyst. With an activation energy of 70-80 kJ mol^{-1} and reaction orders of $\alpha(N_2):\beta(H_2):\gamma(NH_3)$ of 0.84:0.53:-1.2, authors suppose a modification of the reaction mechanism with a change in the rate determining step. With the addition of Ru, Fe, Co on the oxyhydride $BaTiO_{2.5}H_{0.5}$ [103], the rate increases to 28.2, 14, and 5.5 mmol g^{-1} h^{-1} respectively. When compared with their oxide counterparts, the activity has increased significantly for all catalysts, with a factor of 400 for the cobalt containing catalyst. This higher activity is attributed to the elimination of H_2 poisoning that noble metals suffer at high pressures due to excessive adsorption of H_2 as seen with the conventional Ru catalyst. This hydrogen poisoning leads to negative value of the H_2 reaction order as seen with Cs-Ru/MgO with $\beta = - 0.9$ [104]. By providing adequate hydrogen spillover capacity from the active sites, the addition of the hydride avoids H_2 poisoning resulting in positive reaction orders toward H_2. In the case of Co and Fe, the use of oxyhydride support, in comparison with the oxide $BaTiO_3$ support, significantly decreases the activation energy (range of 100-130 to 50-70) and N_2 reaction order α (1.24 for Fe/$BaTiO_3$ to 0.5 for Fe/$BaTiO_{2.4}H_{0.6}$). Another example of low α was seen with Co/LiH in the work of Wang et al. [105], where the authors attributed this significantly smaller N_2-reaction order (0.48 vs conventional 1) to the creation of N-poor transition metal surfaces thus favoring the N_2 dissociation. After the dissociation, the N is transferred from the transition metal to LiH where it hydrogenated to produce NH_3, where the hydrogenation on the LiH phase becomes the rate determining step (N-H step). More works from Hosono's group, published by Hattori et al. [106], investigated the activity of Ru/CaH_2 as well as the effect of the addition of BaO. Unlike TiH_2, as far as we know, no results on the activity of CaH_2 have been reported, but numerous exist on Ru/CaH_2. An activity of around 7.4 mmolNH_3 g^{-1} h^{-1} under ambient pressure and temperatures as low as 340 °C was reported for 10 wt% Ru/CaH_2. The production rate was stable over the first 10 h of reaction, followed by a significant decrease over time informing on the deactivation of the catalyst. Upon the addition of BaO, not only is the catalyst stable for over 200 h, but also at the same conditions a superior activity of 10.5 mmol g^{-1} h^{-1} was reported. When comparing the activation energies (68 kJ mol^{-1} vs 41 kJ mol^{-1} for Ru/BaO-CaH_2) a different mechanism is proposed. The authors suggest that after a solid-state reaction between BaO and CaH_2 , a BaO-BaH_2 phase is formed on which Ru particles are favorably deposited, leading to the formation of hydride defects and hydrides through Ru, due to the ability of hydrogen release and storage reactions of BaO-BaH_2, which in turn enhances the catalytic production of ammonia. One more mention-worthy study on oxynitride-hydrides, is that on specifically Ru/$BaCeO_{3-x}N_yH_z$ [107] with an activity of 5 mmol g^{-1} h^{-1} at 300 °C and 10.1 mmol g^{-1} h^{-1} at 400°C under ambient pressure. The production of ammonia was governed by a MvK mechanism with two possible routes as shown in Figure 14. In the first route, the release of electrons back to anions vacancies (V_a) after the binding of lattice nitrogen species with either H atoms on the TM surface or H^- ions in the lattice, facilitates the N-N triple bond cleavage.

While the second route, is an associative mechanism where N-N cleaves by the addition of hydrogen. In both cases, lattice N^{3-} and H^- ions participate in the ammonia synthesis reaction which accounts for the low activation energies (40-62 kJ mol^{-1}) thus shifting the rate determining step from N_2 dissociation to N-H bond formation.

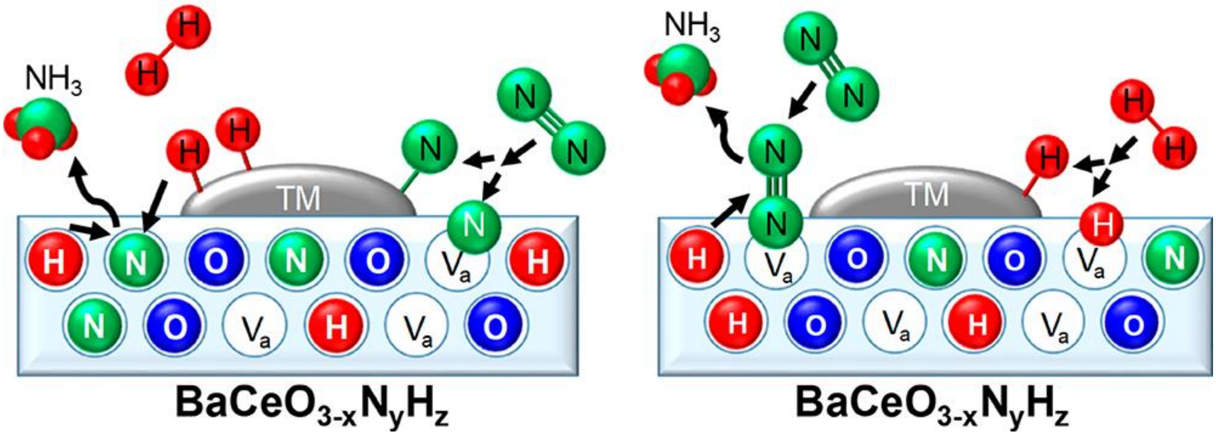

Figure 14: Two possible routes for ammonia synthesis on TM/$BaCeO_{3-x}N_yH_z$ [107]

II.2.6.3 Nitrides

Another route for ammonia synthesis that has been intensively investigated, is catalysis with nitrides. A number of studies describe the nitrogen reduction to NH_3 on bulk nitride catalysts such as binary nitrides of molybdenum, uranium, vanadium, tantalum, rhenium, cerium, and even ternary nitrides such as Co_3Mo_3N, Ni_2Mo_3N, Fe_3Mo_3N. The metal nitride material acts as a nitrogen transfer medium where the nitride can be reduced using H_2 in a first step to produce ammonia and regenerated in a second step using N_2. This nitrogen-based Mars van Krevelen mechanism is expected to result in facilitated N_2 dissociation step over N-vacancies thus diminishing the strength of the N≡N bond [11].

The N_2 binding energy is a critical point for an appropriate ammonia catalyst. In 2001, Jacobsen et al.[108], described a simple strategy in order to develop rational catalysts according to a volcano curve (Figure 15). This figure shows the turnover frequency obtained in the ammonia synthesis reaction carried out at 400 °C and 50 bar of pressure as a function of the adsorption energy of nitrogen over different metal surfaces. This curve predicts the reactivity of the metal for the ammonia synthesis thus allowing the prediction of an optimum catalyst composition. Among the pure metals, the curve shows that Os and Ru are the best catalysts. The dependence of the catalytic activity on the nitrogen adsorption energy is due to the linear relationship of (Bronsted-Evans-Polanyi) between the activation energy and rate limiting step [109]. With this curve, it is possible to observe that since Mo binds to N_2 too strongly, while Co too weakly, their binary nitride resulted in an optimum catalyst, with TOF close to that of Ru. This explains the higher activity of Co_3Mo_3N catalyst compared to the Haber-Bosch catalyst.

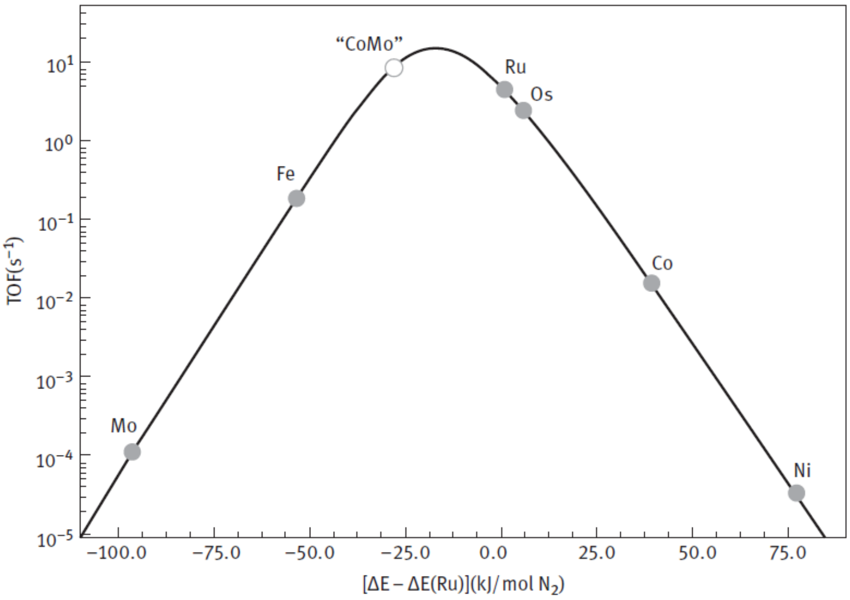

Figure 15: Calculated turnover frequencies for ammonia synthesis as a function of the adsorption energy of nitrogen. The synthesis conditions are 400°C, 50 bar, gas composition H_2:N_2 3:1 containing 5% NH_3 [11]

Hargreaves and coll. worked on several nitride materials for ammonia synthesis and nitrogen transfer properties. One of their works [110] showed that low levels of Co in tantalum nitride in fact enhances the reactivity at lower temperature. Under a flow of 60 mL min^{-1} of H_2:Ar (3:1) at 500 °C, the ammonia yield obtained was around 380 µmol during the first 5 hours and a total of 950 µmol after 24h. This amount corresponds to 52% of the total available lattice nitrogen consumed by reaction with hydrogen [110]. Another noteworthy report on tantalum nitrides, Geng et al. [111] performed a complete cleavage of the triple bond N_2 with Ta_2N^+. This disassembly and reassembly of N_2, constitutes a full catalytic cycle that provides solid evidence for the gas-phase operation of a Mars van Krevelen type mechanism. The full catalytic cycle is suggested to be governed by the donation of d-electrons from the 2 Ta metal centers into antibonding π*-orbitals of N_2 and by the concurrent shift of electrons from bonding π- and σ-orbitals of N_2 into empty d-orbitals of the metal. A DFT study was performed on the adsorption of H_2 and N_2 over Co promoted Ta_3N_5. It was shown that cobalt can lower the vacancy formation energy for nitrogen and also become active centers for chemisorption of hydrogen [112].

Manganese nitrides have also been investigated for ammonia synthesis, but are originally stable and need high temperatures to react. Laassiri et al. [113] showed that the addition of lithium as a dopant results in ammonia synthesis at temperatures as low as 300 °C. Another DFT study, by Shan et al. [114], shows that the manipulation of the geometric and electronic structure of manganese nitrides allows to increase its reactivity towards ammonia synthesis. In conventional manganese nitrides, only 3~8 % of lattice N are converted into NH_3 , while when altered with Fe, Co, or Ni, the conversion is predicted to significantly increase.

In metal nitride type catalysts, Co_3Mo_3N is by far the most studied for ammonia synthesis, for this ternary nitride system is thought to be more active than ruthenium based catalysts according to DFT calculations of TOFs for ammonia synthesis at 400 °C and 50 bar [11]. In 2001, Kojima et al.[115] first investigated Co_3Mo_3N for ammonia generation. Starting with cobalt molybdenum oxide hydrate, an ammonolysis step was performed to transform the oxide into nitride under pure ammonia for a total time of 19 hours at temperatures as high as 700°C. The nitride was then pretreated under 3:1 H_2:N_2 at 700°C for 3 h in order to activate the catalyst. The ternary nitride showed activities of 652 µmol g^{-1} h^{-1} when unpromoted at 400 °C and 1 bar and up to 869 and 986 µmol g^{-1} h^{-1} when promoted with Cs and K respectively. Other works reported on the synthesis and activity of Co_3Mo_3N, but with activities that are significantly lower than that reported by Kojima (167 µmol g^{-1} h^{-1} [116] vs 652 µmol g^{-1} h^{-1}).

To summarize the results of alternative H-B catalysts, specifically at low pressures and temperatures, table 3 reports a wide variety of them below.

Table 4: Catalytic ammonia synthesis activities at low pressures. This table has been reformulated from [117]

Catalyst	**Rate µmol.h^{-1}.g^{-1}**	**Temperature °C**	**Pressure bar**	**Ratio H_2:N_2**	**WHSV mL.g^{-1}.h^{-1}**
Fe-K_2O-Al_2O_3	330	400	1	3:1	
Co_3Mo_3N	652	400	1	3:1	9000
5%-K-Co_3Mo_3N	869	400	1	3:1	9000
30%-K- Co_3Mo_3N	364	400	1	3:1	9000
2%-Cs- Co_3Mo_3N	986	400	1	3:1	9000
20%-Fe-BaH_2	384	350	1	3:1	60 000
95%-Fe-5%Co	820.07	400	1	3:1	-
85%-Fe-15%Ni	334.354	400	1	3:1	-
1% Fe/$BaTiO_{3-x}$ H_x	14 000	400	50	3:1	66000
Fe/40%-LiH	11 428	350	10	3:1	60 000
2%Ru/HT-C12A7:e^-	2290	340	1	3:1	18 000
10%Ru/BaO-CaH_2	10 500	340	1	3:1	36 000
10%Ru/CaH_2	7400	340	1	3:1	36 000
2%Ru/$BaZrO_3$	3630	400	1	3:1	36 000
2%Ru/$BaZr_{0.9}Y_{0.1}O_3$	4000	400	1	3:1	36 000
2%Ru/MgO-6.4wt.% Cs	4200	400	26	3:1	-
4%Ru/Al_2O_3	390	400	50	3:1	-
LaRuSi	5340	400	1	3:1	36 000
CeRuSi	5480	400	1	3:1	36 000
$CoRe_4$	943	400	1	3:1	12 000
Co/C 0.87 Ba/Co	43 200	400	10	3:1	-
Co 11.5 wt% CeO_2, Ba	195 880	400	63	3:1	175 000
ɣ-Mo_2N	34	400	1	3:1	9000
β-$Mo_2N_{0.78}$	35	400	1	3:1	9000
δ-Mo_2N	4	400	1	3:1	9000
Co_3Mo_3N	167	400	1	3:1	9000
Fe_3Mo_3N	95	400	1	3:1	9000
Ni_2Mo_3N	29	400	1	3:1	9000

II.3 Concluding remarks

Considered as a major discovery of the 20th century, and now needed to supply nearly 70% of the world population, ammonia and its synthesis process have been and will continue to be a major focus of academic research. Over 150 million tons of ammonia are produced each year, making it the second most manufactured chemical in the world. While 80% of ammonia production is used in the fertilizer industry, many other industries rely on NH_3 for the manufacture of many products (explosives, some plastics and chemicals, some pharmaceuticals). Recent works have highlighted ammonia for energy storage applications, due to its potential as a carbon-free molecule that hydrogen storage. With this high demand for ammonia, the conventional industrial process, H-B process, yields in significant environmental disadvantages, whether it is the sizeable carbon footprint or the important energy consumption. The need for efficient low-pressure and decentralized ammonia synthesis is therefore becoming urgent. Many recent studies propose new catalysts operating under mild synthesis conditions, using various approaches such as electrosynthesis, photocatalysis, plasma-assisted catalysis as alternatives to traditional thermal catalysis which all have both strong and weak suits. In the case of H-B alternative catalysts for low pressure low temperature synthesis, the following limitations are present in the technologies today:

i. Catalyst operating at low temperature and low pressure: In order to operate the transition from reformed H_2 (produced from natural gas) to electrolyzed H_2 (from water) the working pressure must be between 10-50 bar (alkaline electrolysis). Optimized conditions should be found to work at lower temperatures in the pressure range, to retain sufficient conversion at the thermodynamic equilibrium. Many of the competitor catalysts, developed for Haber Bosch conditions, are not active before a pretreatment process at high temperatures and show no activity at T lower than 400°C.

ii. Oxygen poisoning: Traces of oxygen in the gas feed leads to poisoning of catalysts greatly reducing their activity. Extensive purification of gas feeds, as existing in the Haber Bosch industrial units, result in higher costs industrially and more energy consumption. The engineering of a catalyst that is oxygen tolerant is essential for large scale.

iii. Stability: The incorporation of these catalysts in a reaction system can only be done if the catalysts are stable at the working T and P

iv. The cost: in any industrial process, an economic point of view must be considered. Even with very active and promising catalysts, their expensive precursors will limit their application in real processes in the case of Ru based formulations (electrides, Ru supported).

v. Scalability: To transition from a research laboratory scale to an industrial scale, methods of preparation and scalability must be considered. Processes such as ammonolysis and long annealing hours in arc furnaces render these catalysts harder for large batch production (case of nitrides and electrides).

II.4 References

[1] J. R. Jennings, *Catalytic Ammonia Synthesis*. 1991.

[2] “Gerhard Ertl – Facts. NobelPrize.org. Nobel Media AB 2020. Thu. 2 Jul 2020.”

[3] H. Shen *et al.*, “Electrochemical ammonia synthesis: Mechanistic understanding and catalyst design,” *Chem*, vol. 7, no. 7, pp. 1708–1754, 2021, doi: 10.1016/j.chempr.2021.01.009.

[4] G. Soloveichik, “Electrochemical synthesis of ammonia as a potential alternative to the Haber–Bosch process,” *Nat. Catal.*, vol. 2, no. 5, pp. 377–380, 2019, doi: 10.1038/s41929-019-0280-0.

[5] L. Lloyd, *Handbook of Industrial Catalysts*, 1st ed. 20. New York, NY: Springer US, 2011.

[6] G. Veser, “Taking the pressure off,” *Nat. Energy*, vol. 3, no. 12, pp. 1025–1026, 2018, doi: 10.1038/s41560-018-0293-y.

[7] C. D. Zeinalipour-Yazdi, J. S. J. Hargreaves, S. Laassiri, and C. R. A. Catlow, “The integration of experiment and computational modelling in heterogeneously catalysed ammonia synthesis over metal nitrides,” *Phys. Chem. Chem. Phys.*, vol. 20, no. 34, pp. 21803–21808, 2018, doi: 10.1039/c8cp04216k.

[8] K. Altenburg, H. Bosch, J. G. Van Ommen, and P. J. Gellings, “The role of potassium as a promoter in iron catalysts for ammonia synthesis,” *J. Catal.*, vol. 66, no. 2, pp. 326–334, 1980, doi: 10.1016/0021-9517(80)90037-8.

[9] ICIS, “Kellog- It has the technology.” icis.com/explore/resources/news/1998/06/01/60812/kellog-it-has-the-technology/ (accessed Jul. 15, 2020).

[10] IFA(International Fertilizer Association), PIT, and Market Intelligence and Argiculture Services, “Executive Summary Fertilizer Outlook 2019-2023,” in *IFA Annual Conference*, 2019, no. June, pp. 26–28, [Online]. Available: file:///C:/Users/3PX67LA_RS5/Downloads/2019_IFA_Annual_Conference_Montreal_Fertilizer_Outlook_2019-2023_Summary.pdf.

[11] J. S. J. Hargreaves, “Heterogeneously catalyzed ammonia synthesis,” in

Hydrogenation, 2018, pp. 173–192.

[12] V. Kyriakou, I. Garagounis, E. Vasileiou, A. Vourros, and M. Stoukides, “Progress in the Electrochemical Synthesis of Ammonia,” *Catal. Today*, vol. 286, pp. 2–13, 2017, doi: 10.1016/j.cattod.2016.06.014.

[13] G. Marnellos and M. Stoukides, “Ammonia synthesis at atmospheric pressure,” *Science (80-.).*, vol. 282, no. 5386, pp. 98–100, 1998, doi: 10.1126/science.282.5386.98.

[14] W. B. Wang, X. B. Cao, W. J. Gao, F. Zhang, H. T. Wang, and G. L. Ma, “Ammonia synthesis at atmospheric pressure using a reactor with thin solid electrolyte BaCe0.85Y0.15O3-α membrane,” *J. Memb. Sci.*, vol. 360, no. 1–2, pp. 397–403, 2010, doi: 10.1016/j.memsci.2010.05.038.

[15] Y. Guo, B. Liu, Q. Yang, C. Chen, W. Wang, and G. Ma, “Preparation via microemulsion method and proton conduction at intermediate-temperature of BaCe1−xYxO3−α,” *Electrochem. commun.*, vol. 11, no. 1, pp. 153–156, 2009, doi: https://doi.org/10.1016/j.elecom.2008.10.038.

[16] B. H. Wang, J. De Wang, R. Q. Liu, Y. H. Xie, and Z. J. Li, “Synthesis of ammonia from natural gas at atmospheric pressure with doped ceria-Ca3(PO4)2-K3PO4 composite electrolyte and its proton conductivity at intermediate temperature,” *J. Solid State Electrochem.*, vol. 11, no. 1, pp. 27–31, 2006, doi: 10.1007/s10008-005-0042-6.

[17] R. Lan and S. Tao, “Electrochemical synthesis of ammonia directly from air and water using a Li+/H+/NH4+ mixed conducting electrolyte,” *RSC Adv.*, vol. 3, no. 39, pp. 18016–18021, 2013, doi: 10.1039/c3ra43432j.

[18] S. Licht, C. Baochen, W. Baohui, L. Fang-Fang, L. Jason, and Liu Shuzhi, “Ammonia Synthesis by N2 and Steam Electrolysis in molten hydroxide suspensions of nanoscale Fe2O3,” vol. 345, no. 6197, pp. 637–640, 2014, doi: 10.1126/science.1254234.

[19] Z.-J. Li, R.-Q. Liu, J.-D. Wang, Y.-H. Xie, and F. Yue, “Preparation of BaCe0.8Gd0.2O3−δ by the citrate method and its application in the synthesis of ammonia at atmospheric pressure,” *J. Solid State Electrochem.*, vol. 9, no. 4, pp. 201–204, 2005, doi: 10.1007/s10008-004-0582-1.

[20] J.-D. Wang, Y.-H. Xie, Z.-F. Zhang, R.-Q. Liu, and Z.-J. Li, “Protonic conduction in Ca2+-doped La2M2O7 (M=Ce, Zr) with its application to ammonia synthesis

electrochemically," *Mater. Res. Bull.*, vol. 40, no. 8, pp. 1294–1302, 2005, doi: https://doi.org/10.1016/j.materresbull.2005.04.008.

[21] K. Wang, D. Smith, and Y. Zheng, "Electron-driven heterogeneous catalytic synthesis of ammonia : Current states and perspective," *Carbon Resour. Convers.*, 2018, doi: 10.1016/j.crcon.2018.06.004.

[22] T. Murakami, T. Nishikiori, T. Nohira, and Y. Ito, "Electrolytic Synthesis of Ammonia in Molten Salts under Atmospheric Pressure," *J. Am. Chem. Soc.*, vol. 125, no. 2, pp. 334–335, Jan. 2003, doi: 10.1021/ja028891t.

[23] T. Murakami, T. Nohira, Y. H. Ogata, and Y. Ito, "Electrolytic Ammonia Synthesis in Molten Salts under Atmospheric Pressure Using Methane as a Hydrogen Source," *Electrochem. Solid-State Lett.*, vol. 8, no. 4, p. D12, 2005, doi: 10.1149/1.1870633.

[24] T. Murakami, T. Nohira, T. Goto, Y. H. Ogata, and Y. Ito, "Electrolytic ammonia synthesis from water and nitrogen gas in molten salt under atmospheric pressure," *Electrochim. Acta*, vol. 50, no. 27, pp. 5423–5426, 2005, doi: https://doi.org/10.1016/j.electacta.2005.03.023.

[25] F.-F. Li and S. Licht, "Advances in Understanding the Mechanism and Improved Stability of the Synthesis of Ammonia from Air and Water in Hydroxide Suspensions of Nanoscale Fe2O3," *Inorg. Chem.*, vol. 53, no. 19, pp. 10042–10044, Oct. 2014, doi: 10.1021/ic5020048.

[26] I. A. Amar, R. Lan, C. T. G. Petit, and S. Tao, "Electrochemical Synthesis of Ammonia Using Fe 3 Mo 3 N Catalyst and Carbonate-Oxide Composite Electrolyte," vol. 10, pp. 3757–3766, 2015.

[27] I. A. Amar, R. Lan, and S. Tao, "Electrochemical Synthesis of Ammonia Directly from Wet N2Using La0.6Sr0.4Fe0.8Cu0.2O3-δ-Ce0.8Gd0.18Ca0.02O2-δComposite Catalyst," *J. Electrochem. Soc.*, vol. 161, no. 6, pp. H350–H354, 2014, doi: 10.1149/2.021406jes.

[28] I. A. Amar, R. Lan, C. T. G. Petit, and S. Tao, "Electrochemical Synthesis of Ammonia Based on Co3Mo3N Catalyst and LiAlO2–(Li,Na,K)2CO3 Composite Electrolyte," *Electrocatalysis*, vol. 6, no. 3, pp. 286–294, 2015, doi: 10.1007/s12678-014-0242-x.

[29] I. A. Amar, C. T. G. Petit, G. Mann, R. Lan, P. J. Skabara, and S. Tao,

"Electrochemical synthesis of ammonia from N2 and H2O based on (Li,Na,K)2CO3–Ce0.8Gd0.18Ca0.02O2−δ composite electrolyte and CoFe2O4 cathode," *Int. J. Hydrogen Energy*, vol. 39, no. 9, pp. 4322–4330, 2014, doi: https://doi.org/10.1016/j.ijhydene.2013.12.177.

[30] Z. ZHANG, Z. ZHONG, and R. LIU, "Cathode catalysis performance of SmBaCuMO5+δ (M=Fe, Co, Ni) in ammonia synthesis," *J. Rare Earths*, vol. 28, no. 4, pp. 556–559, 2010, doi: https://doi.org/10.1016/S1002-0721(09)60153-8.

[31] V. Kordali, G. Kyriacou, and C. Lambrou, "Electrochemical synthesis of ammonia at atmospheric pressure and low temperature in a solid polymer electrolyte cell," *Chem. Commun.*, no. 17, pp. 1673–1674, 2000, doi: 10.1039/B004885M.

[32] R. Lan and S. Tao, "Electrochemical synthesis of ammonia directly from air and water using a Li+/H+/NH4+ mixed conducting electrolyte," *RSC Adv.*, vol. 3, no. 39, pp. 18016–18021, 2013, doi: 10.1039/C3RA43432J.

[33] G. Xu, R. Liu, and J. Wang, "Electrochemical synthesis of ammonia using a cell with a Nafion membrane and SmFe0.7Cu0.3−xNixO3 (x = 0−0.3) cathode at atmospheric pressure and lower temperature," *Sci. China Ser. B Chem.*, vol. 52, no. 8, pp. 1171–1175, 2009, doi: 10.1007/s11426-009-0135-7.

[34] J. Kong *et al.*, "Electrochemical Synthesis of NH3 at Low Temperature and Atmospheric Pressure Using a γ-Fe2O3 Catalyst," *ACS Sustain. Chem. Eng.*, vol. 5, no. 11, pp. 10986–10995, Nov. 2017, doi: 10.1021/acssuschemeng.7b02890.

[35] C. J. Pickett and J. Talarmin, "Electrosynthesis of ammonia," *Nature*, vol. 317, no. 6038, pp. 652–653, 1985, doi: 10.1038/317652a0.

[36] M.-M. Shi *et al.*, "Au Sub-Nanoclusters on TiO2 toward Highly Efficient and Selective Electrocatalyst for N2 Conversion to NH3 at Ambient Conditions," *Adv. Mater.*, vol. 29, no. 17, p. 1606550, May 2017, doi: 10.1002/adma.201606550.

[37] Z. Wang *et al.*, "Pore-Size-Tuned Pd Films Grown on Ni Foam as an Advanced Catalyst for Electrosynthesis of Ammonia," *ACS Sustain. Chem. Eng.*, vol. 8, no. 31, pp. 11827–11833, Aug. 2020, doi: 10.1021/acssuschemeng.0c04295.

[38] L. Wang, Y. Zhao, C. Liu, W. Gong, and H. Guo, "Plasma driven ammonia decomposition on a Fe-catalyst: eliminating surface nitrogen poisoning," *Chem.*

Commun., vol. 49, no. 36, pp. 3787–3789, 2013, doi: 10.1039/c3cc41301b.

[39] Uyama H and Matsumoto O, "Synthesis of ammonia in high frequency discharges 0.2. Synthesis of ammonia in a microwave discharge under various conditions," *Plasma Chem. Plasma Process*, vol. 9, no. 3, pp. 421–432, 1989.

[40] Uyama H and Matsumoto O, "Synthesis of ammonia in high-frequency discharges," *Plasma Chem. Plasma Process*, vol. 9, pp. 13–24, 1989.

[41] Uyama H, Uchikura T, N. H, and Matsumoto O, "Synthesis of ammonia with RF discharge. Adsorption of products on zeolite," *Chem. Lett.*, vol. 16, pp. 555–8, 1987.

[42] Uyama H, Matsumoto O, Nakamura T, and Tanaka S, "Catalytic effect of iron wires on the syntheses of ammonia and hydrazine in a radio-frequency discharge," *Plasma Chem. Plasma Process*, vol. 13, pp. 117–31, 1993.

[43] Tanaka S, Uyama H, and Matsumoto O, "Synergistic effects of catalysts and plasmas on the synthesis of ammonia and hydrazine," *Plasma Chem. Plasma Process*, vol. 14, pp. 491–504, 1994.

[44] Nakajima J and Sekiguchi H, "Synthesis of ammonia using microwave discharge at atmospheric pressure," *Thin Solid Films*, vol. 516, no. 13, pp. 4446–4451, 2008.

[45] Bai Xinwei, Tiwari Sarojini, Brandon Robinson, K. Casey, Li Lili, and Hu Jianli, "Microwave Catalytic Synthesis of Ammonia from Methane and Nitrogen," *Catal. Sci. Technol.*, vol. 8, no. 24, pp. 6302–6305, 2018, doi: 10.1039/c8cy01355a.

[46] Tiwari S B, Xinwei Hu, and In J, "Effect of γAl2O3 supported Co and Fe catalysts on synthesis of ammonia from CH4 and N2 using microwave plasma." pp. 18th AIChE Annual Meeting (Pittsburgh, PA, 31 Octo, 2018.

[47] Shah J, Harrison J, and Carreon M, "Ammonia plasmacatalytic synthesis using low melting point alloys," *Catalysts*, vol. 8, p. 437, 2018.

[48] Shah J, Wang W, Bogaerts A, and Carreon M L, "Ammonia synthesis by radio frequency plasma catalysis: revealing the underlying mechanisms," *ACS Appl. Energy Mater.*, vol. 1, pp. 4824–39, 2018.

[49] Shah J, Wu T, Lucero J, Carreon M A, and Carreon M L, "Nonthermal Plasma Synthesis of Ammonia over Ni-MOF-74," *ACS Sustain. Chem. Eng.*, vol. 7, pp. 377–

83, 2019.

[50] Donkin W F, “On the direct synthesis of ammonia,” *Proc. R. Soc.*, vol. 21, pp. 281–2, 1873.

[51] Brewer K A and J. Westhaver, “Chemical action in the glow discharge IV,” *J. Phys. Chem.*, vol. 34, pp. 1280–93, 1930.

[52] Brewer K A and J. Westhaver, “The synthesis of ammonia in the glow discharge 33 883–95,” *J. Phys. Chem.*, vol. 33, pp. 883–95, 1929.

[53] Brewer K A and J. Westhaver, “Chemical action in the glow discharge II.* Further investigation on the synthesis of ammonia,” *J. Phys. Chem.*, vol. 34, pp. 153–64, 1930.

[54] Eremin E N and Maltsev A N, “Activity of heterogeneous catalysts in the synthesis of ammonia in the glow discharge,” *Russ. J. Phys. Chem.*, vol. 9, pp. 1235–7, 1968.

[55] Eremin EN, Maltsev AN, and Syaduk VL, “Behaviour of a catalyst in a glow-discharge plamsa,” *Russ. J. Phys. Chem.*, vol. 3, p. 43, 1969.

[56] Yin K S and Venugopalan M, “Plasma chemical synthesis. I. Effect of electrode material on the synthesis of ammonia,” *Plasma Chem. Plasma Process*, vol. 3, pp. 343–50, 1983.

[57] Touvelle M, Licea J M, and Venugopalan M, “Plasma chemical synthesis. II. Effect of wall surface on the synthesis of ammonia,” *Plasma Chem. Plasma Process*, vol. 7, pp. 101–8, 1987.

[58] R. Brandenburg, “Corrigendum: Dielectric barrier discharges: progress on plasma sources and on the understanding of regimes and single filaments (Plasma Sources Science and Technology (2017) 26 (053001) DOI: 10.1088/1361-6595/aa6426),” *Plasma Sources Sci. Technol.*, vol. 27, no. 7, 2018, doi: 10.1088/1361-6595/aaced9.

[59] J. Hong, S. Prawer, and A. B. Murphy, “Plasma Catalysis as an Alternative Route for Ammonia Production: Status, Mechanisms, and Prospects for Progress,” *ACS Sustain. Chem. Eng.*, vol. 6, no. 1, pp. 15–31, 2018, doi: 10.1021/acssuschemeng.7b02381.

[60] Mingdong B, Xiyao B, Zhitao Z, and Mindi B, “Synthesis of ammonia in a strong electric field discharge at ambient pressure,” *Plasma Chem. Plasma Process*, vol. 20, pp. 511–20, 2000.

[61] Mizushima T, Matsumoto K, Sugoh J-I, Ohkita H, and Kakuta N, “Tubular membrane-like catalyst for reactor with dielectric-barrier-discharge plasma and its performance in ammonia synthesis,” *Appl. Catal. A*, vol. 265, pp. 53–9, 2004.

[62] Mizushima T, Matsumoto K, Ohkita H, and Kakuta N, “Catalytic effects of metal-loaded membrane-like alumina tubes on ammonia synthesis in atmospheric pressure plasma by dielectric barrier discharge,” *Plasma Chem. Plasma Process*, vol. 27, pp. 1–11, 2007.

[63] Gomez-Ramirez A, Montoro-Damas A M, Cotrino J, Lambert R M, and Gonzalez-Elipe A R, “About the enhancement of chemical yield during the atmospheric plasma synthesis of ammonia in a ferroelectric packed bed reactor,” *Plasma Process. Polym.*, vol. 14, p. 1600081, 2017.

[64] Gomez-Ramirez A, Cotrino J, Lambert R, and Gonzalez- Elipe A, “Efficient synthesis of ammonia from N2 and H2 alone in a ferroelectric packed-bed DBD reactor,” *Plasma Sources Sci. Technol.*, vol. 24, pp. 65–11, 2015.

[65] Gomez-Ramirez A M-D A M, Rico V, Rodriguez M A, Cortino J, Lambert R M, and Gonzalez-Elipe A R, “Ammonia production in a packed-bed dielectric barrier discharge reactor,” 2015.

[66] Iwamoto M, Akiyama M, Aihara K, and Deguchi T, “Ammonia synthesis on wool-like Au, Pt, Pd, Ag, or Cu electrode catalysts in nonthermal atmospheric-pressure plasma of N2 and H2,” *ACS Catal.*, vol. 7, pp. 6924–9, 2017.

[67] B. S. Patil, “Plasma (catalyst)-assisted nitrogen fixation: reactor development for nitric oxide and ammonia production,” Eindhoven University of Technology, 2017.

[68] B. S. Patil *et al.*, “Deciphering the synergy between plasma and catalyst support for ammonia synthesis in a packed dielectric barrier discharge reactor,” *J. Phys. D. Appl. Phys.*, vol. 53, no. 14, 2020, doi: 10.1088/1361-6463/ab6a36.

[69] Mehta P *et al.*, “Overcoming ammonia synthesis scaling relations with plasma-enabled catalysis,” *Nat. Catal.*, vol. 1, pp. 269–75, 2018.

[70] K. Ithisuphalap, H. Zhang, L. Guo, Q. Yang, H. Yang, and G. Wu, “Photocatalysis and Photoelectrocatalysis Methods of Nitrogen Reduction for Sustainable Ammonia Synthesis,” *Small Methods*, vol. 3, no. 6, pp. 1–20, 2019, doi:

10.1002/smtd.201800352.

[71] G. N. Schrauzer and T. D. Guth, “Photolysis of Water and Photoreduction of Nitrogen on Titanium Dioxide,” *J. Am. Chem. Soc.*, vol. 99, no. 22, pp. 7189–7193, Oct. 1977, doi: 10.1021/ja00464a015.

[72] X. Xue *et al.*, “Review on photocatalytic and electrocatalytic artificial nitrogen fixation for ammonia synthesis at mild conditions: Advances, challenges and perspectives,” *Nano Res.*, vol. 12, no. 6, pp. 1229–1249, 2019, doi: 10.1007/s12274-018-2268-5.

[73] R. Li, “Photocatalytic nitrogen fixation: An attractive approach for artificial photocatalysis,” *Cuihua Xuebao/Chinese J. Catal.*, vol. 39, no. 7, pp. 1180–1188, 2018, doi: 10.1016/S1872-2067(18)63104-3.

[74] R. Shi, Y. Zhao, G. I. N. Waterhouse, S. Zhang, and T. Zhang, “Defect engineering in photocatalytic nitrogen fixation,” *ACS Catal.*, vol. 9, no. 11, pp. 9739–9750, 2019, doi: 10.1021/acscatal.9b03246.

[75] N. N. Rao, S. Dube, Manjubala, and P. Natarajan, “Photocatalytic reduction of nitrogen over (Fe, Ru or Os) /TiO2 catalysts,” *Appl. Catal. B Environ.*, vol. 5, no. 1, pp. 33–42, 1994, doi: https://doi.org/10.1016/0926-3373(94)00042-5.

[76] M. Lashgari and P. Zeinalkhani, “Photocatalytic N2 conversion to ammonia using efficient nanostructured solar-energy-materials in aqueous media: A novel hydrogenation strategy and basic understanding of the phenomenon,” *Appl. Catal. A Gen.*, vol. 529, pp. 91–97, 2017, doi: https://doi.org/10.1016/j.apcata.2016.10.017.

[77] D. Zhu, L. Zhang, R. E. Ruther, and R. J. Hamers, “Photo-illuminated diamond as a solid-state source of solvated electrons in water for nitrogen reduction,” *Nat. Mater.*, vol. 12, no. 9, pp. 836–841, 2013, doi: 10.1038/nmat3696.

[78] M. Ali *et al.*, “Nanostructured photoelectrochemical solar cell for nitrogen reduction using plasmon-enhanced black silicon,” *Nat. Commun.*, vol. 7, no. 1, p. 11335, 2016, doi: 10.1038/ncomms11335.

[79] K. Ithisuphalap, H. Zhang, L. Guo, Q. Yang, H. Yang, and G. Wu, “Photocatalysis and Photoelectrocatalysis Methods of Nitrogen Reduction for Sustainable Ammonia Synthesis,” *Small Methods*, vol. 3, no. 6, p. 1800352, 2019, doi: doi:10.1002/smtd.201800352.

[80] R. R. Eady and P. J. R., “Nitrogenases,” *Nature*, vol. 249, pp. 805–810, 1974, doi: 10.1007/978-1-4939-8864-8_1.

[81] J. Liu *et al.*, “Nitrogenase-mimic iron-containing chalcogels for photochemical reduction of dinitrogen to ammonia,” *Proc. Natl. Acad. Sci. U. S. A.*, vol. 113, no. 20, pp. 5530–5535, 2016, doi: 10.1073/pnas.1605512113.

[82] D. C. Rees and J. B. Howard, “Nitrogenase : standing at the crossroads,” *Curr. Opin. Chem. Biol.*, vol. 4, pp. 559–566, 2000.

[83] B. M. Hoffman, D. Lukoyanov, Z. Y. Yang, D. R. Dean, and L. C. Seefeldt, “Mechanism of nitrogen fixation by nitrogenase: The next stage,” *Chem. Rev.*, vol. 114, no. 8, pp. 4041–4062, 2014, doi: 10.1021/cr400641x.

[84] B. E. Smith, “Nitrogenase Reveals Its Inner Secrets,” *Science (80-.).*, vol. 297, pp. 1654–1655, 2002, doi: 10.1126/science.1076659.

[85] G. J. Leigh and M. J. Tenorio, “Exchange of Dinitrogen between Iron and Molybdenum Centers and the Reduction of Dinitrogen Bound to Iron Implications for the Chemistry of Nitrogenases,” *J. Am. Chem. Soc.*, vol. 113, no. 9, pp. 5862–5863, 1991.

[86] O. Einsle *et al.*, “Nitrogenase MoFe-Protein at 1.16 A Resolution: A Central Ligand in the FeMo-Cofactor,” *Science (80-.).*, vol. 297, pp. 1696–1699, 2002.

[87] K. M. Lancaster *et al.*, “X-Ray Emission Spectroscopy Evidences a Central Carbon in the Nitrogenase Iron-Molybdenum Cofactor,” *Science (80-.).*, vol. 334, pp. 974–976, 2011, doi: 10.5061/dryad.6m0f6870.

[88] D. V Yandulov and R. R. Schrock, “Catalytic Reduction of Dinitrogen to Ammonia at a Single Molybenum Center,” *Science (80-.).*, vol. 301, 2003, doi: 10.1126/science.1085326.

[89] K. A. Brown *et al.*, “Light-driven dinitrogen reduction catalyzed by a CdS:nitrogenase MoFe protein biohybrid,” *Science (80-.).*, vol. 352, no. 6284, pp. 448–450, 2016, doi: 10.1126/science.aaf2091.

[90] W. M. Aframehr, C. Huang, and P. H. Pfromm, “Chemical Looping of Manganese to Synthesize Ammonia at Atmospheric Pressure: Sodium as Promoter,” *Chem. Eng. Technol.*, vol. 43, no. 10, pp. 2126–2133, 2020, doi: 10.1002/ceat.202000154.

[91] S. Laassiri, C. D. Zeinalipour-Yazdi, N. Bion, C. R. A. Catlow, and J. S. J. Hargreaves, " Combination of theoretical and in situ experimental investigations of the role of lithium dopant in manganese nitride: a two-stage reagent for ammonia synthesis ," *Faraday Discuss.*, 2021, doi: 10.1039/c9fd00131j.

[92] J. Hua, K. Wang, Q. Wang, and R. Peng, "Feasibility of Fe-based nitrogen carrier for chemical looping ammonia synthesis: thermodynamics," *J. Therm. Anal. Calorim.*, no. 0123456789, 2020, doi: 10.1007/s10973-020-10029-x.

[93] L. Li *et al.*, "Operando spectroscopic and isotopic-label-directed observation of LaN-promoted Ru/ZrH2 catalyst for ammonia synthesis via associative and chemical looping route," *J. Catal.*, vol. 389, pp. 218–228, 2020, doi: 10.1016/j.jcat.2020.05.039.

[94] B. Wang, H. Guo, X. Yin, and L. Shen, "N-Sorption Capability of Al2O3-Supported Mn-/Fe-Based Nitrogen Carriers during Chemical Looping Ammonia Synthesis Technology," *Energy and Fuels*, vol. 34, no. 8, pp. 10247–10255, 2020, doi: 10.1021/acs.energyfuels.0c01000.

[95] W. Gao *et al.*, "Production of ammonia via a chemical looping process based on metal imides as nitrogen carriers," *Nat. Energy*, vol. 3, no. 12, pp. 1067–1075, 2018, doi: 10.1038/s41560-018-0268-z.

[96] S. Matsuishi *et al.*, "High-Density Electron Anions in a Nanoporous Single Crystal: [Ca24Al28O64]4+(4e-).," *ChemInform*, vol. 34, no. 44, pp. 626–630, 2003, doi: 10.1002/chin.200344015.

[97] H. Hosono and M. Hirano, *Function cultivation in transparent oxides utilizing natural and artificial nanostructures*. Elsevier Ltd, 2006.

[98] M. Kitano *et al.*, "Ammonia synthesis using a stable electride as an electron donor and reversible hydrogen store," *Nat. Chem.*, vol. 4, no. 11, pp. 934–940, 2012, doi: 10.1038/nchem.1476.

[99] N. Kuganathan, A. Chroneos, and R. W. Grimes, "The encapsulation selectivity for anionic fission products imparted by an electride," *Sci. Rep.*, vol. 9, no. 1, pp. 1–11, 2019, doi: 10.1038/s41598-019-50089-0.

[100] J. Li *et al.*, "Acid-durable electride with layered ruthenium for ammonia synthesis: boosting the activity via selective etching," *Chem. Sci.*, vol. 10, no. 22, pp. 5712–5718,

2019, doi: 10.1039/C9SC01539F.

[101] M. Kitano *et al.*, “Electride support boosts nitrogen dissociation over ruthenium catalyst and shifts the bottleneck in ammonia synthesis,” *Nat. Commun.*, vol. 6, pp. 1–9, 2015, doi: 10.1038/ncomms7731.

[102] Y. Kobayashi *et al.*, “Titanium-Based Hydrides as Heterogeneous Catalysts for Ammonia Synthesis,” *J. Am. Chem. Soc.*, vol. 139, no. 50, pp. 18240–18246, 2017, doi: 10.1021/jacs.7b08891.

[103] Y. Tang *et al.*, “Metal-Dependent Support Effects of Oxyhydride-Supported Ru, Fe, Co Catalysts for Ammonia Synthesis,” *Adv. Energy Mater.*, vol. 8, no. 36, pp. 1–9, 2018, doi: 10.1002/aenm.201801772.

[104] F. Rosowski, A. Hornung, O. Hinrichsen, D. Herein, M. Muhler, and G. Ertl, “Ruthenium catalysts for ammonia synthesis at high pressures: Preparation, characterization, and power-law kinetics,” *Appl. Catal. A Gen.*, vol. 151, no. 2, pp. 443–460, 1997, doi: 10.1016/S0926-860X(96)00304-3.

[105] P. Wang *et al.*, “Breaking scaling relations to achieve low-temperature ammonia synthesis through LiH-mediated nitrogen transfer and hydrogenation,” *Nat. Chem.*, vol. 9, no. 1, pp. 64–70, 2017, doi: 10.1038/nchem.2595.

[106] M. Hattori *et al.*, “Enhanced Catalytic Ammonia Synthesis with Transformed BaO,” *ACS Catal.*, vol. 8, no. 12, pp. 10977–10984, 2018, doi: 10.1021/acscatal.8b02839.

[107] M. Kitano *et al.*, “Low-Temperature Synthesis of Perovskite Oxynitride-Hydrides as Ammonia Synthesis Catalysts,” *J. Am. Chem. Soc.*, vol. 141, no. 51, pp. 20344–20353, 2019, doi: 10.1021/jacs.9b10726.

[108] C. J. H. Jacobsen, S. Dahl, B. G. S. Clausen, S. Bahn, A. Logadottir, and J. K. Nørskov, “Catalyst design by interpolation in the periodic table: Bimetallic ammonia synthesis catalysts [2],” *J. Am. Chem. Soc.*, vol. 123, no. 34, pp. 8404–8405, 2001, doi: 10.1021/ja010963d.

[109] A. Logadottir, T. H. Rod, J. K. Nørskov, B. Hammer, S. Dahl, and C. J. H. Jacobsen, “The Brønsted-Evans-Polanyi relation and the volcano plot for ammonia synthesis over transition metal catalysts,” *J. Catal.*, vol. 197, no. 2, pp. 229–231, 2001, doi: 10.1006/jcat.2000.3087.

[110] S. Laassiri, C. D. Zeinalipour-Yazdi, C. R. A. Catlow, and J. S. J. Hargreaves, "Nitrogen transfer properties in tantalum nitride based materials," *Catal. Today*, vol. 286, pp. 147–154, 2017, doi: 10.1016/j.cattod.2016.06.035.

[111] C. Geng, J. Li, T. Weiske, and H. Schwarz, "Complete cleavage of the N≡N triple bond by Ta2N+ via degenerate ligand exchange at ambient temperature: A perfect catalytic cycle," *Proc. Natl. Acad. Sci. U. S. A.*, vol. 116, no. 43, pp. 21416–21420, 2019, doi: 10.1073/pnas.1913664116.

[112] C. D. Zeinalipour-Yazdi, J. S. J. Hargreaves, S. Laassiri, and C. R. A. Catlow, "DFT-D3 study of H2 and N2 chemisorption over cobalt promoted Ta3N5-(100), (010) and (001) surfaces," *Phys. Chem. Chem. Phys.*, vol. 19, no. 19, pp. 11968–11974, 2017, doi: 10.1039/c7cp00806f.

[113] S. Laassiri, C. D. Zeinalipour-Yazdi, C. R. A. Catlow, and J. S. J. Hargreaves, "The potential of manganese nitride based materials as nitrogen transfer reagents for nitrogen chemical looping," *Appl. Catal. B Environ.*, vol. 223, pp. 60–66, 2018, doi: 10.1016/j.apcatb.2017.04.073.

[114] N. Shan *et al.*, "Manipulating the Geometric and Electronic Structures of Manganese Nitrides for Ammonia Synthesis," *ChemCatChem*, vol. 12, no. 8, pp. 2233–2244, 2020, doi: 10.1002/cctc.201902383.

[115] R. Kojima and K. I. Aika, "Cobalt molybdenum bimetallic nitride catalysts for ammonia synthesis," *Chem. Lett.*, vol. 1, no. 5, pp. 514–515, 2000, doi: 10.1246/cl.2000.514.

[116] D. Mckay, "Catalysis over Molybdenum Containing Nitride Materials," *Philosophy*, no. December, 2007.

[117] J. Humphreys, R. Lan, and S. Tao, "Development and Recent Progress on Ammonia Synthesis Catalysts for Haber–Bosch Process," *Adv. Energy Sustain. Res.*, vol. 2, no. 1, p. 2000043, 2021, doi: 10.1002/aesr.202000043.

Chapter II: Experimental Overview

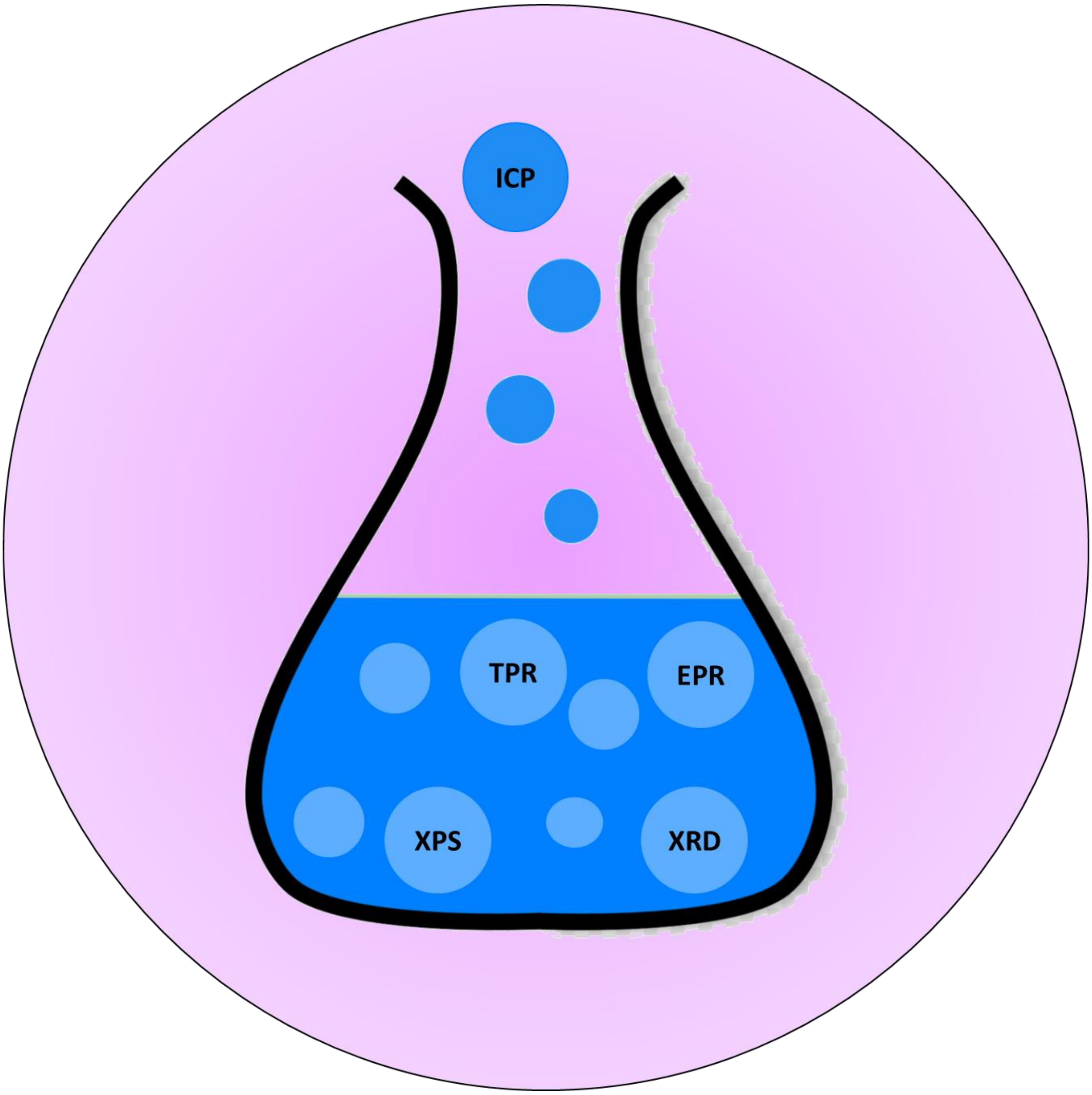

III. Chapter II: Experimental Overview

III.1 Material Synthesis

III.1.1 Starting Materials

All chemicals needed for the preparation of the catalysts mentioned in the manuscript were used without further purification: tetraethylorthosilicate ($Si(OC_2H_5)_4$, TEOS, 98 wt.%, Sigma-Aldrich), non-ionic triblock co-polymer Pluronic P123 (poly(ethylene glycol)-*block*-poly(propylene glycol)-*block*-poly(ethylene glycol), average MW~5 800, Sigma-Aldrich), cobalt nitrate ($Co(NO_3)_2.6H_2O$, 98%, Sigma Aldrich), ammonium para-heptamolybdate $(NH_4)_6Mo_7O_{24}.4.H_2O$, 99%, Alfa Aesar), Al_2O_3 (Saint-Gobain NORPRO SA6176), SiO_2 (Saint-Gobain NORPRO SS61138), TiO_2 (Saint-Gobain NORPRO ST61120) and CeO_2 (Solvay ECL15), Cesium nitrate ($CsNo_3$, 99.8%, Alfa Aesar), Gallium metal (Ga, 99.9%, Alfa Aesar), Molybdenum Carbide (Mo_2C -325 mesh, 99.5 % Alfa Aesar), cobalt chloride hexahydrate ($CoCl_2.6H_2O$, 98%, Sigma Aldrich).

III.1.2 Bulk Mo_2N, and dispersed Mo_2N on different supports

Preparation of Mo_2N. Molybdenum oxide was first prepared by a hydrothermal synthesis method. The Mo precursor (ammonium molybdate tetrahydrate) was dissolved in distilled water. The pH was adjusted to 1 by adding dropwise a 2M solution of HNO_3. Thereafter, the solution was submitted for 12 h to hydrothermal ageing at 180 °C in a Teflon-lined autoclave. After recovering by filtration, the solid was washed with water until neutral pH and dried at 60 °C overnight. The sample was then calcined at 300 °C, 1.5 °C min^{-1} during 5h. The resulting oxides were nitrided during the pretreatment. All nitridation steps will be described in part III.1 (Ammonolysis and Pretreatment.)

Preparation of SBA-15 silica. SBA-15 was synthesized according to a classical procedure initially proposed by Zhao et al [1]. 4 g of Pluronic P123 was dissolved in a 1.6 M solution of HCl at 40 °C under stirring for 24 h. Then, 8.5 g of tetraethyl orthosilicate (TEOS) was added dropwise and left under stirring at 40 °C for 24 h. The resulting suspension was submitted to a hydrothermal ageing at 100 °C during 24 h. After recovering by filtration and washing with water, the solid was dried at 80 °C overnight and then calcined at 550 °C for 6 h at a heating rate of 1.5 °C min^{-1}.

Preparation of Mo-N/support catalysts Supported molybdenum oxides were prepared over different commercial supports (Al_2O_3, SiO_2, TiO_2 and CeO_2) and calcined mesostructured silica

(SBA-15). Molybdenum oxide loading was fixed to 10 wt.% over each support. The supported materials were synthesized by incipient wetness impregnation (IWI). The calculated weight of Mo precursor ($(NH_4)_6Mo_7O_{24}.4H_2O$) was dissolved in a volume corresponding to the pore volume of the respective support and then mixed. The mixture was aged during 5 days at 25 °C and then calcined at 400 °C, 1.5 °C min^{-1} for 5 h.

All the samples underwent a pretreatment step before the catalytic reaction in order to transform the oxide into nitride (III.1).

III.1.3 Bulk Co_3Mo_3N, and dispersed Co_3Mo_3N on different supports

Preparation of Co_3Mo_3N. Firstly, $CoMoO_4$ was prepared by dissolving the required quantities of cobalt nitrate and ammonium heptamolybdate in deionized water (4.00 g Mo precursor and 5.59 g of Co precursor) The solution was then heated under reflux at 85 °C for 12 h. The resulting purple precipitate was recovered by filtration and washed with deionized water and then ethanol, after being dried at 100 °C for 12 h. The powder was then calcined at 500 °C (1.5 °C min^{-1}) for 6 h to form the desired $CoMoO_4$ phase. After calcination, the oxide was converted to its nitride counterpart (Co_3Mo_3N) by an ammonolysis step described in III.1.

Preparation of CoMo-N/SBA-15 catalysts. The SBA-15 support was prepared according to a hydrothermal method, under acidic conditions as described in the previous section. CoMo/SBA-15 catalysts with different loadings (X=10, 20, 30 wt.%) were prepared by an adapted impregnation-infiltration protocol. In the first step, Mo was impregnated on SBA-15 by incipient wetness impregnation followed by mild drying (IWI). The aqueous molybdenum precursor solution was mixed with the support and gently dried at 25 °C for 5 days. The solid was then calcined at 400 °C (1.5 °C min^{-1}) for 5 h. At this step, SBA-15 supported MoO_3 is obtained. In a second step, cobalt was added to the as prepared solid by Melt Infiltration (MI) method. In this method, the cobalt nitrate precursor was first ground with Mo-SBA-15 powder. The resulting solid was then transferred in a Teflon-lined autoclave and submitted to a thermal treatment at 57 °C for 4 days. Then, the solid was calcined at 500 °C (5 °C min^{-1}) for 5 h. Ammonolysis and pretreatment were performed to obtain the corresponding nitride before reaction. (See III.1)

III.1.4 Mo-based MXenes and Co incorporation

The starting material of our MXene multilayers, is the corresponding MAX phase, in our case Mo_2Ga_2C. For this synthesis, appropriate masses of Ga and Mo_2C were added into a quartz tube and placed under vacuum, and annealed at 850 °C for 360 h. A tilted furnace, and the constant rotation of the tube ensured that the phases do not separate. The resulting product was washed overnight with concentrated HCl in order to remove any excess of unreacted Ga to give us Mo_2Ga_2C. Mo_2CT_x multilayer MXenes are prepared by etching Ga from the MAX like phase Mo_2Ga_2C using HF as an etchant as seen in previous work [2]. 4 g of Mo_2Ga_2C where added slowly into a solution of 40 mL of 50% HF and left to etch under stirring at 55 °C for 100 h. The following solution was centrifuged and washed several times until obtaining a neutral pH (~6-7) and then dried in a vacuum oven at 70 °C for 24 h in order to obtain multilayer Mo_2CT_x. A wetness impregnation method was used where 1 g of Mo_2CT_x was impregnated by a volume of 1 mL of precursor solution. The solution was then left in a desiccator for 4 days under ambient temperature. The resulting product was annealed under a flow of 120 mL min^{-1} of Argon at 350 °C for 5 h. Different loadings of cobalt were prepared (1, 5 ,10 wt.%) and different precursors (cobalt chloride and cobalt nitrate) in order to study the effect of both the precursor and the loading percentage.

III.2 Characterization Techniques

This chapter describes all the characterization techniques used throughout the manuscript for structural, morphological, textural, surface, elemental, chemical, and thermal properties, with more detailed information on the most used techniques.

III.2.1 Structural Properties

III.2.1.1 PXRD

PXRD is an analytical technique that allows to examine the crystal structure of powder-like materials. It allows the identification of crystalline phases *via* determination of lattice structural parameters, and can provide an estimation of crystallite size. Within the X-ray source, the cathode, consisting of a filament, is heated to produce electrons which are accelerated by the application of a voltage and used to bombard the anode, a copper tube. When the electrons have sufficient energy to free the inner shell electrons of Cu, they produce characteristic Cu X-Rays, Cu Kα lines, having an energy (E) of ~8.04 keV and a wavelength (λ) of 1.54 Å . These X-rays are collimated and directed towards the sample. It is essential to note that X-Ray diffraction is based on the elastic scattering of X-Rays by atoms that compose a matter periodic lattice structure. Thus, constructive interference takes place once the scattered X-Ray photons become "in phase" which further enables their detection. Therefore, diffraction of X-Rays by crystal planes allows to determine interplanar lattice distance (d) by applying the Bragg's law: $n\lambda = 2d\sin\theta$; where n is an integer describing the "order" of reflection; λ is the X-Ray wavelength, d is the interplanar lattice distance and θ is the angle of incidence. Upon measuring 2θ which is the angle between the incident and the diffracted beam, one can derive the corresponding interplanar distances d which are characteristic of a certain given crystalline compound.

Wide angle PXRD

Wide angle PXRD patterns were collected using a Bruker X-ray AXS D8 Advance diffractometer in Bragg-Brentano geometry configuration fitted with a LynxEye Super Speed detector. XRD patterns were recorded with Cu Kα radiation (λ = 1.54184 Å) at 40 kV and 30 mA. Patterns are recorded over a 2θ range of 10-80 °, at a step size of 0.02 °/step and a counting time of 0.5 s/step. Crystal phase identification was made by comparison with the ICDD database.

For the MXene series, patterns are recorded over a 2θ range of 5-120 °, at a step size of 0.02 °/step and a counting time of 7 s/step.

Low angle PXRD

Low angle PXRD was performed on a Xeuss 2.0 (Xenocs) instrument operating under vacuum with a GeniX3D microsource (λ = 1.54184 Å) at 0.6 mA and 50 kV and a 2D Pilatus 3R 200K detector. This technique was used in order to study the ordered pore crystallinity in SBA-15.

III.2.1.2 Nuclear Magnetic Resonance Spectroscopy (NMR)

NMR is a non-destructive spectroscopic technique used to analyze the molecular structure at the atomic level of a sample. It is fundamentally based on the fact that many nuclei have spin, and all nuclei are electrically charged. An energy transfer between the base energy to a higher energy level is possible upon the application of an external magnetic field. This energy transfer takes place at a wavelength that corresponds to a radio frequency, and when the spin returns to its base level, same frequency energy is also emitted. The signals that match this transfer are measured and processed to yield an NMR spectrum. The exact resonant frequency of this energy transfer is dependent on the effective magnetic field at the nucleus, which is affected by electron shielding, which also depends on the chemical environment. Thus, in brief, the more electronegative the nucleus is, the higher the resonant frequency. A term "Chemical shift" was defined as $\delta = (\nu-\nu_0)/\nu_0$ expressed in ppm where ν is the frequency measured while ν_0 is the frequency of TMS used to normalize the spectrum as a proton reference frequency. The most commonly used NMR nuclei are ^{1}H, ^{13}C, and ^{15}N. For our work, samples obtained in powder form were separately packed into either 7 mm or 1.3 mm (outer diameter) rotors. All 1D ^{1}H and

2D ^1H-^1H correlation experiments were performed on a Bruker Advance NEO4 800 MHz solid-state NMR spectrometer, equipped with a 1.3 mm double-resonance magic-angle spinning (MAS) probe head with 50 kHz magic-angle spinning (MAS), operating at room temperature. 1D ^1H MAS NMR spectra of all samples were acquired with 32 co-added transients. 2D ^1H-^1H spin diffusion spectra were acquired with FIDs, each with 4 co-added transients [3]. All ^1H chemical shifts are calibrated with respect to neat TMS using adamantane as an external reference (^1H resonance, 1.85 ppm). All 1D ^{29}Si MAS NMR experiments were performed on a Bruker Avance II 400 MHz equipped with a 7 mm double-resonance MAS probehead.

III.2.1.3 Electron Paramagnetic Resonance (EPR)

Electron paramagnetic resonance spectroscopy (EPR), also called electron spin resonance (ESR), is a technique used to study chemical species with unpaired electrons. The basic theory behind EPR is analogous to NMR, where the main difference is that in EPR, we study electron spin properties, whereas nuclear spins in NMR. Since the mass of an electron is much lower than that of a proton, the magnetic fields in EPR are less intense than those of NMR, and of higher frequency. EPR uses microwave radiation to probe paramagnetic species (species with unpaired electrons), thus can be very helpful when studying transition metal complexes. In order to understand the principle of EPR, the Zeeman effect comes first to mind. An electron placed under a magnetic field (B_0) behaves like a magnet and aligns with the axis of the field in two possible orientations (spin), either aligned with the field (low spin); or aligned opposite to the magnetic field (high spin). This splitting, also known as the Zeeman splitting, creates a ΔE for paramagnetic species, where $\Delta E = h\nu = g \beta B_o$ (h: Planck’s constant, ν: Frequency, g: g factor, β: Bohr’s magneton). CW EPR (continuous wave) experiments were recorded at 9.5 GHz using the Bruker high temperature resonator at 700°C, under 75 vol.% H_2/N_2 following the kinetics, where the spectra were collected for 2 h with a spectrum recorded each 40. The experimental set up was a modulation amplitude of 1G and a microwave power of 5mW.

III.2.2 Textural Properties

III.2.2.1 N_2 Physisorption

Nitrogen physisorption is a typical analysis done to probe the textural properties of porous materials at N_2 liquefaction temperature, 77 K. The most useful characteristics quantified by N_2 physisorption include surface area (SA), total pore volume (V_t) and pore size distribution (PSD). The critical step prior to a measurement is the sample preparation, done by outgassing it under vacuum at elevated temperatures to liberate its surface from pre-adsorbed molecules. Once outgassed, the sample is exposed to N_2 gas which is adsorbed onto the sample surface through Van der Waals-type weak physical interactions. The quantity of adsorbed gas progressively increases with N_2 pressure therefore yielding a specific adsorption isotherm, while the reverse process results in a desorption isotherm. The resulting adsorption-desorption isotherm serves as a general fingerprint of the porous nature of a material indicating its micro (<2 nm), meso (2-50 nm), macro (>50 nm) or non-porous features. The conventional assessment method used for measuring SA is the "Brunauer-Emmett-Teller method" (BET). It is based on the multi-layer model of adsorption and allows estimation of the surface area by considering the monolayer capacity or the gas quantity in the monolayer and the cross-sectional area of the gas molecule (~0.162 nm^2 for N_2). At the same time, the total pore volume is estimated using the gas quantity at relative pressure close to 1 *i.e.* ~0.99, where it is mostly converted to liquid. In this work, textural properties of the synthesized materials were measured by N_2 physisorption experiments performed at 77 K using a Micromeritics Tristar II instrument. Before analysis, a known mass (~50 mg) of solid was treated at 250 °C for 4-6 h .The specific surface area (S_{BET}) was calculated using the BET method, on the linear part of the BET plot (p/p_0 <0.3). The total pore volume was calculated on the adsorption branch of the isotherms at a p/p_0 value of 0.99.

III.2.3 Morphological Properties

The size and shape of solid particles are routinely examined *via* various types of electron microscopy techniques. Interaction of the matter with high-energy electrons (primary electron beam) having wavelengths in the range of interatomic distances or even smaller causes a variety of phenomena (Figure 1). Thus-produced electrons are used to further derive valuable information on the chemical composition or internal structure of a sample under study therefore greatly expanding the application of electron microscopy.

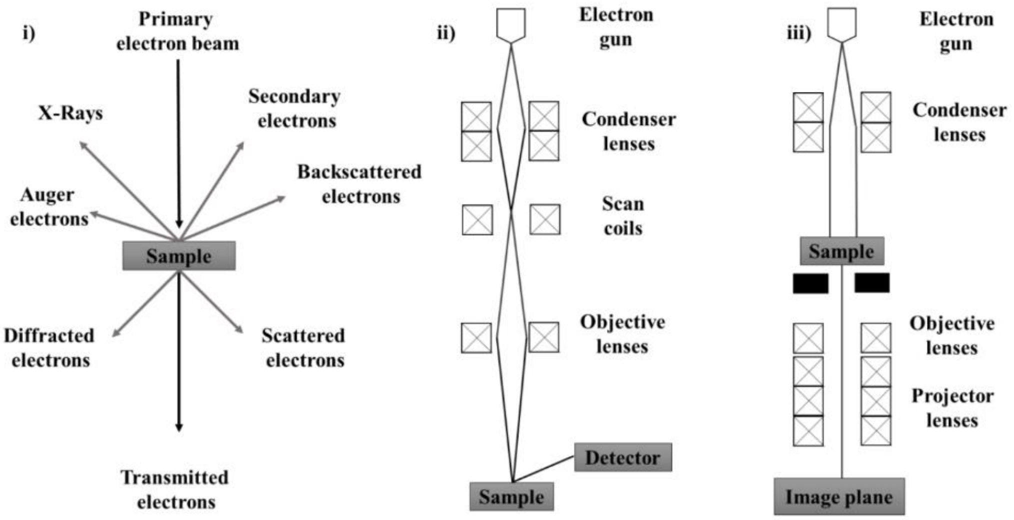

Figure 1: Schematic representation of the detectable signals upon the interaction between the primary electron beam and the sample (i) as well as the simplified configurations of SEM (ii) and TEM (iii).

As depicted in Figure 1-i, the electron-sample interaction causes the emission of the following species:

- secondary electrons (SE) which are emitted by the sample due to inelastic scattering of the primary electron beam and originate from the surface region, thus providing information on its topology;

- backscattered electrons (BSE) which are the result of collisions of the primary electrons with the atoms constituting the sample. They originate from a deeper part than SE and are sensible to the atomic mass. Therefore, heavier atoms appear brighter in a resulting image due to a higher yield of BSE;

- X-rays which are generated in the same way as in XRD experiments *i.e.* due to ejection of an electron from an inner atomic shell, leaving the atom in an ionized state, followed by the filling of the vacancy by an electron from an outer shell. This process generates X-ray photons characteristic to a certain element, which are further used for its identification;

- Auger electrons which are produced following the interaction of X-rays, generated as described above, with electrons from other shells. They are typically used in Auger Electron Spectroscopy (AES);

- diffracted electrons which can be used to further derive crystallographic information *i.e.* orientation of diffracting planes and interplanar distance (d);

- transmitted electrons which are a fraction of electrons passing through the sample without energy loss. Transmission strongly depends on the energy carried by the primary electrons as well as the thickness of the sample. Higher electron energies and thinner samples favor transmission.

III.2.3.1 Scanning Electron Microscopy *(SEM)*

SEM (figure 1, ii) typically uses low-energy electrons of up to 5-15 keV, which are focused on the sample by a series of lenses. This causes generation of secondary electrons, backscattered electrons, X-rays and a small portion of diffracted electrons which are used to derive information on surface topology, particle size and shape (SE), contrast topographic imaging (BSE), elemental analysis and mapping (X-Rays) and atomic planes orientation (diffraction) with a typical resolution of 5-10 nm. In this work, SEM micrographs were registered on a JEOL JSM 6700F microscope using an electron beam energy in the range of 5-15 keV. Before observation, the samples were covered with a thin layer of Cr (150 Å). When SEM was coupled with EDS (Energy Dispersive X-Ray Spectroscopy) for elemental analysis, the samples were covered with a thin carbon layer (~200 Å) and were observed under an applied electron beam energy of 15 keV.

III.2.3.2 High Resolution Transmission Electron Microscopy (TEM)

HRTEM usually employs higher-energy electrons of up to 300 keV which are directed onto the sample following a parallel beam (figure 1-iii). Under these conditions transmission and diffraction dominate the electron-sample interaction which allow for images with high resolution of up to 0.3-0.5 nm as well as diffraction patterns and elemental analysis. Herein, morphology analysis was performed using a TITAN Themis 300 S/TEM equipped with a high brightness Schottky field emission gun, a monochromator and a probe aberration corrector allowing energy and resolution of about 150 meV and 70 pm, respectively. The microscope is equipped with several annular dark field detectors and a super-X detector system with four windowless silicon drift detectors for electron dispersive x-ray spectroscopy (EDS). The experiments have been performed at 300 kV with semi-convergence angle of about 20 mrad, probe size of the order of 500 pm and probe current between 60 and 100 pA. For high angle annular dark field (HAADF) imaging the c collection angles have been between 50 and 200 mrad. EDS mapping has been obtained in spectrum imaging mode with dwell time per pixel of about 15 µs and continuously scanning frames until total acquisition time of about 15 to 20 minutes. All the nitride SBA-15 samples were frozen at -120 °C in distilled water and then cut at 70 nm depth samples on an ultramicrotome equipped with a 35° diamond knife (Leica UCT

Ultracut). Cuts were then deposited on a 200 mesh lacey carbon grid for analysis. For the rest of the samples, powders were simply placed on lacey carbon for analysis.

III.2.4 Surface Properties

III.2.4.1 X-ray Photoelectron Spectroscopy (XPS)

XPS is a semi-quantitative technique for measuring the elemental composition of the surface of the material, and also determines their oxidation states. This ultra-high vacuum technique is able to probe to a depth of 10 nm. XPS is based on the photoelectric effect (Figure 2) during which a sample adsorbs a photon energy (hν) which forces a valence electron with a binding energy (BE) to be ejected with a kinetic energy (KE). The latter is determined by the conservation of energy. Surface electrons escape with no energy loss. Typically, an XPS spectrum represents the intensity of thus-ejected photoelectrons plotted as a function of the binding energy which is derived from their corresponding kinetic energy according to this simplified equation: BE = hν – KE. Each element has a set of characteristic binding energies permitting the identification of elemental species from XPS spectra. Also, the number of photoelectrons is proportional to the concentration of the element, thus after background removal and deconvolution of peaks, elemental quantification is also feasible.

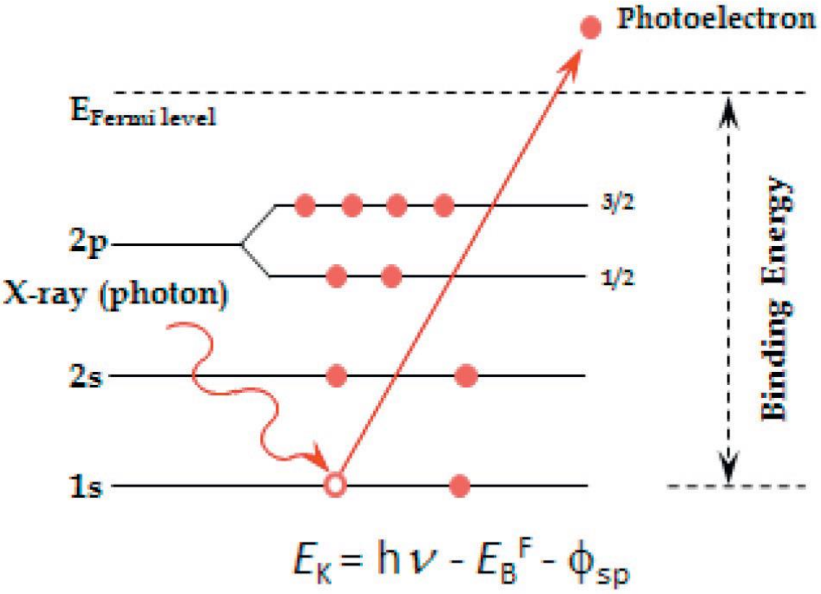

Figure 2. Photoelectric effect diagram [4]

XPS spectra were recorded on a Kratos Analytical AXIS Ultra DLD spectrometer employing a monochromatic Al Kα X-ray radiation (1486.6 eV), with an electron analyzer operating in a fixed pass energy of 20 eV. All Binding Energies (BE) were referenced to the carbon signal corresponding to C-C bonding in the C 1s core level at 284.8 eV. A pre-treatment chamber was used for some samples in order to mimic the catalytic pre-treatment, prior to analysis, at 700 °C for 2 h under a 60 mL min^{-1} flow of 75 vol.% H_2/N_2. For example, in the case of Co_3Mo_3N, a passivation layer is introduced after ammonolysis in order to protect the nitride. Since XPS is a surface analysis technique where around 10 nm of the sample's surface will be analyzed, a pretreatment is necessary to expose the nitride by removing the passivation layer. The results were fitted on CasaXPS V2.3.24. With the help of XPS, it is possible to not only study the evolution of the oxidation states before and after reaction, but also confirm the formation of a nitride from the N 1s peak (overlays in 3p Mo region). Figure 3 shows XPS spectra in the 3p Mo region of the three stages underwent in $CoMoO_4$. Not only is there a shift to lower binding energies that confirms the Mo reduction after ammonolysis and after pretreatment, but also an evident N 1s peak confirming the nitride formation. Fittings were done following work done by Biesinger et al. and Baltrusaitis et al.[5], [6], and other references on nitrides in the literature that will be discussed in detail in upcoming chapters.

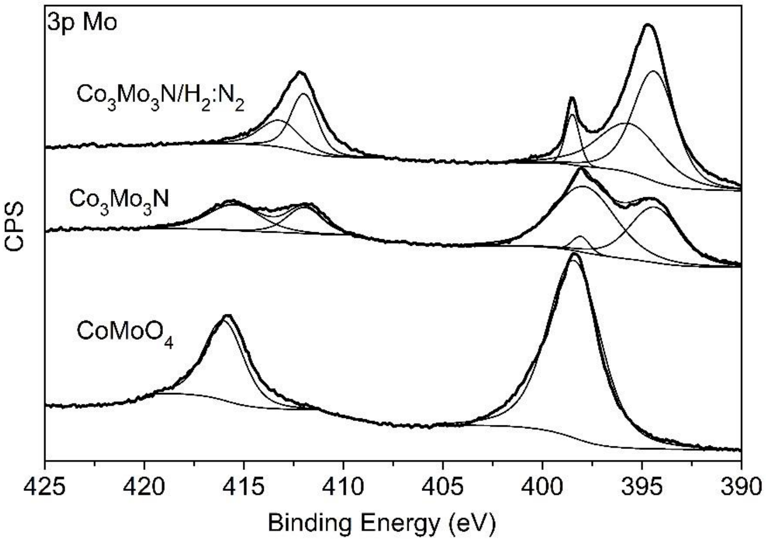

Figure 3: XPS profile of 3p Mo binding energy region for $CoMoO_4$, and Co_3Mo_3N before and after nitridation.

III.2.5 Elemental Analysis

III.2.5.1 Inductively Coupled Plasma – Optical Emission Spectroscopy (ICP-OES)

ICP-OES is a powerful analytical technique used to qualitatively and quantitatively determine the elements composing a sample under study. The principle behind this technique is based on the excitation of electrons from the ground state to an excited state using a hot plasma as an energy source. As electrons return back to the ground state they emit light at a specific wavelength which is analyzed by means of optical emission spectroscopy. By measuring the intensity of each wavelength, it is possible to calculate the proportion of each element in a sample. Therefore, in this thesis, chemical composition of the synthesized materials was determined by means of ICP-OES. Analyses were performed on a Perkin Elmer Optima 2000 DV instrument to determine the chemical composition of the solids based on Co Mo materials. Before analysis, a known amount of sample was dissolved in a diluted HF-HCl solution, and then heated under microwave until complete dissolution before exposition to the plasma.

III.2.5.2 Carbon Hydrogen Nitrogen and Sulfur analysis (CHNS)

CHNS is a technique to qualitatively and quantitively analyze the organic matter in a solid sample. The principle behind the analysis lies in combustion of the specimen followed by determination and quantification of the combustion products. In this thesis, the CHNS compounds were determined using the thermo scientific FlashSmart automated elemental analyzer. The samples (~10 mg) were weighed in tin (Sn) containers and introduced into the combustion reactor maintained at 950 °C and promoting dynamic flash combustion of the sample. The products are then directed into the column reactor filled with copper oxide for their oxidation and pass through the nickel reducer. The N, C, H and S were therefore detected as N_2, CO_2, H_2O and SO_2, respectively. The resulted gases were separated in a packed column heated at 65°C and detected by a thermal conductivity detector. The analysis duration was 10 min with 3 repetitions performed for each sample.

III.2.6 Chemical and Thermal Properties

III.2.6.1 Temperature Programmed Reduction (TPR)

TPR is a material characterization process commonly used in catalysis especially for supported metal and oxides catalysts. This techniques gives insight on the reducibility of the active phase and some notion on its accessibility. During TPR, a diluted H_2 mixture is passed over the catalyst with the linear increase of temperature with time. The consumption of H_2 is measured by a TCD to give us a TPR profile consisting of H_2 consumption as a function of temperature. Temperature programmed reduction under H_2 (H_2-TPR) was conducted in an Autochem chemisorption instrument (Micromeritics) equipped with a TCD. Before analysis, the samples were pre-treated up to 200 °C under 50 ml min^{-1} of synthetic air (heating rate of 5 °C min^{-1}, 30 min). After cooling down to room temperature, the H_2-TPR was performed under 50 ml min^{-1} of 5.0 vol. % H_2:Ar until 1000 °C, with a temperature ramp of 5 °C min^{-1}. The reduction was conducted from 25 °C to 1000 °C, with a temperature ramp of 5 °C min^{-1} and held for 30 min.

III.2.6.2 Temperature Programmed desorption (H_2-TPD)

Similarly, to H_2-TPR, in order to analyze hydrogen chemical adsorption on our active sites, H_2-Temperature programmed desorption (H_2-TPD) was conducted in an Autochem chemisorption instrument (Micromeritics) equipped with a TCD. In a typical test, 0.5 g of Mo-O/support was added to the reactor and pre-treated under similar conditions of the pre-treatment reaction in order to obtain Mo-N/support (700 °C for 2 h under 75 % H_2 in N_2). The reactor is then cooled under the same gas mixture to reach ambient temperature. Ar gas flow was used in order to purge the sample for 1 h followed by the adsorption of H_2 (5% H_2 in Ar) and switched back to Ar for 1 h to remove all the physisorbed molecules of H_2. The H_2 desorption was measured by increasing the temperature (1 °C/min) until reaching 700°C.

III.2.6.3 Thermogravimetry Analysis with Differential Scanning Calorimetry (TGA-DSC)

TGA is an analytical technique of thermal analysis during which the mass of a sample is continuously measured as a function of increasing temperature. Coupled with DTA (Differential Thermal Analysis) or DSC (Differential Scanning Calorimetry), it allows identification of the phenomena taking place at different temperatures and including combustion, desorption, phase transition, and others. Importantly, TGA enables establishing the thermal stability of materials by quantifying, for example, the organic fraction in them and the temperature at which its combustion starts. Therefore, in this work thermal stability properties were evaluated by recording the TG and DSC profiles with a thermal analyzer instrument Q600 from TA Instrument within the temperature range 25-800 °C at a heating rate of 5 $°C\cdot min^{-1}$ under N_2 flow (100 mL min^{-1}).

III.3 Reaction Conditions & Catalytic Tests

III.3.1 Ammonolysis and Pretreatment

To convert certain oxides into their nitride counterparts an ammonolysis step is needed. All the synthesized materials were subject to an ammonolysis step under NH_3 (BOC, 99.98 wt.%) at a flow rate of 60 mL min^{-1} at 785 °C for 5 h. Then, the material was cooled down to ambient temperature under ammonia flow. Upon reaching room temperature, the catalyst was purged using N_2 (100 mL min^{-1}) for 1 h followed by a passivation step under a low concentration of oxygen gas mixture (99.9 % N_2 / 0.1 % O_2) for overnight.

For other oxides, a pretreatment is sufficient to convert the oxide into nitrides as seen in the case of Mo_2N pre-treated at 700 °C under a 75 vol.% H_2/N_2 (BOC, 99.98 %) gas mixture at a total gas flow of 60 mL min^{-1} for 2 h.

In the cases of the catalysts present in this manuscript, $CoMoO_4$ related samples (bulk and supported) underwent ammonolysis and pretreatment before reaction, MoO_3 related samples underwent only pretreatment before reaction, whereas Mo-Mxenes related samples did not undergo either.

III.3.2 Ammonia Synthesis

$$\frac{1}{2}N_2 + \frac{3}{2}H_2 \rightarrow NH_3$$

Experimental setup:

Figure 4. Catalytic set-up for ammonia synthesis and ammonia decomposition developed during this PhD

Figure 4 displays the catalytic rig that was developed during this PhD. It consists of a vertical split-tubular furnace in which the quartz reactor is placed. The latter is suspended with Swagelok fittings (enter and exit) that allow the gases to flow into the reactor and towards the analyzer. Each gas line (N_2, reaction mix 3:1H_2:N_2, 1% O_2:N_2, and NH_3) is equipped with its corresponding gas cylinder and regulator, mass flow controllers (MFC), 2-way valves, and filters and check valves to protect the MFCs and keep different components separate. The selected flow can then pass either through the bypass or the reactor, to the exit which is connected to an FTIR/UV for ammonia decomposition, and into a diluted H_2SO_4 solution that is monitored by a conductimeter for ammonia synthesis. This set-up has been verified for leaks, calibrated, and tested for reproducibility.

Catalytic activity measurement: In a typical reaction test, a certain mass of catalyst was placed in a quartz reactor under a 75 vol.% H_2:N_2 (BOC, 99.98 %) gas mixture at a total gas flow of 60 mL min^{-1}. The reaction was then performed at 400 °C, under the same flow rate of 75 vol.% H_2:N_2 for at least 10 h. Ammonia production was determined by measurement of the decrease in conductivity of a 200 mL 0.0018 M H_2SO_4 solution through which the reactor effluent stream flowed monitored as a function of reaction time. The rate of the reaction was calculated according to the following:

$$r = \frac{\Delta_C \times n_{NH3} \times 60}{m \times 10^{-6} \times X_{wt}}$$

Where: r is the rate of the reaction for a range of time; Δ_C is the average change in conductivity per minute over a range of time; n_{NH3} is the number of moles of ammonia that correspond to the decrease of 1 µS cm^{-1} ; m is the mass of the catalyst; X_{wt} is the load wt.% of active phase. The constants are added for conversion purposes to convert the rate in µmol g^{-1} h^{-1} .The activation energy was also calculated by varying the reaction temperatures (250-400°C) and plotting ln(r)=1/T according to the following:

$$E_a = b \times R \times 10^{-3}$$

Where ***b*** is the slope of the line $\ln(r) = b\ \frac{1}{T} + c$, ***R*** the rate constant, ***r*** the rate, ***T*** the temperature in Kelvin, to obtain E_a in kJ mol^{-1}.

III.3.3 Ammonia Decomposition

$$NH_3 \rightarrow \frac{1}{2}N_2 + \frac{3}{2}H_2$$

For the Mo_2N/support series, we also studied the reverse reaction, ammonia decomposition. The same experimental setup is used, except the detection and quantification of unconverted NH_3 was done using a FTIR/UV (X-STREAM Enhanced General Purpose Process Gas Analyzer). In a typical test, 0.6 g of catalyst was placed in a quartz reactor under a 15 vol.% NH_3:Ar (BOC, 99.98 %) gas mixture at a total gas flow of 100 mL min^{-1}. The temperature was programmed up to 700 °C with a ramp of 30 min every 100°C from 250 to 450 °C then a ramp of 30 min every 50 °C reaching 700°C.

III.4 References

[1] D. Zhao, Q. Huo, J. Feng, B. F. Chmelka, and G. D. Stucky, “Nonionic triblock and star diblock copolymer and oligomeric sufactant syntheses of highly ordered, hydrothermally stable, mesoporous silica structures,” *J. Am. Chem. Soc.*, vol. 120, no. 24, pp. 6024–6036, 1998, doi: 10.1021/ja974025i.

[2] K. Maleski, C. E. Shuck, A. T. Fafarman, and Y. Gogotsi, “The Broad Chromatic Range of Two-Dimensional Transition Metal Carbides,” *Adv. Opt. Mater.*, vol. 9, no. 4, pp. 1–8, 2021, doi: 10.1002/adom.202001563.

[3] P. Raval, J. Trébosc, T. Pawlak, Y. Nishiyama, S. P. Brown, and G. N. Manjunatha Reddy, “Combining heteronuclear correlation NMR with spin-diffusion to detect relayed Cl–H–H and N–H–H proximities in molecular solids,” *Solid State Nucl. Magn. Reson.*, vol. 120, no. June, 2022, doi: 10.1016/j.ssnmr.2022.101808.

[4] M. H. Engelhard, T. C. Droubay, and Y. Du, “X-ray photoelectron spectroscopy applications,” *Encycl. Spectrosc. Spectrom.*, pp. 716–724, 2016, doi: 10.1016/B978-0-12-409547-2.12102-X.

[5] M. C. Biesinger, B. P. Payne, A. P. Grosvenor, L. W. M. Lau, A. R. Gerson, and R. S. C. Smart, “Resolving surface chemical states in XPS analysis of first row transition metals, oxides and hydroxides: Cr, Mn, Fe, Co and Ni,” *Appl. Surf. Sci.*, vol. 257, no. 7, pp. 2717–2730, 2011, doi: 10.1016/j.apsusc.2010.10.051.

[6] J. Baltrusaitis *et al.*, “Generalized molybdenum oxide surface chemical state XPS determination via informed amorphous sample model,” *Appl. Surf. Sci.*, vol. 326, pp. 151–161, 2015, doi: 10.1016/j.apsusc.2014.11.077.

IV. Chapter III: Effect of support on catalytic activity of Molybdenum Nitride – Part I

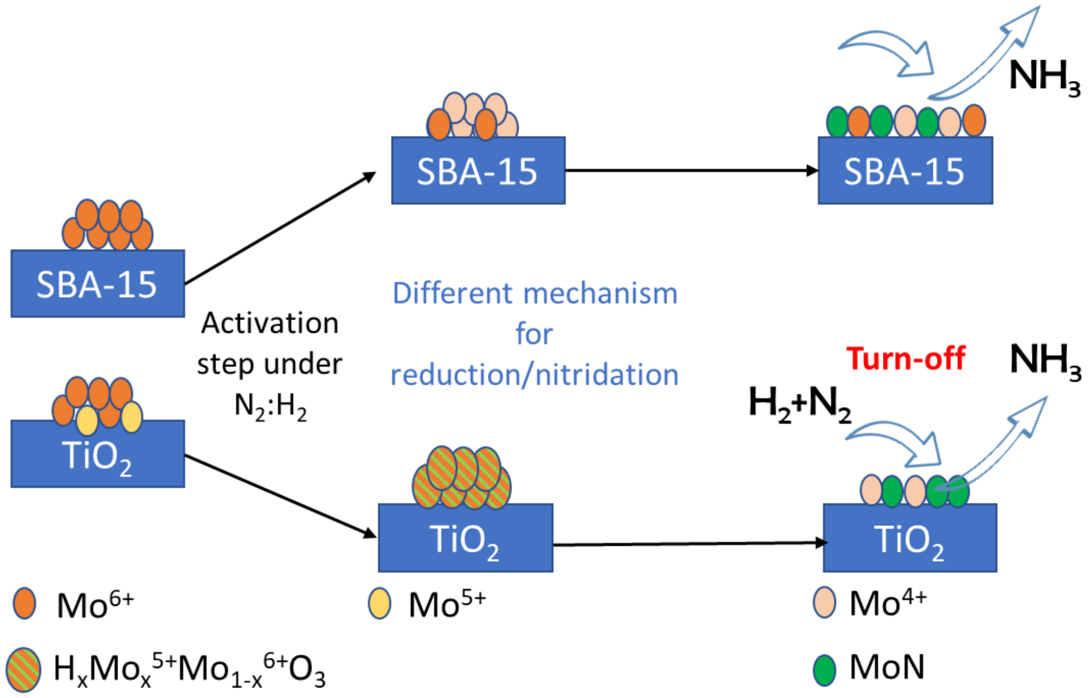

This section is divided into 2 Chapters (articles) and will be referred to as Chapter III and Chapter IV

Part of this Chapter has been published in Faraday Discussions 2023, under the theme collection Sustainable Nitrogen:

A. Sfeir *et al.*, “Switching On/Off molybdenum nitride catalytic activity in ammonia synthesis through modulating metal support interaction,” *Faraday Discuss.*, p., 2023, doi: 10.1039/D2FD00154C.

Switching On/Off molybdenum nitride catalytic activity in ammonia synthesis through modulating metal support interaction

Amanda Sfeir[1], Camila A. Teles[1], Maya Marinova[2], Hérve Vezin[3], Jean-Philippe Dacquin[1], Axel Löfberg[1], Said Laassiri[4*], Sébastien Royer[1*]

[1] *Univ. Lille, CNRS, Centrale Lille, Univ. Artois, UMR 8181 – UCCS – Unité de Catalyse et Chimie du Solide, F-59000 Lille, France.*

[2] *Université de Lille, CNRS, INRA, Centrale Lille, Université Artois, FR 2638 – IMEC – Institut Michel-Eugène Chevreul, 59000 Lille, France.*

[3] *Laboratoire de Spectroscopie pour Les Interactions La Réactivité et L'Environnement Université de Lille, UMR CNRS 8516-LASIRE, 59000 Lille, France*

[4] *Chemical & Biochemical Sciences, Green Process Engineering (CBS), Mohamed VI Polytechnic University, UM6P, 43150, Benguerir, Morocco*

* Corresponding authors: said.laassiri@um6p.ma, sebastien.royer@univ-lille.fr

IV.1 Introduction

Owning high catalytic activity and selectivity, molybdenum-based materials are considered key catalysts in multiple reactions of high industrial and academic interest including hydrodesulfurization (HDS) [1, 2], oxidative desulfurization [3, 4], CO_2 conversion [5, 6] and ammonia synthesis [7]. The versatility of Mo arises from its (i) redox properties as it possesses different oxidation states and (ii) its ability, upon reaction with appropriates precursors, to form a range of carbide [8, 9], nitride [10, 11],phosphide [12, 13] and sulphide [14, 15] materials with different crystalline structures. The high “malleability” of Mo chemical composition allows the careful tuning of its electronic properties, textural and structural properties, surface terminations, site occupancies, defects concentration, and surface properties, which in many cases are determining parameters controlling the catalytic activity and selectivity.

Over the years, molybdenum related phases have driven much interest in ammonia synthesis due to the importance of this latter in the production of reactive nitrogen for fertilizer industries. A wide range of Mo-based catalysts has been studied for ammonia generation including Mo carbides and supported Mo carbides (β-Mo_2C, Mo_2C/C support, Mo_2C/CeO_2) [16-19], nitrides and supported nitrides (γ-Mo_2N, β-Mo_2N, MoN, MoN_x/ZSM-5),[7, 16, 20] bimetallic Mo nitrides and carbides (Co_3MO_3N, Ni_2Mo_3N, Co_3Mo_3C) etc. [21-24]. The application of Mo-based materials was not only restricted to heterogeneous catalytic ammonia synthesis but was also extended to alternatives processes such as chemical looping [25], electro-chemistry [26], and photocatalysis [27, 28]. The interest in molybdenum activity can originally trace its roots back to the earlier work of Volpe and Boudart [20] and Oyama [29] reporting high catalytic activity of Mo_2N for ammonia synthesis, at atmospheric pressure and 400 °C [29]. However, throughout the years, the chemical composition, surface exposition, and structure of Mo has been reported to affect the catalytic activity and reaction mechanism. In instance, differences in the catalytic activity of β-Mo_2N and δ-MoN were reported with the latter being less active at 400°C and ambient pressure [30]. Furthermore, the degree of Mo nitridation was reported to influence greatly the nature of the rate determining step when metallic and nitride phases are compared [31]. These differences have been also reported in the case of molybdenum carbides crystallizing in different structures. The ammonia synthesis activity of β-Mo_2C (5.8 $mmol_{NH3}g_{cat}^{-1}h^{-1}$) was found to be higher than the α-MoC (2.3 $mmol_{NH3}g_{cat}^{-1}h^{-1}$) at 400°C and 1.0 MPa [32]. These results were explained based on changes observed in adsorption-desorption properties of nitrogen, hydrogen and ammonia being dependent on the nature of the crystalline structure of molybdenum carbide[32]. Considering the structure-sensitive nature of ammonia synthesis in molybdenum, it is of paramount importance to devise new strategies to improve the catalytic activity and stability of Mo by the careful tuning of its local structure and chemical composition.

A further consideration, that is not largely envisioned when designing novel Mo-based system, is the importance of metal-support interaction in modulating the activity for a given reaction. Such interactions, referred to in the literature as strong Metal - Support interaction (SMSI), have been studied extensively in particular for noble metal-reducible oxides such as titania, ceria or iron oxide [33]. The classical SMSI is usually characterized by a migration of support-derived species over the metal surface leading to the encapsulation of the active phase which suppresses its ability to chemisorb small molecules and intermediates [34]. SMSI results in fundamental changes in the electronic, geometric, and nature of the active phase. In ammonia synthesis, where the reaction is governed by nitrogen adsorption and activation in the surface, it is of great interest and importance to comprehend the role of Metal-Support interaction in engineering the electronic and geometric properties of Mo and by consequences modulating its catalytic activity. To this end, Mo supported on mesoporous silica (SBA-15) and titanium oxide (TiO_2) has been successfully prepared by incipient wetness impregnation (IWI) and studied for ammonia synthesis reaction and for ammonia decomposition. SBA-15 was studied as a non-reducible support presenting *(i)* high surface area; *(ii)* highly ordered and uniform mesopores; and *(iii)* good thermal stability. On the other hand, TiO_2 was studied as a reducible support capable of manifesting SMSI effect. The effect of the support in altering the catalytic activity of molybdenum was evaluated in ammonia synthesis reaction and in ammonia decomposition. SBA-15 was found to be the most appropriate support for molybdenum dispersion in both ammonia synthesis and ammonia decomposition. When supported on a reducible oxide TiO_2, molybdenum showed poor catalytic activity and was prone to quick deactivation especially in ammonia synthesis reaction. The effect of the nature of support on the physicochemical properties and catalytic activity of Mo species was investigated through an extensive characterization study.

IV.2 Experimental section

IV.2.1 Catalysts preparation

Chemicals. All chemicals needed for the preparation molybdenum nitride supported catalysts and non-supported β-Mo_2N were used as purchased without further purification: tetraethylorthosilicate ($Si(OC_2H_5)_4$, TEOS, 98 wt.%, Sigma-Aldrich), non-ionic triblock co-polymer Pluronic P123 (poly(ethylene glycol)-*block*-poly(propylene glycol)-*block*-poly(ethylene glycol), average MW ~5800, Sigma-Aldrich), ammonium para-heptamolybdate tetrahydrate $(NH_4)_6Mo_7O_{24}.4.H_2O$, 99 wt.%, Alfa Aesar) and TiO_2 (Saint-Gobain NORPRO ST61120).

IV.2.1.1 *Mo-N supported catalyst.*

10-Mo-N/SBA-15. SBA-15 was synthesized by hydrothermal method, under acidic conditions as described elsewhere [35]. The supported material was synthesized by incipient wetness impregnation (IWI). The calculated weight of Mo precursor ($(NH_4)_6Mo_7O_{24}.4H_2O$, Aesar) was dissolved in a volume corresponding to the pore volume of the respective support and then mixed. The mixture was aged for 5 days at 25 °C and then calcined at 400 °C, 1.5 °C min^{-1} for 5 h. The obtained Mo-O/SBA-15 underwent a pre-treatment step at 700 °C under a 75 vol.% H_2/N_2 (BOC, 99.98 %) gas mixture at a total gas flow of 60 mL min^{-1} for 2 h in order to obtain the nitride form Mo-N/SBA-15.

10-Mo-N/TiO_2. Mo-N supported on TiO_2 was prepared using by incipient wetness impregnation (IWI) as described for the preparation of 10-Mo-N/SBA-15, using titania provided by Saint-Gobain NORPRO (ref. ST61120)

IV.2.1.2 β-Mo_2N preparation:

Molybdenum oxide was prepared by the hydrothermal synthesis method. The Mo precursor (ammonium molybdate tetrahydrate, $(NH_4)_6Mo_7O_{24}.4H_2O$, Aesar) was dissolved in distilled water. The pH was adjusted to 1 by adding dropwise a 2M solution of HNO_3. Thereafter, the solution was submitted for 12 h to hydrothermal ageing at 180 °C in a Teflon autoclave. After recovering by filtration, the solid was washed with water and dried at 60 °C overnight. The sample was then calcined at 300 °C, 1.5 °C min^{-1} during 5 h. α-MoO_3 underwent a pre-treatment step at 700 °C under a 75 vol.% H_2/N_2 (BOC, 99.98 %) gas mixture at a total gas flow of 60 mL min^{-1} for 2 h in order to obtain the nitride form β-Mo_2N.

N.B. Herein, the samples obtained after the calcination step are denoted X-Mo-O/support. The catalysts obtained after the pre-treatment step are referred to as X-Mo-N/support, and the post reaction samples as X-Mo-N-PR/support, where X is the wt% of α-MoO_3 (X =10 %. wt).

IV.2.2 Catalyst characterization

In this article, the following characterization techniques were used: XRD (Low and high angle), N_2 physisorption, XPS, TEM, H_2-TPR, H_2-TPD, and EPR. For more information regarding the characterization techniques, please refer to Chapter 2 for all details.

IV.2.3 Catalytic activity

Ammonia synthesis. The reaction was performed at 400°C and atmospheric pressure using a gas mixture of 75 vol.% H_2/N_2 (BOC, 99.98 %) at a total gas flow of 60 mL min^{-1}. 0.15-0.30 g (supported and bulk respectively) of material was placed in a quartz reactor tube and held centrally between two quartz wool in the heated zone of furnace. The material was activated at 700 °C (10 °C min^{-1}) under 75 vol.% H_2/N_2 (BOC, 99.98 %) at 60 mL min^{-1} for 2 h. After the activation step, the reactor was cool down, and the reaction was performed at 400 °C.

The reactor effluent stream was flowed to a 200 mL of H_2SO_4 solution (0.0018 M) and ammonia production was calculated from the decrease in conductivity. The catalytic activity was monitored as a function of reaction time.

Ammonia decomposition. For the reaction, 0.6 g of catalyst was placed in a quartz reactor under a 15 vol.% NH_3/Ar (BOC, 99.98 %) gas mixture at a total gas flow of 100 mL min^{-1}. The catalytic activity was measured between 250 and 700 °C by steps of 100 °C (30 min at each step) from 250 to 450 °C, and steps of 50 °C (30 min at each step) until reaching 700 °C. Ammonia conversion was determined using an FTIR analyzer.

IV.3 Results and Discussion

IV.3.1 Textural and structural properties

IV.3.1.1 X-ray Diffraction

Figure 1 shows the PXRD patterns recorded in the wide-angle domain for the α-MoO_3, β-Mo_2N, 10-Mo-O/SBA-15, 10-Mo-N-PR/SBA-15, 10-Mo-O/TiO_2 and 10-Mo-N-PR/TiO_2.

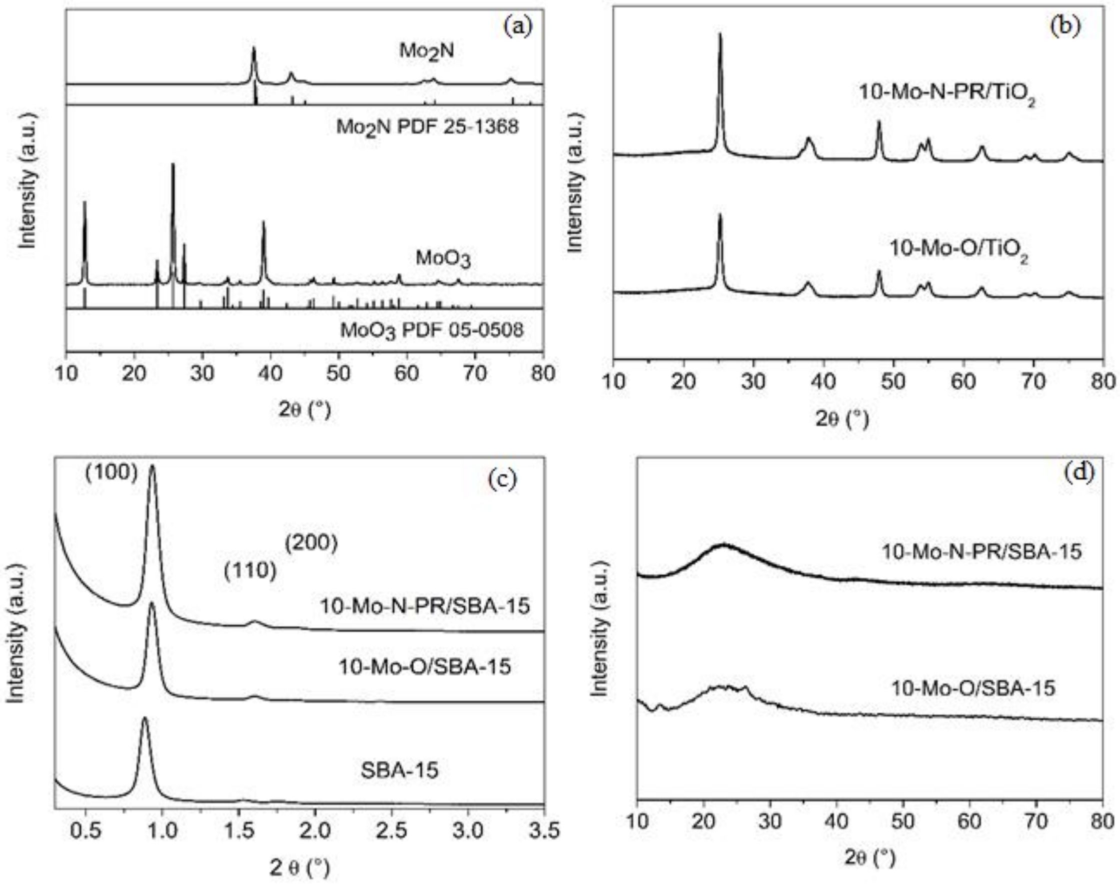

Figure 1. XRD diffractogram of (a) Unsupported α-MoO_3 and β-Mo_2N, (b) 10-Mo-O/TiO_2 and 10-Mo-N-PR/TiO_2, (c) SAXS diffractograms of 10-Mo-O/SBA-15 and 10-Mo-N-PR/SBA-15 and (d) wide angle domain diffractograms of 10-Mo-O/SBA-15 and 10-Mo-N-PR/SBA-15. *10-Mo-N-PR/TiO_2 and 10-Mo-N-PR/SBA-15 are post-ammonia synthesis reaction catalysts obtained after 1000 min in stream.

First the transformation of bulk molybdenum oxide α-MoO_3 into β-Mo_2N after the activation step was verified by PXRD (Figure 1-a). Upon the pre-treatment step, a single β-Mo_2N phase was formed. The diffractogram showed intense PXRD reflections indicating the formation of a well-crystallized material with all the peaks belonging to β-Mo_2N phase (PDF 25-1368).

PXRD diffractograms of 10-Mo-O/TiO_2 and 10-Mo-N-PR/TiO_2 are presented in Figure 1-b. In both materials, only diffraction related to TiO_2 with anatase phase (PDF 78-2486) are observed. The absence of XRD reflections corresponding to the molybdenum oxide/nitride phase suggests that crystallite size is small and molybdenum species are well dispersed on TiO_2.

SAXS patterns of the as-prepared siliceous support were first collected before and after IWI impregnation and are presented in Figure 1-c. The calcined SBA-15 displays the characteristic three well-resolved diffraction peaks that can be associated to the *(100)*, *(110)*, and *(200)* planes of the p6mm hexagonal symmetry structure reflecting the well-defined and uniform range mesoporous structure of SBA-15. Upon Mo impregnation, SAXS patterns of 10-Mo-O/SBA-15 showed that the support maintained its pore structure (Figure 1-c). However, an apparent shift of the reflection peaks to higher 2θ angles can be also observed from 0.88° to 0.93° indicating a slight pore contraction upon Mo impregnation. No further changes were observed upon reaction, confirming the stability of 10-Mo-N/SBA-15 catalyst under reaction conditions. The effectiveness of the dispersion of Mo oxides on the surface of SBA-15 was confirmed by PXRD in the wide-angle domain (Figure 1-d). The PXRD diffractogram was characterized by a broad PXRD peaks of amorphous silica and poorly defined reflection peaks related to the molybdenum oxide phase were observed reflecting a well dispersed active phase. Surprisingly, upon reaction, no molybdenum nitride reflection was observed.

IV.3.1.2 Nitrogen adsorption-desorption analysis

The textural properties of supported molybdenum oxide were investigated by means of N_2-physisorption. The results are summarized in Figure 2, and Table 1.

The unsupported α-MoO_3 exhibited a type II isotherm (Figure 2-a) which is characteristic of non-porous materials and possessed a limited accessible surface area ~ 4 m^2 g^{-1}. The N_2 adsorption/desorption isotherm of 10-Mo-O/SBA-15 exhibited a type IV isotherm with H1 hysteresis loop which is characteristic of ordered mesoporous materials. Additionally, a narrow pore size distribution of cylindrical pores ~ 6.6 nm is observed. When compared to the parent material SBA-15, a significant decrease of surface area from 760 to ~ 465 m^2 g^{-1} which was accompanied with a parallel decrease in pore volume. This concord with partial filling of the mesopore by molybdenum oxide phase. However, both SBA-15 and 10-Mo-O/SBA-15 displays similar pore size distribution indicating the formation of discrete molybdenum oxide nanoparticles in the porosity of SBA-15. 10-Mo-O/TiO_2 exhibited a type IV isotherm with less marked hysteresis. The accessible surface area of 10-Mo-O/TiO_2 was found to be ~ 115 m^2 g^{-1}.

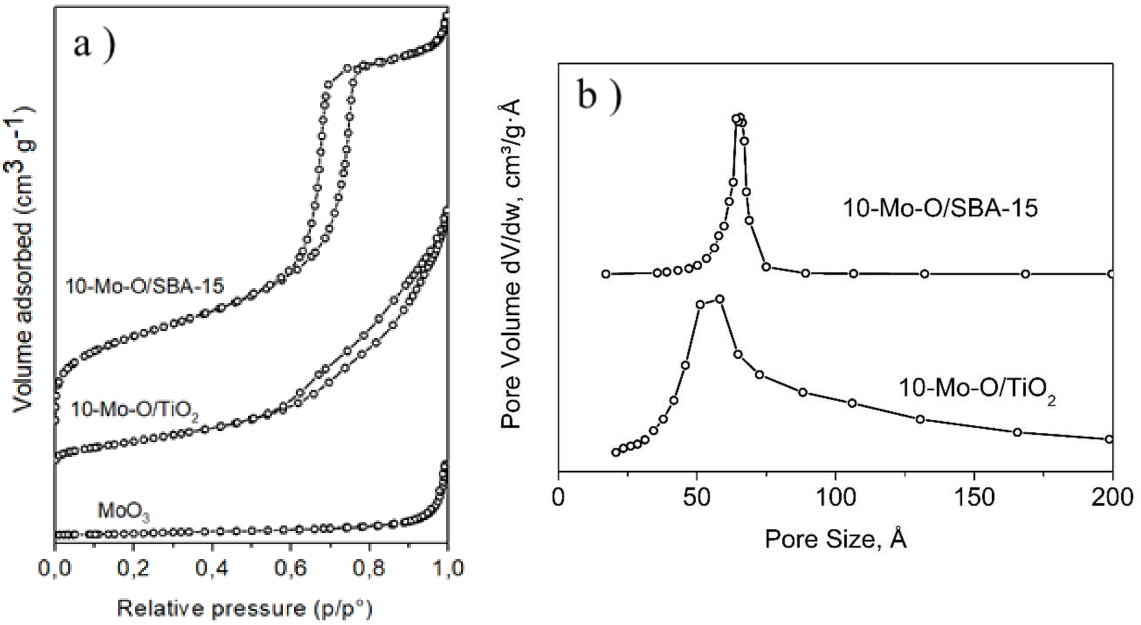

Figure 2. (a) N_2 adsorption–desorption isotherms and (b) pore size distribution of 10-Mo-O/SBA-15 and 10-Mo-O/TiO_2.

Table 1. Textural and reducibility properties of the bulk and supported Mo- based materials.

Sample	α-MoO_3[a] (wt.%)	S_{BET}[b] ($m^2\ g^{-1}$)	S_μ[c] ($m^2\ g^{-1}$)	V_p[d] ($cm^3\ g^{-1}$)	D_p[e] (nm)	Mean particle size[f] (nm)
α-MoO_3	-	4	-	-	-	NA
SBA-15	-	760	131	1.1	6.5	NA
10-Mo-O/SBA-15	10.8	465	68	0.82	6.6	1.3 ± 0.3 nm
TiO_2	-	135	3.8	0.44	12.0	NA
10-Mo-O/TiO_2	13.2	115	1	0.27	9.7	1.7 ± 0.7 nm

[a] α-MoO_3 content measured by ICP-OES in the calcined samples, [b] B.E.T. surface area, [c] Microporous surface area, [d] Total pore volume, [e] B.J.H. mean pore size, [f] mean particles size of MoN_x estimated from HAADF-STEM analysis with a sampling of 25 particles.

IV.3.1.3 TEM-EDS studies.

Upon ammonia synthesis, the morphology of 10-Mo-N/SBA-15 and 10-Mo-N/TiO_2 was studied by means of HAADF-STEM analysis coupled with EDS mapping to investigate the local distribution of molybdenum. A selection of high resolution HAADF images of 10-Mo-N/SBA-15 and 10-Mo-N/TiO_2 is presented in Figure 3 and Figure S1.

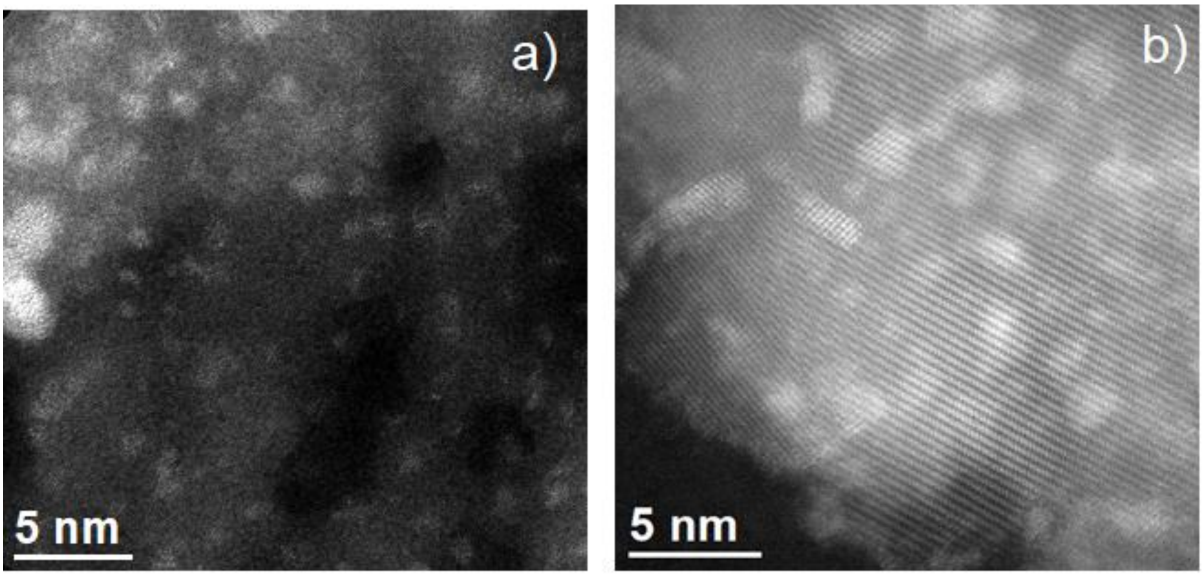

Figure 3. Representative lower magnification HAADF images for a) 10-Mo-N/SBA-15 and b) 10-Mo-N/TiO_2

As observed in Figure S1-a, the characteristic hexagonal arrays of SBA-15 with the typical 2D periodic hexagonal structure was maintained in the 10-Mo-N/SBA-15 upon ammonia synthesis reaction. Furthermore, complementary EDS analysis confirm the high dispersion of molybdenum nitride species within the 2D-channels of SBA-15. In fact, the particle size of molybdenum nitride was found to be averaging 1.3 ± 0.3 nm (sampling of 25 particles). In a similar manner HAADF-STEM analysis revealed a high dispersion of molybdenum nitride species in 10-Mo-N/TiO_2 catalyst (Figure S1-c,d and Figure 3-b). Furthermore, the particle size of molybdenum species was slightly larger; than observed in 10-Mo-N/SBA-15; which has been estimated to be 1.7 ± 0.7 nm. In both 10-Mo-N/TiO_2 and 10-Mo-N/SBA-15 catalysts, STEM-EDS analysis confirmed the formation of small nanoparticles and the homogeneous distribution of molybdenum species within the support. Unfortunately, due to the small particle size, the low N concentration, and the low N-K peak energy it was not possible to detect unambiguously the formation of MoN_x species.

IV.3.2 Electronic properties of Mo supported samples: XPS and EPR studies

XPS studies. XPS analysis was performed for 10-Mo-O/SBA-15 and 10-Mo-O/TiO_2 on calcined materials. The active form of the catalysts was also studied by means of XPS by directly pre-treating the materials in XPS environmental chamber at 700 °C for 2 h under a 60 mL min^{-1} flow of 75 vol.% H_2/N_2. The results are presented in Figure 4, Figure S2, Table 2, and Table S1-S3.

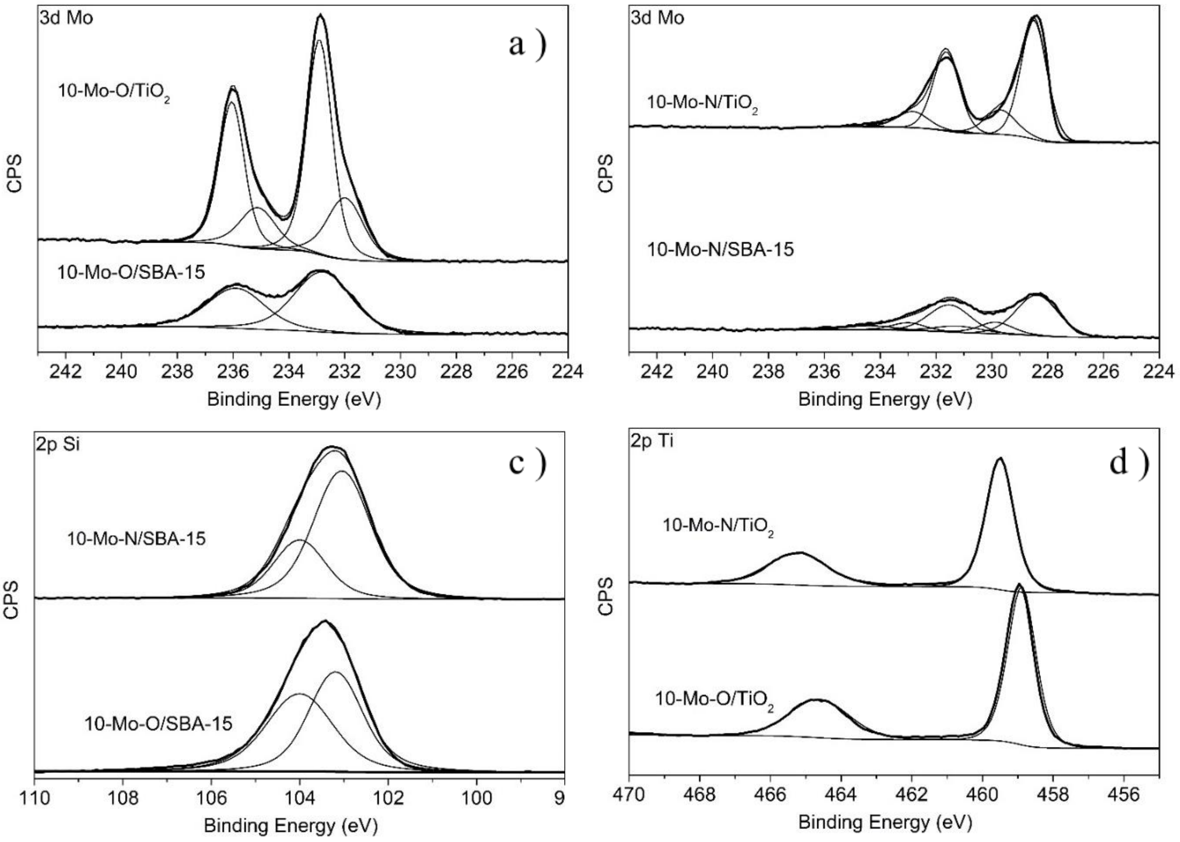

Figure 4. XPS spectra recorded on the calcined materials (10-Mo-O/SBA-15 and 10-Mo-O/TiO_2) and after nitridation under reaction conditions at 700°C for 2 h in environmental XPS chamber. (a) Mo 3d region: 10-Mo-O/SBA-15 and 10-Mo-O/TiO_2, (b) Mo 3d region: 10-Mo-N/TiO_2 and 10-Mo-N/SBA-15, (c) Si 2p region: 10-Mo-O/SBA-15 and 10-Mo-N/SBA-15 and (d) Ti 2p region: 10-Mo-O/TiO_2 and 10-Mo-N/TiO_2.

Table 2. Position of 3d Mo peaks of unsupported and supported Mo based catalyst at different reactive condition

	Mo peaks								**Surface composition**			
	Mo(VI)		**Mo(V)**		**Mo(IV)**		**Mo-N**		**Mo(VI)**	**Mo(V)**	**Mo(IV)**	**Mo-N**
	$3d_{5/2}$	$3d_{3/2}$	$3d_{5/2}$	$3d_{3/2}$	$3d_{5/2}$	$3d_{3/2}$	$3d_{5/2}$	$3d_{3/2}$	*%*	*%*	*%*	*%*
Mo-O/TiO_2	232.91	236.05	231.99	235.13	-	-	-	-	70.93	29.07	-	-
Mo-N/TiO_2	-	-	231.00	234.14	229.7	232.84	228.49	231.63	-	0.73	21.89	77.39
Mo-O/SBA-15	232.8	235.9	-	-	-	-	-	-	100	-	-	-
Mo-N/SBA-15	232.26	235.40	-	-	230.05	233.19	228.36	231.50	12.76	-	20.84	66.40
β-Mo_2N	-	-	-	-	229.50	232.65	228.78	231.92	-	-	36.34	63.65
α-MoO_3	233.19	236.29	-	-	-	-	-	-	100	-	-	-

* catalyst subject to pre-treatment under reaction condition at 700°C for 2h in environmental XPS chamber before analysis

IV.3.2.1 Evolution of Mo oxidation states.

To establish a basis for comparison, unsupported α-MoO_3 and β-Mo_2N were also investigated by XPS. As expected, in α-MoO_3, the predominant molybdenum species are Mo^{6+} (Figure 4) [36, 37]. Upon the pre-treatment, Mo 3d XPS profile shifted to lower binding energy. The spectral decomposition of Mo 3d region was composed predominantly by two oxidation states that can be ascribed to the Mo^{4+} and Mo-N (Table 2).

The evolution of the surface chemical composition of the Mo supported catalyst has been also studied and compared to the unsupported materials. In instance, the 10-Mo-O/SBA-15 showed a similar Mo 3d XPS profile to the unsupported α-MoO_3 phase with only two major spectral lines corresponding to Mo $3d_{5/2}$ and Mo $3d_{3/2}$ spin-orbit components at 232.8 eV and 235.9 eV of Mo^{6+} species detected which was attributed to formal Mo^{6+} oxidation state, with a small shift when compared to the reference material (Figure 4). Interestingly, in the case of 10-Mo-O/TiO_2, the spectral decomposition of the high-resolution Mo 3d region revealed the presence of both Mo^{6+} and Mo^{5+} species [36]. The distribution of Mo oxides species was determined to be ~ 70.93 at.% and ~29.07 at.% for Mo^{6+} and Mo^{5+} respectively (Table 2). The stabilization of a large fraction of Mo^{5+} in 10-Mo-O/TiO_2 might be related to the strong interaction between Mo species and TiO_2. The isomorphic substitution of Ti^{4+} species by Mo^{5+} has been reported in the literature as both species possess very close ionic radii (Ti^{4+}: 0.605 Å, and Mo^{5+}: 0.61 Å) [38].

Upon the pre-treatment step, a noticeable change in the Mo 3d XPS profile can be observed for both 10-Mo-N/SBA-15 and 10-Mo-N/TiO_2 characterized by an important shift to lower binding energies. In the 10-Mo-N/SBA-15, the high-resolution Mo 3d XPS profile can be deconvoluted into several peaks. The peaks at 228.36 eV and 231.50 eV are correlated with $3d_{5/2}$ and $3d_{3/2}$ of Mo-N species [39] which are the main Mo species (66.40 at.%; Table 2) suggesting that the nitridation of Mo species is not complete. Additional peaks at 232.26 eV and 235.40 eV that can be correlated to the presence of Mo^{6+} and peaks at 230.05 eV and 233.19 eV that can be correlated with Mo^{4+} have been also observed. In the case of 10-Mo-N/TiO_2 catalyst, the deconvolution of the high-resolution Mo 3d XPS profile revealed a chemical composition dominated by Mo-N ~ 77.39 at.% and Mo^{4+} ~ 21.89 at.%. In summary, upon the activation process, in all catalysts, a large fraction of Mo species where presents as molybdenum nitrides (> 60 at.%).

Further details on the degree of molybdenum nitridation can be extracted from the high-resolution Mo 3p spectra in which N 1s can also be observed (Figure S2). Due to the overlapping of N 1s with Mo $3p_{3/2}$ peaks, it is difficult to deconvolute these peaks in very detailed manner. Nevertheless, useful information can still be deduced. When compared to the oxides, the high-resolution Mo 3p XPS profiles of β-Mo_2N, 10-Mo-N/SBA-15 and 10-Mo-N/TiO_2 were all shifted to lower binding energies which can be associated to the nitridation of Mo species. For the 10-Mo-N/SBA-15 peaks related to N 1s and Mo $3p_{3/2}$ were significantly overlapped. Nevertheless, in the case of 10-Mo-N/TiO_2 an intense and well resolved peak at 398.00 eV which is attributed in the literature to N 1s in MoN and Mo_2N bulk (397.8 eV) is observed [40]. The same peak was observed in our unsupported β-Mo_2N materials but with less intensity. An additional, very weak in intensity, peak only observed in the case of 10-Mo-N/TiO_2 at 400.8 eV is also detected. It might be attributed to N-H or adsorbed NH_3 as its binding energy is very close to value reported for adsorbed NH_3 [41]. NH_3 species can form during the activation under N_2:H_2 atmosphere in condition favorable for ammonia synthesis.

IV.3.2.2 Evolution of the support surface redox properties

The evolution of the support surface characteristics has been also studied. For the SBA-15, no shift in binding energy was reported which is in agreement with the non-redox nature of the support (Figure 4-c). Although, upon the pre-treatment step, changes in the intensity related to the two components of Si 2p peaks namely Si-O-Si and Si-O-H (104 and 103.1 ±0.05 eV respectively) are detected. The inversion of intensity detected is more related to modification of the concentration of the external functional groups when subject to a reducing atmosphere under reduction conditions (Figure 4-c and Table S1). In the TiO_2 support more visible changes are observed after the pre-treatment. In 10-Mo-O/TiO_2, (Figure 4-d and Table S2) the binding energies of Ti $2p_{3/2}$ and Ti $2p_{1/2}$ were 458.89 and 464.61 eV, at slightly higher binding energies when compared with values reported for Ti^{4+} in undoped TiO_2 anatase phase (Ti $2p_{3/2}$: 458.59 eV and Ti $2p_{1/2}$: 464.31 eV) [42]. This slight shift to higher binding energy (~0.3 eV) has been attributed to charge redistribution between Mo and Ti species [38, 43]. However, after the activation step, a further shift to higher binding energies of Ti^{4+} is observed (Ti $2p_{3/2}$: 459.51 eV and Ti $2p_{1/2}$: 465.23 eV). In our nitridation conditions, the formation of titanium oxynitrides/ nitrides or reduction of Ti^{4+} into Ti^{3+} can be safely ruled out as both outcomes are accompanied by a marked shift to Ti 2p positions to lower binding energy [44] .

IV.3.2.3 Support surface composition.

XPS analysis also allows us to assess the effect of the nature of support and pre-treatment step in affecting the surface composition (Table S3). First of all, the Mo atomic surface concentration was found to be higher in 10-Mo-O/TiO_2 (12.5 at.%) than the 10-Mo-O/SBA-15 (4.3%). This might be related to Mo being impregnated within the pores and channels of SBA-15 rather than the external surface. However, when subject to the activation step, the concentration of Mo in the surface is only slightly modified in 10-Mo-N/SBA-15 (3.57 at.%), whereas in the case of 10-Mo-N/TiO_2 a more pronounced decrease in surface Mo , by ~ 21 %, is observed suggesting a strong interaction between Mo and Ti species.

EPR studies.

While molybdenum displays a range of oxidation states, only Mo^{5+} is paramagnetic and can yield an EPR signal. As such EPR is valuable in studying the process of nitridation of Mo species, the results are shown in Figure 5.

The EPR spectra recorded for 10-Mo-O/TiO_2, prior to the pre-treatment step, displays a weak isotrope signal centred at g=1.95 indicating the presence of Mo^{5+} species. The presence of Mo^{5+} was also confirmed by XPS analysis (Table 2 and Figure 4-a). Additionally, a weak signal is observed, around g=2, revealing the presence of oxygen vacancies [45]. During the activation process, under in-situ H_2/N_2, a sharp increase in Mo^{5+} content is detected reaching its maximum after 15 minutes of reaction at 700 °C. Then after; the concentration of Mo^{5+} decreases and stabilizes after a period of 20 minutes (Figure 5-c). The spectra displayed in Figure 5-a shows the EPR signal recorded at 293K at the end of the kinetics. The spectra display a weak anisotropy of g factor with $g_{x,y}$=1.97 and g_z=1.93. In contrast, the evolution of the oxygen vacancies concentration followed the reverse of Mo^{5+}. First, the concentration of oxygen vacancies decreased until reaching a minimum at 15 min of reaction and slightly increased afterwards to remain stable after 20 min. For 10-Mo-O/SBA-15 only a weak signal of Mo^{5+} and oxygen vacancies is detected. During the pre-treatment step no changes are observed in the concentration of both species. For the 10-Mo-O/SBA-15 catalyst as EPR measure only Mo(V) content, the XPS results can reveal maybe a fast electron exchange between oxygen vacancies and Mo that can contribute to overestimate the Mo(V) content.

Both XPS and EPR spectroscopy proved to be effective in measuring redox changes properties of Mo-based catalysts during the pre-treatment step. The activation process seems to proceed differently depending on the nature of the support. It seems the nitridation process of Mo species, when supported in SBA-15, occurs via the direct reduction of Mo species to Mo^{4+}. However, during the nitridation process of Mo species in the case of TiO_2, the formation of Mo^{5+} was detected hinting that the process might proceed via the formation of an $H_xMo_x^{5+}Mo_{1-x}^{6+}O_3$ species [46].

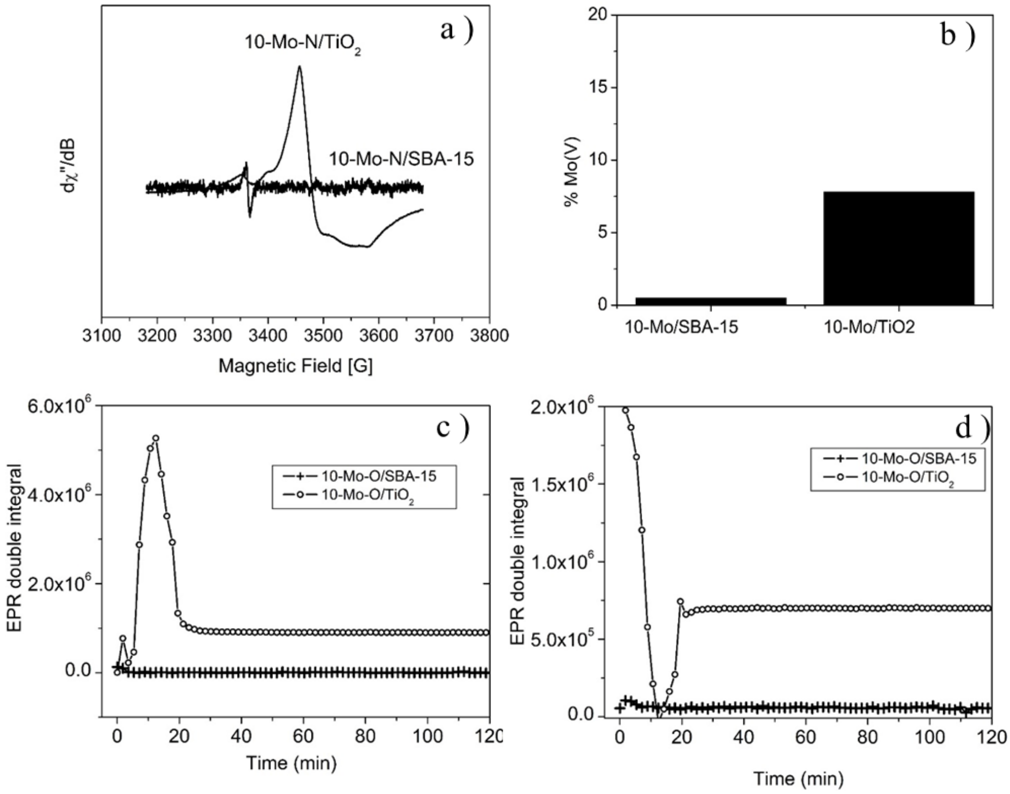

Figure 5. EPR results (a) EPR spectra after reaction, (b) Fraction of Mo^{5+} after pre-treatment conditions, (c) Kinetic evolution of Mo^{5+} species at 700°C under hydrogen, and (d) Kinetic evolution of O^{n-} species at 700°C under hydrogen.

IV.3.2.4 H_2 Temperature programmed reduction (H_2 – TPR)

Figure 6 depicts the results of molybdenum oxide reducibility when supported in SBA-15 and TiO_2. The results were compared against the unsupported α-MoO_3 phase.

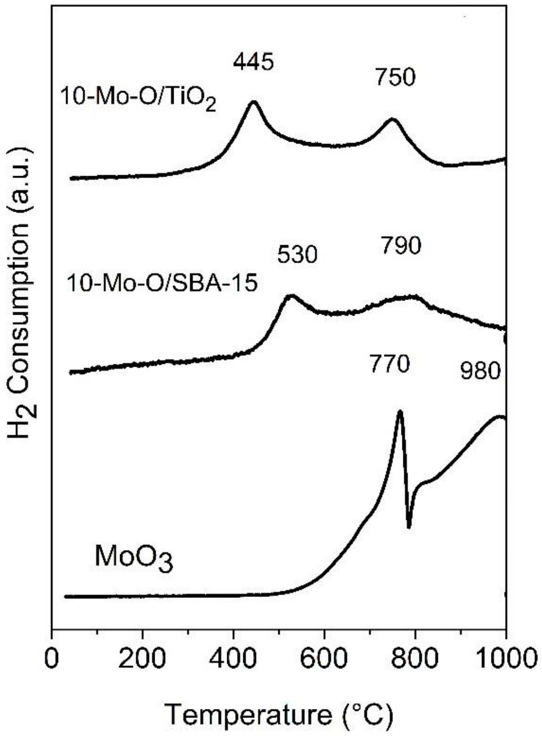

Figure 6. H_2-TPR profiles of α-MoO_3, 10-Mo-O/SBA15 and 10-Mo-O/TiO_2

The reduction profile of the unsupported α-MoO_3 phase was characterized by two main reduction peaks at 770 and 980 °C and a smaller shoulder at around 800 °C. However, the reduction process was not complete at temperature as high as 980°C. The profile agrees well with the literature with a first reduction step of α-MoO_3 into MoO_2, characterized by a sharp reduction peak, followed by the reduction of MoO_2 into the metallic form at high temperature [47]. The shoulder at around 800 °C was attributed in the literature, to the formation of intermediates phases, during the reduction process such as Mo_4O_{11} [47].

The reducibility of Mo oxides species was strongly affected upon its dispersion in SBA-15 and TiO_2. In both 10-Mo-O/SBA-15 and 10-Mo-O/TiO_2, the reduction profile shifted to lower temperature. Depending on the nature of the support, the first reduction step started as temperature as low as 445 °C for 10-Mo-O/TiO_2 and a slightly higher reduction temperature of

~ 530 °C for 10-Mo-O/SBA-15 was observed. These small differences between SBA-15 and TiO_2 might be related to the differences, observed by XPS, in the surface composition of both samples (Table 2). The second reduction step has also shifted to lower temperature with slight differences observed between SBA-15 and TiO_2. In summary, the reactivity of molybdenum oxides increased significantly upon its dispersion into high surface area supports confirming the high reactivity of small nanoparticles towards hydrogen when compared to unsupported molybdenum species.

IV.3.2.5 H_2-temperature programmed desorption (H_2-TPD)

The effect of support on the adsorption-desorption properties of 10-Mo-N/TiO_2 and 10-Mo-N/SBA-15 was studied by means of H_2-TPD. The results are shown in Figure 7 and Table S5. For 10-Mo-N/TiO_2, the desorption profile was characterized by two desorption peaks, the first one starting from 100 °C to 350 °C and the second desorption peak from 350 °C to 600 °C. In both desorption events, only small quantity of hydrogen is observed. However, in 10-Mo-N/SBA-15, the quantities of hydrogen desorbed where more pronounced especially for the second peak of hydrogen desorption. Furthermore, H_2-desorption continued at higher temperature (> 600°C) which was not the case in 10-Mo-N/TiO_2 sample. These results indicate a strong effect of the nature of the support in tuning molybdenum hydrogen adsorption-desorption properties. The drop of H_2-desorption capacity at high temperature might be indicative of SMSI behaviors affecting Mo species ability to activate hydrogen.

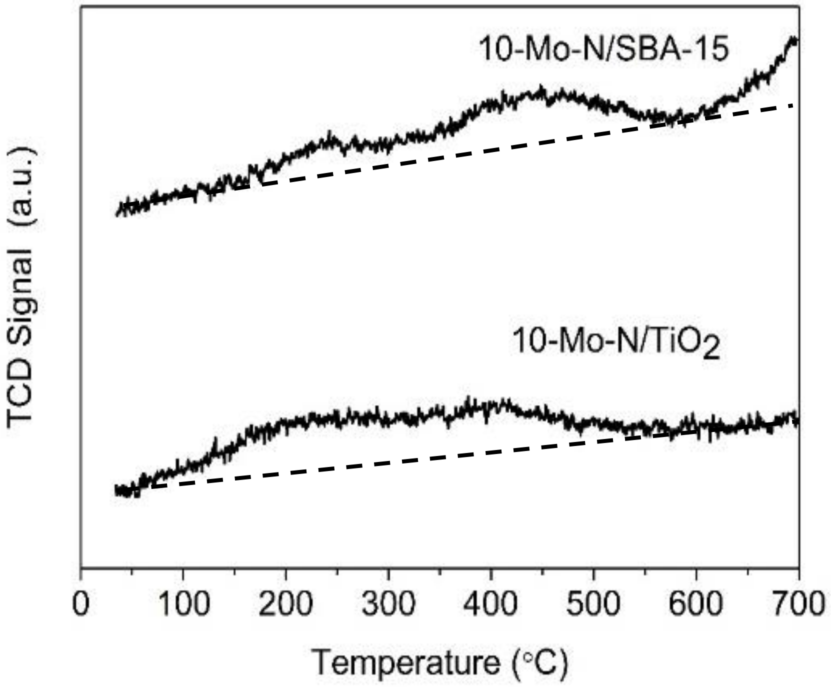

Figure 7. H_2-TPD profile of 10-Mo-N/SBA15 and 10-Mo-N/TiO_2

IV.3.3 Catalytic activity in model reactions: Ammonia synthesis and ammonia decomposition

The performance of 10-Mo-N/SBA-15 and 10-Mo-N/TiO$_2$ was studied in ammonia synthesis and the opposite reaction, ammonia decomposition. The results are summarized in Figure 8 and Table 3.

The catalytic activity of 10-Mo-N/SBA-15 and 10-Mo-N/TiO$_2$ catalyst was studied in ammonia synthesis and compared against the unsupported β-Mo$_2$N (Figure 8-a, Table 3). 10-Mo-N/SBA-15 exhibits catalytic activity that is comparable to the reference materials despites large differences in Mo loading (10-Mo-N/SBA-15: 84.6 µmol $g_{catalyst}^{-1}$ $h^{-1}$and β-Mo$_2$N: 76 µmol $g_{catalyst}^{-1}$ h^{-1} for initial rate (30-60 min)). When normalized against the active phase loading a rate of 1208 µmol $g_{active\ phase}^{-1}$ h^{-1} is obtained over the 10-Mo-N/SBA-15 catalyst. After a period of stabilization, the catalyst did not show any sign of deactivation over time demonstrating its stability in H$_2$:N$_2$ stream. Surprisingly, 10-Mo-N/TiO$_2$ displayed a very poor catalytic activity and deactivated very quickly. The limited catalytic activity of 10-Mo-N/TiO$_2$ despite its enhanced textural and structural properties demonstrated a marked influence of the nature of the support in altering the ability Mo in catalyzing ammonia synthesis reaction.

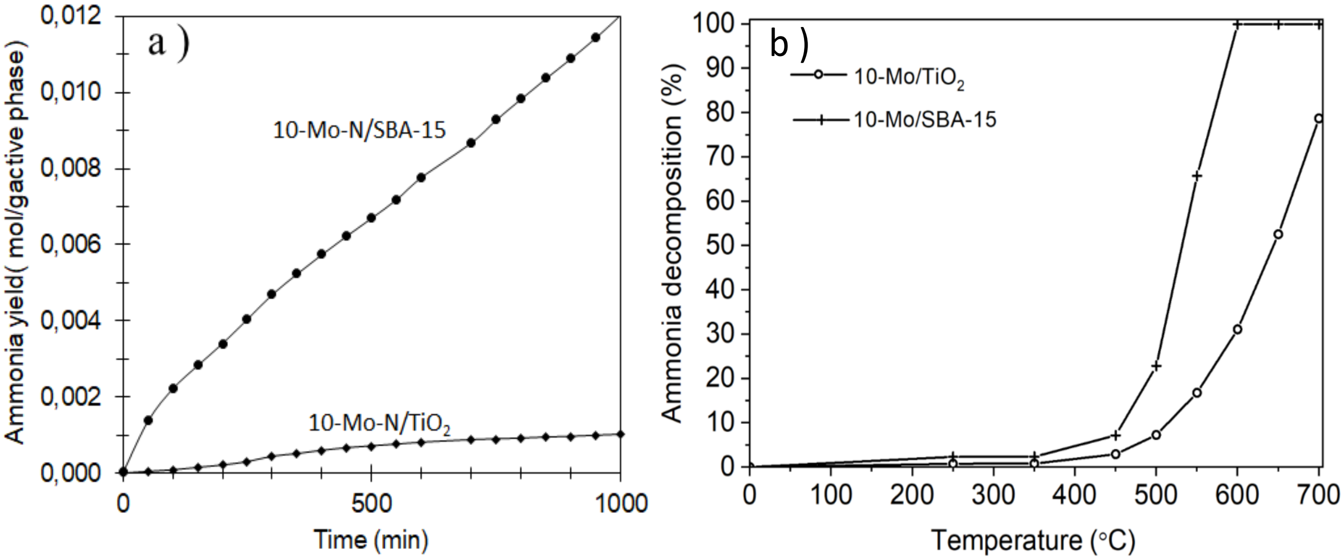

Figure 8. a) Cumulative ammonia yield obtained of 10-Mo-N/SBA-15 and 10-Mo-N/TiO$_2$. Reaction performed under 60 mL min^{-1} flow rate of 75 vol.% H$_2$/N$_2$ at 400 °C and ambient pressure. b) Ammonia decomposition conducted under 15% NH$_3$ in Ar at different temperatures and atmospheric pressure.

To confirm whether TiO_2 will affect in similar manner the activity of Mo species in the reverse reaction, the activity of 10-Mo-N/SBA-15 and 10-Mo-N/TiO_2 has been also studied in ammonia decomposition. The catalytic activity was measured at temperature ranging between 50 °C and 700 °C and the results are presented in Figure 8-b and Table 3. Unlike in ammonia synthesis, both catalysts 10-Mo-N/SBA-15 and 10-Mo-N/TiO_2 are active in ammonia decomposition. However, differences on the catalytic activity are observed especially at high temperature. At low temperature, 10% NH_3 conversion is achieved at 460 °C in 10-Mo-N/SBA-15 while the same conversion value is achieved at slightly higher temperature ~ 510 °C in the case of 10-Mo-N/TiO_2. The activation energy is slightly lower in case 10-Mo-N/SBA-15 (71 kJ mol^{-1}) when compared to the 10-Mo-N/TiO_2 (78 kJ mol^{-1}). At higher temperature, complete conversion of NH_3 was achieved at 600 °C in 10-Mo-N/SBA-15, while in 10-Mo-N/TiO_2 catalyst complete conversion was not attained even at temperature as high as 700 °C. In summary, while supporting Mo over Titania did not turn-off the catalytic activity in ammonia decomposition, lower conversions are clearly obtained compared to the 10-Mo-N/SBA-15.

Table 3. Summary of the catalytic activity of 10-Mo-N/SBA-15 and 10-Mo-N/TiO_2

	Ammonia synthesis reaction				**Ammonia decomposition**		
	Initial rate (µmol $g_{catalyst}^{-1}$ h^{-1})	**Initial rate (µmol $g_{active\ phase}^{-1}$ h^{-1})**	**Steady state rate (µmol $g_{catalyst}^{-1}$ h^{-1})**	**N^a (wt%)**	**T_{10}**	**T_{100}**	**Ea (kJ mol^{-1})**
α-MoO_3	76	76	77	5.9	-	-	-
10-Mo-N/SBA-15	84.6	1208	50.74	1.1	460	585	71
10-Mo-N/TiO_2	ND[b]	ND	ND	1.2	510	-	78

* ammonia synthesis under 60 mL min^{-1} of 75% H_2 in N_2 (BOC, 99.98 %) at 400 °C and atmospheric pressure. * ammonia decomposition conducted under 15% NH_3 in Ar at different temperatures and atmospheric pressure. [a] Nitrogen content measured by CHNS in the post-reaction samples. [b]ND:Not detected. T_{10}: temperature at which 10% NH_3 conversion is achieved. T_{100}: temperature at which 100% NH_3 conversion is achieved.

IV.3.4 Discussion

The catalytic properties of the supported Mo nitrides in both ammonia synthesis and ammonia decomposition was found to be markedly affected by the nature of the support (TiO_2 or SBA-15). Depending on the catalytic reaction, disparities in how the support affects the catalytic activity of Mo species was found. When ammonia synthesis is studied, Mo nitrides supported on SBA-15 was found to be active and stable over time. While when supported in TiO_2 a very limited catalytic activity was observed and the catalyst deactivated quite rapidly. This indicates that the properties of Mo active species varied with the nature of the support. In ammonia decomposition, the effect of support was not as “radical” as observed in ammonia synthesis. While 10-Mo-N/SBA-15 was by far more active than 10-Mo-N/TiO_2, the activity of this latter did not turn-off completely.

In the current study, the active phase, MoN_x, was prepared by nitridation under 75 vol.% H_2/N_2 (BOC, 99.98 %) gas mixture at a total gas flow of 60 mL min^{-1} for 2 h at 700 °C. To investigate the differences between the catalysts, the textural and structural properties have been studied. Both catalysts displayed high accessible surface area (10-Mo-O/SBA-15: 465 m^2 g^{-1} and 10-Mo-O/TiO_2 : 194 m^2 g^{-1}). Furthermore, in both catalysts, no PXRD signals related to Mo phases oxides or nitrides are observed in the wide-angle domain confirming the high dispersion of the active sites. The formation of small Mo nanoparticles was also confirmed by HAADF-STEM analysis. The particle size of molybdenum species was found to be sensibly similar in 10-Mo-N/SBA-15 (1.3 ± 0.3 nm) and in 10-Mo-N/TiO_2 (1.7 ± 0.7 nm). Thus, in both catalysts, after the activation step, small size nano-particles were formed. Hence the effect of particle size influencing the catalytic activity can be considered minimal.

The influence of the support on the surface composition was investigated by means of XPS spectroscopy and compared against a reference material. Before the activation step, difference on Mo species detected by XPS was already observed. In both α-MoO_3 and Mo-O/SBA-15, the predominant Mo species was Mo^{6+} (Table 2, Figure 4). However, almost ~ 29 atm. % of Mo species in 10-Mo-O/TiO_2 was found to be composed of Mo^{5+} and possible substitution of Ti^{4+} species by Mo^{5+} can occur.[38] Furthermore, In 10-Mo-O/TiO_2, the binding energies of Ti $2p_{3/2}$ and Ti $2p_{1/2}$ were found at 458.89 and 464.61 eV, which are slightly higher when compared with values reported from the literature which further confirm the strong interaction of Mo species with titanium species.[42, 43] Upon nitridation, a range of oxidation states have been detected. In both catalyst, high proportion of Mo species were found to be in the nitride form (> 60 atm.%). However, after the activation step, only Mo^{4+} species and MoN_x species are detected in the 10-Mo-N/TiO_2 while in 10-Mo-N/SBA-15, in addition to Mo^{4+} species and MoN_x a fraction of Mo^{6+} was still present in the catalyst after the activation step denoting incomplete nitridation process. Despite these differences, the percentage of Mo nitrides population in both systems seems to be rather close (10-Mo-N/TiO_2: 77.39 at.% and 10-Mo-N/SBA-15: 66.40 at.%). The degree of Mo species nitridation was also observed from the high-resolution Mo 3p spectra in which N 1s also can be observed. Only in the case of 10-Mo-N/TiO_2 an intense and well resolved peak at 398.00 eV which is attributed in the literature to N 1s in MoN and Mo_2N bulk (397.8 eV) is observed which it may be reflecting a different Mo/N ratio in the catalyst. An additional, very weak in intensity, peak only observed in the case of 10-Mo-N/TiO_2 at 400.8 eV is also detected which was attributed to N-H or adsorbed NH_3.

To gain insight in the nitridation process of supported Mo oxides species EPR and H_2-TPR has been conducted. When compared to α-MoO_3 phase, the reduction process started earlier in the supported catalysts with the first reduction step starting as temperature as low as 445 °C for 10-Mo-O/TiO_2 and a slightly higher reduction temperature of ~530 °C for 10-Mo-O/SBA-15. These differences might be related to the difference in Mo oxides species presents in the surface as evidenced by XPS. Furthermore, the activation process was studied by EPR under 75 vol.% H_2/N_2 (BOC, 99.98 %) gas mixture mimicking the activation step. Fundamental differences were observed between 10-Mo-O/SBA-15 and 10-Mo-O/TiO_2 materials. In the case of Mo supported in TiO_2, the nitridation/reduction process occurs first via the formation of Mo^{5+} species as detected by EPR which reached a maximum concentration after 15 min reaction before start decreasing. Although only a very small fraction is detected by XPS, EPR shows that a fraction of Mo^{5+} (7.8%) is still present in the 10-Mo-O/TiO_2 catalyst directly after the activation step. The fast formation of Mo^{5+} might be indicative of multistep reduction process with first intercalation of hydrogen into α-MoO_3 to forming first hydrogen molybdenum bronzes $H_xMo_x^{5+}Mo_{1-x}^{6+}O_3$ [46]. Hydrogen molybdenum bronze are metastable phases that will decomposes eventually to form MoO_2 and water.[48] In the contrary, no Mo^{5+} was detected when Mo species were supported in SBA-15 indicating that the process is rather dominated by direct reduction of Mo^{6+} to Mo^{4+}. These differences might be related to different mechanism by which Mo species are reduced/nitrided. In the literature, different mechanism has been proposed including the formation of either molybdenum bronze ($H_xMo_x^{5+}Mo_{1-x}^{6+}O_3$) and/or MoO_2 and Mo metallic intermediates before nitridation. Depending on the nitridation conditions (*i.e.* gas composition, space velocity and/or heating rate), the nitridation mechanism can be altered leading to the formation of either cubic γ-Mo_2N with or tetragonal β-Mo_2N [49, 50]. The formation of β-Mo_2N has been reported to follows a non-topotactic route via a multiple step reduction ($MoO_3 \rightarrow MoO_2 \rightarrow Mo \rightarrow MoN_x$) [51, 52] while the formation γ-Mo_2N has been reported to proceed through a topotactic route with the formation of Hydrogen molybdenum bronze as an intermediate species before nitridation.[53] It is clear from our investigation that the mechanism of reduction/nitridation is strongly affected by the degree of interaction between Mo species and the support species. However, due the formation of small nanoparticles in both SBA-15 and TiO_2, and close chemical composition of β-Mo_2N and γ-Mo_2N, it was rather difficult to ambiguously determine the nature of MoN_x species based on XRD and XPS results. As the activity of Mo_2N species in many catalytic reactions was found to vary depending on the crystallographic phase, it is alluring to explain the differences in the catalytic activity of 10-Mo-N/SBA-15 and 10-Mo-N/TiO_2 ammonia synthesis by the formation of different Mo_2N allotropic forms. However, it is worth mentioning that no large differences in the catalytic activity has been found between bulk β-Mo_2N and γ-Mo_2N in ammonia synthesis and only δ-MoN nitride phase was found to be poorly active in ammonia synthesis.[30] As such the identification of the catalytically active site and the origin of deactivation in Mo species supported in TiO_2 remains very challenging. In the literature, the performance of catalysts in ammonia synthesis reaction has been correlated to nitrogen binding energy with ideal surface displaying intermediate nitrogen binding energies. The adsorption properties of metal nitrides were found to be sensitive to chemical composition (surface vs bulk), Mo oxidation states, $Mo^{\delta+}/N$ ratio, and nitrogen-deficient site density [52]. To some extent, differences in H_2 adsorption-desorption capacities at least at high temperature was observed between 10-Mo-N/SBA-15 and 10-Mo-N/TiO_2. The surface composition after the activation step, and the reduction/nitridation process was found to be different depending on the nature of the support. Thus, the differences in the catalytic activity observed might be related to the differences observed in the surface composition and changes in the adsorption of ammonia synthesis reactants.

IV.4 Conclusion

In the current study supported Mo nitrides species on SBA-15 and TiO_2 was prepared by nitridation under 75 vol.% H_2/N_2 (BOC, 99.98 %) gas mixture at a total gas flow of 60 mL min^{-1} for 2 h at 700°C. The results of characterization demonstrate the formation of small molybdenum nanoparticles in both 10-Mo-N/SBA-15 and 10-Mo-N/TiO_2 catalysts. Although both samples exhibited ameliorated structural properties when compared to the bulk material, β-Mo_2N, only 10-Mo-N/SBA-15 was found to be active in ammonia synthesis (1208 µmol $g_{\text{active phase}}^{-1}$ h^{-1}) while 10-Mo-N/TiO_2 only displayed a poor catalytic activity before completely deactivating over time. The catalysts were also studied for ammonia decomposition where 10-Mo-N/SBA-15 was found to be more active than 10-Mo-N/TiO_2. XPS analysis showed a strong interaction between Mo species and TiO_2 support leading to differences in the process of Mo species reduction/nitridation process. EPR spectroscopy proved to be effective in determining the nitridation mechanism of Mo species. In the case of Mo supported in TiO_2, EPR showed that reduction/nitridation process via the formation of Mo^{5+} species which was not the case in Mo supported SBA-15 suggesting the formation of different Mo nitrides species. Upon nitridation, the distribution of Mo oxidation states was found to be different depending on the nature of the support. Furthermore, a weak XPS signal related to adsorbed NH_x species was detected in 10-Mo-N/TiO_2 catalyst. It is also worth noting that 10-Mo-N/SBA-15 hydrogen chemisorption capacity and desorption (during TPD) was superior to 10-Mo-N/TiO_2 catalyst. The origin of Mo species deactivation in ammonia synthesis when supported in TiO_2 originates probably from the strong interaction between Mo species and the support. This phenomenon resulted in the alteration of the Mo nitridation mechanism leading to a catalyst with different surface composition, and probably different surface termination, vacancies concentrations, etc. These results demonstrate that the catalytic activity of Mo nitride species can be tuned via the modulation the interaction between the active species and the support.

IV.5 References

[1] A.N. Varakin, A.V. Mozhaev, A.A. Pimerzin, P.A. Nikulshin, Comparable investigation of unsupported MoS2 hydrodesulfurization catalysts prepared by different techniques: Advantages of support leaching method, Applied Catalysis B: Environmental, 238 (2018) 498-508.

[2] H. Topsøe, B.S. Clausen, Active sites and support effects in hydrodesulfurization catalysts, Applied Catalysis, 25 (1986) 273-293.

[3] M.M.H. Mondol, B.N. Bhadra, S.H. Jhung, Molybdenum nitride@porous carbon, derived from phosphomolybdic acid loaded metal-azolate framework-6: A highly effective catalyst for oxidative desulfurization, Applied Catalysis B: Environmental, 288 (2021) 119988.

[4] J. Zou, Y. Lin, S. Wu, Y. Zhong, C. Yang, Molybdenum Dioxide Nanoparticles Anchored on Nitrogen-Doped Carbon Nanotubes as Oxidative Desulfurization Catalysts: Role of Electron Transfer in Activity and Reusability, Advanced Functional Materials, 31 (2021) 2100442.

[5] S. Singh, A. Modak, K.K. Pant, A. Sinhamahapatra, P. Biswas, MoS2–Nanosheets-Based Catalysts for Photocatalytic CO2 Reduction: A Review, ACS Applied Nano Materials, 4 (2021) 8644-8667.

[6] Y. Kuwahara, T. Mihogi, K. Hamahara, K. Kusu, H. Kobayashi, H. Yamashita, A quasi-stable molybdenum sub-oxide with abundant oxygen vacancies that promotes CO2 hydrogenation to methanol, Chemical Science, 12 (2021) 9902-9915.

[7] N. Liu, L. Nie, N. Xue, H. Dong, L. Peng, X. Guo, W. Ding, Catalytic Ammonia Synthesis over Mo Nitride/ZSM-5, ChemCatChem, 2 (2010) 167-174.

[8] N. Gavrilova, M. Myachina, V. Dyakonov, V. Nazarov, V. Skudin, Synthesis of Microporous Mo2C-W2C Binary Carbides by Thermal Decomposition of Molybdenum-Tungsten Blues, Nanomaterials, 10 (2020).

[9] H.B. Wu, B.Y. Xia, L. Yu, X.Y. Yu, X.W. Lou, Porous molybdenum carbide nano-octahedrons synthesized via confined carburization in metal-organic frameworks for efficient hydrogen production, Nature Communications, 6 (2015).

[10] M. Nagae, T. Yoshio, Y. Takemoto, J. Takada, Microstructure of a molybdenum nitride layer formed by nitriding molybdenum metal, Journal of the American Ceramic Society, 84 (2001) 1175-1177.

[11] S. Wang, H. Ge, S. Sun, J. Zhang, F. Liu, X. Wen, X. Yu, L. Wang, Y. Zhang, H. Xu, J.C. Neuefeind, Z. Qin, C. Chen, C. Jin, Y. Li, D. He, Y. Zhao, A New Molybdenum Nitride Catalyst with Rhombohedral MoS2 Structure for Hydrogenation Applications, Journal of the American Chemical Society, 137 (2015) 4815-4822.

[12] P. Xiao, M.A. Sk, L. Thia, X. Ge, R.J. Lim, J.-Y. Wang, K.H. Lim, X. Wang, Molybdenum phosphide as an efficient electrocatalyst for the hydrogen evolution reaction, Energy & Environmental Science, 7 (2014) 2624-2629.

[13] W. Cui, Q. Liu, Z. Xing, A.M. Asiri, K.A. Alamry, X. Sun, MoP nanosheets supported on biomass-derived carbon flake: One-step facile preparation and application as a novel high-active electrocatalyst toward hydrogen evolution reaction, Applied Catalysis B: Environmental, 164 (2015) 144-150.

[14] J. Lei, Y. Xie, A. Kutana, K.V. Bets, B.I. Yakobson, Salt-Assisted MoS2 Growth: Molecular Mechanisms from the First Principles, Journal of the American Chemical Society, 144 (2022) 7497-7503.

[15] S. Park, A.T. Garcia-Esparza, H. Abroshan, B. Abraham, J. Vinson, A. Gallo, D. Nordlund, J. Park, T.R. Kim, L. Vallez, R. Alonso-Mori, D. Sokaras, X. Zheng, Operando Study of Thermal Oxidation of Monolayer MoS2, Advanced Science, 8 (2021) 2002768.

[16] R. Kojima, K. Aika, Molybdenum nitride and carbide catalysts for ammonia synthesis, Applied Catalysis a-General, 219 (2001) 141-147.

[17] A.-M. Alexander, J.S.J. Hargreaves, Alternative catalytic materials: carbides, nitrides, phosphides and amorphous boron alloys, Chemical Society Reviews, 39 (2010) 4388-4401.

[18] B.Y. Fang, C.F. Zhang, Z.L. Qi, C.Y. Li, J. Ni, X.Y. Wang, J.X. Lin, C.T. Au, B.Y. Lin, L.L. Jiang, Combining molybdenum carbide with ceria overlayers to boost Mo/CeO2 catalyzed ammonia synthesis, Aiche Journal, 68 (2022).

[19] B.Y. Fang, C.F. Zhang, J.H. Li, M.D. Yang, C.Y. Li, J. Ni, X.Y. Wang, J.X. Lin, B.Y. Lin, L.L. Jiang, Enhanced ammonia synthesis activity of carbon-supported Mo catalyst by Mo carburization, Chemical Communications, 58 (2022) 7785-7788.

[20] L. Volpe, M. Boudart, Ammonia synthesis on molybdenum nitride, The Journal of Physical Chemistry, 90 (1986) 4874-4877.

[21] C.J.H. Jacobsen, Novel class of ammonia synthesis catalysts, Chemical Communications, (2000) 1057-1058.

[22] I. AlShibane, A. Daisley, J.S.J. Hargreaves, A.L. Hector, S. Laassiri, J.L. Rico, R.I. Smith, The Role of Composition for Cobalt Molybdenum Carbide in Ammonia Synthesis, ACS Sustainable Chemistry & Engineering, 5 (2017) 9214-9222.

[23] R. Kojima, K.-i. Aika, Cobalt molybdenum bimetallic nitride catalysts for ammonia synthesis: Part 2. Kinetic study, Applied Catalysis A: General, 218 (2001) 121-128.

[24] S. Al Sobhi, N. Bion, J.S.J. Hargreaves, A.L. Hector, S. Laassiri, W. Levason, A.W. Lodge, A.R. McFarlane, C. Ritter, The reactivity of lattice nitrogen within the Ni2Mo3N and NiCoMo3N phases, Materials Research Bulletin, 118 (2019) 110519.

[25] S. Yang, T. Zhang, Y.Y. Yang, B.X. Wang, J. Li, Z.T. Gong, Z.Y. Yao, W.G. Du, S.J. Liu, Z.L. Yu, Molybdenum-based nitrogen carrier for ammonia production via a chemical looping route, Applied Catalysis B-Environmental, 312 (2022).

[26] L. Li, W.K. Yu, W.B. Gong, H. Wang, C.L. Chiang, Y.P. Lin, J. Zhao, L.B. Zhang, J.M. Lee, G.F. Zou, Sulfur-induced electron redistribution of single molybdenum atoms promotes nitrogen electroreduction to ammonia, Applied Catalysis B-Environmental, 321 (2023).

[27] X.-W. Guo, S.-M. Chen, H.-J. Wang, Z.-M. Zhang, H. Lin, L. Song, T.-B. Lu, Single-atom molybdenum immobilized on photoactive carbon nitride as efficient photocatalysts for ambient nitrogen fixation in pure water, Journal of Materials Chemistry A, 7 (2019) 19831-19837.

[28] S. Kim, Y. Park, J. Kim, T.P. Pabst, P.J. Chirik, Ammonia synthesis by photocatalytic hydrogenation of a N2-derived molybdenum nitride, Nature Synthesis, 1 (2022) 297-303.

[29] S.T. Oyama, Preparation and catalytic properties of transition metal carbides and nitrides, Catalysis Today, 15 (1992) 179-200.

[30] D. McKay, J.S.J. Hargreaves, J.L. Rico, J.L. Rivera, X.L. Sun, The influence of phase and morphology of molybdenum nitrides on ammonia synthesis activity and reduction characteristics, Journal of Solid State Chemistry, 181 (2008) 325-333.

[31] K.-i. Aika, A. Ozaki, Mechanism and isotope effect in ammonia synthesis over molybdenum nitride, Journal of Catalysis, 14 (1969) 311-321.

[32] B. Fang, M. Yang, C. Zhang, J. Li, C. Li, J. Ni, X. Wang, J. Lin, B. Lin, L. Jiang, Molybdenum carbide phase effects in heterogeneous catalytic ammonia synthesis, Chemical Engineering Science, 259 (2022) 117834.

[33] Z. Luo, G. Zhao, H. Pan, W. Sun, Strong Metal–Support Interaction in Heterogeneous Catalysts, Advanced Energy Materials, 12 (2022) 2201395.

[34] H. Tang, Y. Su, B. Zhang, A.F. Lee, M.A. Isaacs, K. Wilson, L. Li, Y. Ren, J. Huang, M. Haruta, B. Qiao, X. Liu, C. Jin, D. Su, J. Wang, T. Zhang, Classical strong metal–support interactions between gold nanoparticles and titanium dioxide, Science Advances, 3 (2017) e1700231.

[35] D. Zhao, J. Sun, Q. Li, G.D. Stucky, Morphological Control of Highly Ordered Mesoporous Silica SBA-15, Chemistry of Materials, 12 (2000) 275-279.

[36] J. Baltrusaitis, B. Mendoza-Sanchez, V. Fernandez, R. Veenstra, N. Dukstiene, A. Roberts, N. Fairley, Generalized molybdenum oxide surface chemical state XPS determination via informed amorphous sample model, Applied Surface Science, 326 (2015) 151-161.

[37] T. Weber, J.C. Muijsers, J.H.M.C. van Wolput, C.P.J. Verhagen, J.W. Niemantsverdriet, Basic Reaction Steps in the Sulfidation of Crystalline MoO3 to MoS2, As Studied by X-ray Photoelectron and Infrared Emission Spectroscopy, The Journal of Physical Chemistry, 100 (1996) 14144-14150.

[38] S. Esposito, N. Ditaranto, G. Dell’Agli, R. Nasi, P. Rivolo, B. Bonelli, Effective Inclusion of Sizable Amounts of Mo within TiO2 Nanoparticles Can Be Obtained by Reverse Micelle Sol–Gel Synthesis, ACS Omega, 6 (2021) 5379-5388.

[39] L. Huo, X. Han, L. Zhang, B. Liu, R. Gao, B. Cao, W.-W. Wang, C.-J. Jia, K. Liu, J. Liu, J. Zhang, Spatial confinement and electron transfer moderating MoN bond strength for superior ammonia decomposition catalysis, Applied Catalysis B: Environmental, 294 (2021) 120254.

[40] M. Nagai, J. Takada, S. Omi, XPS Study of Nitrided Molybdena/Titania Catalyst for the Hydrodesulfurization of Dibenzothiophene, The Journal of Physical Chemistry B, 103 (1999) 10180-10188.

[41] R.J.J. Jansen, H. van Bekkum, XPS of nitrogen-containing functional groups on activated carbon, Carbon, 33 (1995) 1021-1027.

[42] M.C. Biesinger, L.W.M. Lau, A.R. Gerson, R.S.C. Smart, Resolving surface chemical states in XPS analysis of first row transition metals, oxides and hydroxides: Sc, Ti, V, Cu and Zn, Applied Surface Science, 257 (2010) 887-898.

[43] D. Mittal, W.F. Chen, P. Koshy, H.K. Chen, I. Kabir, Y. Jiang, Z.Y. Liu, C.C. Sorrell, Intervalence charge transfer and thermodynamic effects on the photocatalytic performance of Fe/Mo single and codoped TiO2 thin films, SN Applied Sciences, 1 (2019).

[44] J. Wang, D.N. Tafen, J.P. Lewis, Z. Hong, A. Manivannan, M. Zhi, M. Li, N. Wu, Origin of Photocatalytic Activity of Nitrogen-Doped TiO2 Nanobelts, Journal of the American Chemical Society, 131 (2009) 12290-12297.

[45] C. Drouilly, J.-M. Krafft, F. Averseng, S. Casale, D. Bazer-Bachi, C. Chizallet, V. Lecocq, H. Vezin, H. Lauron-Pernot, G. Costentin, ZnO Oxygen Vacancies Formation and Filling Followed by in Situ Photoluminescence and in Situ EPR, The Journal of Physical Chemistry C, 116 (2012) 21297-21307.

[46] A. Borgschulte, O. Sambalova, R. Delmelle, S. Jenatsch, R. Hany, F. Nüesch, Hydrogen reduction of molybdenum oxide at room temperature, Scientific Reports, 7 (2017) 40761.

[47] T. Bhaskar, K.R. Reddy, C.P. Kumar, M.R.V.S. Murthy, K.V.R. Chary, Characterization and reactivity of molybdenum oxide catalysts supported on zirconia, Applied Catalysis A: General, 211 (2001) 189-201.

[48] J.J. Birtill, P.G. Dickens, Thermochemistry of hydrogen molybdenum bronze phases HxMoO3, Journal of Solid State Chemistry, 29 (1979) 367-372.

[49] J.-G. Choi, R.L. Curl, L.T. Thompson, Molybdenum nitride catalysts: I. Influence of the synthesis factors on structural properties, Journal of Catalysis, 146 (1994) 218-227.

[50] S. Jujjuri, F. Cárdenas-Lizana, M.A. Keane, Synthesis of group VI carbides and nitrides: application in catalytic hydrodechlorination, Journal of Materials Science, 49 (2014) 5406-5417.

[51] F. Cárdenas-Lizana, S. Gómez-Quero, N. Perret, L. Kiwi-Minsker, M.A. Keane, β-Molybdenum nitride: synthesis mechanism and catalytic response in the gas phase hydrogenation of p-chloronitrobenzene, Catalysis Science & Technology, 1 (2011) 794-801.

[52] N. Perret, D. Lamey, L. Kiwi-Minsker, F. Cárdenas-Lizana, M.A. Keane, New insights into the effect of nitrogen incorporation in Mo: catalytic hydrogenation vs. hydrogenolysis, Catalysis Science & Technology, 9 (2019) 1891-1901.

[53] F. Cárdenas-Lizana, D. Lamey, L. Kiwi-Minsker, M.A. Keane, Molybdenum nitrides: a study of synthesis variables and catalytic performance in acetylene hydrogenation, Journal of Materials Science, 53 (2018) 6707-6718.

IV.6 Supplementary Information

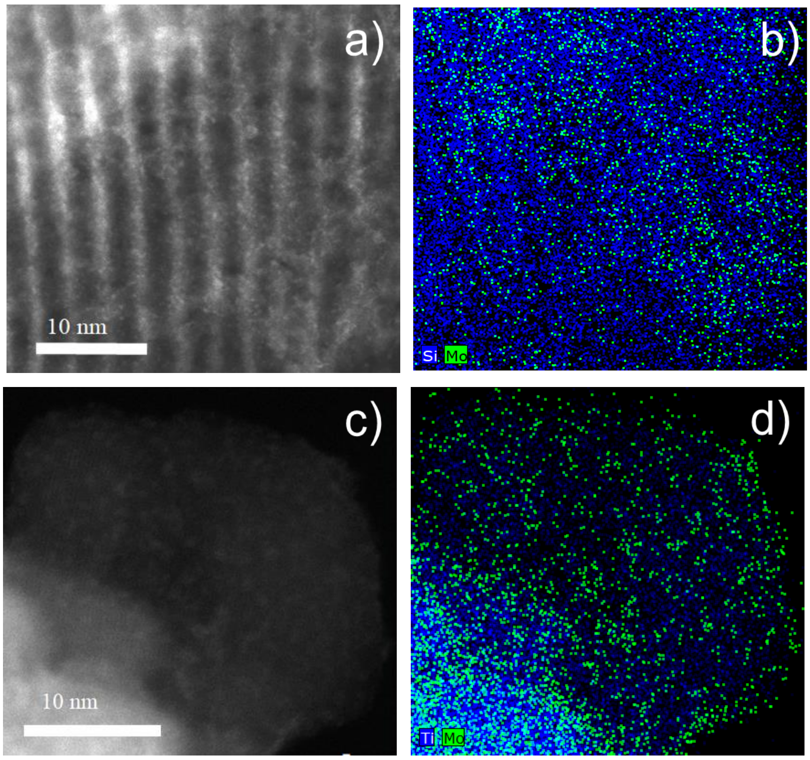

Figure S1 Representative lower magnification HAADF images and the corresponding STEM-EDS elemental maps for 10-Mo-N/SBA-15 (a,and b) 10-Mo-N/TiO_2 (c and d)

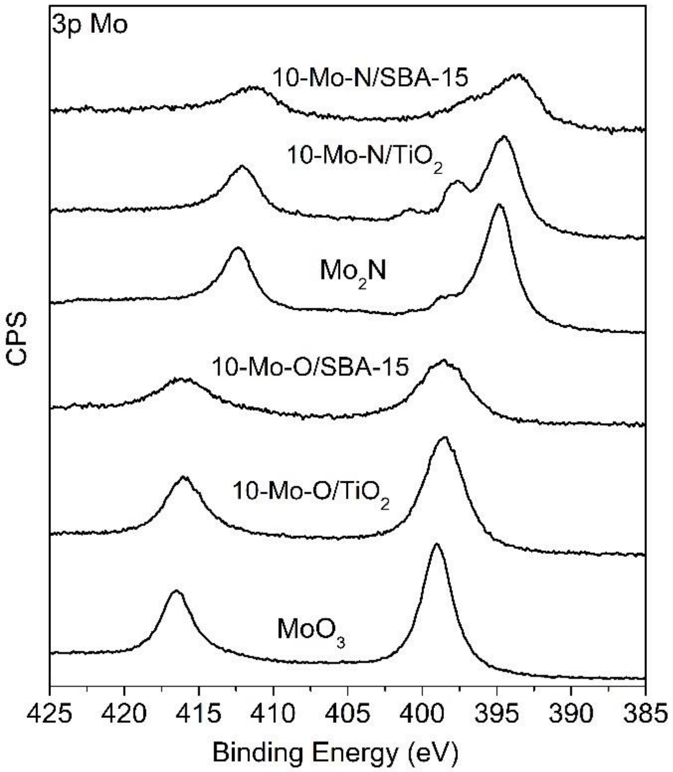

Figure S2 XPS spectra recorded on the calcined materials in Mo 3p Region (10-Mo-O/SBA-15 and 10-Mo-O/TiO$_2$) and after nitridation under reaction conditions at 700°C for 2h in environmental XPS chamber

Table S1. Position of Si 2p peaks of unsupported and supported Mo based catalyst at different reactive condition

	Si 2p peak position		**Surface composition**	
	Si-O-Si	**Si-O-H**	**Si-O-Si (%)**	**Si-O-H (%)**
10-Mo/SBA-15	104.00	103.16	54.96	45.04
10-Mo-N/SBA-15*	104.00	103.05	29.58	70.42

* catalyst subject to pre-treatment under reaction condition at 700°C for 2h in environmental XPS chamber before analysis

Table S2. Position of Ti 2p peaks of unsupported and supported Mo based catalyst at different reactive condition

	Ti 2p peak position	
	Ti $2p_{3/2}$	Ti $2p_{1/2}$
10-Mo/TiO$_2$	458.89	464.61
10-Mo-N/TiO$_2$*	459.51	465.23

* catalyst subject to pre-treatment under reaction condition at 700°C for 2h in environmental XPS chamber before analysis

Table S3. Atomic Concentration of Mo on the surface before and after nitridation according to XPS.

% atm Concentration of Mo	**Oxide**	**Nitride**
10-Mo/TiO$_2$	**12.5**	**9.86**
10-Mo/SBA-15	**4.3**	**3.57**

Table S4. H_2 uptake from TPR on MoO_3 10-Mo-O/TiO$_2$ and 10-Mo-O/SBA-15

Sample	H_2 uptake (mmol g^{-1})	
	Exp.^{f}	Calc.^{g}
MoO_3	23.3	20.8
10-Mo-O/SBA-15	1.9	2.2
10-Mo-O/TiO$_2$	2.9	2.8

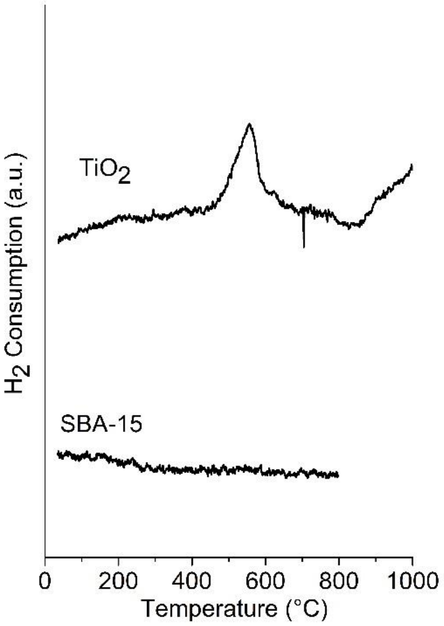

Figure S3 H_2-TPR profiles of TiO_2 and SBA-15

Table S5. H_2 desorption quantities for H_2-TPD in the range 25 – 550 °C

Catalyst	**H_2 desorption (mmol/g)**
10-Mo-N/TiO_2	**0.11481**
10-Mo-N/SBA-15	**0.13033**

V. Chapter IV: Effect of support on catalytic activity of Molybdenum Nitride –Part II

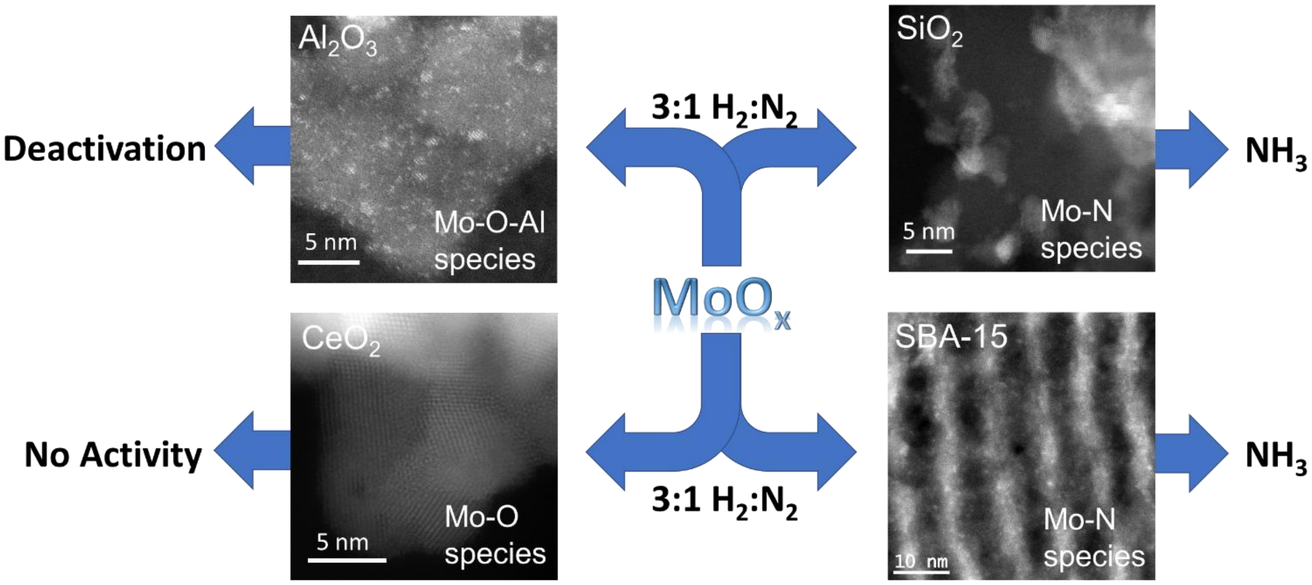

This section is divided into 2 Chapters (articles) and will be referred to as Chapter III and Chapter IV

Part of this Chapter has been submitted to ACS energy letters in 2023.

Catalytic ammonia synthesis by supported molybdenum nitride: new insight into the support effect

Amanda Sfeir[1], Camila A. Teles[1], Herve Vezin[2], Maya Marinova[3], Axel Löfberg,[1] Jean-Philippe Dacquin[1], Said Laassiri,[4] Sébastien Royer[1]**

1 Université de Lille, CNRS, ENSCL, Centrale Lille, Univ. Artois, UMR 8181-UCCS-Unité de Catalyse et de Chimie du Solide, F-59000 Lille, France.

2 Laboratoire de Spectroscopie pour Les Interactions La Réactivité et L'Environnement Université de Lille, UMR CNRS 8516-LASIRE, 59000 Lille, France

3 Université de Lille, CNRS, INRA, Centrale Lille, Université Artois, FR 2638 – IMEC – Institut Michel-Eugène Chevreul, 59000 Lille, France.

4 Chemical & Biochemical Sciences, Green Process Engineering (CBS), Mohammed VI Polytechnic University, UM6P, 43150, Benguerir, Morocco

*** Corresponding authors**: sebastien.royer@univ-lille.fr, said.laassiri@um6p.ma

V.1 Introduction

Due to its characteristic, such as high hydrogen gravimetric content (17.6 wt.%), high energy density (5.2 kWh kg^{-1}) based on the low heat value (LHV), facile liquefaction and low flammability, ammonia is foreseen to play a major role in long-term and large scale of renewable energy storage [1]. Beyond its use as a hydrogen carrier, ammonia has been also considered for direct energy generation as combustible in combustion engines for commercial maritime and aviation [2, 3] and as energy carrier for fuels cells [4]. Furthermore, the transformation of unreactive atmospheric dinitrogen into highly reactive nitrogen building blocks (*i.e.* ammonia), via the Haber Bosch (H-B) process, has been instrumental in the industrialization of nitrogen based fertilizers. Thus, this process is sustaining a large fraction of human population through ensuring availability of nitrogen based fertilizers for intensive agriculture.

In spite of the potential of ammonia in decarbonizing both the energy and agriculture sectors, its production remains closely tied to hydrogen production from non-renewable fossil-based feedstock. Currently the industrial production of ammonia is dominated by the H-B process in which highly purified N_2 and H_2 react over a promoted iron-based catalyst under high pressure (up to 200 bar) and temperature varying between 400 and 500°C. The decarbonization of the H-B process has driven much research effort especially in replacing hydrogen derived from fossil fuels by green hydrogen generated by water electro-catalysis powered by renewable energy. However, the development of a decarbonized H-B process capable of coping with the intermittency and uneven geographic distribution of renewable energy still requires further optimization in several of the H-B components. An emerging key sector where innovation and optimization have the potential to reshape the H-B process is the development of novel catalytic materials active under milder ammonia synthesis conditions.

Over the last years, several materials with enhanced catalytic properties when compared to the industrial doubly promoted iron based catalyst have been reported in the literature. In this regard, Ru on activated carbon has driven significant interest due to its high catalytic activity. In this type of catalysts, the B_5 site in Ru nanoparticles has been identified as the active site, with the most suitable energetic properties for nitrogen activation and dissociation at low temperature [5-8]. Since ammonia is a structure-sensitive reaction over Ru based catalysts, the catalytic performance is affected by electronic and geometric properties of the active site.

Considerable effort has been devoted to increase the catalytic activity through promoting by (i) alkali and alkaline earth promoters [9, 10] and (ii) by modifying the nature of the support [11-15]. Exceptional high catalytic activity has been reported with a marked influence of the support on Ru active phase. Although high catalytic activity is achieved using Ru supported on advanced support (electrides, hydrides, perovskites), the high cost of Ru and its scarcity are still a barrier for widespread utilizations as an industrial catalyst. However, the remarkable effect of a support on tuning the catalytic activity of Ru in ammonia synthesis showcases the importance of modulating support-metal interaction to achieve high catalytic activity. Taking into account these considerations, the development of alternative materials presenting reasonable high catalytic activity, low-cost and availability is of utmost importance. From that aspect, molybdenum based materials display high catalytic activity in multiple reactions including hydrodesulfurization (HDS) [16, 17], oxidative desulfurization [18, 19] and CO_2 conversion [20, 21], ammonia synthesis, and ammonia decomposition. In ammonia synthesis, the catalytic activity of the γ-Mo_2N phase has been reported as early as 1986 by the works of Volpe and Boudart [22] and Oyama [23] at atmospheric pressure and 400 °C. However, the strong interaction between Mo and nitrogen/NH_x intermediate species results in limited catalytic activity in ammonia synthesis. Several strategies have been adopted throughout the years to increase the catalytic activity of Mo-based catalysts by (i) addition of second metal resulting on the formation of bimetallic molybdenum nitrides/carbides (Co_3Mo_3N, Co_3Mo_3C, Ni_2Mo_3N)[24-27] displaying optimized nitrogen binding properties, and (ii) dispersion of Mo species into suitable supports (MoN_x/ZSM-5, Mo_2C/CeO_2) [28, 29]. These modifications alter the structural and electronic properties of Mo leading to significantly different catalytic behaviours which promote different reaction mechanisms. In the literature, the effect of the nature of support on tuning the physicochemical properties of Mo species and by consequences their catalytic activity is scarce due to the difficulties to characterize the nature of Mo-N nanoparticle species formed during the nitridation process. For instance, strong interaction between Mo-Ti has been reported to alter the nitridation mechanism of Mo species, when compared to a non-reducible support, leading to a complete turn-off of the catalytic activity in ammonia synthesis [30].

In this work, we aim to improve our understanding on the interaction of Mo with different classical catalyst supports, i.e. CeO_2, Al_2O_3, SiO_2 and SBA-15. The identity of the active phase formed during the nitridation process has been studied by advanced characterization techniques such as *in-situ* EPR and XPS connected to an *in-situ* treatment chamber allowing to minimize the contamination by air exposure. Furthermore, the performances of supported Mo-N species were studied in ammonia synthesis and ammonia decomposition revealing the role of the support in tuning the catalytic activity of ammonia synthesis.

V.2 Experimental section

V.2.1 Catalyst preparation

Chemicals. The following chemicals and commercial supports were purchased and used with no further purification: ammonium para-heptamolybdate tetrahydrate $(NH_4)_6Mo_7O_{24}.4.H_2O$, 99 wt.%, Alfa Aesar) , SiO_2 (Saint-Gobain NORPRO SS61138), Al_2O_3 (Saint-Gobain NORPRO SA6176) and CeO_2 (Solvay ECL15).

Mo-N supported catalyst. Mesoporous SBA-15 support was produced by hydrothermal method, under acidic conditions as described elsewhere [31], whereas available commercial supports (*i.e.* Al_2O_3, SiO_2, and CeO_2) were utilized without specific preliminary treatment. Supported molybdenum oxides were prepared by an incipient wetness impregnation (IWI) method. In this procedure, the required weight of Mo precursor ($(NH_4)_6Mo_7O_{24}.4H_2O$, Aesar) was first dissolved in a volume corresponding to the pore volume of the respective support and then mixed with the support. The mixture was aged for 5 days at 25 °C and then calcined at 400 °C, 1.5 °C min^{-1} for 5 h. All the samples underwent a calcination step at 400 °C, 1.5 °C min^{-1} for 5 h, to form MoO_3 oxide phase. The nitridation process was conducted during the pre-treatment step, prior to catalytic reaction, at 700 °C under a 75 vol.% $H_2:N_2$ (BOC, 99.98 %) gas mixture at a total gas flow of 60 mL min^{-1} for 2 h.

N.B. Herein, the samples obtained after the calcination step are denoted 10-Mo-O/support. The catalysts obtained after the pre-treatment step are referred to as 10-Mo-N/support, and the post reaction samples as 10-Mo-N-PR/support, where X is the wt.% of α-MoO_3 (X =10 wt.%).

V.2.2 Catalyst characterization

In this article, the following characterization techniques were used: XRD (Low and high angle), N_2 physisorption, XPS, TEM, H_2-TPR, H_2-TPD, and EPR. For more information regarding the characterization techniques, please refer to Chapter 2 for all details.

V.2.3 Catalytic activity

Ammonia synthesis. 0.15 g of Mo-O/support was placed in a quartz reactor tube held centrally in a vertical furnace. Prior to ammonia synthesis reaction, the sample was activated at 700 °C (10 °C min^{-1}) under 75 vol.% $H_2:N_2$ (BOC, 99.98 %) at 60 mL min^{-1} for 2 h. After the activation step, the reactor was cooled down, and the reaction was performed at 400 °C and atmospheric pressure using the same gas mixture and gas flow.

The reactor effluent steam was flowed to a 200 mL of H_2SO_4 solution (0.0018 M) and ammonia production was calculated from the decrease in conductivity. The catalytic activity was monitored as a function of reaction time.

Ammonia decomposition. The same activation step as seen previously was performed on 0.6 g of catalyst placed in a quartz reactor, to obtain the corresponding nitride X-Mo-N/support. The reactor was cooled to ambient temperature under 75 vol.% H_2:N_2. The decomposition test was done under a 15 vol.% NH_3:Ar (BOC, 99.98 %) gas mixture at a total gas flow of 100 mL min^{-1}. The catalytic activity was measured between 250 and 700°C, by steps of 100 °C (30 min at each step) from 250 to 450 °C, and steps of 50 °C (30 min at each step) from 450 to 700 °C. Ammonia conversion was determined using an FTIR analyzer.

V.3 Results and Discussion

V.3.1 Catalyst characterizations.

V.3.1.1 XRD.

Figure 1 displays the PXRD of post-reaction catalysts obtained after 20 h under ammonia synthesis conditions. The formation of Mo-N species, which are the known to be active species in ammonia synthesis, are usually obtained following the pre-treatment step at 700 °C under 75 vol.% H_2:N_2 (BOC, 99.98 %) gas mixture at a total gas flow of 60 mL min^{-1} for 2 h. This was verified by the nitridation of molybdenum oxide α-MoO_3 into β-Mo_2N (PDF 25-1368) under the same conditions (FigureS1). However, upon nitridation and ammonia synthesis test, no diffraction peaks related to Mo-N species have been detected in 10-Mo-N-PR/Al_2O_3, 10-Mo-N-PR/CeO_2 and 10-Mo-N-PR/SBA-15, suggesting that the active phase is well dispersed within these supports. Whereas in the case of 10-Mo-N-PR/SiO_2, poorly defined and broad peaks at 2θ =37.8°, 43.4°, 64.2° are assigned to β-Mo_2N phase (PDF 25-1368), reflecting the formation of molybdenum nitride with limited crystallite size.

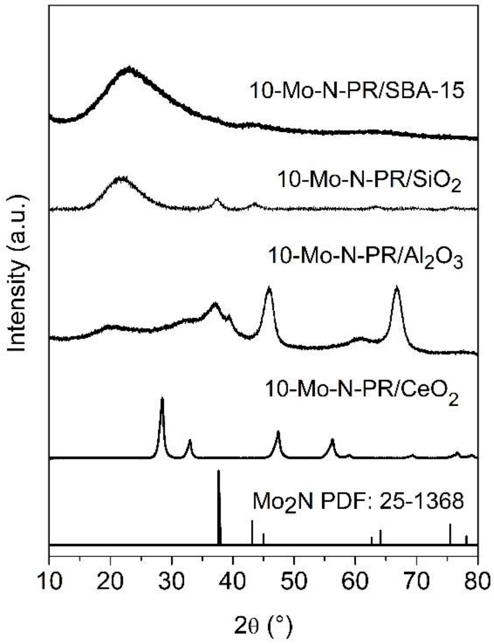

Figure 1 PXRD diffractograms of the supported Mo-N catalysts, after 20 h of reaction under ammonia synthesis conditions.

V.3.1.2 Nitrogen adsorption-desorption analysis.

The nitrogen adsorption/desorption isotherms of the freshly calcined catalysts and their corresponding pore volume and pore size distribution are shown in Figure 2 and Table 1. In all the studied materials, a predominant type IV isotherm characteristic of mesoporous materials is observed. However, the characteristic of the hysteresis loop differs from a material to another which reflects differences in the porosity and/or particle size of the solid supports. For instance, only CeO_2 and SBA-15 displayed a narrowed pore size distribution centered at ~ 3.0 nm and 6.6 nm respectively. However, the BET surface area and pore volume of CeO_2 were 194 m^2 g^{-1} and 0.16 cm^3 g^{-1}, while SBA-15 displayed a surface area of ~ 465 m^2 g^{-1} and a pore volume of 0.82 cm^3 g^{-1}. In the case of 10-Mo-O/Al_2O_3 and 10-Mo-O/SiO_2 samples, much broader pore size distributions are observed with respect to CeO_2 and SBA-15. The surface area of 10-Mo-O/Al_2O_3 and 10-Mo-O/SiO_2 were 208 m^2 g^{-1} and 262 m^2 g^{-1} respectively. It is worth noting that upon Mo impregnation only a small decrease in the surface area is observed with respect to the surface area measured on parent Al_2O_3, SiO_2 and CeO_2 (Table 1). Interestingly, the BET surface area of SBA-15 showed a more pronounced decrease after Mo loading (from 760 to 465 m^2 g^{-1}). The evolution of the surface area was also accompanied with a decrease in pore volume from 1.1 to 0.82 cm^3 g^{-1} resulting probably from partial clogging of mesoporous channels of SBA-15.

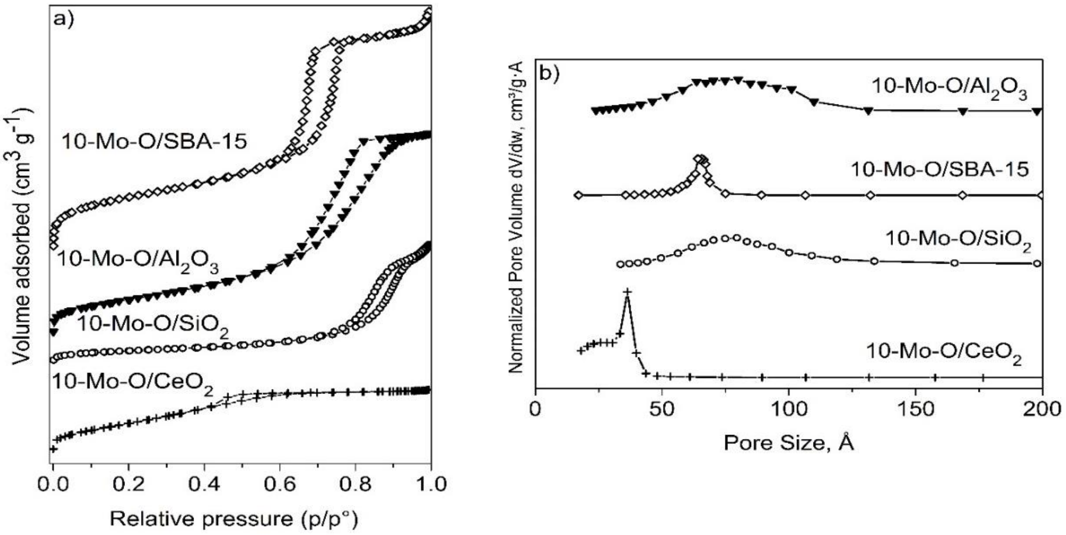

Figure 2 (a) N_2 adsorption-desorption isotherms and (b) BJH pore size distribution measured for the Mo-O supported materials.

Table 1. Textural properties of unsupported MoO_3 and supported Mo-O based materials after calcination.

	MoO_3[a] (wt.%)	**S_{BET}[b] ($m^2 g^{-1}$)**	**S_μ[c] ($m^2 g^{-1}$)**	**V_p[d] ($cm^3 g^{-1}$)**	**D_p[e] (nm)**	**Mo mean particle size (nm)**
MoO_3	-	4	-			-
Al_2O_3	-	251	10	1.00	8.2	-
CeO_2	-	237	-	0.16	3.1	-
SiO_2	-	294	24	0.92	13.8	-
SBA-15	-	760	131	1.1	6.5	-
10-Mo-O/Al_2O_3	10.7	208	-	0.99	8.3	1.7±0.1
10-Mo-O/CeO_2	11.8	194	-	0.16	3.0	N.D
10-Mo-O/SiO_2	10.8	262	-	1.07	13.2	2.9± 0.3
10-Mo-O/SBA-15	10.8	465	68	0.82	6.6	1.3±0.3

[a] MoO_3 content measured by ICP-OES in the calcined samples, [b]S_{BET} Calculated by the BET method; [c]S_μ microporous surface area; [d]V_p total pore volume calculated using BJH method; [e] D_p mean pore size calculat using B.J.H method ; N.D. non determined

V.3.1.3 HAADF-TEM Analysis.

Upon activation, the morphology of supported Mo-N species as well as the local distribution were studied by means of HAADF-TEM analysis coupled with EDS. Representative high resolution HAADF images for the 10-Mo-N/support catalysts are reported in Figure 3 and Figure S2.

In HAADF images, where the intensity is proportional to the atomic number of the element ($Z^{1.7}$), Mo atoms appear brighter on Al_2O_3, SBA-15 and SiO_2. In these materials, the mean particle size of Mo species has been estimated and the results are reported in Table 1. For siliceous based supports, the mean particle size of Mo species was found to be ~ 2.9±0.3 nm and ~ 1.3±0.3 nm on SiO_2 and SBA-15 respectively (Figure 3). These differences are in line with PXRD results where broad XRD peaks characteristic of β-Mo_2N are detected when Mo-species are supported on SiO_2 but not observed on SBA-15. In the 10-Mo-N/Al_2O_3 catalyst, the mean particle size was found to be ~ 1.6±0.1 nm which is slightly higher than the particle size measured in 10-Mo-N/SBA-15 sample. Unfortunately, in the case of 10-Mo-N/CeO_2 catalyst, as the atomic number Z of Mo is lower compared to Ce, Mo-species could not be detected in the HAADF images (Figure 3-c). Therefore, the d-spacing visible in Figure 3-c is associated to CeO_2 crystallographic structure.

Complementary EDS analysis, presented in Figure S2, confirmed the high dispersion of Mo species in all the different supports. Unfortunately, due to limitation related to Mo small particle size, low Mo species concentration and low N-K peak energy, the identification of Mo-N species was found to be rather challenging. The identification of Mo-N species was only possible in the case of 10-Mo-N/SiO_2 displaying the largest nitride particle size (2.9±0.3 nm).

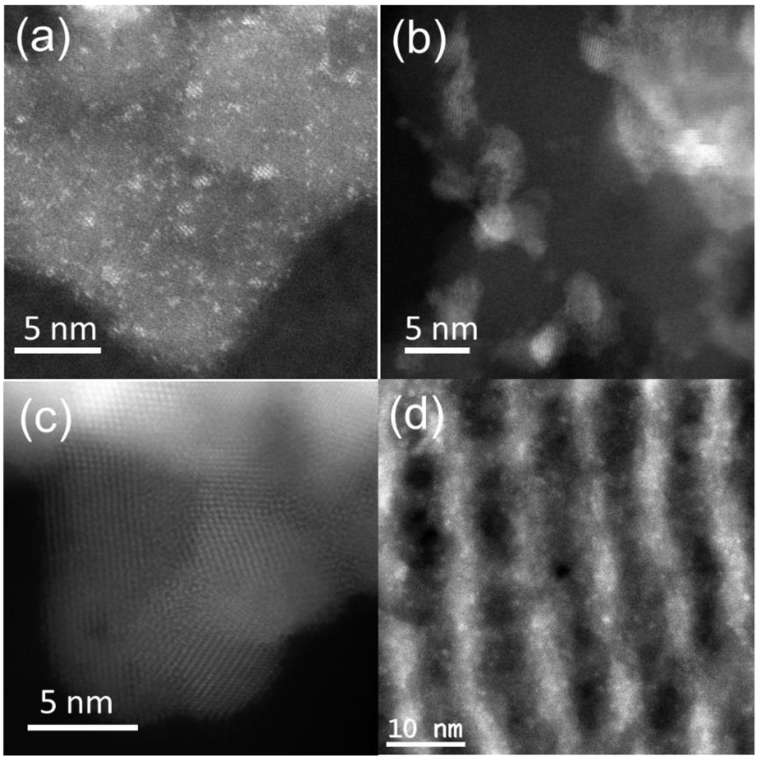

Figure 3 Representative HAADF images of (a) 10-Mo-N/Al_2O_3, (b) 10-Mo-N/SiO_2, (c) 10-Mo-N/CeO_2 and (d) 10-Mo-N/SBA-15.

V.3.2 Surface properties of Mo-N supported catalysts

The surface properties, *i.e.* chemical composition and oxidation states of elements, were investigated using X-ray photoelectron spectroscopy. In order to understand the evolution of the surface composition under the activation step, XPS spectra of the 10-Mo-O/supports obtained directly after the calcination step and the nitride 10-Mo-N/supports formed after the activation step were acquired. The activation step was conducted in an *in-situ* pretreatment chamber connected to the XPS (700 °C under H_2:N_2 for 2 h), in order to minimize surface contamination. The results are summarized in Figure 4 and Figure S3, Table 2 and Table S1-S3.

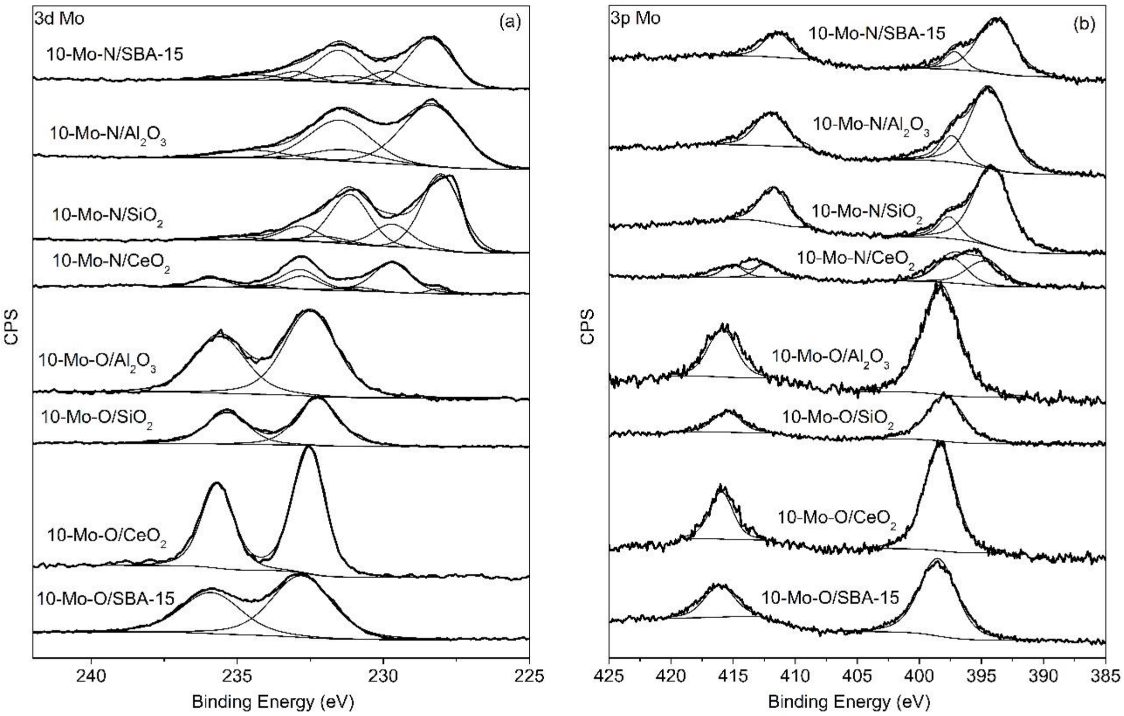

Figure 4. XPS spectra of solids before (10-Mo-O/support) and after *in situ* nitridation step (10-Mo-N/support) in (a) Mo 3d region (b) Mo 3p region.

10-Mo-O/supports. The spectral decomposition of Mo 3d region for the calcined samples are presented in Figure 4-a. All the supported oxides 10-Mo-O/Al_2O_3 , 10-Mo-O/SiO_2, 10-Mo-O/SBA-15 and 10-Mo-O/CeO_2 displayed a similar Mo 3d XPS profile characterized by two major spectral lines corresponding to Mo $3d_{5/2}$ and Mo $3d_{3/2}$ spin-orbit components which correspond to formal Mo^{6+} oxidation state [32].

10-Mo-N/supports. Upon the activation step, 700 °C under H_2:N_2 for 2 h, a shift to lower binding energies was observed in all the catalysts indicating successful oxidation state reduction of Mo species. However, disparities in Mo-3d / Mo-3p binding energies are observed, pointing the impact of the support nature on the stabilization of different chemical environments Mo species (figure 4 and table 2).

In the case of siliceous supports (SiO_2 and SBA-15), the high-resolution Mo 3d XPS profile can be deconvoluted into several peaks (figure 4-a). In both materials, the major contribution is related to the presence of Mo-N species with two major spectral lines at 228.36 eV and 231.5 eV [33]. Additional peaks correlated to the presence of Mo^{5+} and Mo^{4+} have been also observed in both catalysts. The surface composition of Mo species was found to be fairly similar between SiO_2 and SBA-15, where in both catalysts, Mo-N species were predominant ~ 66.4% and ~ 69.7% in 10-Mo-N/SBA-15 and 10-Mo-N/SiO_2 respectively. Moreover, in both catalysts, at least 20 at.% of Mo species was found to be present as Mo^{4+}, and finally, the remaining fraction of Mo species that was not reduced in SBA-15, a fraction of Mo^{6+}~ 12.8 at.%, and in SiO_2 Mo^{6+} ~ 8.3 at.% was detected. Such results indicate that Mo-Si interaction affected the nitridation mechanism similarly in both amorphous SiO_2 and SBA-15. In a similar manner, when 10-Mo-N/Al_2O_3 was subjected to the activation step, the surface was mainly populated with Mo-N species ~ 82.0%. Furthermore, the spectral decomposition of the high-resolution Mo 3d region revealed the presence of an important fraction of Mo species as Mo^{5+} ~ 18.0 at.%.

Interestingly, when investigating 10-Mo-N/CeO_2, the spectral decomposition of Mo 3d XPS profile showed the predominance of Mo^{4+} species with $3d_{5/2}$ and Mo $3d_{3/2}$ spin-orbit components of 229.70 eV and 232.84 eV. An addition set of peaks related to Mo^{6+}, Mo^{5+} and Mo-N were also identified. The distribution of Mo oxides species was determined to be ~ 65.5 at.% for Mo^{4+}, ~ 25.6 at.% for Mo^{6+}, 7.4 at.% for Mo^{5+} and only 4.5 at.% was found to be in the form of Mo-N. Such observations indicate that supporting Mo on CeO_2 increased the Mo^{4+} content at the expense of Mo-N formation.

The impact of the activation step on the support elements has also been examined by XPS (Figure S4). In the case of 10-Mo-O/Al_2O_3, the Al 2p XPS profile was fitted as a single peak at ~ 74.1 eV since Al 2p peak has closely-spaced spin-orbit components. Upon the activation step, a slight shift of the Al 2p XPS profile to lower binding energies of 73.6 eV was observed. This might be an indication of the formation of Al-O-Mo structures. In the case of SiO_2, the Si 2p XPS profile was characterized by one peak as well with a binding energy of 103.25 eV and a slightly higher BE after nitridation at 103.98 eV (table S2) . In the case of SBA-15, both Si-O-Si and Si-OH corresponding peaks were identified in the Si 2p region, with BE of 104.00 eV and 103.16 eV respectively. Upon the activation step, only a slight shift of Si-OH peak to lower binding energy 103.05 eV was observed.

Table 2. Position of 3d Mo peaks of unsupported and supported Mo based catalysts before and after nitridation

	Mo peaks B.E. (eV)								**Surface composition (at.%)**			
	Mo^{6+}		**Mo^{5+}**		**Mo^{4+}**		**Mo-N**		**Mo^{6+}**	**Mo^{5+}**	**Mo^{4+}**	**Mo-N**
	$3d_{5/2}$	$3d_{3/2}$	$3d_{5/2}$	$3d_{3/2}$	$3d_{5/2}$	$3d_{3/2}$	$3d_{5/2}$	$3d_{3/2}$				
10-Mo-O/Al$_2$O$_3$	232.50	235.60	-	-	-	-	-	-	100	-	-	-
10-Mo-N/Al$_2$O$_3$*	-	-	231.31	234.46	-	-	228.33	231.48	-	18.0	-	82.0
10-Mo-O/CeO$_2$	232.56	235.66	-	-	-	-	-	-	100	-	-	-
10-Mo-N/CeO$_2$*	232.76	235.90	231.00	234.14	229.70	232.84	228.12	231.26	25.6	7.4	65.5	4.5
10-Mo-O/SiO$_2$	232.25	235.35	-	-	-	-	-	-	100	-	-	-
10-Mo-N/SiO$_2$*	232.11	235.25	-	-	229.70	232.84	228.0	231.14	8.3	-	22.1	69.7
10-Mo-O/SBA-15	232.8	235.9	-	-	-	-	-	-	100	-	-	-
10-Mo-N/SBA-15*	232.26	235.40	-	-	230.05	233.19	228.36	231.50	12.8	-	20.8	66.4

***** Catalyst subject to pre-treatment under reaction condition at 700 °C for 2 h in *in situ* chamber connected to XPS before analysis

EPR studies

The process of Mo nitridation during the activation step has been further investigated by EPR. Prior to the activation step, all the Mo-O supported materials are EPR silent due to the absence of paramagnetic centers as Mo is mainly present in the +6 oxidation state. Upon activation, Mo displayed a range of oxidation state. However, only Mo^{5+} is paramagnetic and can yield an EPR signal (Figure 5).

10-Mo-N/Al$_2$O$_3$. Upon the activation step, the EPR spectra recorded for the 10-Mo-N/Al$_2$O$_3$, displayed a strong Mo^{5+} signal with an isotropic line centered at a g-value of 1.95. During the activation step, the reduction of Mo^{6+} resulted in a sharp increase in the formation of Mo^{5+} which reached a plateau after 40 min of reaction (Figure 5-c). The reduction process was accompanied by an increase in the concentration of oxygen vacancies where the signal then rapidly disappears as the temperature increases. In order to have information about the local structure of Mo^{5+} in the case of 10-Mo-N/Al$_2$O$_3$ we performed a HYSCORE experiment at 5K (Figure S4). On this HYSCORE spectrum we can observe in the weak coupling quadrant the presence of a signal centered at 3.9 MHz resulting from the interaction of an aluminum weakly coupled by dipolar mechanism. In the strong coupling quadrant, we observe 4 peaks of correlations in the antidiagonal separated by two times the Larmor frequency of Al (7.8 MHz). This profile indicates the presence of two strongly coupled aluminum via Mo-O-Al covalent bonds with respective A_{iso} coupling constants of 15 and 16 MHz. Therefore, these EPR results show that the formation of Mo^{5+} species is a bulk phenomenon and not only a surface one as suggested by XPS analysis.

10-Mo-N/CeO_2. Upon the activation step, the recorded EPR spectrum indicated the presence of Mo^{5+} (Figure 5-a). In this case, the EPR signal was anisotropic with a square plane symmetry (g_z=1.97 and $g_{x,y}$=1.95). During the kinetics studies at 700 °C, the reduction/nitridation process was characterized by an increase in the concentration of Mo^{5+} species accompanied with an increase of oxygen vacancies concentration reaching a maximum at 10 min and gradually decreasing afterwards to stabilize after 60 min of reaction (Figure 5-c,d).

10-Mo-N/SiO_2 and 10-Mo-N/SBA-15. When Mo is supported on siliceous based supports, only a weak isotropic Mo^{5+} signal with a g-factor of 1.94 is observed (Figure 5-a). During the temperature kinetics at 700°C under H_2:N_2, this signal quickly disappears indicating the loss of Mo^{5+}, leaving only weak signal related to the presence of oxygen vacancies (Figure 5-d). The formation of Mo^{5+} seems to be marginal during the nitridation step for silica supported catalysts.

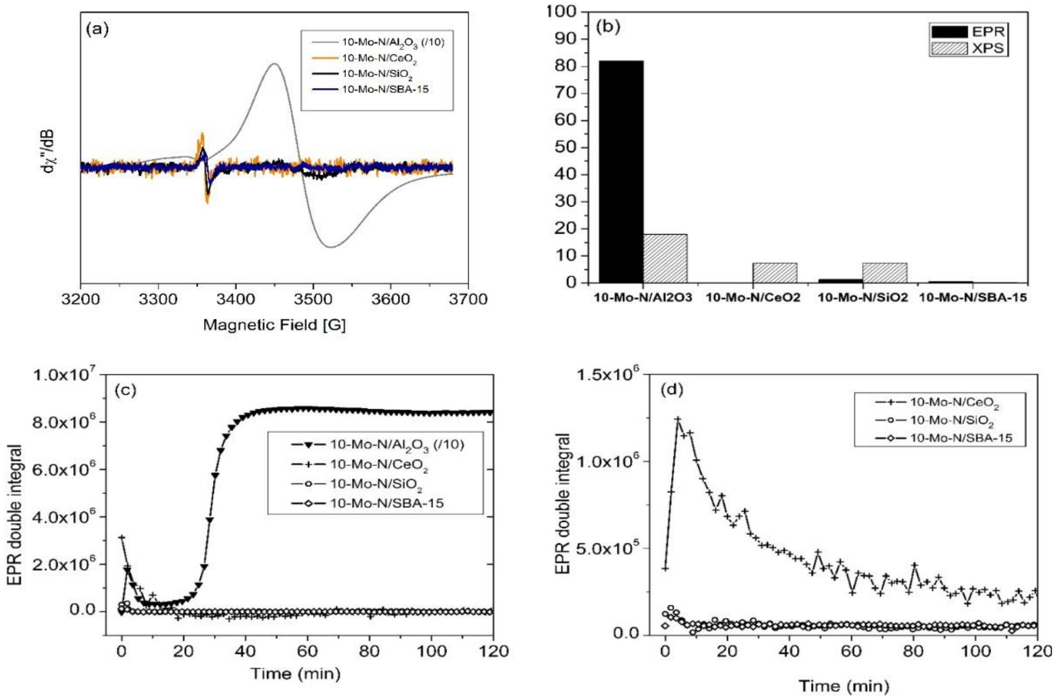

Figure 5 (a) EPR spectra registered for the catalysts after pre-treatment 700 °C under H_2:N_2, (b) Fraction of Mo^{5+} after pre-treatment conditions by EPR and XPS, (c) Kinetic evolution of Mo^{5+} species at 700 °C under H_2:N_2, and (d) Kinetic evolution of O^{n-} species at 700°C under H_2:N_2.

V.3.3 Effect of Mo-Support interactions on Mo reducibility and affinity towards hydrogen

The effect of the nature of the support on the reduction kinetics of Mo oxides was evaluated by means of H_2-TPR measurements and the results are compared to those collected for the unsupported α-MoO_3. The results are presented in Figure 6 and Table S4.

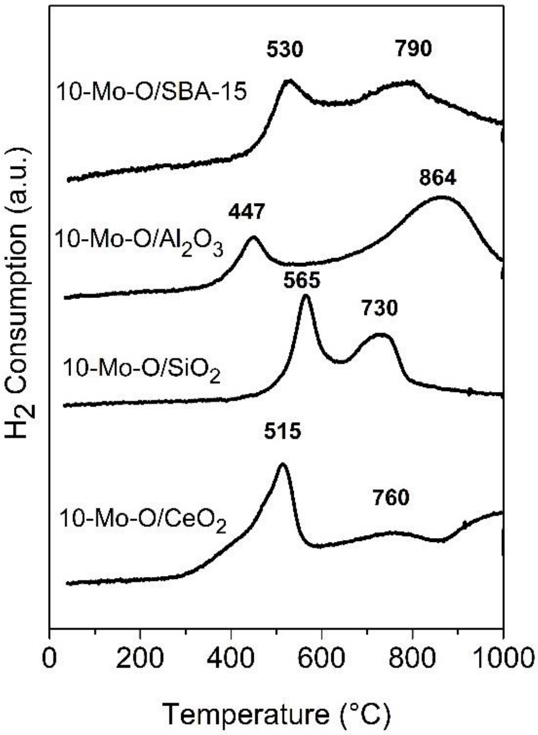

Figure 6 H_2-TPR profiles of 10-Mo-O/Al_2O_3, 10-Mo-O/SiO_2, 10-Mo-O/CeO_2, and 10-Mo-O/SBA-15

The reduction profile of unsupported α-MoO_3 proceeds via two steps as previously seen in the literature. First the reduction of α-MoO_3 into MoO_2 occurs, and process is characterized by a sharp hydrogen consumption peaks at 770 °C. It is followed by the reduction of MoO_2 into metallic Mo at high temperature [34]. During the reduction process the formation of intermediates species such as Mo_4O_{11} has also been reported in the literature [34]. When the H_2-TPR profiles of supported Mo oxides are compared to the unsupported α-MoO_3, significant changes in the reduction process are observed. In all supported catalysts, the reduction process started at lower temperatures with respect to α-MoO_3. Depending on the nature of the support, the temperature of the first maximum reduction domain shifted to lower temperatures, with the following order: 10-Mo-O/Al_2O_3 (~ 447 °C) < 10-Mo-O/CeO_2 (~ 515 °C) < 10-Mo-O/SBA-15 (~530 °C) < 10-Mo-O/SiO_2 (~ 565 °C) < α-MoO_3 (~ 770 °C). In a similar manner, the temperature of the second reduction peak associated with the formation of metallic Mo shifted to lower temperature with slight differences observed between the different supports. In 10-Mo-O/CeO_2, the second reduction event was characterized by a broad and small reduction peak observed between 600 and 800°C denoting the stabilization of Mo-oxides intermediates. Furthermore, a third reduction process starting at temperatures as high as 880°C was observed. This might be related to the reduction of CeO_2 bulk species at higher temperatures and/or reduction of Mo species in strong interaction with the support. For comparison, the H_2-TPR profiles of the supports are presented in Figure S5. As expected only CeO_2 displayed redox properties. The H_2-TPR profile was characterized by two peaks with temperature of reduction maxima at ~ 450 and ~ 790 °C. The first peak assigned to the reduction of superficial CeO_x species while the second peak has been correlated to the reduction of bulk CeO_2 species respectively [35]. The temperature of the second maximum reduction peak was also fairly high on 10-Mo-O/Al_2O_3 (~864°C) especially when compared to Mo-O supported on siliceous supports (10-Mo-O/SiO_2 ~ 730 °C and ~ 10-Mo-O/SBA-15 ~ 790 °C). Furthermore, small differences in Mo oxides reducibility where also observed between SiO_2 and SBA-15. As mentioned above, the reduction process started earlier in 10-Mo-O/SBA-15 when compared to 10-Mo-O/SiO_2 signifying that particle size has a role in influencing the reduction behaviors of Mo oxides species. In summary, the reactivity of Mo oxides species towards hydrogen was greatly impacted by the nature of the support and particle size.

The effect of Mo-support interaction on the activation of H_2 was studied by means of H_2-temperature programmed desorption (Figure 7). The H_2-TPD profile of 10-Mo-N/Al_2O_3 was characterized by two desorption peaks, the first peak being in the range of 350-550°C and the second desorption peak starting from 550°C. When Mo is supported on siliceous supports, similar H_2-TPD profiles are observed for SBA-15 and SiO_2. The corresponding H_2-TPD profiles were characterized by three desorption peaks. The first one starting from 100 °C to 300 °C, the second desorption peak from 350 °C to 550 °C and a third desorption peak at high temperature (> 550°C). Small disparities between the two desorption profiles are however observed especially when the temperatures of the maximum desorption are compared which are slightly shifted to higher temperatures in the case of 10-Mo-N/SBA-15. These differences might be related to differences in Mo species particle size observed by HAADF-TEM analysis. As shown in Figure 7, the desorption profile of 10-Mo-N/CeO_2 was characterized by a first desorption peak at low temperature between 50 and 150°C which can be related to the desorption of H_2 adsorbed on the O_{vac} sites from $CeO_{2-\delta}$ surface [36]. A second broad H_2-desorption peak is observed at temperature ranging between 150 and 550°C. Surprisingly, no H_2 desorption was observed at higher temperature. The differences in H_2-TPD profiles reveals the co-existence of different possible H_2 adsorption sites, with each support displaying different Mo species population (Mo-N, Mo^{6+}, Mo^{5+}, Mo^{4+}, Mo) after the activation steps, and eventually contributing to the adsorption of H_2 (case of CeO_2).

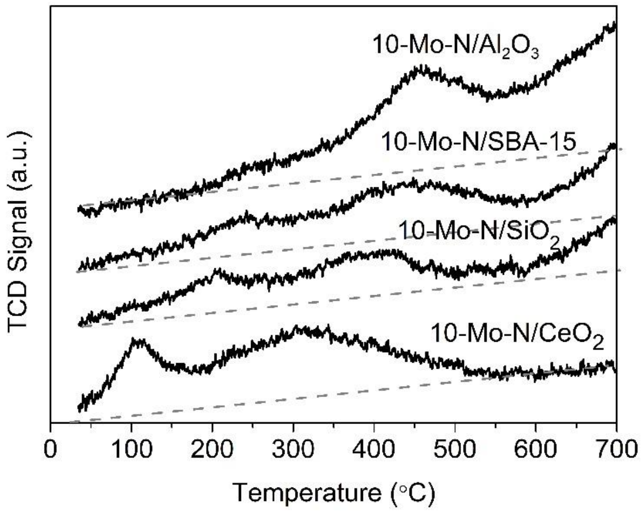

Figure 7 H_2-TPD profiles of 10-Mo-N/Al_2O_3 ,10-Mo-N/SiO_2, 10-Mo-N/SBA-15, and 10-Mo-N/CeO_2

V.3.4 Ammonia synthesis and ammonia decomposition.

The catalytic activity of Mo supported catalyst was evaluated in ammonia synthesis and ammonia decomposition reaction (Figure 8, Figure S6 and Table 3).

Table 3. Summary of the catalytic activity of supported Mo-N supported catalysts in ammonia synthesis and ammonia decomposition reactions.

	Ammonia synthesis reaction			**Ammonia decomposition**		
	Initial rate (μmol $g_{catalyst}^{-1}$ h^{-1})	**Initial rate (μmol $g_{active\ phase}^{-1}$ h^{-1})***	**Steady state rate (μmol $g_{catalyst}^{-1}$ h^{-1})**	**T_{10}**	**T_{100}**	**Ea (kJ mol^{-1})**
β-Mo_2N	76	76	77	-	-	-
10-Mo-N/SBA-15	84.6	1208	51	460	585	71
10-Mo-N/SiO_2	33.7	481	33.7	425	560	71
10-Mo-N/Al_2O_3	26.0	372	0	450	575	59
10-Mo-N/CeO_2	ND[b]	ND	ND	470	-	78

* Rate normalized by the of Mo; [b] ND: not detected

The catalytic activity of Mo-N supported catalysts in ammonia synthesis was evaluated at a Weight Hourly Space Velocity (WHSV) of 24 000 mL g^{-1} h^{-1} at 400 °C and at ambient pressure (Figure 8-a). When compared to the unsupported β-Mo_2N (initial rate of 76 µmol $g_{catalyst}^{-1}$ h^{-1}), only 10-Mo-N/SBA-15 catalyst (initial rate of ~ 84,6 µmol $g_{catalyst}^{-1}$ h^{-1}) displayed a higher catalytic activity for ammonia synthesis. Under the same catalytic conditions, the 10-Mo-N/SiO_2 (initial rate of ~ 33.7 µmol $g_{catalyst}^{-1}$ h^{-1}) exhibited lower catalytic activity than those observed for β-Mo_2N phase and 10-Mo-N/SBA-15. However, when normalized against the active phase loading an initial rate of ~ 1208 µmol $g_{active\ phase}^{-1}$ h^{-1} and ~ 481 µmol $g_{active\ phase}^{-1}$ h^{-1} is obtained over 10-Mo-N/SBA-15 and 10-Mo-N/SiO_2 respectively. While 10-Mo-N/SiO_2 catalyst did not show any sign of deactivation over time of reaction, the 10-Mo-N/SBA-15 on the other hand showed a slight deactivation during the first hour, to stabilize at a constant production rate of 51 µmol $g_{catalyst}^{-1}$ h^{-1} which is 60% above the stable rate obtained for 10-Mo-N/SiO_2 catalyst (Table 3). In 10-Mo-N/Al_2O_3, the initial ammonia synthesis rate was found to be 26.0 µmol $g_{catalyst}^{-1}$ h^{-1} denoting a decrease in the catalytic activity when the active phase is supported on Al_2O_3 with respect to 10-Mo-N/SBA-15 and 10-Mo-N/SiO_2 catalysts. Furthermore, the catalytic activity of 10-Mo-N/Al_2O_3 was found to decrease gradually with time until completely deactivating after 10 h of reaction. Finally, the 10-Mo-N/CeO_2 sample did not display any catalytic activity in ammonia synthesis despite improved textural and structural properties.

The effect of the nature of the support in tuning the catalytic activity of Mo species in ammonia decomposition was also studied and the results are shown in Figure 8-b and in Table 3. As expected, depending on the nature of the support, differences in the catalytic activity of Mo species are observed. However, all the studied catalysts were found to be active in ammonia decomposition. At low temperature, the order of activity, classified as a function of 10% NH_3 conversion temperature is: 10-Mo-N/SiO_2 (425°C) < 10-Mo-N/Al_2O_3 (450°C) < 10-Mo-N/SBA-15 (460°C) < 10-Mo-N/CeO_2 (470°C). At higher temperature, complete conversion of NH_3 was achieved in the following order: 10-Mo-N/SiO_2 (560°C) < 10-Mo-N/Al_2O_3 (575°C) < 10-Mo-N/SBA-15 (585°C) < 10-Mo-N/CeO_2 (~ 700°C). These results imply that the nature of the support was not altering severely the catalytic activity of Mo species in ammonia decomposition as was the case in ammonia synthesis. Surprisingly, by a quick comparison between the siliceous supports, the catalytic activity seems to be favored by the increase in Mo species particle size.

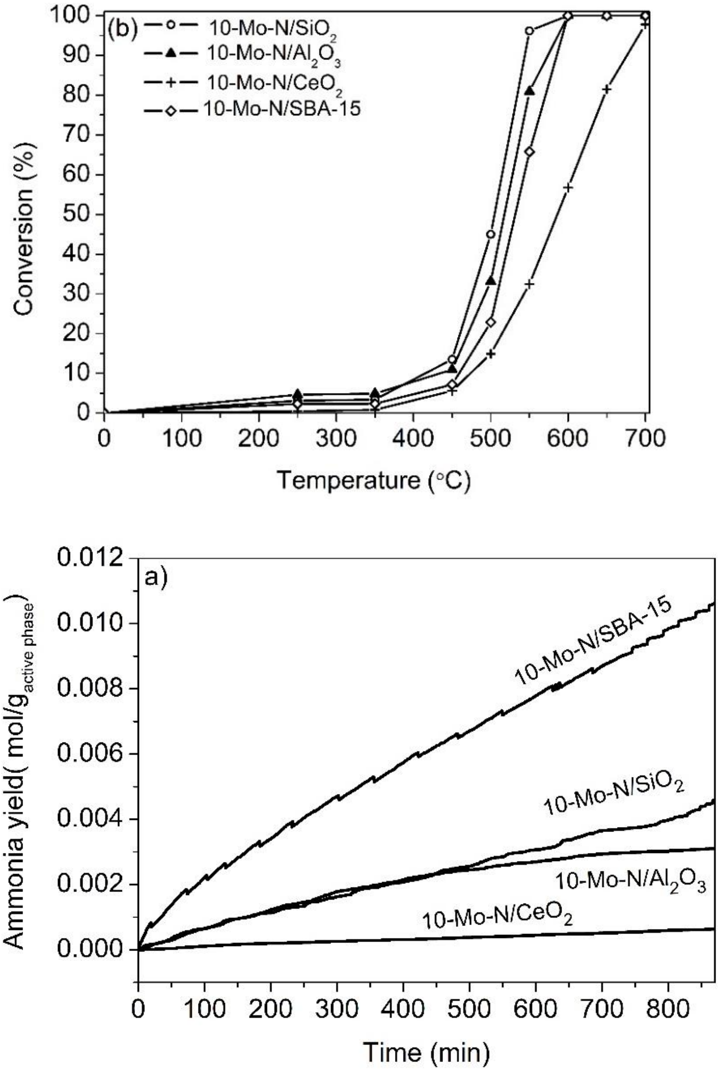

Figure 8 Catalytic activity of 10-Mo-N/Al_2O_3 ,10-Mo-N/SiO_2, and 10-Mo-N/CeO_2 for (a) ammonia synthesis at 400 °C (b) ammonia decomposition from 250 °C to 700 °C.

V.3.5 Discussion

In this work, a series of supported Mo-N catalysts (10-Mo-N/SBA-15, 10-Mo-N/SiO_2, 10-Mo-N/Al_2O_3, and 10-Mo-N/CeO_2) was prepared by impregnation followed by nitridation under 75 vol.% H_2:N_2 (BOC, 99.98 %) gas mixture at a total gas flow of 60 mL min^{-1} for 2 h at 700°C. Physico-chemical characterizations of the supported catalysts confirmed the formation of small Mo nanoparticles as seen by HAADF-STEM, STEM-EDS and PXRD. The mean particle size of molybdenum species was found to be 1.3 ± 0.3 nm in 10-Mo-N/SBA-15, 3.0± 0.3 nm in 10-Mo-N/SiO_2, and 1.6±0.1 nm in 10-Mo-N/Al_2O_3. Despite achieving high dispersion of Mo species and limited particle size in all the catalysts, large disparities on the catalytic activity in ammonia synthesis were observed. The deactivation of 10-Mo-N/Al_2O_3

after 10 h of reaction and 10-Mo-N/CeO_2 displaying no catalytic activity in ammonia synthesis suggesting an important role of the support in modulating the final state of the Mo phase. To probe the origin of the catalytic activity differences, the surface composition was studied by means of XPS. Before the activation step, Mo^{6+} was the predominant species in all the supported 10-Mo-O/support materials. However, upon nitridation and depending on the nature of the support, various oxidation states were detected. Over siliceous based supports, the catalysts showed similar XPS profiles where most of Mo-O species were converted successfully to Mo-N species ~66.4 at.% and ~69.2 at.% in 10-Mo-N/SBA-15 and 10-Mo-N/SiO_2 respectively. In addition, at least 20% of Mo species was found to be present as Mo^{4+} in both catalysts, whereas the remaining Mo species was found to be an unreduced fraction of Mo^{6+}. This stands to show that the nitridation mechanism remained unchanged when switching between two supports of same nature. A high level of nitridation was also noticed for alumina supported catalyst, for which Mo-N species were quantified at 82.0 at.%, alongside to Mo^{5+} (18.0 at.%). Surprisingly, the distribution of Mo species was found to be quite different in 10-Mo-N/CeO_2 catalyst. Only a small fraction of Mo species was successfully nitrided, 4.5 at.%**.** Following the activation step, Mo species predominantly formed are Mo^{4+}(65.5 at.%), Mo^{6+} (25.6 at.%) and to a lesser extent Mo^{5+} (7.4 at.%). The stabilization of Mo oxides species when supported on CeO_2 might explain the absence of catalytic activity of 10-Mo-N/CeO_2 catalyst in ammonia synthesis.

The differences on the catalytic behaviors cannot be solely explained by the differences in Mo-N species concentrations. As determined by XPS, 10-Mo-N/Al_2O_3 displayed the highest surface concentration of Mo-N species but displayed lower catalytic activity and poor stability as function of time, leading to a complete deactivation measured after 10 h of reaction. In many catalytic reactions, the activity of Mo-N species was found to be dependent to crystallographic phases formed (i.e. β-Mo_2N and δ-MoN) [37] and degree of nitridation (δ-MoN) [37, 38] hinting that different Mo-N species can lead to different catalytic activity. Furthermore, the hydrogen chemisorption capacity of Mo-N species were observed to be influenced by several factors such as chemical composition ($Mo^{\delta+}$/N ratio), Mo oxidation states, and nitrogen-deficient site density [39]. The mechanism of MoO_3 nitridation is indeed sensitive to several parameters including particle size, nature of the support, gas composition, space velocity and/or heating rate leading to the formation of different Mo-N species [40, 41]. For instance, the nitridation of MoO_3 into β-Mo_2N is reported to proceed through a mechanism involving multiple reduction steps: initial reduction to MoO_2, then Mo can be nitrided to MoN_x [39, 42]. However γ-Mo_2N synthesis involved the formation of molybdenum bronze

($H_xMo_x^{5+}Mo_{1-x}^{6+}O_3$) as an intermediate species before nitridation [40]. Thus, the formation of a specific Mo-N phase can be modified by an appropriate control of the nitridation conditions [43, 44] and/or by controlling the Mo-support interaction. Therefore, to further elucidate the role of support in influencing the mechanism of reduction/nitridation process, *in-situ* EPR and H_2-TPR have been conducted. *In-situ* EPR has been particularly relevant in determining the formation of Mo^{5+} during the activation step. The nitridation process was observed to be significantly different in the case of 10-Mo-N/Al_2O_3 catalyst. Only when supported on Al_2O_3, the formation of large quantity of Mo^{5+} species was detected. The concentration of Mo^{5+} increased with the time of reaction to reach a plateau after 40 min of reaction. In these conditions, the formation of hydrogen molybdenum bronze ($H_xMo_x^{5+}Mo_{1-x}^{6+}O_3$) intermediates could be supposed. However, considering the stability of Mo^{5+} species under reaction stream, the formation of $Al_2(MoO_4)_3$ hosting the pentavalent Mo species is more probable [45]. Thus, it is more likely, as seen in XPS, that a part of Mo species is located in the aluminum-molybdate extra phase which might explain the low initial activity rate of 10-Mo-N/Al_2O_3 (26.0 µmol $g_{catalyst}^{-1}$ h^{-1}) when compared to 10-Mo-N/SBA-15 (84.6 µmol $g_{catalyst}^{-1}$ h^{-1}). The progressive formation of $Al_2(MoO_4)_3$ might be also responsible for the deactivation of the catalyst [46]. In contrast with 10-Mo-N/Al_2O_3, only a weak isotropic Mo^{5+} signal is observed for silica-based catalysts, which rapidly disappeared during the activation step of Mo species. It indicates that the process of nitridation is rather dominated by direct reduction of Mo^{6+} to Mo^{4+} without Mo^{5+} intermediate. The differences in the nitridation mechanism suggest the formation of different Mo-N species depending on the nature of the support. Part of the discrepancies in the catalytic activity of Mo-N supported catalysts in ammonia synthesis might be also explained by the differences of Mo-species populating the surface of the catalysts. The example of 10-Mo-N/CeO_2 catalyst showcased the role of CeO_2 in stabilizing MoO_x species and slowing down the nitridation process leading to an inactive catalytic material under the same conditions of activation used for silica and alumina supported catalysts.

V.4 Conclusion

The preparation of supported nitrides phases offers an elegant approach for the preparation of small Mo-N nanoparticles in order to boost the catalytic activity for ammonia synthesis and ammonia decomposition. Herein, by investigating the nature of the active phases, we showed a strong dependence on the distribution of Mo species according to the nature of the support. In this context, the results of characterization demonstrated a high dispersion of Mo species in all the studied catalysts. Nonetheless, it has been demonstrated that the identity of Mo species generated during the activation process is significantly influenced by the type of support utilized, leading to important variations in Mo species formed (Mo-N, Mo^{6+}, Mo^{5+}, Mo^{4+}, Mo). Considering the critical role of nitrogen mobility, surface termination and vacancies concentration in the mechanism of ammonia synthesis, tuning the interaction between Mo species and the support is a crucial parameter that greatly influences the catalytic activity observed in ammonia synthesis. Superior activity for ammonia synthesis was achieved with 10-Mo-N/SBA-15 with an initial rate of ~ 84,6 µmol $g_{catalyst}^{-1}$ h^{-1}, with the other catalysts lagging behind in the following order: 10-Mo-N/SBA-15 > 10-Mo-N/SiO_2 > 10-Mo-N/Al_2O_3 > and inactivity for 10-Mo-N/CeO_2 ; whereas for ammonia decomposition, all catalysts had close activities with 10-Mo-N/SiO_2 > 10-Mo-N/Al_2O_3 > 10-Mo-N/SBA-1 5> 10-Mo-N/CeO_2 . Upon comparison of the two siliceous supports, the impact of the particle size on the activity can be concluded, where larger particle size was influential in the case of ammonia decomposition but not necessarily for ammonia synthesis.

V.5 References

[1] S. Giddey, S.P.S. Badwal, C. Munnings, M. Dolan, Ammonia as a Renewable Energy Transportation Media, ACS Sustainable Chemistry & Engineering, 5 (2017) 10231-10239.

[2] A. Boretti, S. Castelletto, NH3 Prospects in Combustion Engines and Fuel Cells for Commercial Aviation by 2030, ACS Energy Letters, 7 (2022) 2557-2564.

[3] B. Stolz, M. Held, G. Georges, K. Boulouchos, Techno-economic analysis of renewable fuels for ships carrying bulk cargo in Europe, Nature Energy, 7 (2022) 203-212.

[4] G. Jeerh, M. Zhang, S. Tao, Recent progress in ammonia fuel cells and their potential applications, Journal of Materials Chemistry A, 9 (2021) 727-752.

[5] C. Leterme, C. Fernández, P. Eloy, E.M. Gaigneaux, P. Ruiz, The inhibitor role of NH3 on its synthesis process at low temperature, over Ru catalytic nanoparticles, Catalysis Today, 286 (2017) 85-100.

[6] C. Fernández, N. Bion, E.M. Gaigneaux, D. Duprez, P. Ruiz, Kinetics of hydrogen adsorption and mobility on Ru nanoparticles supported on alumina: Effects on the catalytic mechanism of ammonia synthesis, Journal of Catalysis, 344 (2016) 16-28.

[7] S. Dahl, A. Logadottir, R.C. Egeberg, J.H. Larsen, I. Chorkendorff, E. Törnqvist, J.K. Nørskov, Role of Steps in N_2 Activation on Ru(0001), Physical Review Letters, 83 (1999) 1814-1817.

[8] K. Honkala, A. Hellman, I.N. Remediakis, A. Logadottir, A. Carlsson, S. Dahl, C.H. Christensen, J.K. Nørskov, Ammonia Synthesis from First-Principles Calculations, Science, 307 (2005) 555-558.

[9] K. Aika, A. Ohya, A. Ozaki, Y. Inoue, I. Yasumori, Support and promoter effect of ruthenium catalyst: II. Ruthenium/alkaline earth catalyst for activation of dinitrogen, Journal of Catalysis, 92 (1985) 305-311.

[10] K.-i. Aika, Heterogeneous Catalysis of Ammonia Synthesis at Room Temperature and Atmospheric Pressure, Angewandte Chemie International Edition in English, 25 (1986) 558-559.

[11] Z. Wang, J. Lin, R. Wang, K. Wei, Ammonia synthesis over ruthenium catalyst supported on perovskite type BaTiO3, Catalysis Communications, 32 (2013) 11-14.

[12] B. Lin, Y. Liu, L. Heng, X. Wang, J. Ni, J. Lin, L. Jiang, Morphology Effect of Ceria on the Catalytic Performances of Ru/CeO2 Catalysts for Ammonia Synthesis, Industrial & Engineering Chemistry Research, 57 (2018) 9127-9135

[13] Y. Kobayashi, Y. Tang, T. Kageyama, H. Yamashita, N. Masuda, S. Hosokawa, H. Kageyama, Titanium-Based Hydrides as Heterogeneous Catalysts for Ammonia Synthesis, Journal of the American Chemical Society, 139 (2017) 18240-18246.

[14] Y. Inoue, M. Kitano, S.-W. Kim, T. Yokoyama, M. Hara, H. Hosono, Highly Dispersed Ru on Electride [Ca24Al28O64]4+(e–)4 as a Catalyst for Ammonia Synthesis, ACS Catalysis, 4 (2014) 674-680.

[15] Y. Lu, J. Li, T. Tada, Y. Toda, S. Ueda, T. Yokoyama, M. Kitano, H. Hosono, Water Durable Electride Y5Si3: Electronic Structure and Catalytic Activity for Ammonia Synthesis, Journal of the American Chemical Society, 138 (2016) 3970-3973.

[16] A.N. Varakin, A.V. Mozhaev, A.A. Pimerzin, P.A. Nikulshin, Comparable investigation of unsupported MoS2 hydrodesulfurization catalysts prepared by different techniques: Advantages of support leaching method, Applied Catalysis B: Environmental, 238 (2018) 498-508.

[17] H. Topsøe, B.S. Clausen, Active sites and support effects in hydrodesulfurization catalysts, Applied Catalysis, 25 (1986) 273-293.

[18] M.M.H. Mondol, B.N. Bhadra, S.H. Jhung, Molybdenum nitride@porous carbon, derived from phosphomolybdic acid loaded metal-azolate framework-6: A highly effective catalyst for oxidative desulfurization, Applied Catalysis B: Environmental, 288 (2021) 119988.

[19] J. Zou, Y. Lin, S. Wu, Y. Zhong, C. Yang, Molybdenum Dioxide Nanoparticles Anchored on Nitrogen-Doped Carbon Nanotubes as Oxidative Desulfurization Catalysts: Role of Electron Transfer in Activity and Reusability, Advanced Functional Materials, 31 (2021) 2100442.

[20] S. Singh, A. Modak, K.K. Pant, A. Sinhamahapatra, P. Biswas, MoS2–Nanosheets-Based Catalysts for Photocatalytic CO2 Reduction: A Review, ACS Applied Nano Materials, 4 (2021) 8644-8667.

[21] Y. Kuwahara, T. Mihogi, K. Hamahara, K. Kusu, H. Kobayashi, H. Yamashita, A quasi-stable molybdenum sub-oxide with abundant oxygen vacancies that promotes CO2 hydrogenation to methanol, Chemical Science, 12 (2021) 9902-9915.

[22] L. Volpe, M. Boudart, Ammonia synthesis on molybdenum nitride, The Journal of Physical Chemistry, 90 (1986) 4874-4877.

[23] S.T. Oyama, Preparation and catalytic properties of transition metal carbides and nitrides, Catalysis Today, 15 (1992) 179-200.

[24] C.J.H. Jacobsen, Novel class of ammonia synthesis catalysts, Chemical Communications, (2000) 1057-1058.

[25] I. AlShibane, A. Daisley, J.S.J. Hargreaves, A.L. Hector, S. Laassiri, J.L. Rico, R.I. Smith, The Role of Composition for Cobalt Molybdenum Carbide in Ammonia Synthesis, ACS Sustainable Chemistry & Engineering, 5 (2017) 9214-9222.

[26] R. Kojima, K.-i. Aika, Cobalt molybdenum bimetallic nitride catalysts for ammonia synthesis: Part 2. Kinetic study, Applied Catalysis A: General, 218 (2001) 121-128.

[27] S. Al Sobhi, N. Bion, J.S.J. Hargreaves, A.L. Hector, S. Laassiri, W. Levason, A.W. Lodge, A.R. McFarlane, C. Ritter, The reactivity of lattice nitrogen within the Ni2Mo3N and NiCoMo3N phases, Materials Research Bulletin, 118 (2019) 110519.

[28] N. Liu, L. Nie, N. Xue, H. Dong, L. Peng, X. Guo, W. Ding, Catalytic Ammonia Synthesis over Mo Nitride/ZSM-5, ChemCatChem, 2 (2010) 167-174.

[29] B. Fang, C. Zhang, Z. Qi, C. Li, J. Ni, X. Wang, J. Lin, C.-T. Au, B. Lin, L. Jiang, Combining molybdenum carbide with ceria overlayers to boost Mo/CeO2 catalyzed ammonia synthesis, AIChE Journal, 68 (2022) e17849.

[30] A. Sfeir, C. Abreu Teles, M. Marinova, H. Vezin, A. Lofberg, J.-p. Dacquin, S. Laassiri, S. Royer, Switching On/Off molybdenum nitride catalytic activity in ammonia synthesis through modulating metal support interaction, Faraday Discussions, (2023).

[31] D. Zhao, J. Sun, Q. Li, G.D. Stucky, Morphological Control of Highly Ordered Mesoporous Silica SBA-15, Chemistry of Materials, 12 (2000) 275-279.

[32] J. Baltrusaitis, B. Mendoza-Sanchez, V. Fernandez, R. Veenstra, N. Dukstiene, A. Roberts, N. Fairley, Generalized molybdenum oxide surface chemical state XPS determination via informed amorphous sample model, Applied Surface Science, 326 (2015) 151-161.

[33] L. Huo, X. Han, L. Zhang, B. Liu, R. Gao, B. Cao, W.-W. Wang, C.-J. Jia, K. Liu, J. Liu, J. Zhang, Spatial confinement and electron transfer moderating MoN bond strength for superior ammonia decomposition catalysis, Applied Catalysis B: Environmental, 294 (2021) 120254.

[34] T. Bhaskar, K.R. Reddy, C.P. Kumar, M.R.V.S. Murthy, K.V.R. Chary, Characterization and reactivity of molybdenum oxide catalysts supported on zirconia, Applied Catalysis A: General, 211 (2001) 189-201.

[35] S. Watanabe, X. Ma, C. Song, Characterization of Structural and Surface Properties of Nanocrystalline TiO2−CeO2 Mixed Oxides by XRD, XPS, TPR, and TPD, The Journal of Physical Chemistry C, 113 (2009) 14249-14257.

[36] K. Sohlberg, S.T. Pantelides, S.J. Pennycook, Interactions of Hydrogen with CeO2, Journal of the American Chemical Society, 123 (2001) 6609-6611.

[37] D. McKay, J.S.J. Hargreaves, J.L. Rico, J.L. Rivera, X.L. Sun, The influence of phase and morphology of molybdenum nitrides on ammonia synthesis activity and reduction characteristics, Journal of Solid State Chemistry, 181 (2008) 325-333.

[38] K.-i. Aika, A. Ozaki, Mechanism and isotope effect in ammonia synthesis over molybdenum nitride, Journal of Catalysis, 14 (1969) 311-321.

[39] N. Perret, D. Lamey, L. Kiwi-Minsker, F. Cárdenas-Lizana, M.A. Keane, New insights into the effect of nitrogen incorporation in Mo: catalytic hydrogenation vs. hydrogenolysis, Catalysis Science & Technology, 9 (2019) 1891-1901.

[40] F. Cárdenas-Lizana, D. Lamey, L. Kiwi-Minsker, M.A. Keane, Molybdenum nitrides: a study of synthesis variables and catalytic performance in acetylene hydrogenation, Journal of Materials Science, 53 (2018) 6707-6718.

[41] A. Lilić, L. Cardenas, A. Mesbah, E. Bonjour, P. Jame, C. Michel, S. Loridant, N. Perret, Guidelines for the synthesis of molybdenum nitride: Understanding the mechanism and the control of crystallographic phase and nitrogen content, Journal of Alloys and Compounds, 924 (2022) 166576.

[42] F. Cárdenas-Lizana, S. Gómez-Quero, N. Perret, L. Kiwi-Minsker, M.A. Keane, β-Molybdenum nitride: synthesis mechanism and catalytic response in the gas phase hydrogenation of p-chloronitrobenzene, Catalysis Science & Technology, 1 (2011) 794-801.

[43] J.-G. Choi, R.L. Curl, L.T. Thompson, Molybdenum nitride catalysts: I. Influence of the synthesis factors on structural properties, Journal of Catalysis, 146 (1994) 218-227.

[44] S. Jujjuri, F. Cárdenas-Lizana, M.A. Keane, Synthesis of group VI carbides and nitrides: application in catalytic hydrodechlorination, Journal of Materials Science, 49 (2014) 5406-5417.

[45] V.T.T. Ha, A. Sarıoğlan, A. Erdem-Şenatalar, Y.B. Taârit, An EPR and NMR study on Mo/HZSM-5 catalysts for the aromatization of methane: Investigation of the location of the pentavalent molybdenum, Journal of Molecular Catalysis A: Chemical, 378 (2013) 279-284.

[46] J.J. Birtill, P.G. Dickens, Thermochemistry of hydrogen molybdenum bronze phases HxMoO3, Journal of Solid State Chemistry, 29 (1979) 367-372.

V.6 Supplementary information

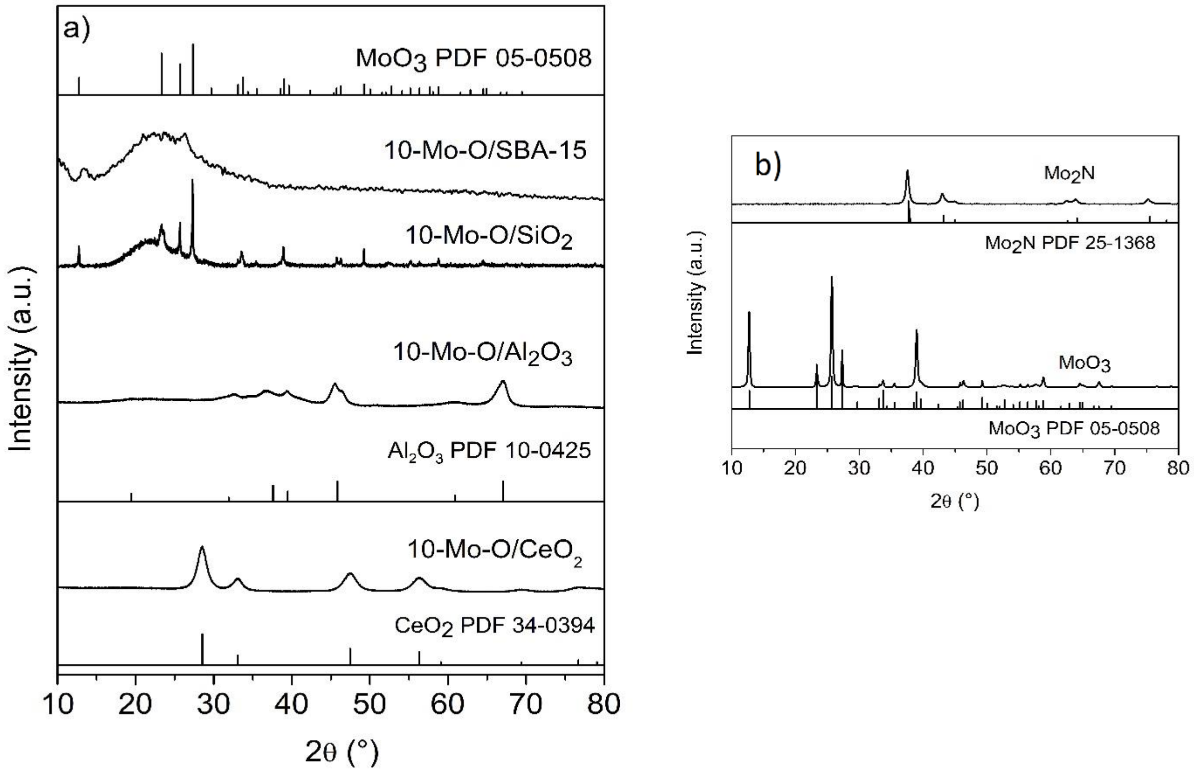

Figure S1 XRD diffractograms of (a) Supported Mo catalyst oxides before nitridation (b) Molybdenum oxide and the corresponding nitride after nitridation under the same treatment

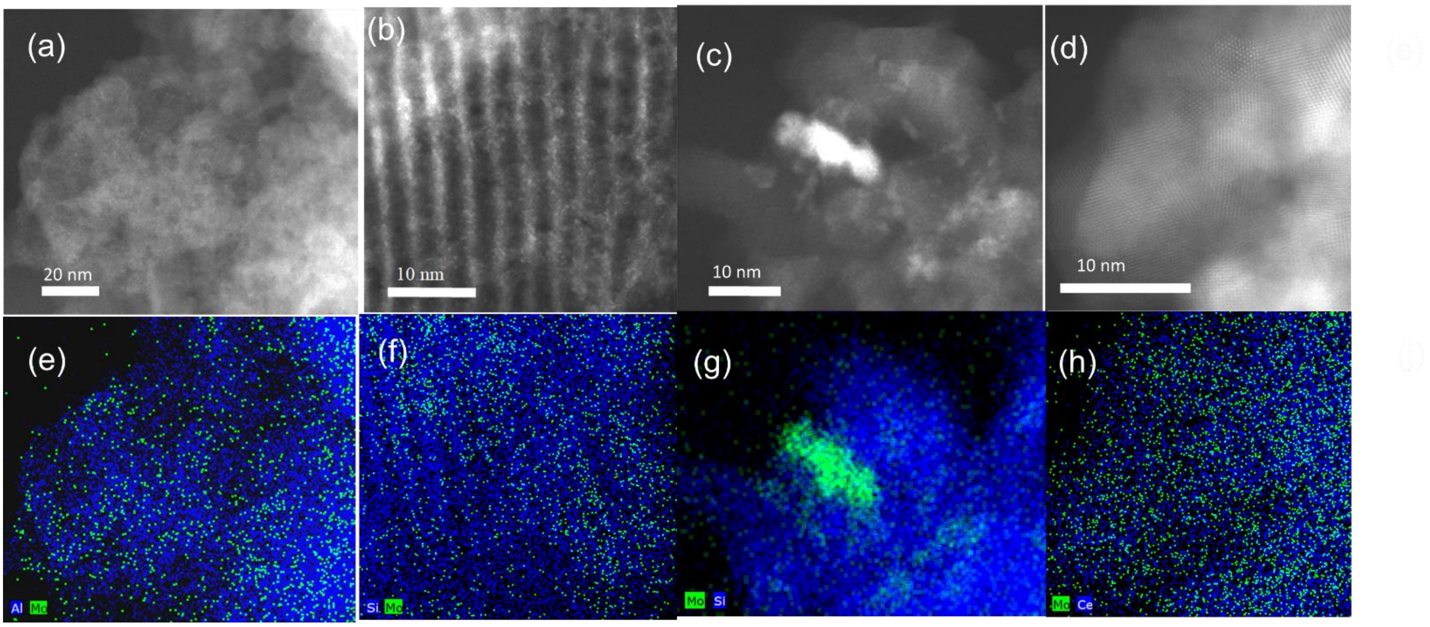

Figure S2 Representative low magnification HAADF images and corresponding STEM-EDS elemental maps obtained for 10-Mo-N/Al_2O_3 (a and e), 10-Mo-N/SBA-15 (b and f), 10-Mo-N/SiO_2 (c and g), 10-Mo-N/CeO_2 (d and h)

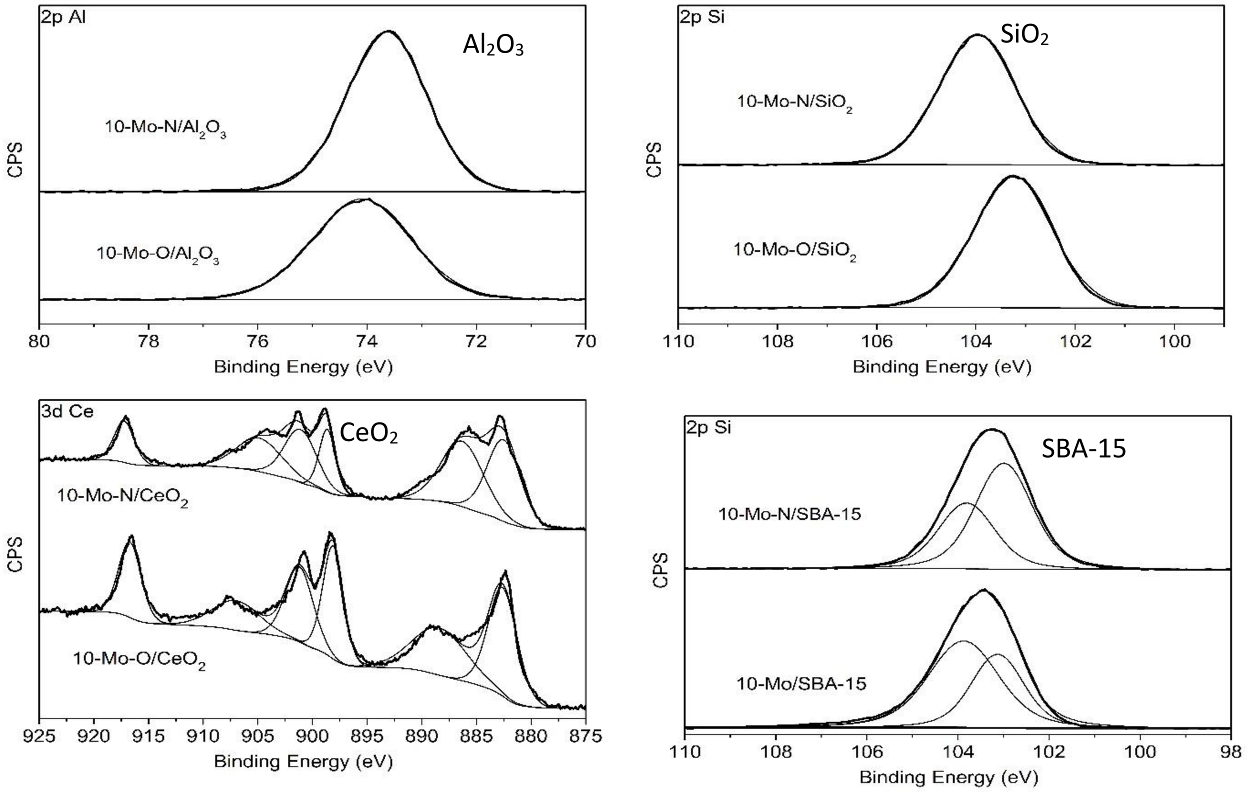

Figure S3. XPS spectra recorded on the calcined materials in the support region for the catalysts before and after nitridation under reaction conditions at 700 °C for 2 h in *in situ* chamber connected to XPS.

Table S1. Position of Si 2p peaks of SBA-15 in 10-Mo-O/SBA-15 before and after nitridation

	Si 2p peak position		**Surface composition**	
	Si-O-Si	**Si-O-H**	**Si-O-Si (%)**	**Si-O-H (%)**
10-Mo-O/SBA-15	104.00	103.16	54.96	45.04
10-Mo-N/SBA-15*	104.00	103.05	29.58	70.42

* catalyst subject to pre-treatment under reaction condition at 700 °C for 2 h in *in situ* chamber connected to XPS before analysis

Table S2. Position of Si 2p peaks of SiO_2 in 10-Mo-O/SiO_2 before and after nitridation

	SiO_2 (eV)	**%**
10-Mo-O/SiO_2	103.25	100
10-Mo-N/SiO_2	103.98	100

* catalyst subject to pre-treatment under reaction condition at 700 °C for 2 h in *in situ* chamber connected to XPS before analysis

Table S3.Position of Al 2p peaks of Al_2O_3 in 10-Mo-O/ Al_2O_3 before and after nitridation

	Al_2O_3 (eV)	**%**
10-Mo-O/Al_2O_3	74.1	100
10-Mo-N/Al_2O_3	73.6	100

* catalyst subject to pre-treatment under reaction condition at 700 °C for 2 h in *in situ* chamber connected to XPS before analysis

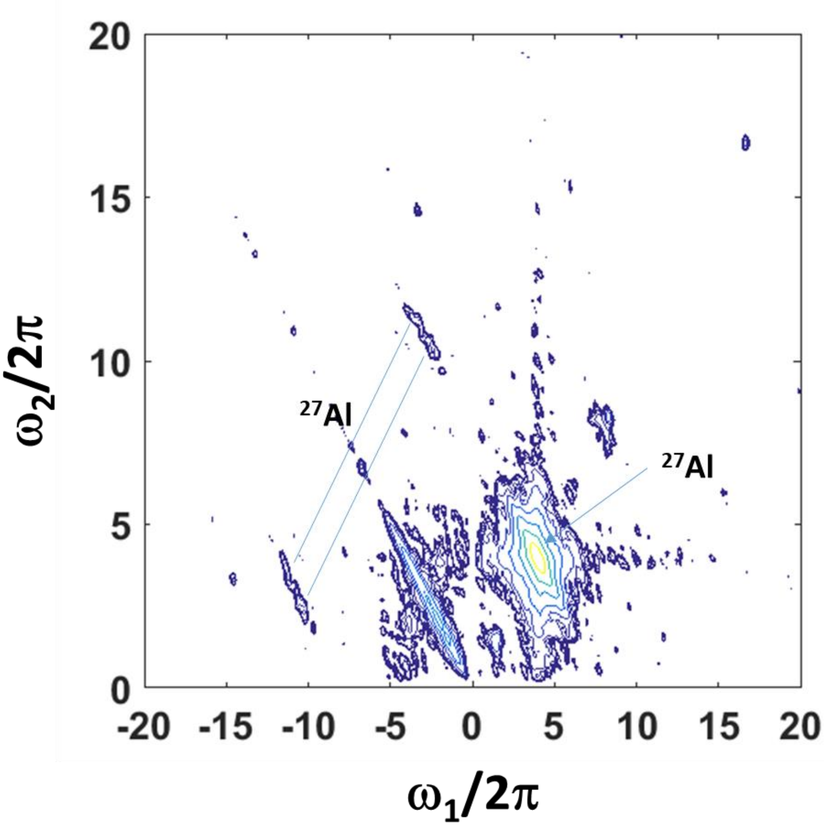

Figure S4. 2D-HYSCORE of nuclear interaction for 10-Mo-N/Al_2O_3

Table S4. H_2 uptake during H_2-TPR for different molybdenum supported catalysts

Sample	H_2 consumption (mmol g^{-1})	
	Exp.[e]	Calc.[f]
MoO_3	23.3	20.8
10-Mo-O/Al_2O_3	2.2	2.1
10-Mo-O/SiO_2	1.53	2.1
10-Mo-O/CeO_2	3.1	2.1
10-Mo-O/SBA-15	1.9	2.1

[e] Quantity of consumed H_2 obtained from TPR experiments

[d] Quantity of theoretical H_2 calculated according the nominal composition to the following reaction:

$MoO_3 + 3\ H_2 \longrightarrow Mo + 3\ H_2O$

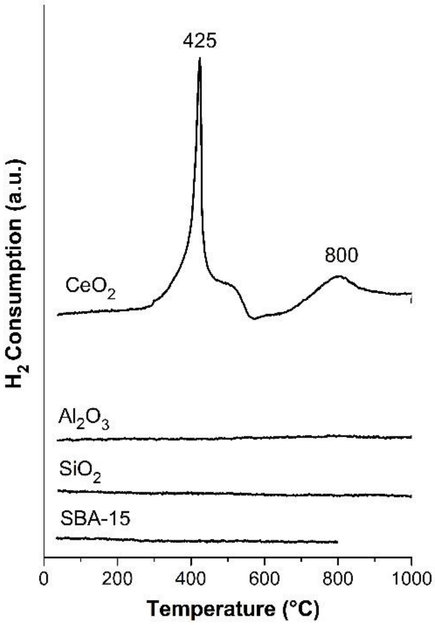

Figure S5. H_2 – TPR profiles of bare supports

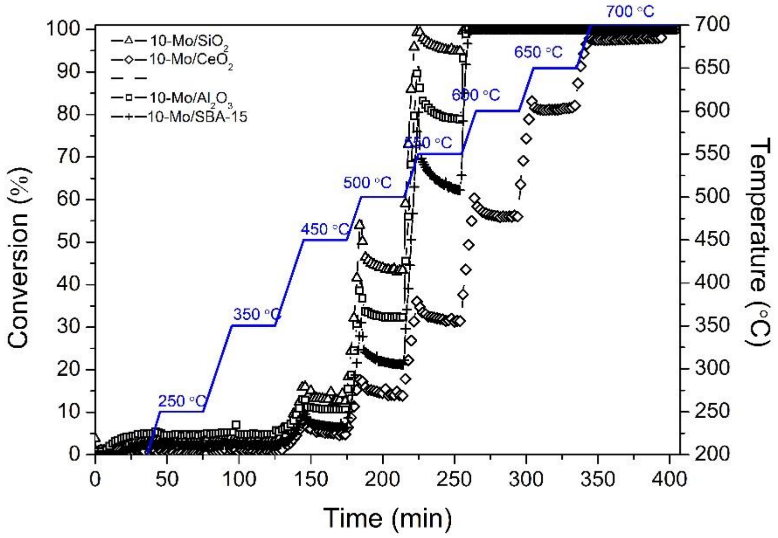

Figure S6. Ammonia decomposition conversion % of the different catalysts with temperatures varying from 0-700 °C as a function of time

VI. Chapter V: Ternary nitride NPS supported on SBA-15

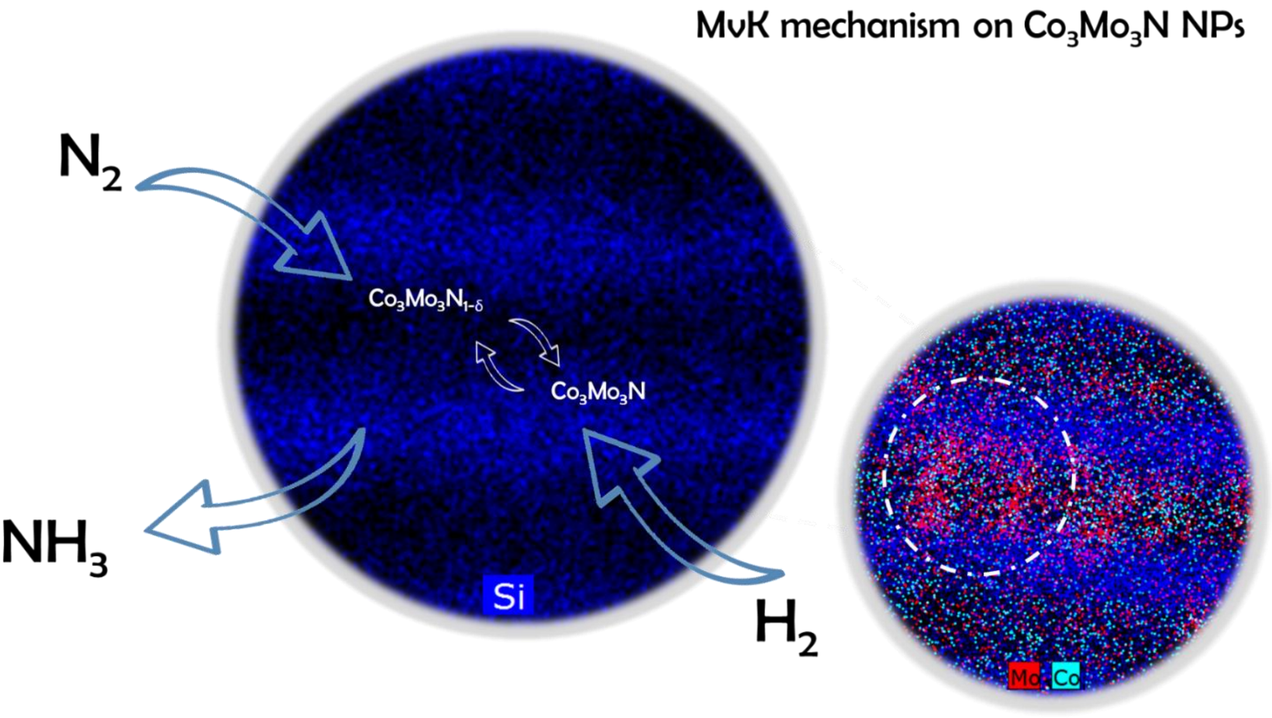

Part of this Chapter has been published in Applied Catalysis B: Environmental:

A. Sfeir *et al.*, “Enhancing ammonia catalytic production over spatially confined cobalt molybdenum nitride nanoparticles in SBA-15,” *Appl. Catal. B Environ.*, vol. 325, no. August 2022, 2023, doi: 10.1016/j.apcatb.2022.122319.

Enhancing ammonia catalytic production over spatially confined cobalt molybdenum nitride nanoparticles in SBA-15

Amanda Sfeir[1], Camila A. Teles[1], Carmen Ciotonea,[1,2] G. N. Manjunatha Reddy[1], Maya Marinova[3], Jérémy Dhainaut,[1] Axel Löfberg,[1] Jean-Philippe Dacquin[1], Sébastien Royer[1*], Said Laassiri[4*]

[1] *Université de Lille, CNRS, ENSCL, Centrale Lille, Univ. Artois, UMR 8181-UCCS-Unité de Catalyse et de Chimie du Solide, F-59000 Lille, France.*

[2] *Univ. Littoral Côte d'Opale, UR 4492, UCEIV, Unité de Chimie Environnementale et Interactions sur le Vivant, SFR Condorcet FR CNRS 3417, F-59140 Dunkerque, France*

[3] *Université de Lille, CNRS, INRA, Centrale Lille, Université Artois, FR 2638 – IMEC – Institut Michel-Eugène Chevreul, 59000 Lille, France.*

[4] *Chemical & Biochemical Sciences, Green Process Engineering (CBS), Mohammed VI Polytechnic University, UM6P, 43150, Benguerir, Morocco.*

* Corresponding authors: sébastien.royer@univ-lille.fr, said.laassiri@um6p.ma

VI.1 Introduction

To compensate the natural variation of power derived from natural resources, the development of smart grid capable of cooperative electricity generation (mix of energy resources) and offering a range of energy storage possibilities (short-, mid- and long- term energy storage) is of high importance for large-scale renewable energy production. Among the energy storage systems, Power to X (P2X) is expected to play a major role in long-term, large scale energy storage (days to months). Within the multiples candidates for P2X, ammonia possesses suitable characteristics to be considered as green, safe and sustainable energy carrier such as high hydrogen gravimetric content (17.6 wt.%), high energy density (5.2 kWh kg^{-1}) based on the low heat value (LHV), facile liquefaction and low flammability [1]. More importantly, there is an existing infrastructure for the safe and cost-effective ammonia transportation and distribution worldwide which alas is not the case for hydrogen [2].

The implementation of large-scale power to green ammonia, in the energy landscape is limited by the development of novel and efficient processes for cost-effective green ammonia production. Currently, large-scale ammonia production is achieved through the industrial Haber-Bosch process (H-B) in which highly purified N_2 and H_2 react over a promoted iron-based catalyst under high pressure (up to 200 bar) and temperature varying between 400 and 500 °C [3, 4]. While it sustains a significant proportion of the global population through providing affordable nitrogen-based fertilizers, the process is highly energy demanding. The H-B process is estimated to consume ~ 1-2 % of the world's annual energy production of which 15 % of energy requirements are solely consumed by high-pressure operations [5]. Currently, a considerable effort is centred upon the development of highly active catalysts capable of accelerating ammonia synthesis reaction at milder conditions and preferably at pressures aligned to those of green hydrogen produced by water electrolysis (10 ~ 80 bar) [6]. From a thermodynamic point of view, producing ammonia at pressures lower than those used in the H-B process is possible provided that the reaction is conducted under low temperatures [7]. Thus, the development of novel generation of catalysts capable of operating at milder conditions is an important milestone in the deployment of large-scale Power to Ammonia process for energy storage.

Among the catalysts studied for ammonia synthesis, noble-metal based materials (e.g. Ru/graphite and $CoRe_4$) have been reported to display superior catalytic activity when compared to the industrial catalyst. [8] However, considering the cost of noble metals and their scarcity, there is much interest in the development of non-noble metal-based catalyst for ammonia generation. One of the most active catalysts reported in the literature is Co_3Mo_3N ternary nitride (ammonia synthesis rate of 330 - 652 μmol h^{-1} g^{-1} at 400 °C and atmospheric pressure) [9] with catalytic performance at high pressure exceeding the industrial H-B doubly promoted iron-based catalyst [10]. Hence, there is a legitimate interest in further increasing the catalytic activity of Co_3Mo_3N. In the earlier studies, the high catalytic activity of Co_3Mo_3N was attributed to the presence of both Co and Mo in the termination plan *(111)* resulting in an optimal N-binding energy [11]. Initially, the role of nitrogen was believed to be limited to creating the right termination plan containing both Co and Mo. However, recent studies shed the light on the mobility and reactivity of nitrogen in Co_3Mo_3N via $^{15}N/^{14}N$ isotopic exchange studies and by DFT calculation pinpointing the potential role of the lattice nitrogen in ammonia synthesis via routes akin to the Mars-van Krevelen (MvK) mechanism [12-14]. Recently, the mobility and reactivity of lattice nitrogen, in binary and ternary nitrides, towards hydrogen has been the focus of several research activities [15-17]. The capacity of some metal nitrides (*e.g.* Ta_3N_5, θ-Mn_6N_{5+x}, AlN, Li_3N) to act as a source of pre-activated nitrogen has been of high interest especially for the development of ammonia production by chemical looping. In this approach, the lattice nitrogen reacts first with hydrogen to produce ammonia. The depleted nitrogen transfer material is regenerated upon reaction with atmospheric N_2 in a second step. Related to this concept, the nitrogen mobility and reactivity of several nitrogen transfer materials have been explored including Mn_6N_{5+X}, AlN and Li_3N [18-20]. In several cases, the activity of catalysts operating through mechanism akin to MvK was found to be strongly dependent upon: *(i)* structural and textural properties (e.g. exposed surface and crystal size) *(ii)* chemical composition and/or *(iii)* a combination of both [21, 22]. Unfortunately, the preparation of Co_3Mo_3N requires at least one calcination step at 550 °C to form the oxide precursor ($CoMoO_4$), once the oxide is obtained, the nitride phase is formed by an ammonolysis step, under a flow of pure ammonia, at 750 °C. The different thermal treatments result in crystal growth and unavoidable surface reduction (~ 10 m^2 g^{-1}). As such, there is a high interest in the development of novel approaches for the preparation of divided nitride phases, displaying high surface area and retaining small nanoparticle size. At the nanoscale level, the catalytic activity is expected to increase due to the increase of the surface to volume (A/V) atom ratio, which increases both available surface area and active site density for catalytic reaction. Furthermore, ammonia synthesis reaction has been evidenced to be structure-sensitive [23, 24]. Tsuji et al. demonstrated that the formation of bimetallic Co-Mo nanoparticle supported on CeO_2, prepared by NaNaph driven reduction, resulted in higher catalytic activity in ammonia synthesis [25]. The authors concluded that the formation of nitrogen vacancies occurs more easily on Co-Mo nanoparticles when supported over ceria than for bulk Co_3Mo_3N. Such vacancies formation can explain the better performances reported for Co-Mo/CeO_2 catalyst. Thus, enhancing the surface concentration on steps and defects through the dispersion of active nanoparticles nitrides is a tantalizing approach for improving the catalytic activity of nitrides materials.

In this work, we implemented a novel strategy to improve the catalytic activity of Co_3Mo_3N by confining the active phase within the mesopore of SBA-15 silica. SBA-15 was utilized as a suitable support due to its: *(i)* high surface area; *(ii)* highly ordered and uniform mesopores; and *(iii)* good thermal stability. The catalysts were evaluated in the ammonia synthesis reaction conducted at 400 °C and under atmospheric pressure. The effect of the textural and structural properties on the physicochemical properties and catalytic activity was investigated through an extensive characterization study. The positive effect of confining the active phase within the porosity of SBA-15 was demonstrated in ammonia synthesis.

VI.2 Experimental Procedure

VI.2.1 Catalyst Preparation

Chemicals. All chemicals needed for the preparation of mesoporous SBA-15 support and CoMo-N/SBA-15 materials were used as purchased without further purification: tetraethylorthosilicate ($Si(OC_2H_5)_4$, TEOS, 98 wt.%, Sigma-Aldrich), non-ionic triblock co-polymer Pluronic P123 (poly(ethylene glycol)-*block*-poly(propylene glycol)-*block*-poly(ethylene glycol), average MW ~5800, Sigma-Aldrich), cobalt nitrate hexahydrate ($Co(NO_3)_2.6H_2O$, 98 wt.%, Sigma Aldrich) and ammonium para-heptamolybdate tetrahydrate ($(NH_4)_6Mo_7O_{24}.4.H_2O$, 99 wt.%, Alfa Aesar).

Preparation of Co_3Mo_3N. Firstly, $CoMoO_4$ was prepared by dissolving the required quantities of cobalt nitrate and ammonium heptamolybdate in deionized water. The solution was then heated under reflux at 85 °C for 12 h. The resulting purple precipitate was recovered by filtration and washed with deionized water and ethanol, followed by drying at 100 °C overnight. The powder was then calcined at 500 °C (1.5 °C min^{-1}) for 6 h to form the desired $CoMoO_4$ phase. After calcination, the oxide was converted to its nitride counterpart (Co_3Mo_3N) by an ammonolysis step.

Preparation of CoMo-N/SBA-15 catalysts. The SBA-15 support was prepared according to hydrothermal method, under acidic conditions as described elsewhere [26].

CoMo/SBA-15 catalysts with different loadings were prepared by an adapted impregnation-infiltration protocol. In the first step, Mo was impregnated on SBA-15 by incipient wetness impregnation under mild drying (IWI) [27]. The aqueous molybdenum precursor solution was mixed with the support and gently dried at 25 °C for 5 days. The solid was then calcined at 400 °C (1.5 °C min^{-1}) for 5 h. At this step, SBA-15 supported MoO_3 is obtained. In a second step, cobalt was added to the latter by Melt Infiltration (MI) method. In this method, the cobalt nitrate precursor was first ground with Mo-SBA-15 powder. The resulting solid was then transferred into a Teflon-lined autoclave and submitted to a thermal treatment at 57 °C for 4 days. The solid was then calcined at 500 °C (5 °C min^{-1}) for 5 h.

Ammonolysis process. To convert the oxides into their nitrides counterpart, all the synthesized materials were subject to an ammonolysis step under NH_3 (BOC, 99.98 wt.%) at a flow rate of 60 mL min^{-1} at 785 °C for 5 h. Then, the material was cooled down to ambient temperature under ammonia flow. Upon reaching room temperature, the catalyst was purged using N_2 (100 mL min^{-1}) for 1 h followed by a passivation step under a low concentration of oxygen gas mixture (99.9 % N_2 / 0.1 % O_2) for 5 h.

N.B. Herein, the samples obtained after the calcination step are denoted as X-CoMo/SBA-15. The X represents the weight percentage of $CoMoO_4$. The catalysts obtained after the ammonolysis step are denoted as X-CoMo-N/SBA-15, while post-reaction materials are referred to as X-CoMo-N-Pr/SBA-15. The properties of SBA-15 were also studied and will be referred to as N/SBA-15 for SBA-15 after ammonolysis, and N-Pr/SBA-15 for post-reaction material.

VI.2.2 Characterization Techniques

In this article, the following characterization techniques were used: XRD (Low and high angle), N_2 physisorption, XPS, TEM, H_2-TPR, CHN, and Solid-state ^{29}Si and ^{1}H NMR. For more information regarding the characterization techniques, please refer to Chapter 2 for all details

Catalytic activity: In a typical temperature programmed reaction test, 0.150 g of CoMo-N/SBA-15 catalyst was placed in a quartz reactor and pre-treated at 700 °C under a 75 vol.% H_2/N_2 (BOC, 99.98 %) gas mixture at a total gas flow of 60 mL min^{-1} for 2 h. The reaction was then performed at 400 °C, under the same flow rate of 75 vol.% H_2/N_2 for at least 10 h. Ammonia production was determined by measurement of the decrease in conductivity of a 200 mL 0.0018 M H_2SO_4 solution through which the reactor effluent stream flowed and was monitored as a function of reaction time. The rate of the reaction was calculated according to the following:

$$r = \frac{\Delta_C \times n_{NH3} \times 60}{m \times 10^{-6} \times X_{wt}}$$

Where: r is the rate of the reaction for a range of time; Δ_C is the average change in conductivity per minute over a range of time; n_{NH3} is the number of moles of ammonia that correspond to the decrease of 1 $\mu S/cm$; m is the mass of the catalyst; X_{wt} is the load wt.%. The constants are added for conversion purposes to obtain the rate in $\mu mol/h.g_{active\ phase}$

Ammonia production under reducing conditions. Lattice nitrogen reactivity of the 10-CoMo-N/SBA-15 towards hydrogen was evaluated under reducing condition. 0.6 g of catalyst was placed in a quartz reactor and pre-treated at 700 °C under a 75 vol.% H_2/N_2 (BOC, 99.98 %) gas mixture at a total gas flow of 60 mL min^{-1} for 2 h. Therefore, the reactor was purged under argon and the temperature decreased at 400°C. The reaction was then performed at 400 °C, under the same flow rate under a 5 vol.% H_2/Ar for at least 10 h. Low H_2 concentration flow was applied in order to decrease the N consumption rate from the catalyst. Quantification of ammonia was done in a similar manner to the catalytic test.

VI.3 Results and Discussion

VI.3.1 Structural and textural properties of CoMo-N/ SBA-15

VI.3.1.1 Stability of SBA-15 under reactive conditions

PXRD. While the properties of SBA-15 support are extensively studied, the stability of this latter under ammonolysis conditions and under conditions relevant to ammonia synthesis is less available in the literature. In order to verify the stability of SBA-15 support through the different steps of the synthesis, SAXS patterns of the as-prepared siliceous support were first collected before and after nitridation and are presented in Figure S1. As expected, the as-prepared siliceous support displays the characteristic three well-resolved diffraction peaks that can be associated to the *(100)*, *(110)*, and *(200)* planes of the p6mm hexagonal symmetry structure reflecting the well-defined and uniform range mesoporous structure of SBA-15 (Figure S1-a). After ammonolysis treatment, the support maintained its pore structure quality (Figure S1-b) albeit a shift of the reflection peaks can be observed at higher 2θ angles from 0.889° to 0.933°. This shift indicates a slight pore contraction of the sample and could originate from the sintering occurring during the ammonolysis process (785 °C). Nevertheless, as illustrated in Figure S1-c, SBA-15 support still presents its characteristic reflections after 10 h of reaction under conditions relevant to ammonia synthesis (75 vol.% H_2 in N_2 at a total flow rate of 60 mL min^{-1}, 400 °C) indicating the conservation of a good pore structure ordering within the sample.

N_2 adsorption/desorption. Complementary information on the impact of the ammonolysis treatment on the textural properties of SBA-15 was obtained through nitrogen physisorption analysis (Table 1 and Figure S2). Before treatment, SBA-15 exhibited an adsorption/desorption isotherm of type IV with a hysteresis loop of type H1, at a relative pressure between $P/P_0 = 0.6 - 0.8$, which is typical of a mesoporous solid with highly uniform arrays of cylindrical pores with an average diameter of 6.5 nm (Figure S2-a). After ammonolysis, the study of the isotherm profile confirmed that N/SBA-15 maintained a uniform mesoporosity (Figure S2-b). However, an important decrease of 33 % in the SBA-15 accessible surface area (760 m^2 g^{-1} to 504 m^2 g^{-1}), accompanied by a decrease in pore volume (1.12 cm^3 g^{-1} to 0.75 cm^3 g^-1) are observed. Moreover, upon ammonolysis, N/SBA-15 was found to contain smaller pores with size centred around 6.1 nm which is in line with pore contraction observed by SAXS. These changes might be related to the sintering at high temperature or to the corrosive and basic atmosphere of the ammonolysis process. However, no significant changes in the textural properties of the support were detected under ammonia synthesis reaction conditions (Figure S2-c).

TEM. The morphology of the N/SBA-15 material was observed by means of HRTEM. The images (Figure S3) show the well-ordered hexagonal arrays of the mesopores, confirming that after ammonolysis step, the characteristic porous structure of SBA-15 material is maintained as previously indicated by SAXS and N_2 porosimetry results. Accumulation of nitrogen on the support is evidenced, through elemental mapping. This accumulation is also confirmed by N chemical analysis through elemental analysis (CHN), which gives a N content in the material of ~ 2.74 wt.%.

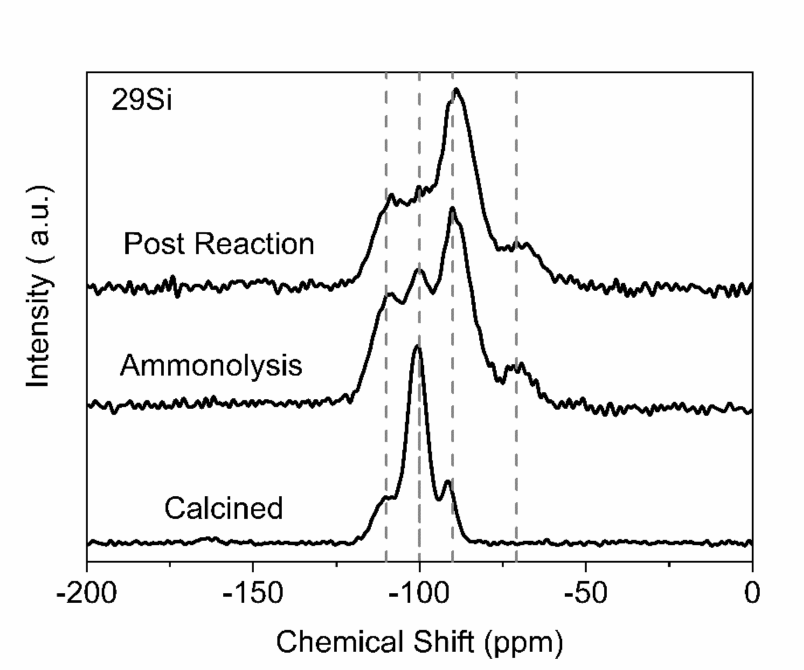

Figure 1 Solid-state 1D ^{29}Si MAS NMR spectra of (a) calcined SBA-15, (b) after ammonolysis, and (c) after 10h of reaction.

Solid-state ^{29}Si and ^{1}H NMR spectroscopy. Figure 1 presents 1D ^{29}Si MAS NMR spectra of the as prepared SBA-15 (post-calcination), N/SBA-15 (post-ammonolysis) and N-Pr/SBA-15 (post-reaction). In the ^{29}Si NMR spectrum of SBA-15, peaks at □90, □100, and □110 ppm that can be attributed to Si-$(OSi)_2(OH)_2$ units (Q^2), Si-$(OSi)_3(OH)$ units (Q^3), and Si-$(OSi)_4$ units (Q^4), respectively are observed [29]. After ammonolysis, the overall line-shape of ^{29}Si NMR spectrum associated with the Q^2, Q^3 and Q^4 sites was retained to some degree, but slightly shifted towards high frequency values (Q^2: □89, Q^3: □100, and Q^4: □109 ppm). However, the relative peaks intensities are different. In addition, these peaks are broader which may be related to the heterogeneity of the Si local field (non-uniform distribution of bond length and angles) after ammonolysis. More importantly, an additional strong intensity resonance at ca. □71 ppm and a weak intensity broad peak in the vicinity from □75 ppm to □60 ppm are expected to originate from the formation of surface silanol by ammonia to surface silyl-amine site ($SiO_2N(NH)_x$) moieties [29]. However, the extent of these surface sites is likely limited as reflected in the low intensity peak. The complete formation of an amorphous silicon nitride Si_3N_4 can be safely ruled out from these results as the spectra obtained for these materials are usually characterized by large peak with maxima of ~ 48 ppm, which is not observed in the ^{29}Si MAS NMR spectra [30]. Elemental analysis further corroborates NMR results and confirms the low nitrogen content in the sample ~ 2.74 wt.%. In the post-reaction SBA-15 catalyst, minor changes in ^{29}Si NMR are observed as the intensity ratio of Q^2/Q^3 is slightly different, with respect to the post-ammonolysis sample, which may be related to differences in silanol concentration in both samples. Furthermore, calcined, post-ammonolysis, and post-reaction SBA-15 were studied using ^{1}H-^{1}H 2D spin diffusion (SD) NMR to characterize through-space ^{1}H-^{1}H proximities. In measurements of this type, magnetization is allowed to exchange between the ^{1}H neighboring sites using a mixing delay (as referred to as spin diffusion delay), which leads to the on- and off-diagonal peaks for chemically equivalent and inequivalent ^{1}H sites, respectively. Figure 2 displays 1D ^{1}H MAS and 2D ^{1}H-^{1}H SD spectra of SBA-15 before and after the reaction. Prior to the ammonolysis treatment, the ^{1}H NMR spectrum of calcined SBA-15 is mainly dominated by a major peak at ~3.8 ppm corresponding to the surface adsorbed water, and a broad distribution of weak intensity peaks cantered at 6.5 ppm are attributable to the strong hydrogen bonding interactions between these groups and silanol protons. In the 2D ^{1}H-^{1}H SD spectrum of the same material (Figure 2b), the off-diagonal peak between 3.8 ppm and 6.5 ppm indicate the through space proximity between silanol and the hydrogen bonded hydroxyl moieties. By comparison, after ammonolysis, and in the post-reaction material, the ^{1}H peak associated with silanol groups is displaced towards high frequency values (4.5 ppm and 5.2 ppm) with this latter peaks is hypothesized to originate from weakly adsorbed silyl-amine sites [31-33]. In addition, a broad peak between 0 and 4 ppm appeared after ammonolysis which is likely due to the formation of silanol groups (SiOH) at different local chemical environments [32].

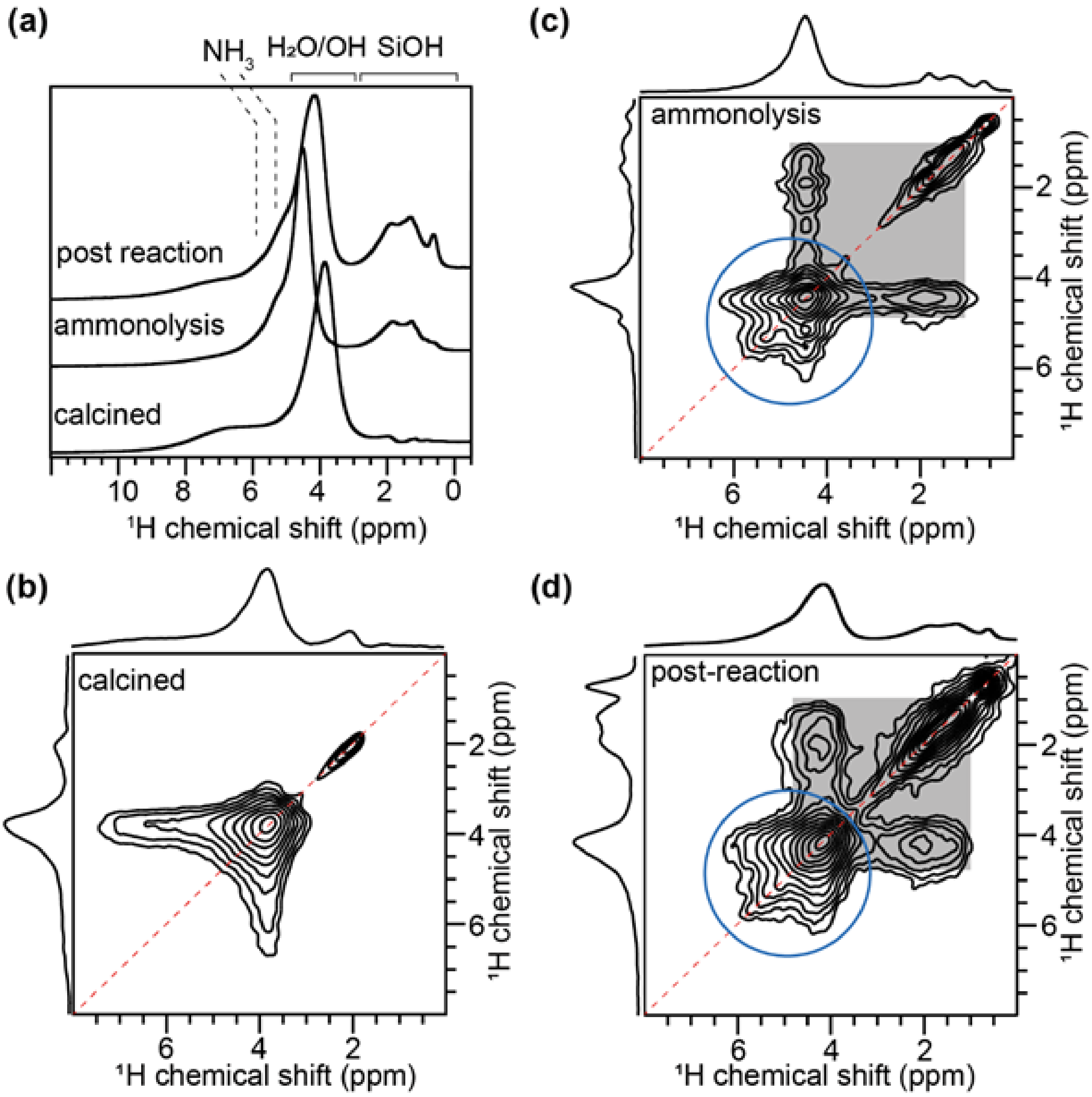

Figure 2 Solid-state 1D ^{1}H spectra of SBA-15, ^{1}H-^{1}H 2D NMR spin diffusion spectra of (b) calcined SBA-15, (c) after ammonolysis, and (d) after 10 h of reaction. For (b-d), the spin diffusion mixing time was 500 ms. All spectra were acquired at 18.8 T (Larmor frequency of ^{1}H = 800.1 MHz) with 50 kHz MAS at room temperature.

Further changes are observed after the post-reaction, whereby the intensities of peaks in the 0-4 ppm range (SiOH groups) are increased with respect to the water/silanol protons (4.2 ppm) which is consistent with the increased intensities of Q^3 and Q^2 silicon sites observed in ^{29}Si NMR spectra. The increase in silanol concentration is likely due to the reaction between Si-O-SiO(OH) and NH_3 which leads to the formation of OSiOH and $H_2NSiO(OH)$. Additionally, subtle changes to the lineshape at 5.2 and 5.7 ppm are observed with partially resolved shoulder peaks are expected to stem from the NH_3-like groups adsorbed on the SBA-15 [33, 34]. This is further supported by the analysis of 2D SD spectra of ammonolysis and post-synthesis reaction (Figure 2c, d) in which strong correlation peaks between the surface adsorbed water and the silyl-amine sites are observed, as depicted in the blue circles. The off-diagonal 2D peaks connecting the chemical shifts at 1.3 and 1.8 ppm and 4.5 ppm (grey boxes) are due to the close proximities between the surface adsorbed water and the silanol groups.

Overall, structural and textural properties of the SBA-15 support was indubitably impacted by the reactive conditions applied in the study. However, it was observed that N/SBA-15 maintained its ordered porous structure and satisfying surface area ~504 m^2 g^{-1}, which is still fairly high for catalytic applications. Besides, changes in the local Si environment were evidenced by ^{29}Si and ^{1}H NMR and could be attributed to the formation of silyl-amine sites ($SiO_2N(NH)_x$) on the silica surface. In the other hand, HRTEM and SAXS results clearly indicate that N/SBA-15 maintain the initial characteristics of a 2D hexagonally ordered structure. Thus, we demonstrate that SBA-15 is sufficiently robust under reaction conditions and is to be considered as an appropriate support for the dispersion of small metal nitride particles within its porosity.

VI.3.1.2 Characterization and Structural Evolution of CoMo/SBA-15 and CoMo-N/SBA-15

PXRD. Bulk Co_3Mo_3N catalyst. Before ammonolysis, the presence of a pure and well crystallized $CoMoO_4$ precursor phase (PDF: 21-0868) was confirmed by PXRD (Figure S4). The diffractogram exhibited intense and sharp PXRD diffraction peaks indicating the preparation of a well-crystallized material with a large coherent diffraction domain. Following the ammonolysis step, all the detected XRD diffraction peaks (Figure 3) matched the Co_3Mo_3N (PDF 89-7953) confirming the formation of a pure nitride phase. As in the case of $CoMoO_4$ intense and sharp reflections XRD peaks are observed indicating the formation of a well-crystallized nitride phase.

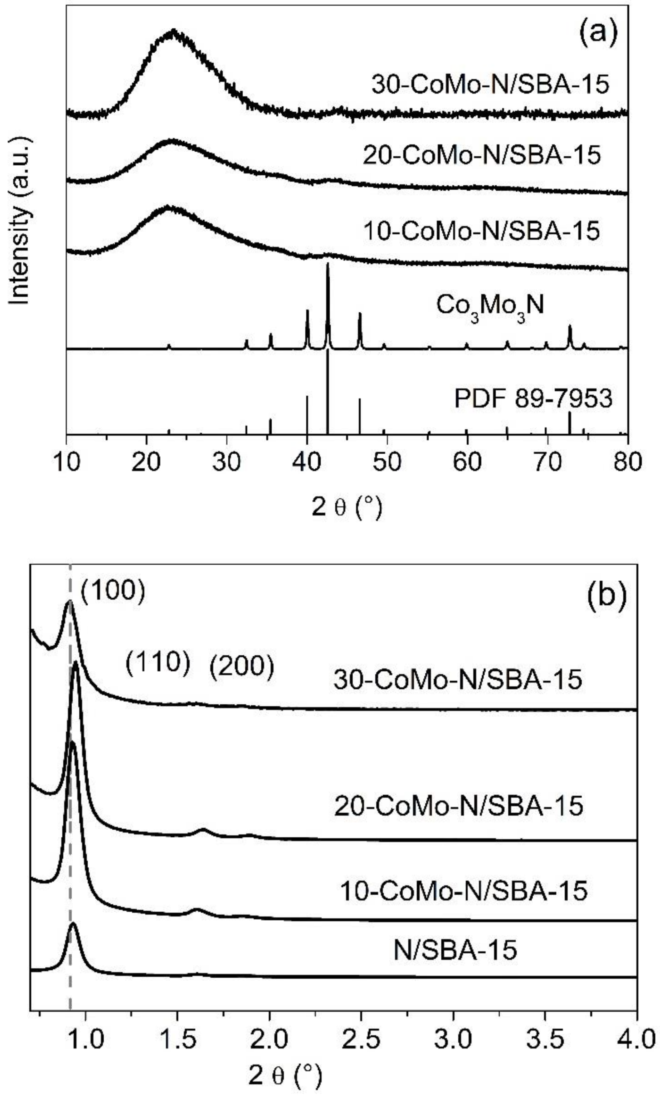

Figure 3 PXRD patterns of Co_3Mo_3N and CoMo-N/SBA-15 with different loading. (a) wide-angle PXRD and (b) SAXS patterns

CoMo/SBA-15 catalysts. Prior to the ammonolysis step, the effective dispersion of $CoMoO_4$ phase in SBA-15 was confirmed by PXRD in the wide-angle domain (Figure S4) for which only poorly defined reflections of the oxide phase are observed despite loading reaching 30 wt.% in the supported catalysts. Interestingly, after the ammonolysis step, no peaks related to either Co_3Mo_3N phase or single Co-N / Mo-N phases were detected on supported samples. Only a broad PXRD peak of amorphous silica was retained (Figure 3-a). The absence of reflections related to the Co_3Mo_3N phase may be related to a possible re-dispersion of this latter during ammonolysis process. The presence of single Co-N or Mo-N phases can however not be ruled out, even if the broad signal positions below the main reflections of the Co_3Mo_3N bulk phase.

SAXS patterns collected after the ammonolysis step displayed the same diffraction patterns, with respect to the parent N/SBA-15, confirming that the derived catalysts maintained their regular pore structure through ammonolysis conditions (Figure 3-b).

Nitrogen adsorption-desorption analysis

The evolution of the textural properties of the catalysts was investigated by means of N_2 physisorption. The results are shown in Figure 4, Figure S5, and Table 1. **Bulk $CoMoO_4$ and Co_3Mo_3N.** The unsupported $CoMoO_4$ and Co_3Mo_3N materials exhibited a limited accessible specific surface area (Table 1). After the ammonolysis, the surface area increased slightly from 6.1 m^2g^{-1} on $CoMoO_4$ to 13 m^2g^{-1} on the Co_3Mo_3N counterpart. Both materials exhibited a type II isotherm reflecting their non-porous nature.

CoMo/SBA-15. The N_2 adsorption/desorption isotherms of CoMo/SBA-15 (10, 20 and 30 wt.% of CoMo) are presented in Figure S5. 10-CoMo/SBA-15 and 20-CoMo/SBA-15 preserve a similar type IV isotherm with a hysteresis loop of type H1 with respect to the parent SBA-15. Furthermore, only a small increase in the pore size from 6.5 nm on SBA-15 to ~ 7.2 nm on 20-CoMo/SBA-15 was observed. These results confirm that these catalysts retain the initial characteristics of SBA-15. However, the 30-CoMo/SBA-15 showed an H2b hysteresis loop, reflecting pore blocking at high CoMo loading. Compared to the SBA-15, the BET surface area of CoMo/SBA-15 catalysts showed a marked decrease with CoMo loading (from 760 m^2 g^{-1} on SBA-15 to 295 m^2 g^{-1} on 30-CoMo-SBA-15 sample, see Table 1), indicating the filling of $CoMoO_4$ in the channels of SBA-15.

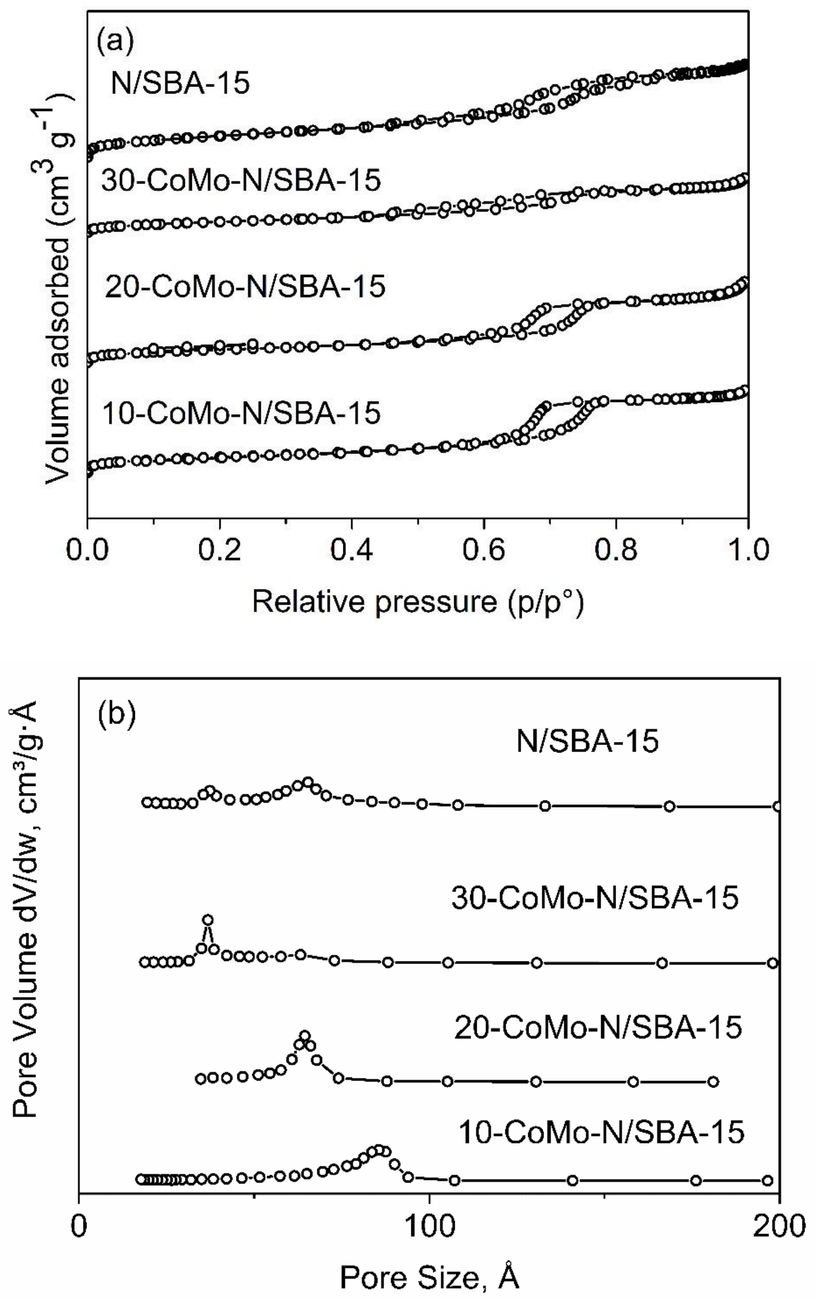

Figure 4 (a) N_2 adsorption–desorption isotherms and (b) pore size distribution of SBA-15 and CoMo-N/SBA-15 catalysts after ammonolysis.

CoMo-N/SBA-15: The N_2 adsorption/desorption isotherms obtained after the ammonolysis step are presented in Figure 4. The results confirm that, at low CoMo loading, the ordered mesoporous structure is mostly not altered by the ammonolysis step, while the microporous domain is strongly reduced (Table 1). Interestingly, in the CoMo-N/SBA-15, the changes, upon ammonolysis, are less significant than those observed on the bare SBA-15. In fact, only a small decrease in the accessible surface area and pore volume occurring over CoMo-N/SBA-15 is observed which might be due to the presence of nanoparticles inside SBA-15 mesoporosity.

Table 1. Textural properties of SBA-15, unsupported CoMo and supported CoMo-based catalysts after calcination, ammonolysis and post-reaction.

		S_{BET},[a] $m^2.g^{-1}$	**$S\mu$,[b] $m^2.g^{-1}$**	**Vp,[c] $cm^3.g^{-1}$**	**$V\mu$,[d] $cm^3.g^{-1}$**	**Dp,[e] nm**	**a_0,[f] nm**	**t_0,[g] nm**
$CoMoO_4$	After calcination	6.1	-	-	-	-	-	-
Co_3Mo_3N	After ammonolysis	13.0	-	-	-	-	-	-
	Post-reaction	8.6	-	-	-	-	-	-
SBA-15	After calcination	760	131	1.12	0.06	6.5	11.48	4.98
	After ammonolysis	504	9.6	0.75	-	6.1	10.92	4.82
	Post-reaction	526	19.3	0.82	-	6.1	10.89	4.79
10-CoMo-N/SBA-15	After calcination	390	50	0.71	0.02	7.1	11.11	4.01
	After ammonolysis	348	19	0.71	0.005	6.8	10.87	4.07
	Post-reaction	376	-	0.65	-	6.9	11.35	4.45
20-CoMo-N/SBA-15	After calcination	344	44	0.64	0.02	7.2	10.99	3.79
	After ammonolysis	361	14.4	0.70	-	7.6	10.76	3.16
	Post-reaction	359	9.3	0.61	-	6	10.65	4.65
30-CoMo-N/SBA-15	After calcination	295	44	0.43	0.02	5.8	11.35	5.55
	After ammonolysis	285	14	0.49	-	5.8	11.11	5.31
	Post-reaction	213	4	0.35	-	5.7	11.11	5.41

[a] S_{BET} Calculated by the BET method; [b] S_μ microporous surface area; [c] V_p total pore volume calculated using BJH method; [d] $V\mu$ micropore volume; [e] D_p mean pore size calculated using B.J.H method, [f] lattice parameter calculated by hexagonal structure and bragg's equation, [g] wall thickness, $a_0 - D_p$

TEM-EDS analysis

After ammonolysis, the morphology of CoMo-N/SBA-15 as well as the local distribution of cobalt and molybdenum species in mesoporous SBA-15 were studied by means of HAADF-STEM analysis coupled with EDS mapping. A selection of representative images of the supported samples is presented in Figure 5 and Figure S6.

As observed on the slice analyses (~75 nm thickness), the characteristic porous structure of SBA-15 material is preserved with well-ordered mesoporous hexagonal arrays in all CoMo-N/SBA-15 which is consistent with SAXRD and N_2 physisorption. Furthermore, the distribution profile of the metal species throughout the porosity of SBA-15 was observed by HAADF micrographs performed over various areas of the supported samples. As observed, nanoparticles are highly dispersed within the 2D-channels of SBA-15 for the 10-CoMo-N/SBA-15 catalyst (Figure 5 and Figure 6-a).

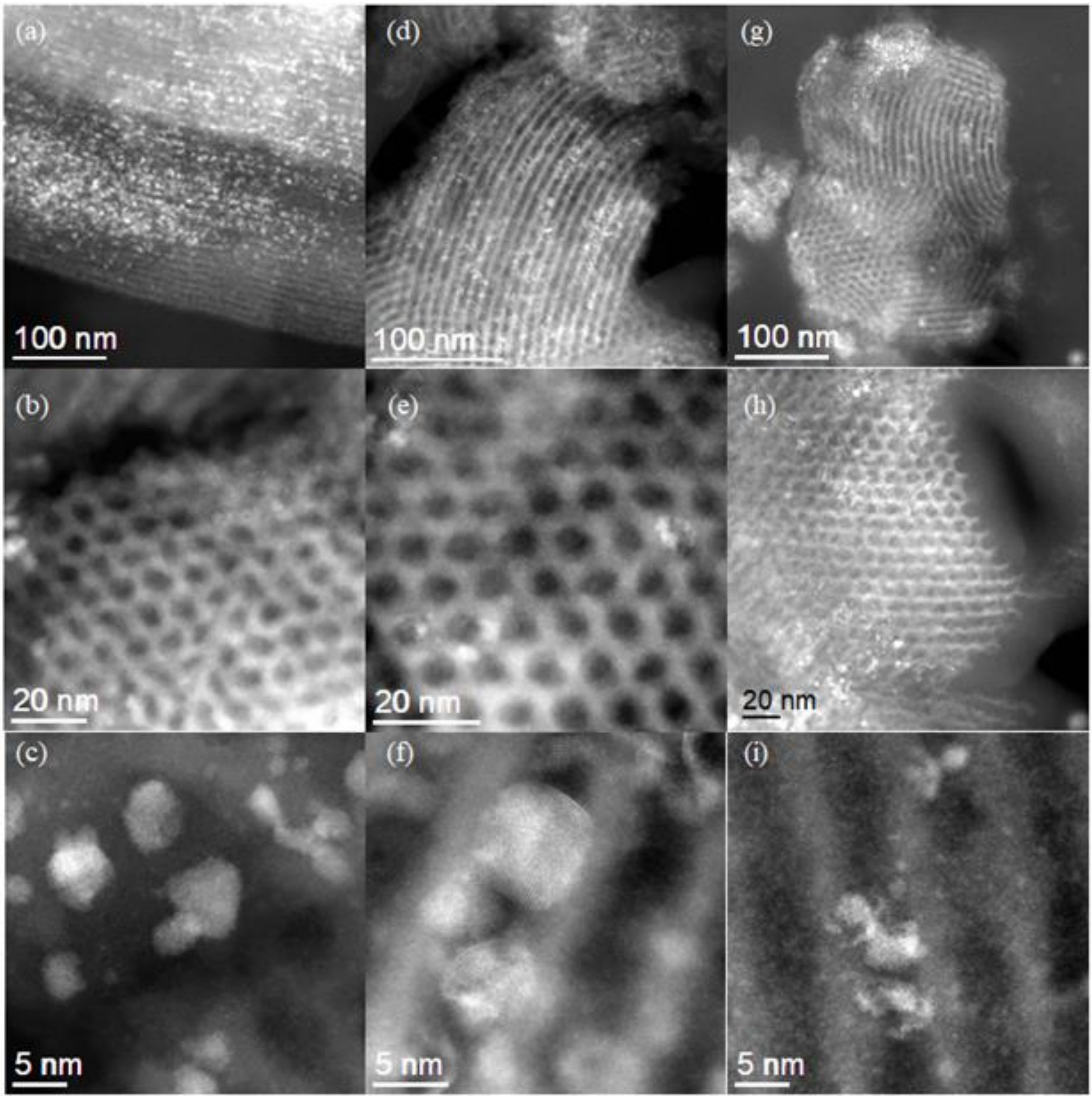

Figure 5 Representative HAADF images for supported CoMo/SBA-15 after ammonolysis reaction. 10-CoMo-N/SBA-15 (a, b, and c), 20-CoMo-N/SBA-15 (d, e, and f) and 30-CoMo-N-SBA-15 (g, h, and i)

Complementary EDS analysis confirm the high dispersion of Co and Mo species throughout the siliceous framework albeit some enrichment of metal species on the external surface of the grain cannot be ruled out (Figure S6). The progressive increase of CoMo amount within the SBA-15 support could slightly amplify such external Co enrichment that is more noticeable especially on 30CoMo-N/SBA-15 (Figure S6-c), due to the first Mo incorporation in the support that can lead to some pore entrance constriction thus limiting the infiltration of Co precursors. Therefore, Co_3O_4 phase was identified by PXRD (Figure S4) as a segregated secondary phase on the oxide material (30-CoMo/SBA-15). However, most of the Co and Mo signatures in the EDS micrographs are in close proximity, supporting the formation of CoMo-N mixed phase instead of single Co-N and Mo-N phases.

VI.3.2 Oxidation states and chemical composition by XPS.

To gain insight into the evolution of the surface chemical composition, XPS analysis was performed for the calcined and post-ammonolysis catalysts. Furthermore, the effect of catalytic pre-treatment on the oxidation state and surface composition was also studied. The results are summarized in Figure 6, Table S1, Table S2, and Figure S7.

Co_3Mo_3N. As expected, in $CoMoO_4$, the predominant species are Co^{2+} and Mo^{6+} (Table S1 and Table S2). However, after the ammonolysis step, Mo 3d and Co 2p XPS profiles showed a range of different oxidation states similar to those reported in the literature with the presence of Mo-O and Co-O [35]. The spectral decomposition of the high-resolution Mo 3d region can be ascribed to the Mo^{6+}, Mo^{5+}, Mo^{4+} and Mo-N species. The peaks characteristics of Mo-N species are of weaker intensity suggesting the formation of an oxidation layer at the surface of Co_3Mo_3N. These results are consistent with the oxidation layer observed by HAADF-STEM (Figure S8) which was passivated after the ammonolysis step.

In order to access the surface composition of the catalyst under reaction conditions, Co_3Mo_3N was pre-treated in an XPS environmental chamber permitting to mimic the pre-treatment used prior the catalytic test. The use of an environmental chamber allowed us to study the surface composition of Co_3Mo_3N with minimal surface contamination. A drastic change was observed in both Mo 3d and Co 2p XPS profiles. After the pre-treatment under a flow of H_2/N_2, an important shift to lower binding energies is observed in both Co and Mo XPS profiles.

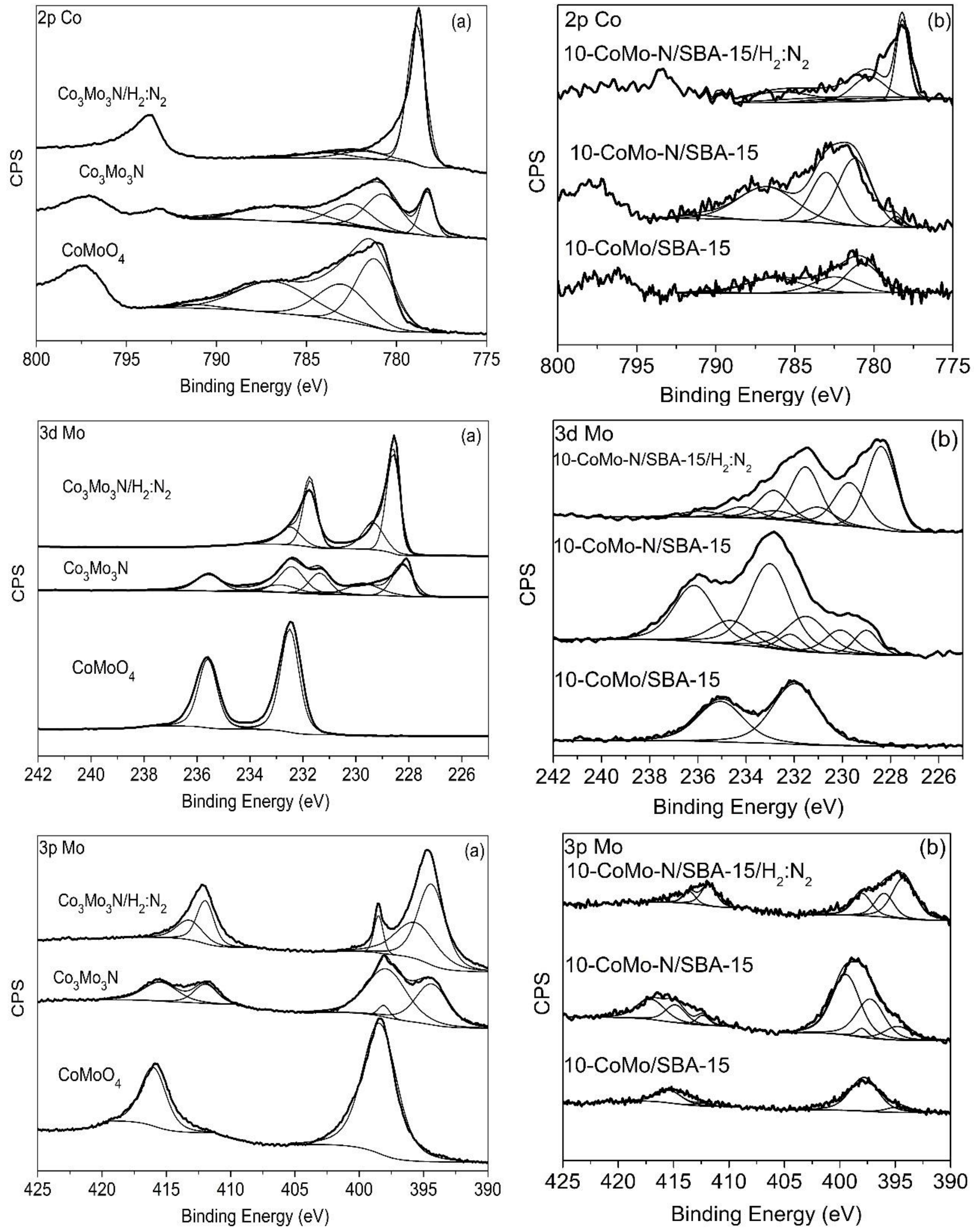

Figure 6 XPS spectra in the Mo 3d region, Co 2p region and Mo 3p region of (a) Co_3Mo_3N and (b) 10-CoMo-N/SBA-15. Co_3Mo_3N/H_2: N_2 and 10-CoMoN/SBA-15/H_2:N_2 were subject to pre-treatment under reaction condition at 700°C for 2h in environmental XPS chamber before analysis.

These values are more aligned with the intermetallic nature of Co_3Mo_3N presenting a low valent state of metals. The high resolution of Mo 3d spectra (Figure 6) show two major spectral lines corresponding to Mo $3d_{5/2}$ and Mo $3d_{3/2}$ spin-orbit components 228.59 eV and 231.73 eV of Mo-N species [25, 35]. The intensity and fraction of Mo-N is much pronounced in this case revealing the true composition of the active surface phase under reaction conditions. In the high-resolution Co 2p spectra, the position of the major spectral line was found at 778.88 eV which is in agreement with the value reported in Co_3Mo_3N prepared by Hosono's group [25]. Although this value is very close to metallic cobalt, this latter is usually reported at lower binding energy (777.9 eV).

Figure 6 shows the spectral decomposition of high-resolution Mo 3p spectra in which N 1s can also be observed. In this region, an intense and well resolved peak is observed at 398.4 eV which is very comparable to N 1s observed in Co_3Mo_3N (397,9 eV) and in Mo_2N and MoN bulk (397.8 eV) [25, 36]. Thus, after the pre-treatment, it can be concluded that the surface is mostly populated with N adatoms.

CoMo-N/SBA-15: The evolution of the surface composition of CoMo-N/SBA-15 catalysts were studied and compared to the unsupported catalyst (Figure 6, Figure S7, Table S1, and Table S2). In a similar manner to $CoMoO_4$, all the CoMo/SBA-15 obtained after calcination were composed predominantly of Mo^{6+} and Co^{2+} species. For 30-CoMo/SBA-15, an additional set of peaks were identified in the Co 2p spectra at 779.4, 780.70, 782.00, 785.00 and 789.30 eV, corresponding to Co_3O_4 [37] (Figure S7) which is in line with PXRD results. Such signals were not observed for 10-CoMo/SBA-15 sample, confirming the absence of Co_3O_4 formation in this solid in agreement with PXRD results.

Upon ammonolysis, all the catalysts showed a range of oxidation states that are similar to those observed in the unsupported Co_3Mo_3N. For instance, the spectral decomposition of the high-resolution Mo 3d region showed the presence of a range of oxidation state including Mo^{6+}, Mo^{5+}, Mo^{4+} and Mo-N. For the 30-CoMo-N/SBA-15, Co_3O_4 peaks are not observed after ammonolysis, suggesting that the latter has been successfully nitrided (Table S2). After the pre-treatment, most of the materials were composed of Mo-N and Co-N confirming that under reaction conditions, the surface is mainly populated with N adatoms. In summary, the surface composition of CoMo-N/SBA-15 was found to be very similar to the Co_3Mo_3N.

VI.3.3 Reducibility of CoMo/SBA-15

The degree of interaction between the dispersed phase and SBA-15 support can be indirectly evaluated upon studying the reduction of cobalt molybdenum oxide species by H_2-TPR. The

H_2-TPR results of CoMo/SBA-15 catalysts are presented in Figure 7 and in Table S3. alongside the $CoMoO_4$.

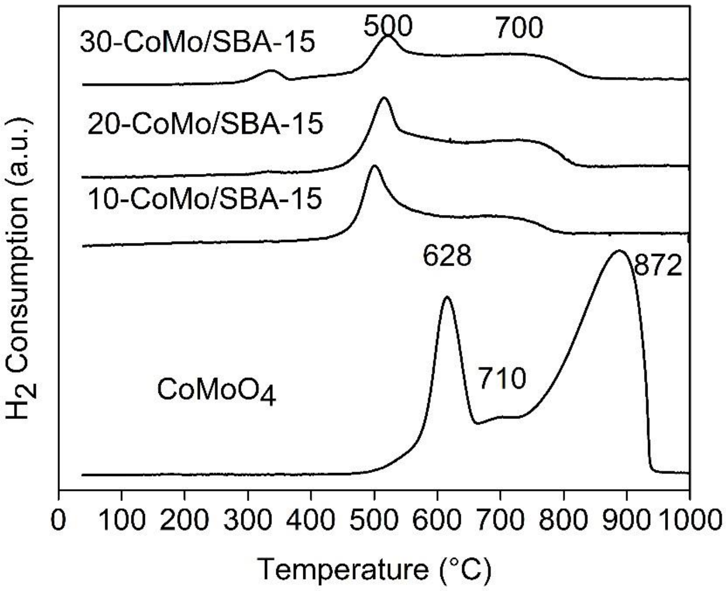

Figure 7 H_2-TPR profiles of $CoMoO_4$ and CoMo/SBA-15 catalysts

The reduction temperature and H_2 consumption are presented in Table S3. TPR-profile of $CoMoO_4$ showed that the reduction process started at 600 °C. The reduction profile was characterized by two main reduction peaks at 628 and 872 °C with a smaller shoulder at 710 °C. The H_2-TPR profile agrees well with previous studies where the reduction of $CoMoO_4$ is generally accompanied with the formation of suboxides intermediates such as $Co_2Mo_3O_8$ and/or $CoMoO_3$ [38, 39]. Substantial changes in the reduction behavior are observed for the CoMo/SBA-15 samples. The reduction peaks are shifted to lower temperatures, with reduction starting at temperatures as low as 450 °C. In this case, the reduction peak at lower temperature which presents higher intensity and the shoulder between both main peaks is no longer observed. Interestingly, the main reduction peak slightly shifted to higher temperatures with the increase in CoMo loading. For the 30-CoMo/SBA15 sample, an additional peak is observed at a temperature of ~ 338 °C which might be attributed to the reduction of segregated Co_3O_4 phase, previously identified by PXRD analysis [40]. In summary, the reactivity of cobalt molybdates towards hydrogen was greatly improved upon dispersion on SBA-15, confirming the stabilization of small nanoparticles within the siliceous framework.

VI.3.4 Catalytic performance in ammonia synthesis

The catalytic activity of N/SBA-15 was first evaluated (Figure 8 and Figure 9). After 10 h of reaction, no ammonia production was measured which ruled-out the possibility of ammonia formation/desorption from the silylamine sites observed by ^{19}Si and ^{1}H NMR.

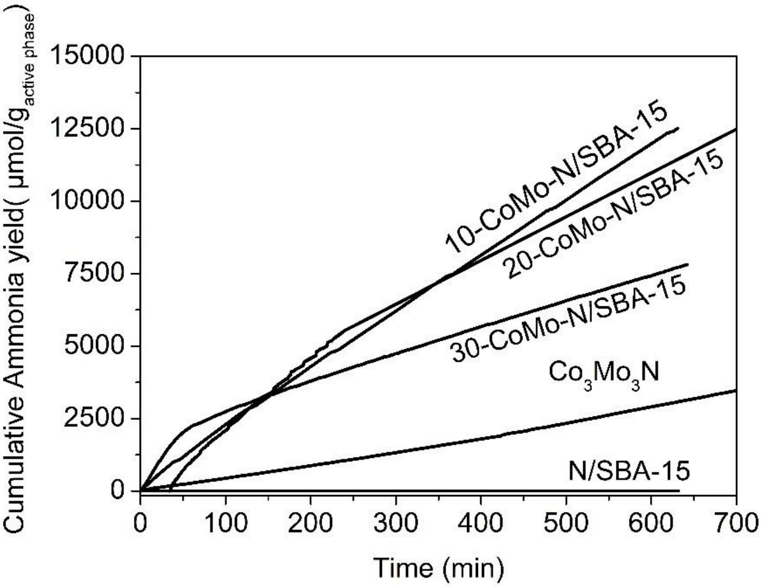

Figure 8 Cumulative ammonia yield obtained of N-SBA-15, Co_3Mo_3N, 10-CoMo-N/SBA-15, 20-CoMo-N/SBA-15, and 30-CoMo-N/SBA-15. Reaction performed under 60 mL min^{-1} flow rate of 75 vol.% H_2/N_2 at 400 °C and ambient pressure.

Thereafter, the catalytic activity of CoMo-N/SBA-15 was studied and compared to the well-established Co_3Mo_3N catalyst. Co_3Mo_3N exhibits high catalytic activity for ammonia synthesis at ambient pressure (rate of 248 µmol $g_{catalyst}^{-1}$ h^{-1}, WHSV 24 000 mL g^{-1} h^{-1}) which is consistent with values reported in the literature but at lower WHSV 9 000 mL g^{-1} h^{-1} [41, 42]. However, it is worth noting that increasing WHSV might affect ammonia synthesis rate, and therefore a direct comparison of activity with values from the literature is difficult. Under the same catalytic testing conditions, the 10-CoMo-N/SBA-15 (rate of 263 µmol $g_{catalyst}^{-1}$ h^{-1}, WHSV 24 000 mL g^{-1} h^{-1}) exhibits close initial catalytic activity than for the Co_3Mo_3N, despite a significantly lower content of active phase in the reactor. When the active phase loading increases up to 20 wt.%, almost a linear increase in the catalytic activity was observed (20-CoMo-N/SBA-15: 479 µmol $g_{catalyst}^{-1}$ h^{-1}, WHSV 24 000 mL g^{-1} h^{-1}). Increasing the loading of the active phase to 30 wt.%, resulted in a further increase in the catalytic activity up to 518 µmol $g_{catalyst}^{-1}$ h^{-1}.

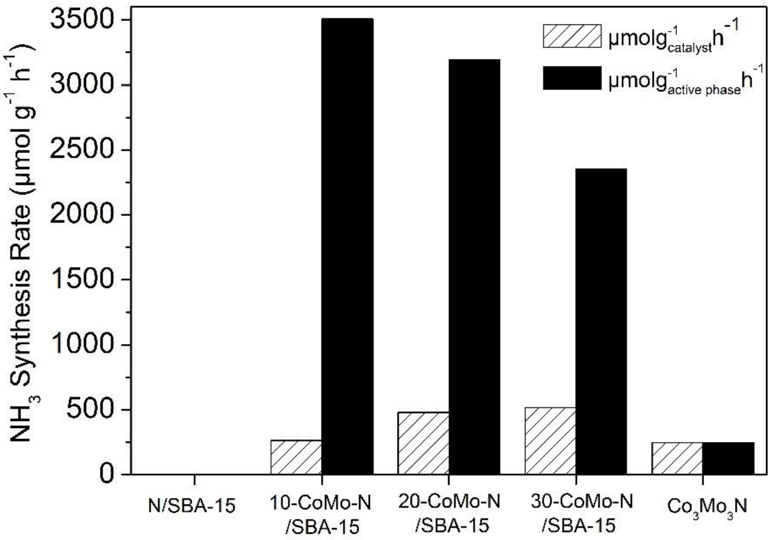

Figure 9 Initial rate of NH_3 synthesis calculated for N-SBA-15, Co_3Mo_3N, 10-CoMo-N/SBA-15, 20-CoMo-N/SBA-15, and 30-CoMo-N/SBA-15. Reaction performed under 60 mL min^{-1} flow rate of 75 vol.% H_2/N_2 at 400 °C and ambient pressure.

However, upon reaction, differences between initial catalytic activity and activity after reaching steady state conditions are observed (Table 2). The supported CoMo-N/SBA-15 displayed a stationary rate of 120, 200 and 170 μmol $g_{catalyst}^{-1}$ h^{-1} corresponding to the loadings of 10, 20, 30 wt.% respectively. It can be seen that the stationary ammonia synthesis rate is lower than the initial rate which may denote the contribution of surface nitride decomposition by hydrogenation during the first hour of reaction. The decrease in the catalytic activity is more apparent with the 30-CoMo-N/SBA-15 which might be related to the presence of a single phase of cobalt prone to decomposition and deactivation.

The beneficial effect of the CoMo-N phase dispersion becomes more evident when ammonia synthesis rate is normalized with respect to the active phase loading (wt.% of Co_3Mo_3N phase). For instance, at steady state conditions, a rate of 1714 μmol $g_{active\ phase}^{-1}$ h^{-1} is obtained over the 10-CoMo-N/SBA-15 catalyst. A gradual decrease is observed while increasing the cobalt molybdenum charge. Thus, the normalized ammonia synthesis rate decreased to 1429 μmol $g_{active\ phase}^{-1}$ h^{-1} and 810 μmol $g_{active\ phase}^{-1}$ h^{-1} for the 20-CoMo-N/SBA-15 and 30-CoMo-N/SBA-15 catalysts respectively. All values however remain far above the production rate registered for bulk Co_3Mo_3N (248 μmol $g_{catalyst}^{-1}$ h^{-1}). From these results, it can be concluded that the stabilization of cobalt molybdenum nitride at a nanoscale level ameliorates significantly its catalytic performance in ammonia synthesis. The progressive decrease in normalized ammonia synthesis rate with the CoMo-N loading could be linked to the pore plugging phenomenon that becomes more significant at high loading. Indeed, we observe a decrease of the normalized ammonia synthesis rate by 53% between 10% and 30% CoMo-loading. At the same time, the surface area and pore volume of the catalysts are reduced by 43% and 51% respectively. Consequently, the decrease of active phase reactivity is preferably associated to the decrease in particle accessibility inside the pores than to a reduction of the nitride phase surface/bulk reactivity.

Table 2. Summary of the catalytic activity of CoMo-N/SBA-15 catalysts in the ammonia synthesis under 60 mL min^{-1} of 75 % H_2 in N_2 (BOC, 99.98 %) at 400 °C and atmospheric pressure.

	Mo/Co atomic ratio*	**Initial rate**		**Stationary rate****	
		µmol $g_{catalyst}^{-1}$ h^{-1}	**µmol $g_{active\ phase}^{-1}$ h^{-1}**	**µmol $g_{catalyst}^{-1}$ h^{-1}**	**µmol $g_{active\ phase}^{-1}$ h^{-1}**
SBA-15	0	0	0	0	0
Co_3Mo_3N	0.99	248	248	259	259
10-CoMo-N/SBA-15	1.088	263	3507	120	1714
20-CoMo-N/SBA-15	0.796	479	3193	200	1429
30-CoMo-N/SBA-15	0.386	518	2355	170	810

* ratio calculated from TEM/EDS quantification

** Ammonia synthesis rate calculated after reaching steady state condition

VI.3.5 Thermal, textural, and structural stability of CoMo-N/SBA-15 catalysts after reaction.

The thermal stability of CoMo-N/SBA-15 catalysts is a significant challenge, especially under ammonia synthesis condition. To provide a distinct comparison between post-ammonolysis and post-reaction catalysts, a systematic study on the thermal stability of catalysts has been conducted.

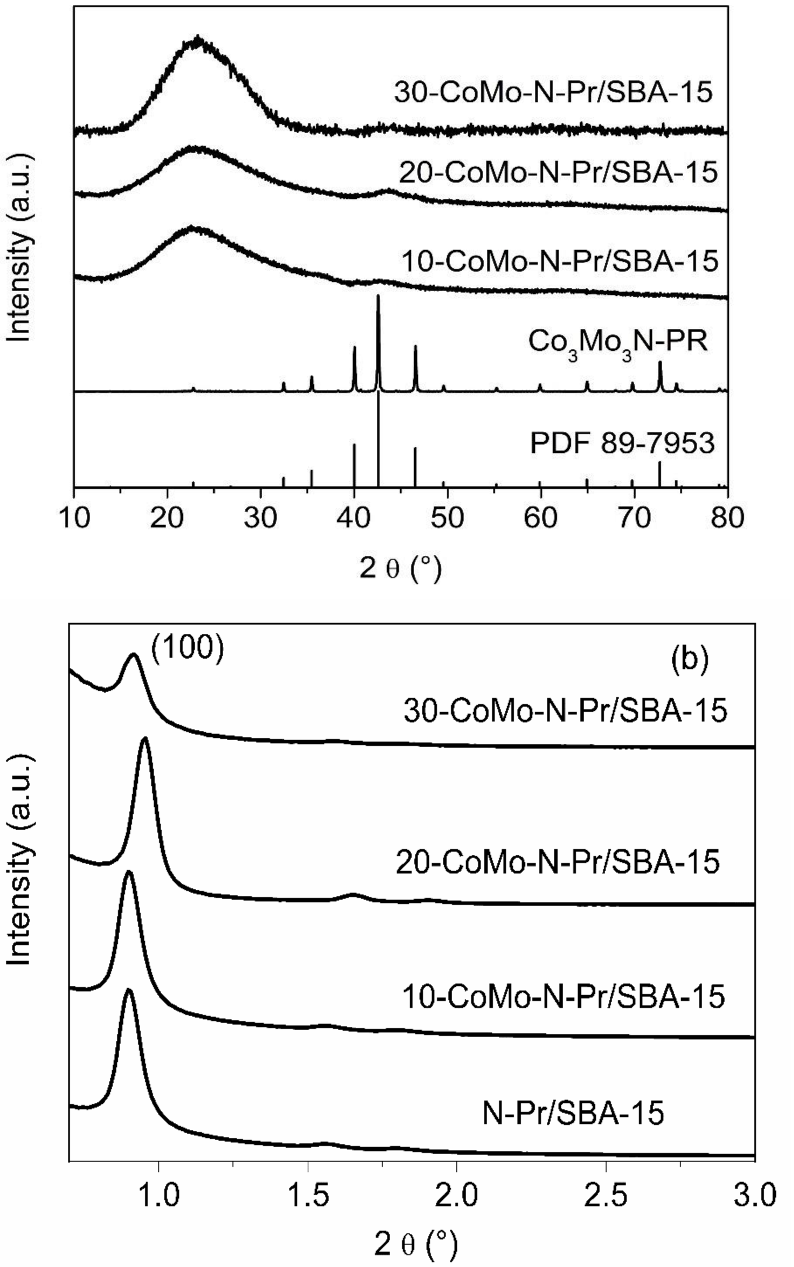

Figure 10 PXRD patterns of post-reaction Co_3Mo_3N-Pr and CoMo-N-Pr/SBA-15. (a) wide-angle PXRD and (b) SAXS patterns

Figure 10-a shows the PXRD patterns recorded in the wide-angle domain, for the post-reaction CoMo-N/SBA-15 samples. After 10 h of reaction, no well-defined peaks related crystalline Co_3Mo_3N are detected denoting the stability of the Co_3Mo_3N phase formed under ammonia synthesis conditions. Indeed, the small broad peak observed at $2\theta \sim 43°$ might be related to the presence of nitride phase, crystallizing at the nanoscale level or that remain not crystallized. SAXS patterns collected at low angle domain shows the typical diffraction peaks related to the *(100)*, *(110)*, and *(200)* planes of the p6mm hexagonal SBA-15 symmetry structure showing that the support maintained its uniform pore structure under ammonia synthesis conditions (Figure 10-b). The N_2 adsorption/desorption isotherms of CoMo-N-Pr/SBA-15 samples are

presented in Figure 11. After the catalytic reaction, the 10-CoMo-N-Pr/SBA-15 and 20-CoMo-N-Pr/SBA-15 catalysts maintained their isotherms of type IV with a hysteresis loop of type H1, characteristic of highly ordered structures with uniform disposition of cylindrical pore. Furthermore, only minor changes in the surface area and pore volume are observed between the post-ammonolysis and post-reaction catalyst, thus showing the good textural and structural stability of CoMo-based nitrides when supported on SBA-15. However, the 30-CoMo-N-Pr/SBA-15 showed a more pronounced surface reduction (285 to 213 m^2g^{-1}) which might be related to structural collapse or eventually minor sintering of nitride particles occurring on external surface of silica grains.

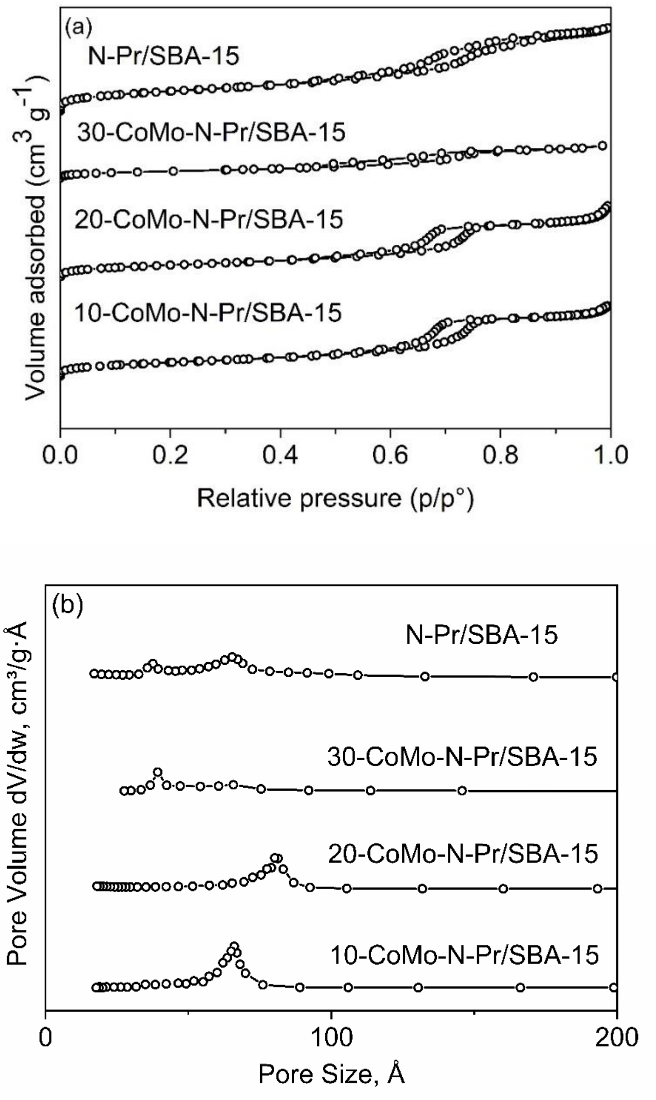

Figure 11 (a) N_2 adsorption–desorption isotherms and (b) pore size distribution of post-reaction N-Pr/SBA-15 and CoMo-N-Pr/SBA-15 catalysts.

VI.3.6 Discussion

In the literature, the high catalytic activity of Co_3Mo_3N in ammonia synthesis has been correlated to the presence of active crystallographic faces that contains both Co and Mo components resulting in optimal binding energy with N_2. Initially, the role of nitrogen was believed to be limited to the creation of the appropriate surface termination planes *(111)*. However, experimental work, enhanced by DFT-calculation, highlighted that Co_3Mo_3N might operate via the Mars-van Krevelen mechanism in which the lattice nitrogen in metal nitrides being the active species in ammonia synthesis. In this mechanism, lattice nitrogen is directly hydrogenated yielding ammonia and nitrogen lattice vacancy [43]. The nitrogen vacancy can afterwards activate molecular nitrogen to regenerates the active site. Furthermore, Zeinalipour-Yazdi *et al.* demonstrated via DFT computational study that Co_3Mo_3N contains a high concentration of nitrogen vacancies (1.6×10^{16} to 3.7×10^{16} cm^{-2}) that can adsorb and activate N_2 in conditions relevant to ammonia synthesis. Furthermore, Tsuji et al. reported enhanced catalytic activity of Co-Mo nanoparticles when supported on CeO_2. The better performance of Co-Mo/CeO_2 catalyst was explained on the basis of nitrogen vacancies more easily stabilized in the Co-Mo nanoparticles than in bulky Co_3Mo_3N crystals [25]. In this context, the generation of cobalt molybdenum nanoparticles is of high interest due to its high surface area to volume ratio and the high proportion of accessible surface atoms. In the current investigation, the XPS study indicates a close surface composition of the CoMo-N/SBA-15 to Co_3Mo_3N. However, strong disparities exist between Co_3Mo_3N and CoMo-N/SBA-15 in terms of structural and textural properties. For instance, all the catalysts showed high surface area with respect to the unsupported Co_3Mo_3N catalyst (up to 10 times higher). Furthermore, no XRD diffraction peaks where observed at high angle domain confirming the high dispersion of the active phase in SBA-15 structure. These finding are supported with TEM which reveals the formation of cobalt molybdenum nanoparticles stabilized within the mesopores of SBA-15. As demonstrated from the catalytic activity measurement, CoMo-N/SBA-15 displays an intrinsically high catalytic activity towards ammonia production (10-CoMo-N/SBA-15: 1714 $\mu mol\ g_{active\ phase}^{-1}\ h^{-1}$, 20-CoMo-N/SBA-15: $\mu mol\ g_{active\ phase}^{-1}\ h^{-1}$, and 30-CoMo-N/SBA-15: 810 $\mu mol\ g_{active\ phase}^{-1}\ h^{-1}$) when compared to the unsupported catalyst (298 $\mu mol\ g^{-1}\ h^{-1}$). The increase in reaction rates is seemingly consistent with the increase in accessible surface area and crystal size reduction observed by S/TEM. A parallel can be established with oxides (e.g. perovskite, hexaaluminate) operating via MvK mechanism, where previous studies, demonstrated an important increase in oxygen mobility with the decrease in crystal size leading to enhanced catalytic activities [44].

Furthermore, the mobility of lattice nitrogen and its reactivity in 10-CoMo-N/SBA-15 was confirmed under reducing conditions using 60 mL min^{-1} flow of 5 vol.% H_2: Ar. Upon reaction, ammonia production in the absence of dinitrogen, was confirmed at 400°C (Figure S9). Thus, the amount of ammonia produced can be directly linked to lattice nitrogen reacting with hydrogen. The process however, occurs in two steps, the first step suggesting the reduction of Co_3Mo_3N nanoparticle into Co_6Mo_6N as seen in the literature [45], followed by a second step transforming the reduced nitride into intermetallic phase. This mechanism is supported PXRD and HRTEM images coupled with EDS and FFT performed over post-reaction 10-CoMo-N/SBA-15 sample with evidence of formation of the intermetallic $Mo_{6.25}Co_{6.75}$ phase (PDF number: 04-018-9512) (Figure S10 and Table S4). The reduction process in the supported nitrides resulted in the formation of $Mo_{6.25}Co_{6.75}$ intermetallic phase, whereas unsupported Co_3Mo_3N was only reported to reduce to the Co_6Mo_6N, which might suggest that the lattice nitrogen mobility and reactivity is crystallite size dependent. This would be consistent with the improved catalytic activity of CoMo-N/SBA-15 catalysts operating via MvK mechanism. It is also noteworthy, that beyond the improvement of nitrogen mobility in nanoparticles, given the structure-sensitivity of ammonia synthesis reaction, the performance of CoMo-N/SBA-15 could also results from an increase the high proportion of accessible surface atoms and/or increases in steps and nitrogen defects in the surface.

VI.4 Conclusion

In summary, SBA-15 was found to be a robust support for ammonia synthesis reaction displaying good thermal and chemical stability under ammonolysis and ammonia synthesis reaction conditions. CoMo-N/SBA-15, with different loadings, was successfully prepared by two consecutive impregnation steps. The results of characterization demonstrate a high dispersion of metal nitrides within SBA-15 resulting in improved textural and structural properties. Although, changes in the local Si environment due to the formation of silyl-amine sites were evidenced by ^{29}Si and ^{1}H NMR upon ammonolysis, SBA-15 was found to be stable enough to maintain an ordered porous structure and high surface area ~504 m^2 g^{-1} for catalytic application. XPS analysis revealed that the surface composition of CoMo-N/SBA-15 catalysts is similar to the non-supported Co_3Mo_3N which is a paramount condition to develop high catalytic activity for ammonia synthesis. Because of their structural properties, i.e. a reduced crystal size and a high level of dispersion for the nitride phase, all CoMo-N/SBA-15 (10, 20 and 30 wt.%) displayed enhanced catalytic activity in ammonia synthesis (1714, 1429 and 810 µmol $g_{\text{active phase}}^{-1}$ h^{-1} respectively) with respect to the Co_3Mo_3N catalyst (298 µmol g_{catalyst}^{-1} h^{-1}).

The lattice nitrogen mobility and reactivity towards hydrogen in the supported CoMo-N/SBA-15 was also demonstrated under reducing condition, in the absence of dinitrogen, which indicative of ammonia synthesis occurring via mechanism similar to MvK. The enhanced catalytic activity originates probably from improving nitrogen mobility and/or alteration of the surface composition (*e.g.* vacancies concentrations, surface termination). The results reported in this work demonstrate that the performance of nitrides related catalyst can be greatly improved upon improving their textural and structural properties.

VI.5 References

[1] S. Giddey, S.P.S. Badwal, C. Munnings, M. Dolan, Ammonia as a Renewable Energy Transportation Media, ACS Sustainable Chemistry & Engineering, 5 (2017) 10231-10239.

[2] A. Klerke, C.H. Christensen, J.K. Nørskov, T. Vegge, Ammonia for hydrogen storage: challenges and opportunities, Journal of Materials Chemistry, 18 (2008) 2304-2310.

[3] K.-i. Aika, L. Christiansen, I. Dybkjaer, J. Hansen, P.H. Nielsen, A. Nielsen, P. Stoltze, K. Tamaru, Ammonia: catalysis and manufacture, Springer Science & Business Media2012.

[4] A. Mittasch, W. Frankenburg, Early Studies of Multicomponent Catalysts, in: W.G. Frankenburg, V.I. Komarewsky, E.K. Rideal (Eds.) Advances in Catalysis, Academic Press1950, pp. 81-104.

[5] I. Rafiqul, C. Weber, B. Lehmann, A. Voss, Energy efficiency improvements in ammonia production—perspectives and uncertainties, Energy, 30 (2005) 2487-2504.

[6] C. Smith, A.K. Hill, L. Torrente-Murciano, Current and future role of Haber–Bosch ammonia in a carbon-free energy landscape, Energy & Environmental Science, 13 (2020) 331-344.

[7] L.J. Christiansen, Thermodynamic Properties in Ammonia Synthesis, in: A. Nielsen (Ed.) Ammonia: Catalysis and Manufacture, Springer Berlin Heidelberg, Berlin, Heidelberg, 1995, pp. 1-15.

[8] J. Humphreys, R. Lan, S. Tao, Development and Recent Progress on Ammonia Synthesis Catalysts for Haber–Bosch Process, Advanced Energy and Sustainability Research, 2 (2021) 2000043.

[9] R. Kojima, K.-i. Aika, Cobalt Molybdenum Bimetallic Nitride Catalysts for Ammonia Synthesis, Chemistry Letters, 29 (2000) 514-515.

[10] C.J.H. Jacobsen, Novel class of ammonia synthesis catalysts, Chemical Communications, (2000) 1057-1058.

[11] C.J.H. Jacobsen, S. Dahl, B.S. Clausen, S. Bahn, A. Logadottir, J.K. Nørskov, Catalyst Design by Interpolation in the Periodic Table: Bimetallic Ammonia Synthesis Catalysts, Journal of the American Chemical Society, 123 (2001) 8404-8405.

[12] C.D. Zeinalipour-Yazdi, J.S.J. Hargreaves, C.R.A. Catlow, Nitrogen Activation in a Mars–van Krevelen Mechanism for Ammonia Synthesis on Co3Mo3N, The Journal of Physical Chemistry C, 119 (2015) 28368-28376.

[13] S.M. Hunter, D.H. Gregory, J.S.J. Hargreaves, M. Richard, D. Duprez, N. Bion, A Study of 15N/14N Isotopic Exchange over Cobalt Molybdenum Nitrides, ACS Catalysis, 3 (2013) 1719-1725.

[14] A. Daisley, L. Costley-Wood, J.S.J. Hargreaves, The Role of Composition and Phase upon the Lattice Nitrogen Reactivity of Ternary Molybdenum Nitrides, Topics in Catalysis, 64 (2021) 1021-1029.

[15] C.D. Zeinalipour-Yazdi, J.S.J. Hargreaves, S. Laassiri, C.R.A. Catlow, The integration of experiment and computational modelling in heterogeneously catalysed ammonia synthesis over metal nitrides, Physical Chemistry Chemical Physics, 20 (2018) 21803-21808.

[16] S. Laassiri, C.D. Zeinalipour-Yazdi, C.R.A. Catlow, J.S.J. Hargreaves, Nitrogen transfer properties in tantalum nitride based materials, Catalysis Today, 286 (2017) 147-154.

[17] X. Wang, M. Su, H. Zhao, Process design and exergy cost analysis of a chemical looping ammonia generation system using AlN/Al2O3 as a nitrogen carrier, Energy, 230 (2021) 120767.

[18] R. Michalsky, A.M. Avram, B.A. Peterson, P.H. Pfromm, A.A. Peterson, Chemical looping of metal nitride catalysts: low-pressure ammonia synthesis for energy storage, Chemical Science, 6 (2015) 3965-3974.

[19] M.E. Gálvez, M. Halmann, A. Steinfeld, Ammonia Production via a Two-Step Al2O3/AlN Thermochemical Cycle. 1. Thermodynamic, Environmental, and Economic Analyses, Industrial & Engineering Chemistry Research, 46 (2007) 2042-2046.

[20] R. Michalsky, P.H. Pfromm, A. Steinfeld, Rational design of metal nitride redox materials for solar-driven ammonia synthesis, Interface Focus, 5 (2015) 20140084.

[21] S. Laassiri, N. Bion, D. Duprez, H. Alamdari, S. Royer, Role of Mn+ cations in the redox and oxygen transfer properties of BaMxAl12−xO19−δ (M = Mn, Fe, Co) nanomaterials for high temperature methane oxidation, Catalysis Science & Technology, 3 (2013) 2259-2269.

[22] S. Laassiri, C.D. Zeinalipour-Yazdi, N. Bion, C.R.A. Catlow, J.S.J. Hargreaves, Combination of theoretical and in situ experimental investigations of the role of lithium dopant

in manganese nitride: a two-stage reagent for ammonia synthesis, Faraday Discussions, 229 (2021) 281-296.

[23] I.B. Parker, K.C. Waugh, M. Bowker, On the structure sensitivity of ammonia synthesis on promoted and unpromoted iron, Journal of Catalysis, 114 (1988) 457-459.

[24] Z. Song, T. Cai, J.C. Hanson, J.A. Rodriguez, J. Hrbek, Structure and Reactivity of Ru Nanoparticles Supported on Modified Graphite Surfaces: A Study of the Model Catalysts for Ammonia Synthesis, Journal of the American Chemical Society, 126 (2004) 8576-8584.

[25] Y. Tsuji, K. Ogasawara, M. Kitano, K. Kishida, H. Abe, Y. Niwa, T. Yokoyama, M. Hara, H. Hosono, Control of nitrogen activation ability by Co-Mo bimetallic nanoparticle catalysts prepared via sodium naphthalenide-reduction, Journal of Catalysis, 364 (2018) 31-39.

[26] H. Lin, X. Zhong, C. Ciotonea, X. Fan, X. Mao, Y. Li, B. Deng, H. Zhang, S. Royer, Efficient degradation of clofibric acid by electro-enhanced peroxydisulfate activation with Fe-Cu/SBA-15 catalyst, Applied Catalysis B: Environmental, 230 (2018) 1-10.

[27] A. Ungureanu, B. Dragoi, A. Chirieac, C. Ciotonea, S. Royer, D.A. Duprez, A.S. Mamede, E. Dumitriu, Composition-dependent morphostructural properties of Ni-Cu oxide nanoparticles confined within the channels of ordered mesoporous SBA-15 silica, ACS applied materials & interfaces, 5 8 (2013) 3010-3025.

[28] P. Raval, J. Trébosc, T. Pawlak, Y. Nishiyama, S.P. Brown, G.N. Manjunatha Reddy, Combining heteronuclear correlation NMR with spin-diffusion to detect relayed Cl–H–H and N–H–H proximities in molecular solids, Solid State Nuclear Magnetic Resonance, 120 (2022) 101808.

[29] B. Singh, K.R. Mote, C.S. Gopinath, P.K. Madhu, V. Polshettiwar, SBA-15-Oxynitrides as a Solid-Base Catalyst: Effect of Nitridation Temperature on Catalytic Activity, Angewandte Chemie International Edition, 54 (2015) 5985-5989.

[30] P.M. Rewatkar, T. Taghvaee, A.M. Saeed, S. Donthula, C. Mandal, N. Chandrasekaran, T. Leventis, T.K. Shruthi, C. Sotiriou-Leventis, N. Leventis, Sturdy, Monolithic SiC and Si3N4 Aerogels from Compressed Polymer-Cross-Linked Silica Xerogel Powders, Chemistry of Materials, 30 (2018) 1635-1647.

[31] T. Asefa, M. Kruk, N. Coombs, H. Grondey, M.J. MacLachlan, M. Jaroniec, G.A. Ozin, Novel Route to Periodic Mesoporous Aminosilicas, PMAs: Ammonolysis of Periodic

Mesoporous Organosilicas, Journal of the American Chemical Society, 125 (2003) 11662-11673.

[32] B. Grünberg, T. Emmler, E. Gedat, I. Shenderovich, G.H. Findenegg, H.-H. Limbach, G. Buntkowsky, Hydrogen Bonding of Water Confined in Mesoporous Silica MCM-41 and SBA-15 Studied by 1H Solid-State NMR, Chemistry – A European Journal, 10 (2004) 5689-5696.

[33] S. Lang, M. Benz, U. Obenaus, R. Himmelmann, M. Scheibe, E. Klemm, J. Weitkamp, M. Hunger, Mechanisms of the AlCl3 Modification of Siliceous Microporous and Mesoporous Catalysts Investigated by Multi-Nuclear Solid-State NMR, Topics in Catalysis, 60 (2017) 1537-1553.

[34] Z. Li, C. Rieg, A.-K. Beurer, M. Benz, J. Bender, C. Schneck, Y. Traa, M. Dyballa, M. Hunger, Effect of aluminum and sodium on the sorption of water and methanol in microporous MFI-type zeolites and mesoporous SBA-15 materials, Adsorption, 27 (2021) 49-68.

[35] Y. Sun, L. Wang, O. Guselnikova, O. Semyonov, J. Fraser, Y. Zhou, N. López, A.Y. Ganin, Revealing the activity of Co3Mo3N and Co3Mo3N0.5 as electrocatalysts for the hydrogen evolution reaction, Journal of Materials Chemistry A, 10 (2022) 855-861.

[36] L. Wang, S. Zhao, Y. Liu, D. Liu, J.M. Razal, W. Lei, Interfacial Engineering of 3D Hollow Mo-Based Carbide/Nitride Nanostructures, ACS Applied Materials & Interfaces, 13 (2021) 50524-50530.

[37] M.C. Biesinger, B.P. Payne, A.P. Grosvenor, L.W.M. Lau, A.R. Gerson, R.S.C. Smart, Resolving surface chemical states in XPS analysis of first row transition metals, oxides and hydroxides: Cr, Mn, Fe, Co and Ni, Applied Surface Science, 257 (2011) 2717-2730.

[38] J.A. Rodriguez, S. Chaturvedi, J.C. Hanson, J.L. Brito, Reaction of H2 and H2S with CoMoO4 and NiMoO4: TPR, XANES, Time-Resolved XRD, and Molecular-Orbital Studies, The Journal of Physical Chemistry B, 103 (1999) 770-781.

[39] J.A. Rodriguez, J.Y. Kim, J.C. Hanson, J.L. Brito, Reduction of CoMoO4 and NiMoO4: in situ Time-Resolved XRD Studies, Catalysis Letters, 82 (2002) 103-109.

[40] E. Van Steen, G.S. Sewell, R.A. Makhothe, C. Micklethwaite, H. Manstein, M. De Lange, C.T. O'Connor, TPR study on the preparation of impregnated Co/SiO2 catalysts, Journal of Catalysis, 162 (1996) 220-229.

[41] R. Kojima, K.-i. Aika, Cobalt molybdenum bimetallic nitride catalysts for ammonia synthesis: Part 1. Preparation and characterization, Applied Catalysis A: General, 215 (2001) 149-160.

[42] J.S.J. Hargreaves, D. McKay, A comparison of the reactivity of lattice nitrogen in Co3Mo3N and Ni2Mo3N catalysts, Journal of Molecular Catalysis A: Chemical, 305 (2009) 125-129.

[43] T.-N. Ye, S.-W. Park, Y. Lu, J. Li, M. Sasase, M. Kitano, H. Hosono, Contribution of Nitrogen Vacancies to Ammonia Synthesis over Metal Nitride Catalysts, Journal of the American Chemical Society, 142 (2020) 14374-14383.

[44] S. Laassiri, N. Bion, D. Duprez, S. Royer, H. Alamdari, Clear microstructure–performance relationships in Mn-containing perovskite and hexaaluminate compounds prepared by activated reactive synthesis, Physical Chemistry Chemical Physics, 16 (2014) 4050-4060.

[45] S.M. Hunter, D. McKay, R.I. Smith, J.S.J. Hargreaves, D.H. Gregory, Topotactic Nitrogen Transfer: Structural Transformation in Cobalt Molybdenum Nitrides, Chemistry of Materials, 22 (2010) 2898-2907.

VI.6 Supplementary information

Figure S1 SAXS diffractogram of SBA-15 (a) after calcination, (b) after ammonolysis, and (c) after ammonia synthesis reaction.

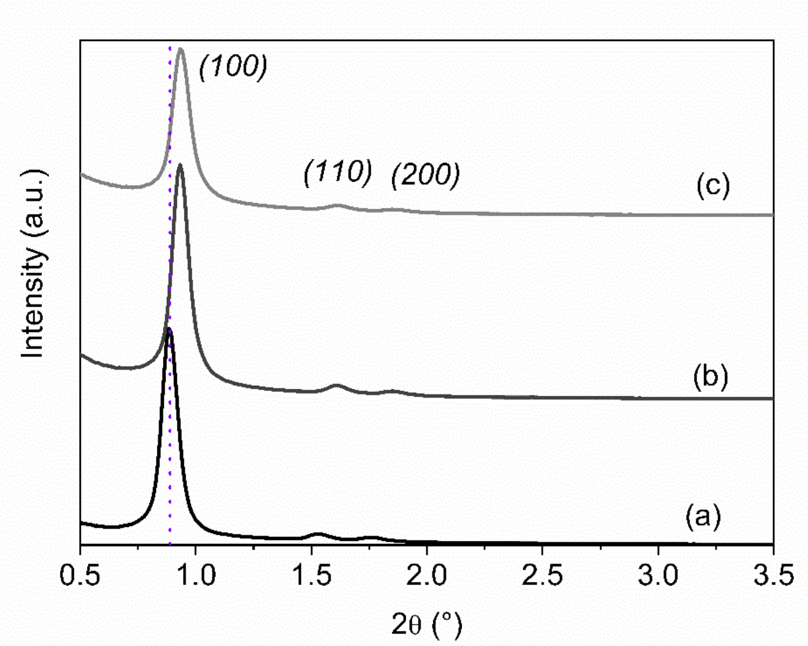

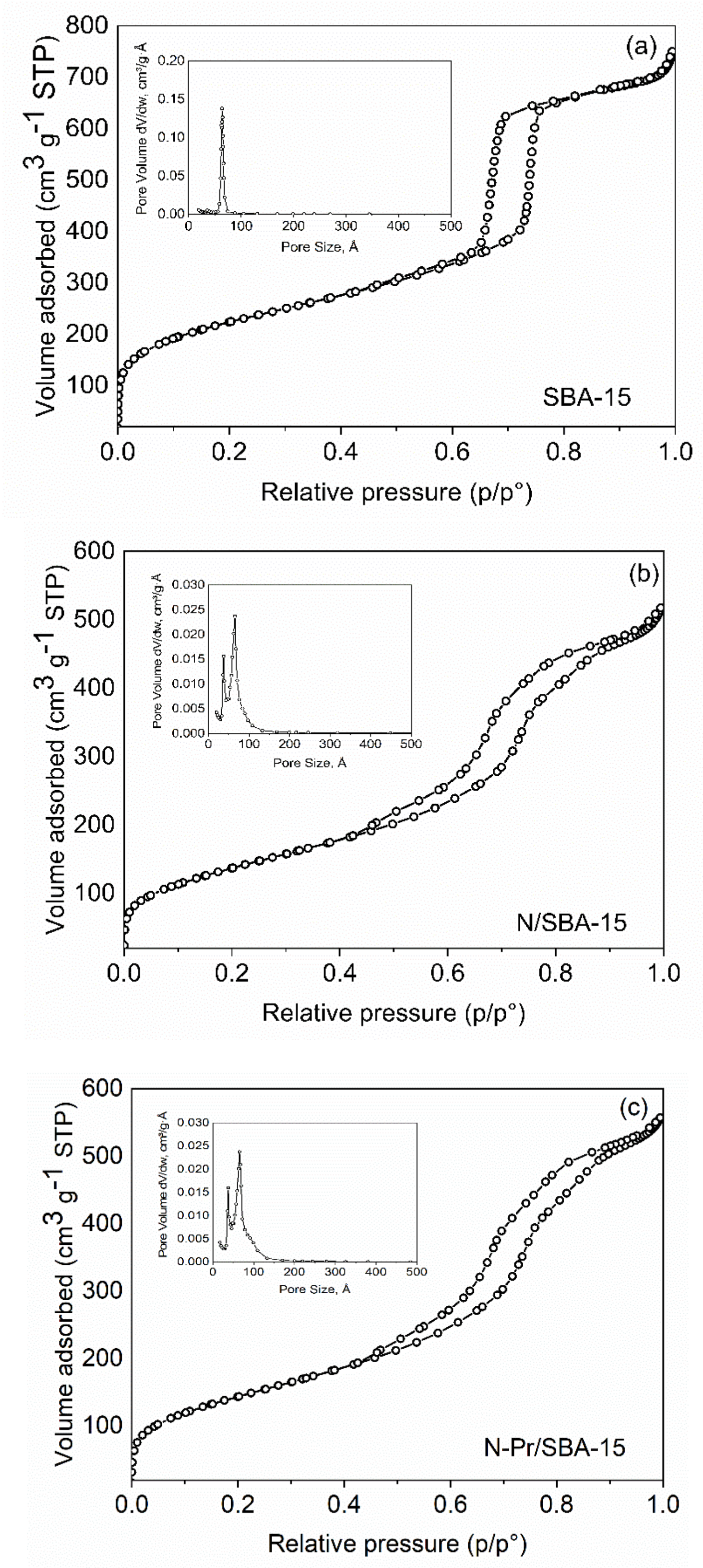

Figure S2 N_2 adsorption/desorption isotherms and pore size distribution of SBA-15. (a) after calcination, (b) N/SBA-15: after ammonolysis, and (c) N-Pr/SBA-15: post-reaction.

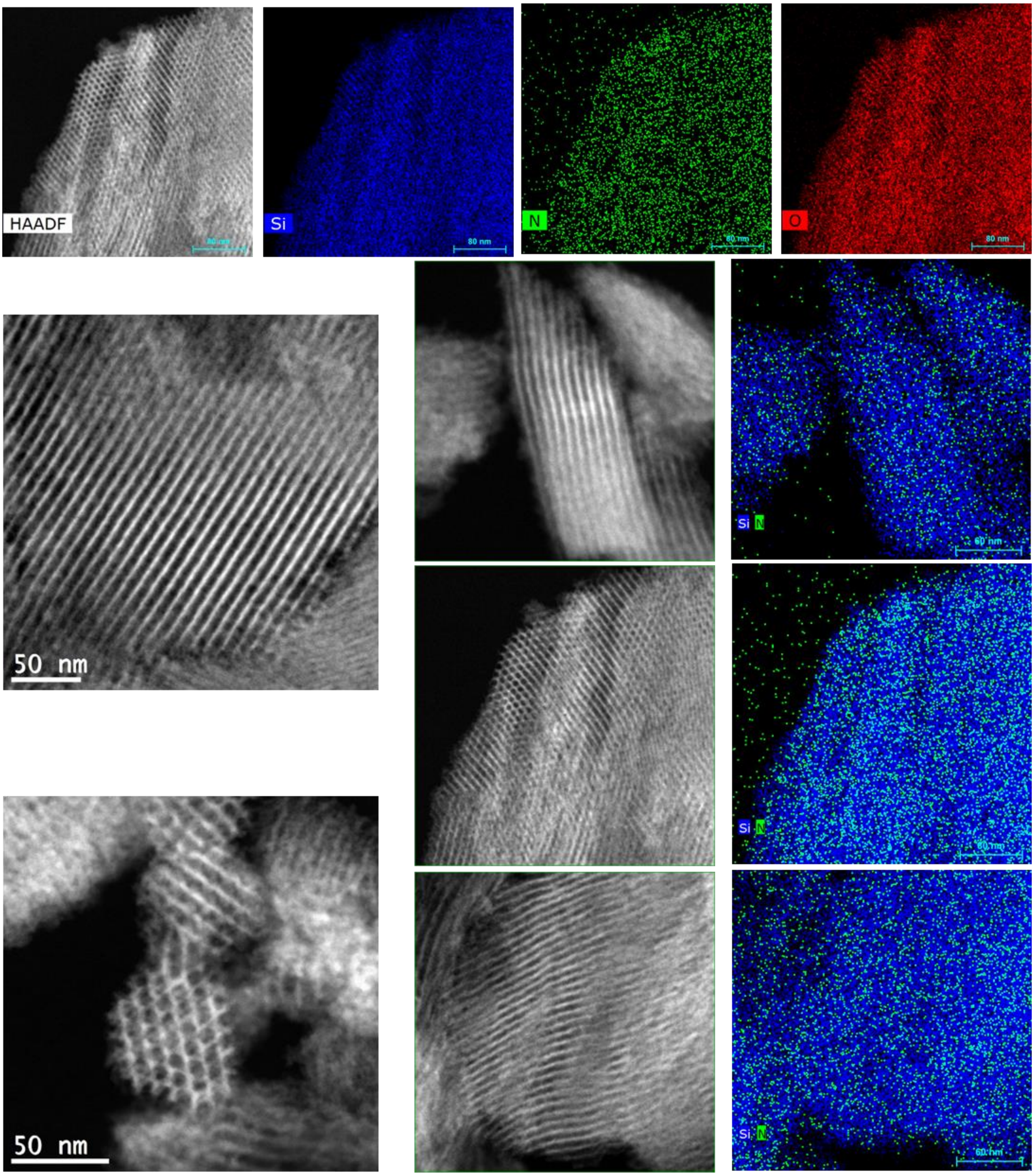

Figure S3 Representatives HAADF micrograph of N/SBA-15 coupled with EDS for chemical analysis

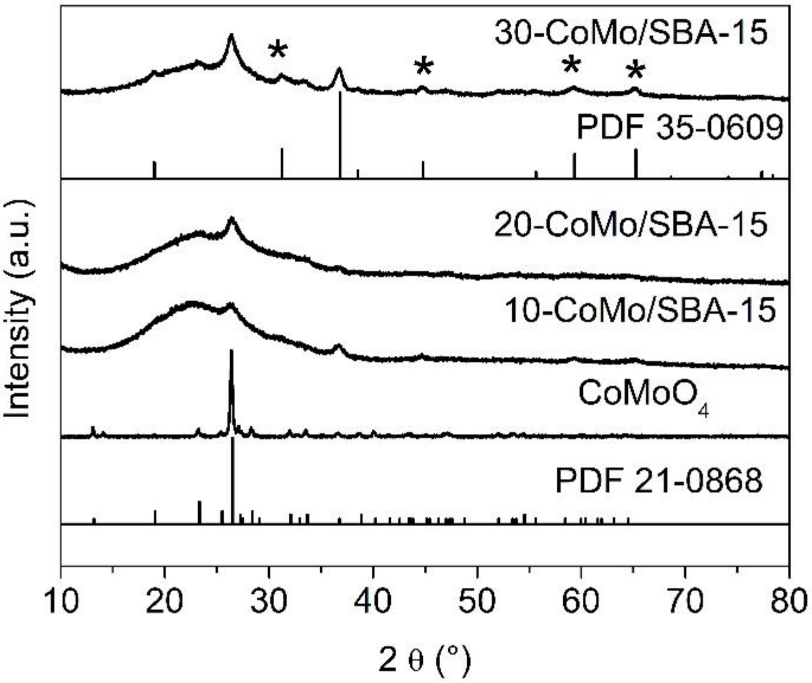

Figure S4 Wide angle PXRD patterns of $CoMoO_4$ and supported CoMo/SBA-15 with different loading after the calcination step

For all the supported materials, a typical broad XRD peak of amorphous silica at 2θ ~ 24° is observed. In addition to the characteristic XRD signature of SBA-15, an XRD reflection peak at 2θ ~ 26° that can be attributed to $CoMoO_4$ phase is also detected for all CoMo/SBA-15 loadings (10, 20 and 30 wt.%). The low intensity of these peaks suggests that the CoMoO4 phase is well dispersed over the support. However, at high CoMo loading (30-CoMo/SBA-15), additional XRD diffraction peaks appear at 2θ ~ 31.3°, 36.8°, and 44.8°. These peaks are characteristic of a Co_3O_4 spinel phase (PDF 35-0609) indicating phase segregation.

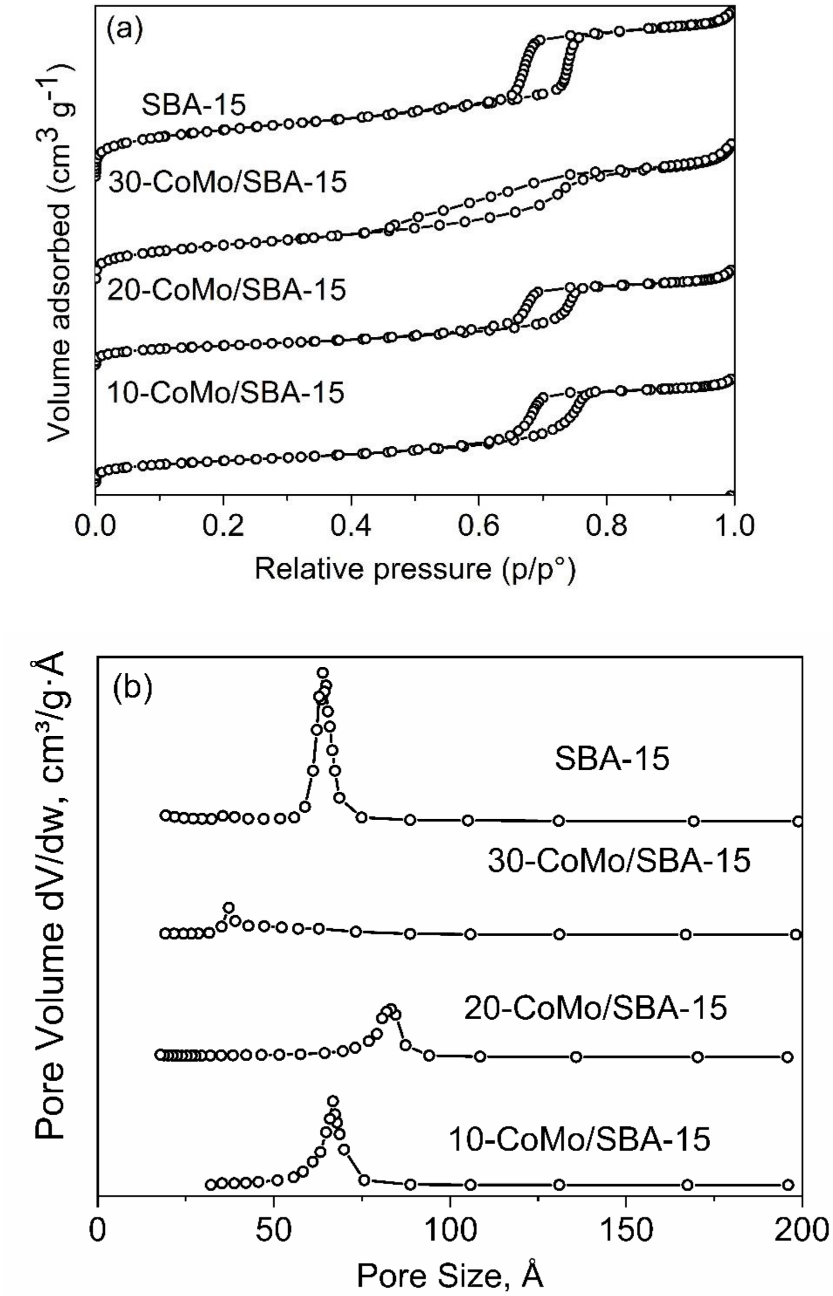

Figure S5 (a) N_2 adsorption/desorption isotherms and (b) pore size distribution of SBA-15 and CoMo/SBA-15 catalysts with different amounts of metal loading after the calcination step

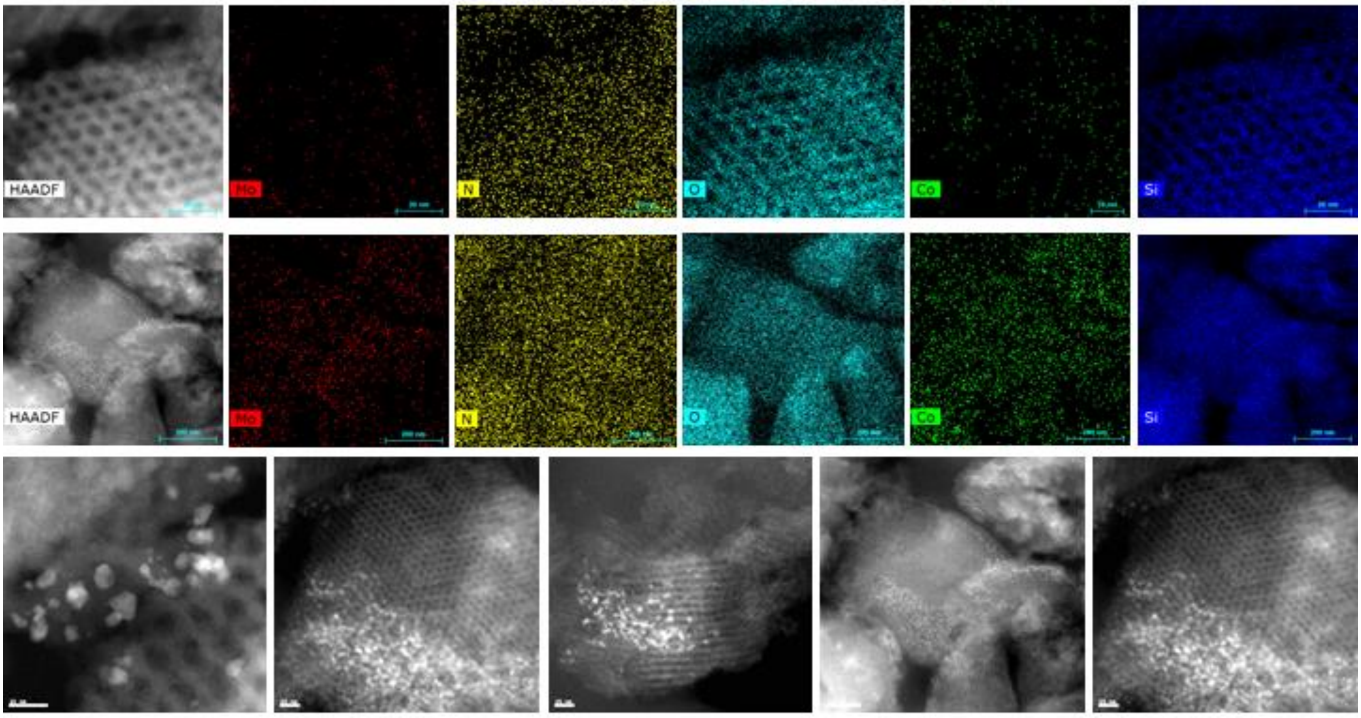

Figure S6-a representatives HAADF-STEM micrograph of 10-CoMo-N/SBA15 coupled with EDS for chemical analysis

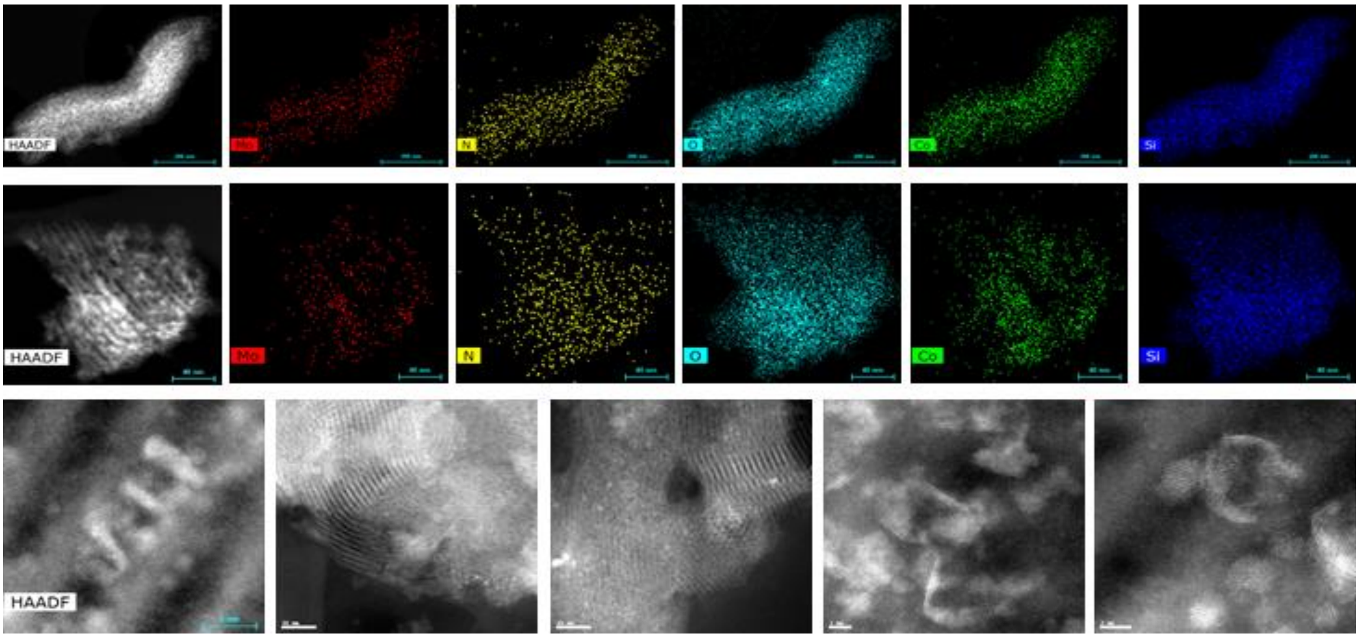

Figure S6-b representatives HAADF-STEM micrograph of 20-CoMo-N/SBA15 coupled with EDS for chemical analysis

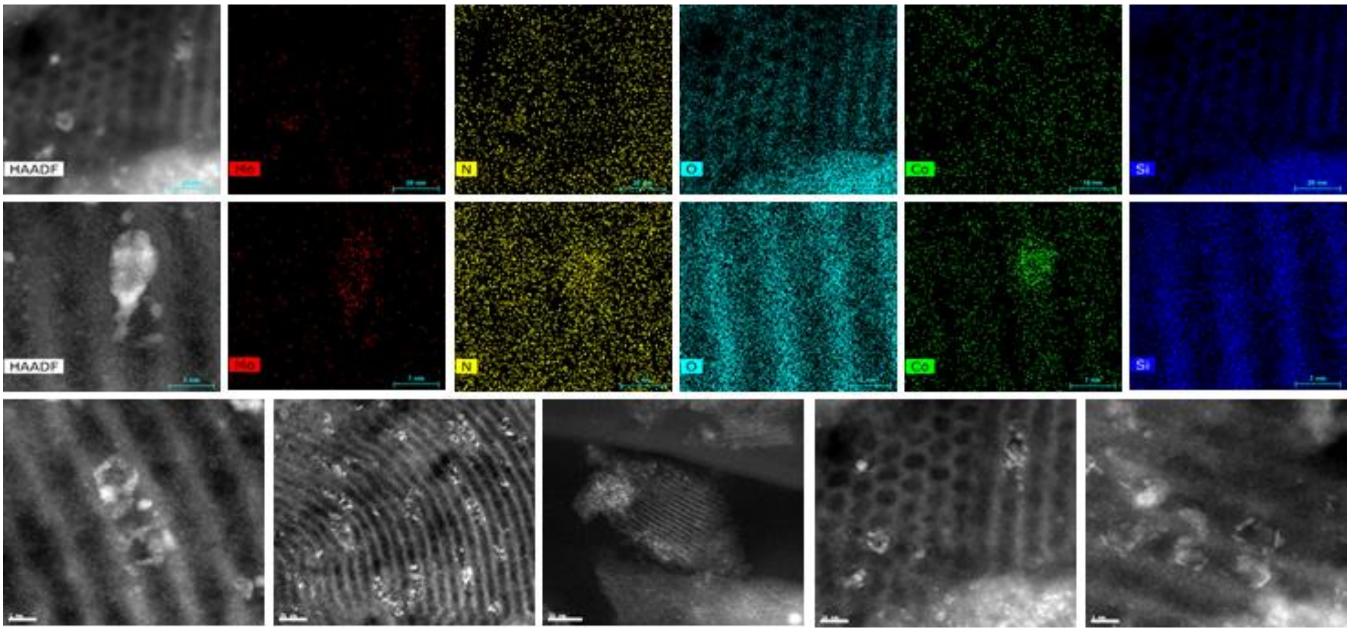

Figure S6-c representatives HAADF-STEM micrograph of 30-CoMo-N/SBA15 coupled with EDS for chemical analysis

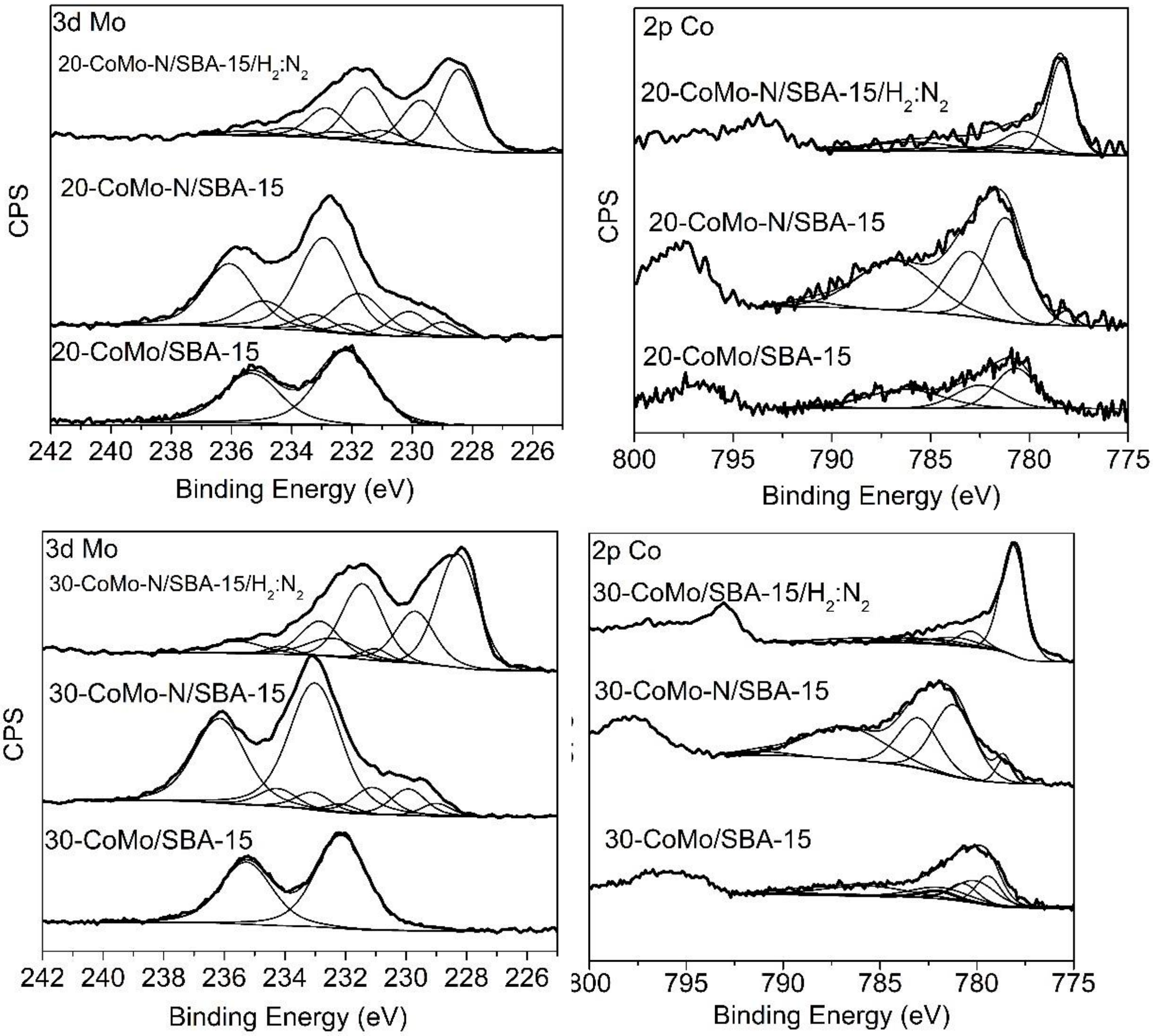

Figure S7 High resolution XPS spectra in the Mo 3d region and Co 2p region for 20-CoMo/SBA-15 and 30-CoMo/SBA-15

Table S1. Position of Mo peaks of unsupported and supported CoMo-N/SBA-15 at different synthesis steps

	Mo Peaks								**Surface Composition**			
	Mo^{6+}		**Mo^{5+}**		**Mo^{4+}**		**Mo-N**		**Mo^{6+}**	**Mo^{5+}**	**Mo^{4+}**	**Mo-N**
	$3d_{5/2}$	$3d_{3/2}$	$3d_{5/2}$	$3d_{3/2}$	$3d_{5/2}$	$3d_{3/2}$	$3d_{5/2}$	$3d_{3/2}$	(%)	(%)	(%)	(%)
$CoMoO_4$	232.50	235.60	-	-	-	-	-	-	100	-	-	-
Co_3Mo_3N	232.43	235.57	231.00	234.14	229.70	232.84	228.23	231.37	38.64	5.35	22.52	33.49
Co_3Mo_3N-PT*			-	-	229.35	232.49	228.59	231.73		-	32.82	67.18
10-CoMo/SBA-15	232.96	235.10	-	-	-	-	-	-	100	-	-	-
10-CoMo-N/SBA-15	233.00	236.14	231.49	234.63	230.08	233.22	229.00	232.14	56.35	23.69	11.77	8.19
10-CoMo-N/SBA-15*	232.74	235.88	231.00	234.14	229.70	232.84	228.38	231.52	7.74	12.32	30.58	49.36
20-CoMo/SBA-15	232.20	235.35	-	-	-	-	-	-	100	-	-	-
20-CoMo-N/SBA-15	232.92	236.06	231.77	234.91	230.1	233.24	229.00	232.14	59.27	24.28	11.66	4.79
20-CoMo-N/SBA-15*	232.43	235.57	231.00	234.14	229.7	232.84	228.29	231.43	12.99	4.3	27.5	55.21
30-CoMo/SBA-15	232.13	235.27	-	-	-	-	-	-	100	-	-	-
30-CoMo-N/SBA-15	233.00	236.40	231.10	234.24	229.92	233.06	229.0	232.14	74.21	11.55	10.46	3.78
30-CoMo-N/SBA-15*	232.43	235.57	231.00	234.14	229.7	232.84	228.29	231.43	12.98	4.29	27.5	55.23

* catalyst subject to pre-treatment under reaction condition at 700°C for 2h in environmental XPS chamber before analysis

Table S2. Position of Co peaks of unsupported and supported CoMo nitride materials at each synthesis step

	Co peaks							**Surface composition**	
	Co^{2+} 2p$_{3/2}$	**Co^{2+}** 2p$_{3/2}$	**Co^{2+}** 2p$_{3/2}$	**Co^{2+}** 2p$_{3/2}$	**Co-N** 2p$_{3/2}$	**Co-N** 2p$_{3/2}$	**Co-N** 2p$_{3/2}$	**Co^{2+}** (%)	**Co-N** (%)
$CoMoO_4$	781.20	783.00	786.79	791.19	-	-	-	100	-
Co_3Mo_3N	780.71	782.51	786.30	790.70	778.30	781.30	783.30	81.58	18.43
Co_3Mo_3N-PT*					778.88	781.88	783.88		100
10-CoMo/SBA-15	780.7	782.50	786.29	790.69	-	-	-	100	-
10-CoMo-N/SBA-15	781.20	783.0	786.79	791.19	778.60	781.60	783.60	97.25	2.75
10-CoMo-N/SBA-15*	780.30	782.10	785.89	790.29	778.26	781.26	783.26	50.2	49.8
20-CoMo/SBA-15	780.7	782.50	786.29	790.69	-	-	-	100	-
20-CoMo-N/SBA-15	781.20	783.0	786.79	791.19	778.15	781.15	783.15	97.49	2.51
20-CoMo-N/SBA-15*	780.30	782.10	785.89	790.29	778.39	781.39	783.39	44.62	55.38
30-CoMo/SBA-15	780.1	781.9	785.69	790.09	-	-	-	57.99**	-
30-CoMo-N/SBA-15	781.20	783.0	786.79	791.19	778.60	781.60	783.60	94.39	5.61
30-CoMo-N/SBA-15*	780.30	782.10	785.89	790.29	778.13	781.13	783.13	24.12	75.88

* catalyst subject to pre-treatment under reaction condition at 700°C for 2h in environmental XPS chamber before analysis

** 42.0% of the surface composition of Co was in the form of Co_3O_4

Table S3. Reducibility of CoMo/SBA-15

Catalyst	**H_2 consumption (mmol/g)**
$CoMoO_4$	13.72
10-CoMo/SBA-15	2.18
20-CoMo/SBA-15	2.95
30-CoMo/SBA-15	5.05

Table S4. d spacing and corresponding hkl planes observed by TEM coupled with FFT on 10-CoMo-N/SBA-15 upon 48 h of reaction with 60 mL.min^{-1} of a 5% H_2/Ar mixture at 400°C and ambient pressure

d- spacing (Å) observed	d- spacing (Å) standard*	2 θ	I fix	*(h k l)*
2.38	2.3880	37.637	811	*(1 1 0)*
2.30	2.30028	39.130	7	*(1 1 3)*
2.03	2.03408	44.506	462	*(0 1 11)*
1.90	1.91857	47.344	293	*(2 0 5)*
1.20	1.19400	80.353	177	*(2 2 0)*

* intermetallic $Mo_{6.25}Co_{6.75}$ (PDF number: 04-018-9512)

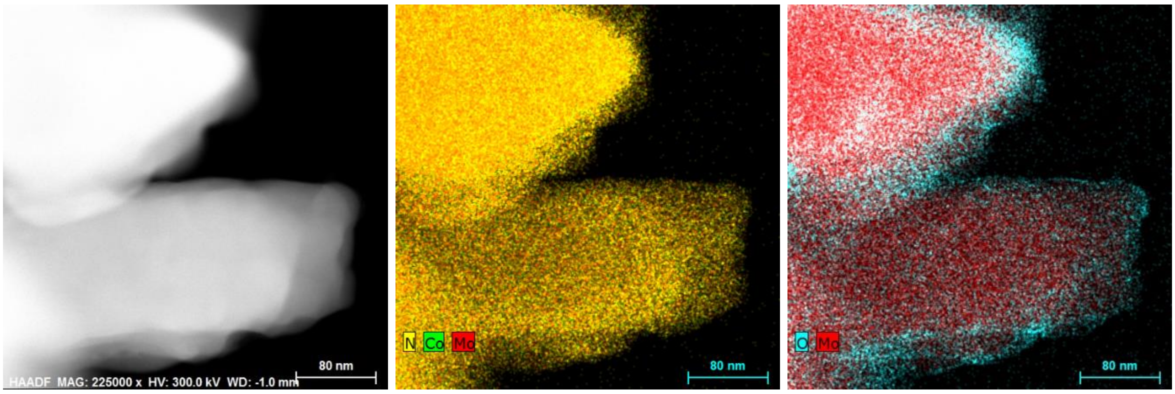

Figure S8 Representative HAADF-STEM micrographs of Co_3Mo_3N coupled with EDS for elemental analysis (Light blue: O ; Green: Co ; Yellow: N ; Red: Mo)

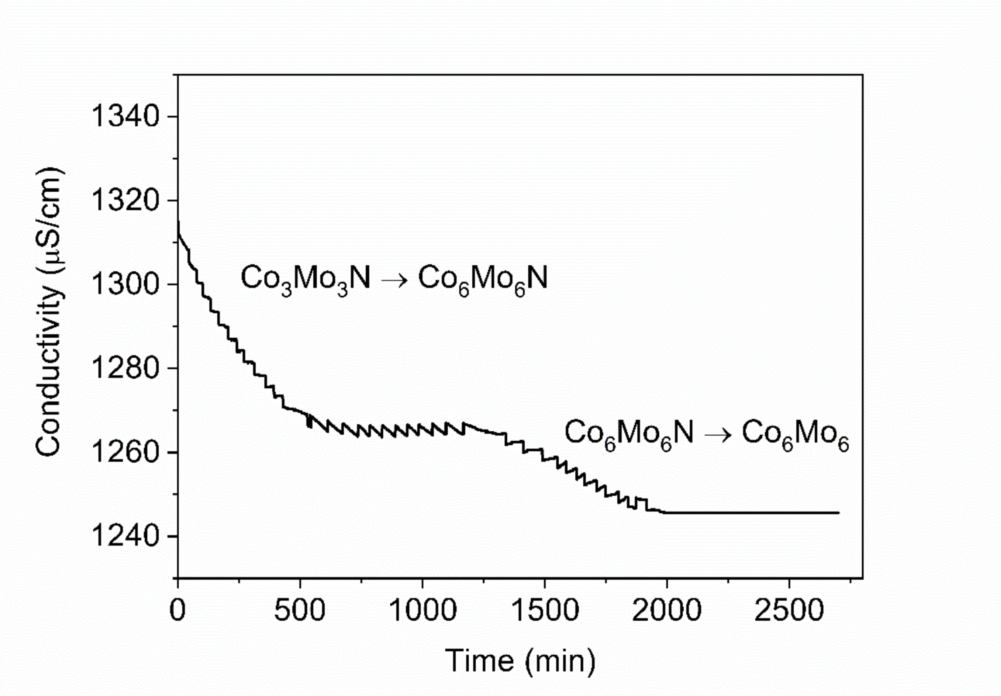

Figure S9 Ammonia production rate of 10-CoMo-N/SBA-15 reacted with 60 mL.min^{-1} of a 5% H_2/Ar mixture at 400°C and ambient pressure

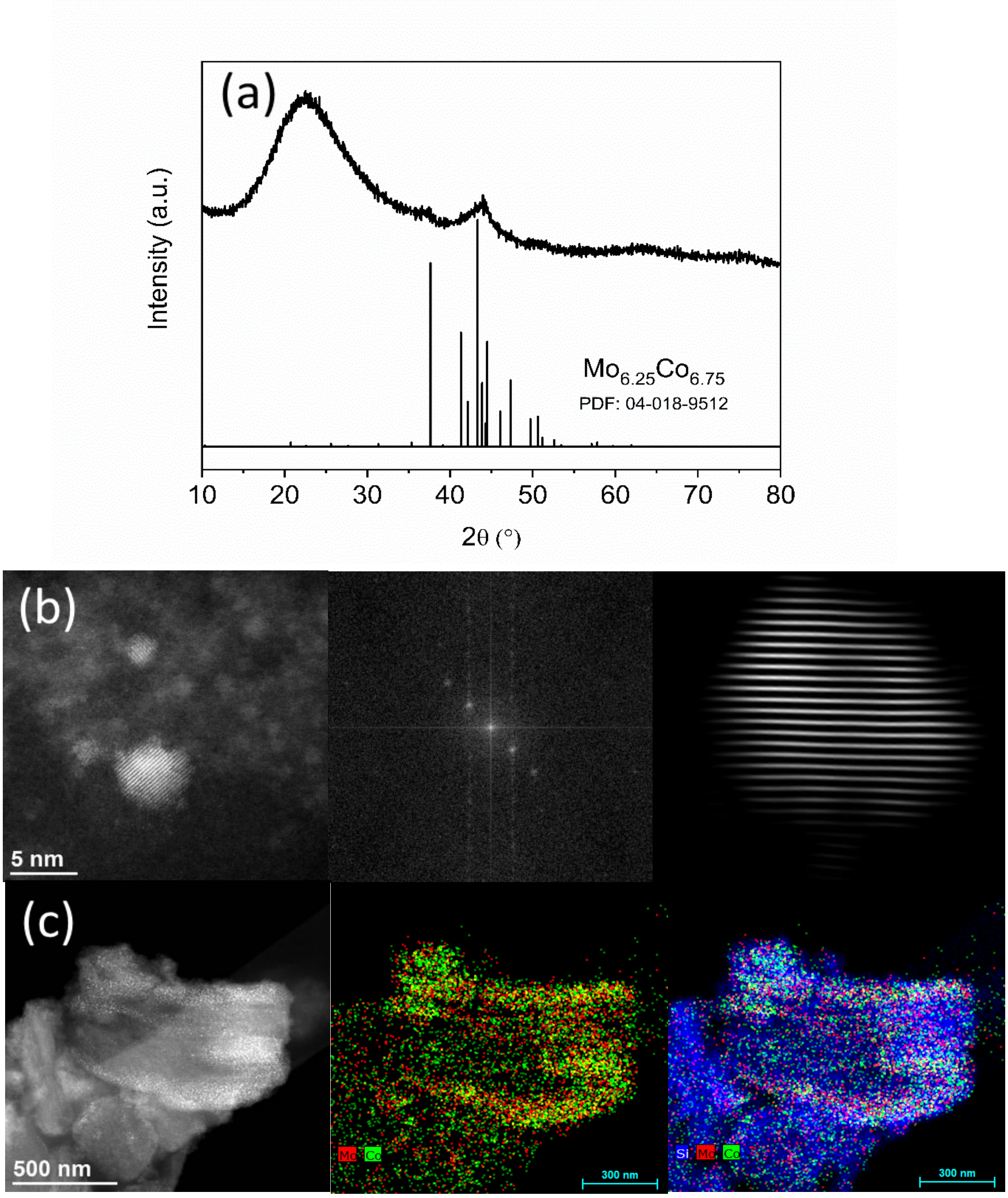

Figure S10 Post-reaction catalyst 10-CoMo-N/SBA-15 after 48 h of reaction with 60 mL.min^{-1} of a 5% H_2/Ar mixture at 400°C and ambient pressure (a) XRD pattern (b) FFT image indicating the (1 1 0) plane (c) HAADF image coupled with EDS

VII. Chapter VI: MXenes for ammonia synthesis

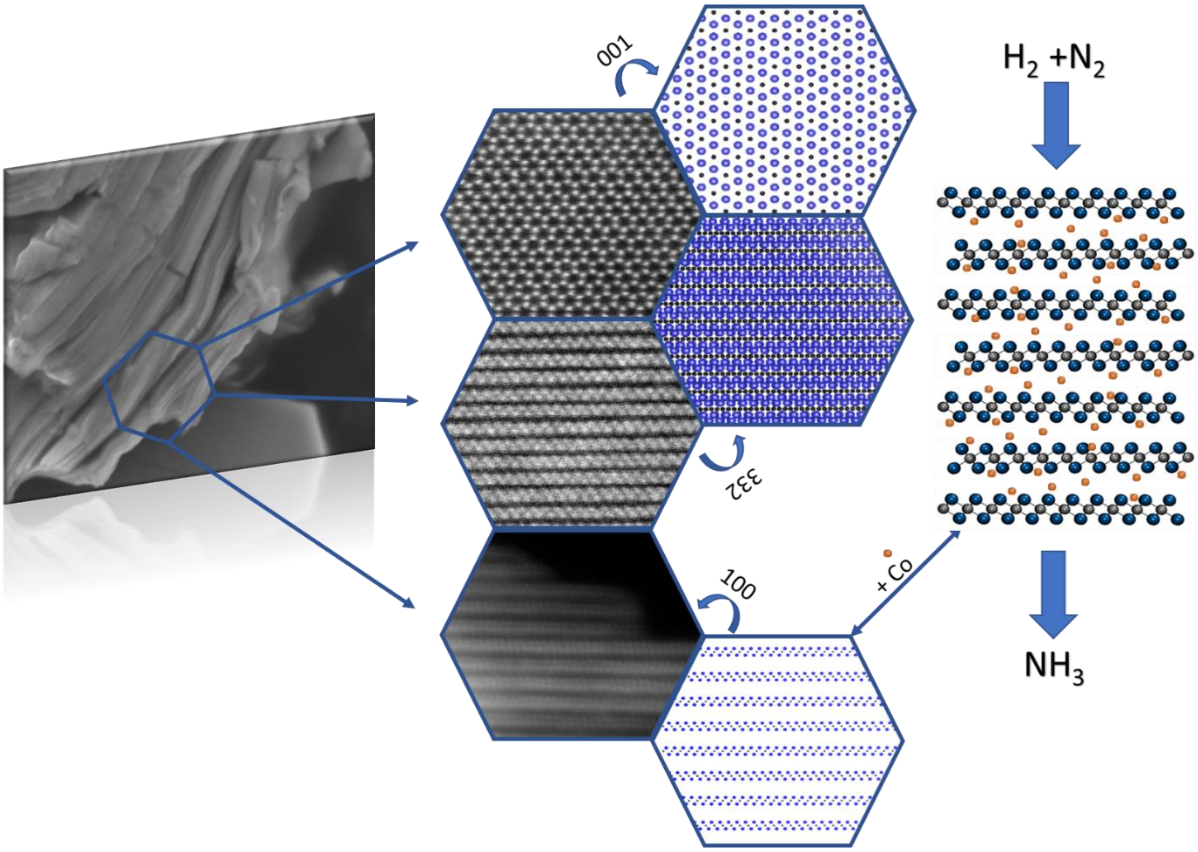

Transition metal decorated MXene: a novel low temperature catalyst for ammonia synthesis

Amanda Sfeir[1], Christopher Shuck[2], Alexandre Fadel[3], Maya Marinova[3], Axel Löfberg[1], Jean-Philippe Dacquin[1], Yury Gogotsi,[2*] Sébastien Royer,[1*] Said Laassiri[4*]

[1] Université de Lille, CNRS, ENSCL, Centrale Lille, Univ. Artois, UMR 8181-UCCS-Unité de Catalyse et de Chimie du Solide, F-59000 Lille, France.

[2] A.J. Drexel Nanomaterials Institute and Department of Materials Science and Engineering, Drexel University, Philadelphia, PA 19104, USA.

[3] Université de Lille, CNRS, INRA, Centrale Lille, Université Artois, FR 2638 – IMEC – Institut Michel-Eugène Chevreul, 59000 Lille, France.

[4] Chemical & Biochemical Sciences, Green Process Engineering (CBS), Mohammed VI Polytechnic University, UM6P, 43150, Benguerir, Morocco.

* Corresponding authors: sebastien.royer@univ-lille.fr, gogotsi@drexel.edu, said.laassiri@um6p.ma

VII.1 Introduction

The performance of ammonia synthesis catalysts and the reaction mechanisms are dictated by the complex interaction of the catalyst surface with reactants (N_2 and H_2), intermediates species (NH_x) and reaction products (NH_3) [5-8]. As such, modulating the electronic states of the active sites either by (i) doping with elements with strong electron donation properties such as alkaline or alkaline earth materials, (ii) allowing with transition metal and/or (ii) by controlling support-active site interaction is of paramount importance to improve the catalytic activity and stability at lower temperature. Co-based catalysts serve as excellent examples of how fine-tuning the properties of the active sites can lead to a notable improvement in the performance of ammonia synthesis. Undoped and unsupported Co does not exhibit a significant catalytic activity in ammonia synthesis due to the limited affinity of cobalt to N_2 (small adsorption energy) [5, 9]. Combining Co with various transition metals (*i.e.* Mo, Fe, Re) was one of the first strategies to modulate the catalytic performance in ammonia synthesis [10-13]. Among these combinations, the association of Co with Mo in Co_3Mo_3N resulted in substantial increases in ammonia synthesis when compared to the activity expressed by individual components (ammonia synthesis rate of 330 - 652 μmol h^{-1} g^{-1} at 400 °C and atmospheric pressure, WHSV 9 000 mL g^{-1} h^{-1}) [14, 15]. The high catalytic activity of Co_3Mo_3N was previously explained as results of Co and Mo being both present in the termination plan *(111)* which lead to an optimal N-binding energy [5]. However, new insight from DFT calculations and $^{15}N/^{14}N$ isotopic exchange studies have highlighted the potential role of nitride lattice nitrogen in ammonia synthesis via routes akin to the Mars-van Krevelen (MvK) mechanism [16-18]. Promoting the catalytic activity of Co throughout doping with alkaline earth metals such as Ba and La has also been reported as an effective strategy. For instance, the addition of Ba to carbon-supported cobalt catalyst was found to strongly promote the catalytic activity with respect to non-promoted Co/C catalyst by more than 2 orders of magnitude [19, 20]. A strong decrease in the apparent activation energy from 149 to 102 kJ mol^{-1} upon Ba doping was reported.[19] A similar promotional effect of BaO on cobalt nanoparticles, supported on MgO, has been reported by Sato *et al*. [21] The activation of the N≡N, which is the rate-determining step in the synthesis of ammonia conventionally, was found to be facilitated by strong electron donation from BaO to surface Co atoms. The utilization of non-oxidic form of Ba such as barium hydride (BaH_2) proved to be as well a very efficient route for promoting the catalytic activity of Co at low temperature [22]. In this case, BaH_2 was suggested to play an active role in ammonia synthesis, as a second active center, rather than electronic or structural promoter.

The results of the kinetic studies implied that the presence of BaH_2 strongly affect the reaction mechanism and possibly shift the rate determining step from N_2 dissociation to other steps [22]. Similar to BaH_2, LiH was found to act as a second catalytic sites resulting an improved catalytic activity of Co [23]. The effect of support has been also evidenced in tuning the catalytic properties of Co. Interestingly, electride based-supports characterized by strong electron donation properties and low work function (2.4 eV), enhanced drastically the catalytic activity of Co.[24] Co/$2CaO\cdot7Al_2O_3$ displayed low apparent activation energy ~ 50 kJ mol^{-1} and ammonia generation was detected at temperatures as low as 200°C. Likewise, the effect of different supports such as CeO_2, $BaTiO_{3-x}H_x$, $BaCeO_{3-x}N_yH_z$, Ba-$Ca(NH_2)_2$ in modulating the electronic state of Co favourably to promote ammonia synthesis has been studied in the literature.[25-27] These results clearly demonstrate the importance of modulating cobalt electronic states, through electron transfer from dopants and/or support, leading to high catalytic activity at low temperature. While supporting cobalt on emerging materials such as electrides, hydrides, amides, nitrides, and oxynitrides holds great promise for developing alternative industrial catalysts to H-B and Kellogg processes, there are challenges related to (i) scalability of synthesis method and (ii) reactivity under ambient conditions that must be addressed before successful implementation.

In this context, MXenes, a novel 2D family of transition metal carbides, nitrides and carbonitrides, have driven much interest as promising supports due to their unique properties including superior electronic conductivity, high specific surface area, high mechanical stability, hydrophilic properties and ability to accommodate various ions/molecules between their layers [28, 29]. The chemical structure of 2D MXene is $M_{n+1}X_nT_x$ (n = 1, 2, 3, 4) where M represents an early transition metal (Mo, V, Ti, W, Nb, etc.), X is a carbon and/or nitrogen atom and T_x, the surface-terminating functional group (-O, -OH, -F). MXene offers a high degree of flexibility in terms of tailoring its chemical composition, which can be achieved through the appropriate selection of transition metal and/or surface terminations. The malleability of MXenes chemical compositions permits a precise adjustment of the density of states [30] and work function [31], making MXene a versatile material with a range of potential applications. Furthermore, the presence of functional groups on the surface of MXenes has been reported to facilitate the adsorption of metal precursors via electrostatic interactions, making them ideal anchors for active catalytic sites. With this unique and modular surface chemistry, as well as recent advances in scalable synthesis routes [32], MXene has the potential to be utilized as a catalyst or as a support for various catalytic reactions. Despite its appealing features, the use of MXene in heterogeneous catalysis is still limited to only a few examples in the literature.

In this work, we report the performance of a post-synthesis modified 2D MXene (Mo_2CT_x) by cobalt in catalytic ammonia synthesis. The post-functionalization of MXene by Co resulted in materials that are active at temperature as low as 250°C. Interestingly, Co decorated MXene were found to be active without any pretreatment required. X-Co-Mo_2CT_x catalysts were found to be highly active for ammonia synthesis, where at steady state conditions a rate of 9499 and 4380 µmol $g^{-1}{}_{\text{active phase}}$ h^{-1} is obtained over the 5-Co_{Nit}-Mo_2CT_x and 1-Co_{Nit}-Mo_2CT_x at 400 °C respectively. Furthermore, these catalysts demonstrated catalytic activity in ammonia synthesis at temperature as low as 250°C.

VII.2 Experimental Procedure

VII.2.1 Catalyst Preparation

Chemicals. All chemicals needed for the preparation of Mo_2CT_x and its corresponding decorated Co-Mo_2CT_x were used with no further purification: Molybdenum Carbide (Mo_2C - 325 mesh, 99.5 % Alfa Aesar), Gallium metal (Ga, 99.9%, Alfa Aesar), cobalt nitrate hexahydrate ($Co(NO_3)_2.6H_2O$, 98 wt.%, Sigma Aldrich), cobalt chloride hexahydrate ($CoCl_2.6H_2O$, 98%, Sigma Aldrich), hydrofluoric acid (HF, 50%, Sigma-Aldrich) and hydrochloric acid (HCl, 69%, Sigma-Aldrich).

Preparation of pseudo- MAX phase Mo_2Ga_2C . Mo_2Ga_2C was synthesized following a modified synthesis procedure the literature by Hu et al.[33] In short, Mo_2Ga_2C was prepared by heating under vacuum of a mixture of Mo_2C powder and Gallium metal in appropriate ratios for 15 days at 850 °C. After furnace cooling, the resulting powder was immersed in a concentrated HCl solution overnight to dissolve any residual Ga and Ga_2O_3.

Preparation of Multilayer Mo_2CT_x. Mo_2CT_x was synthesized by selectively etching Ga of MAX phase Mo_2Ga_2C using 10 mL of 50 wt.% of HF per 1g of MAX phase at 55°C and for a duration of 4 days. The resulting multilayer MXene was then thoroughly washed until reaching neutral pH, and dried overnight under vacuum to obtained Mo_2CT_x multilayer.

Decoration of Multilayer Mo_2CT_x by Co. A series of X-Co-Mo_2CT_x catalysts were prepared by post-synthesis modification of Mo_2CT_x surface by Co^{2+}. In this approach, appropriate amount of cobalt precursor was first dissolved in 1 mL of deionized water. Upon sonication, 1 g of MXene (Mo_2CT_x) was added to the mixture which was then aged in a desiccator for 4 days. The resulting material was then calcined under argon at 350 °C (1.5 °C min^{-1}) to obtain X-Co-Mo_2CT_x.

N.B. Herein, the samples obtained after the calcination step are denoted as X-Co_y-Mo_2CT_x ,X representing the weight percentage of Co, while y represents the cobalt precursor (Nit-nitrate; Chl-chloride) whereas the post reaction samples are denoted as X-Co_y-Mo_2CT_x- PR.

VII.2.2 Physical and textural characterizations

In this article, the following characterization techniques were used: XRD, SEM, XPS, TEM, , CHN, EPR and TGA. For more information regarding the characterization techniques, please refer to Chapter 2 for all details

VII.2.3 Catalytic activity.

Catalytic tests are conducted in a tubular reactor, operated at atmospheric pressure. In a typical reaction test, 0.4 g of catalyst was placed tubular quartz reactor under a 75 vol.% H_2/N_2 (BOC, 99.98 %) gas mixture at a total gas flow of 60 mL min^{-1}. The reaction was performed at 400 °C, without any pretreatment (ammonolysis or high temperature nitridation) under the same flow rate of 75 vol.% $H_2:N_2$. Ammonia production was determined by measurement of the decrease in conductivity of a 200 mL 0.0018 M H_2SO_4 solution through which the reactor effluent stream flowed and was monitored as a function of reaction time. Reaction at 400°C is conducted to reach stationary regime, before temperature is decreased by steps of 50°C until no significant ammonia production is measured. For each temperature, reaction is conducted for at least 20 h to ensure obtaining a stationary regime.

VII.3 Results and Discussion

VII.3.1 Synthesis and characterisation of Mo_2CT_x MXene support

Multilayared Co-Mo_2CT_x catalysts where prepared by post-modification of MXene phase (Mo_2CT_x). First the parent MAX phase (Mo_2Ga_2C) was prepared by reaction of Mo_2C powder and metallic gallium (15 days at 850 °C). The formation of MAX phase was confirmed by PXRD results (Figure 1-a). Upon Ga removal by etching, the PXRD showed that the (002) peak shifted to lower 2θ from ~ 9.8° to 8.1° corresponding to the modification of the interlayer spacing and formation of the MXene phase. However, a remnant of (002) peak at 9.8° was still visible in the multilayer diffractogram indicating the presence of a fraction of unetched MAX phase alongside the MXene phase. The typical accordion-like structure was confirmed by SEM suggesting the successful exfoliation of individual MXene sheets. (Figure 1-d). High angle annular dark field scanning transmission electron microscopy (HAADF-STEM) showing the (001) surface of Mo_2CT_x is presented in Figure 1-e where the bright dots correspond to heavier Mo atoms compared to C atoms. The chemical composition was investigated by means of energy dispersive spectroscopy (EDS) elemental mapping showing a homogenous distribution of Mo atoms along some Ga from the parent material (Figure 1-f). Proper etching was confirmed in the high resolution XPS spectrum of the Ga 2p that only shows very low intensity Ga related peaks with less than 2.7 at.% with respect to the parent material. Thermogravimetric analysis was also conducted on Mo_2CT_x multilayer (Figure S1) in order to investigate its thermal stability for high temperature reactions. Only 0.7 wt.% weight loss, correlated to water desorption and some surface terminations, was reported reaching 450 °C, confirming that Mo_2CT_x multilayer is thermally stable for reaction at 400 °C.

The identity of Mo species in Mo_2CT_x was investigated by XPS (Figure 1-b, Table S1). The spectral decomposition of the high-resolution Mo 3d region can be ascribed to Mo^{6+}, Mo^{5+}, Mo^{4+}, Mo^{2+} and T_x-Mo-C species. The major contribution is related to the presence of C-Mo-T_x (41.5 wt.%) with lines corresponding to Mo $3d_{5/2}$ and Mo $3d_{3/2}$ spin-orbit components at 229.4 and 232.6 eV respectively which are slightly higher than those reported for the parent material Mo_2Ga_2C (228.1 and 231.3 eV) and for β-Mo_2C (Mo $3d_{5/2}$ binding energy of 228.4 eV).[34-36] The strong interaction of Mo-C with electronegative surface terminations (-OH, -F,-O) might be the reasoning behind the observed shift to higher binding energy. Furthermore, the 3d molybdenum spectra features the presence of oxidic molybdenum species (Mo^{6+}, Mo^{5+} and Mo^{4+}) which is related to the partial oxidation of MXene surface during the synthesis process and/or reactivity of the surface with ambient air during storage.

The presence of oxygen vacancies and Mo^{5+} species in Mo_2CT_x MXene material was investigated using electron paramagnetic resonance (Figure 1-c). The EPR spectrum was composed of three distinct signals. The first was a strong anisotropic signal at g_{xy}=1.93 and g_z=1.88, which was attributed to Mo^{5+} species located in axial symmetry. The other two signals, weaker in intensity, were associated with oxygen vacancies, located in the bulk and in the surface. The latter signal had a g factor of 2.06 and was ascribed to the presence of oxo (O^{n-}) species on the surface [37].

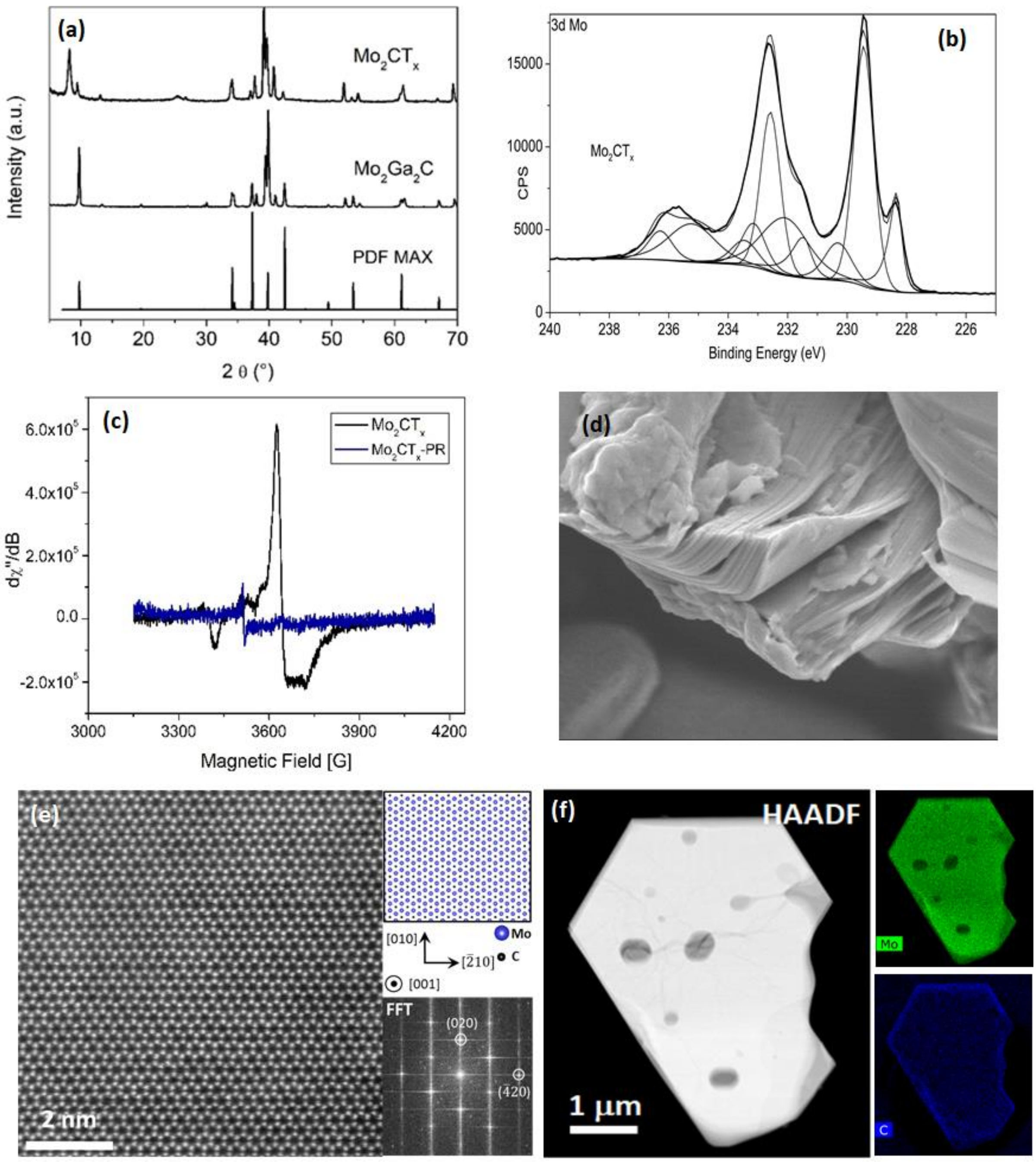

Figure 1 Structural and textural characterizations of Mo_2CT_x support: (a) PXRD pattern of the parent MAX phase (Mo_2Ga_2c) and the MXene phase (Mo_2CT_x), (b) XPS spectra in the Mo 3d region of Mo_2CT_x, (c) EPR spectra recorded prior and after ammonia synthesis reaction, (d) Typical SEM image of Mo_2CT_x displaying characteristic stacked layers with platelet morphology; (e) Figure. High resolution HAADF images and the corresponding atomic projection of the crystal lattice and fast Fourier transforms for the [001] zone axis (f) Characteristic HAADF images and the corresponding STEM-EDS intensity maps for Mo-L_a edge at 2.292 keV (green) and C-K at 0.277 keV (blue).

VII.3.2 Characterisation of Co-Mo_2CT_x catalysts

X-Co-Mo_2CT_x catalysts were prepared by post-synthesis modification of Mo_2CT_x surface by Co^{2+} at different loadings (1 and 5 wt.%). The integrity of the MXene structure, upon cobalt impregnation was confirmed using SEM, TEM, and XRD (Figure 2, Figure 3 and Figure 4-a).

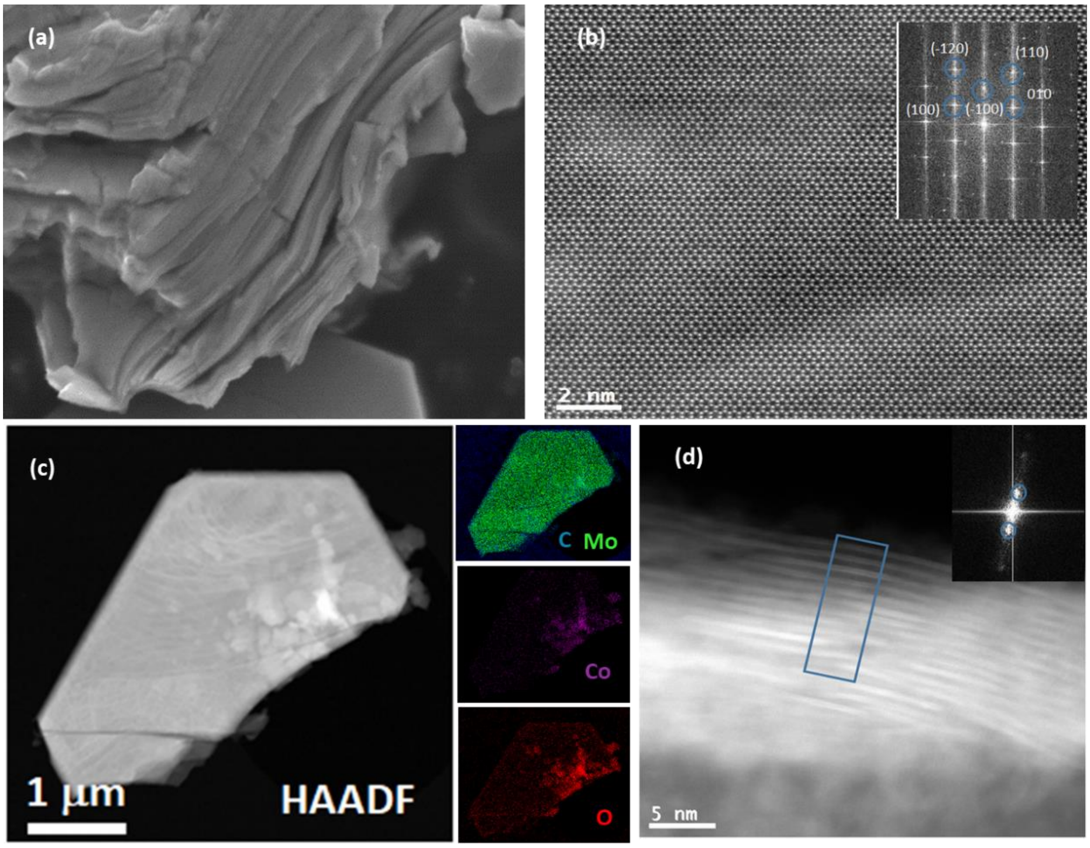

Figure 2 Microscopy characterisation of 1-Co_{Nit}-Mo_2CT_x catalyst**:** (a) Typical SEM image of 1-Co_{Nit}-Mo_2CT_x displaying characteristics stacked layers with platelet morphology, (b) high-resolution HAADF-STEM displaying (001) high-resolution HAADF-STEM of viewed along the [001] axis, inset shows Fast Fourier Transform (FFT) pattern, and (c) Characteristic HAADF images and the corresponding STEM-EDS intensity maps for Mo-L_a edge at 2.292 keV (green), C-K at 0.277 keV (blue), Co-K_a at 6.926 keV (purple), O-K at 0.525 keV (red) of 1-Co_{Nit} -Mo_2CT_x, (d) HAADF-STEM image showing 1-Co_{Nit}-Mo_2CT_x MXene layers.

In Figure 2, the accordion-like structure of MXene multilayers is retained for 1-Co_{Nit}-Mo_2CT_x a with minor unetched MAX phase (Figure 2 and Figure 3). STEM-EDS demonstrates the high dispersion of Co species within Mo_2CT_x. (Figure 2-c). At high cobalt loading, 5-Co_{Nit}-Mo_2CT_x, showed an amorphous layer of cobalt oxides enveloping Mo_2CT_x phase (Figure 3-a). However, the typical accordion morphology distinctive of MXene multilayers was maintained at high cobalt loading. PXRD was performed to further study the phase transformation upon cobalt impregnation (Figure 4-a). In all of the samples, both (002) diffraction peaks corresponding to the unetched MAX phase Mo_2Ga_2C (2θ ~ 9.79° ; d ~9.03 Å) and MXene Mo_2CT_x (2θ ~ 8.21° ; d ~10.76 Å) are present. However, due to the changes in plane orientation of 2D materials (z = 0), the intensity of the (00*l*) peaks decrease significantly after cobalt incorporation.

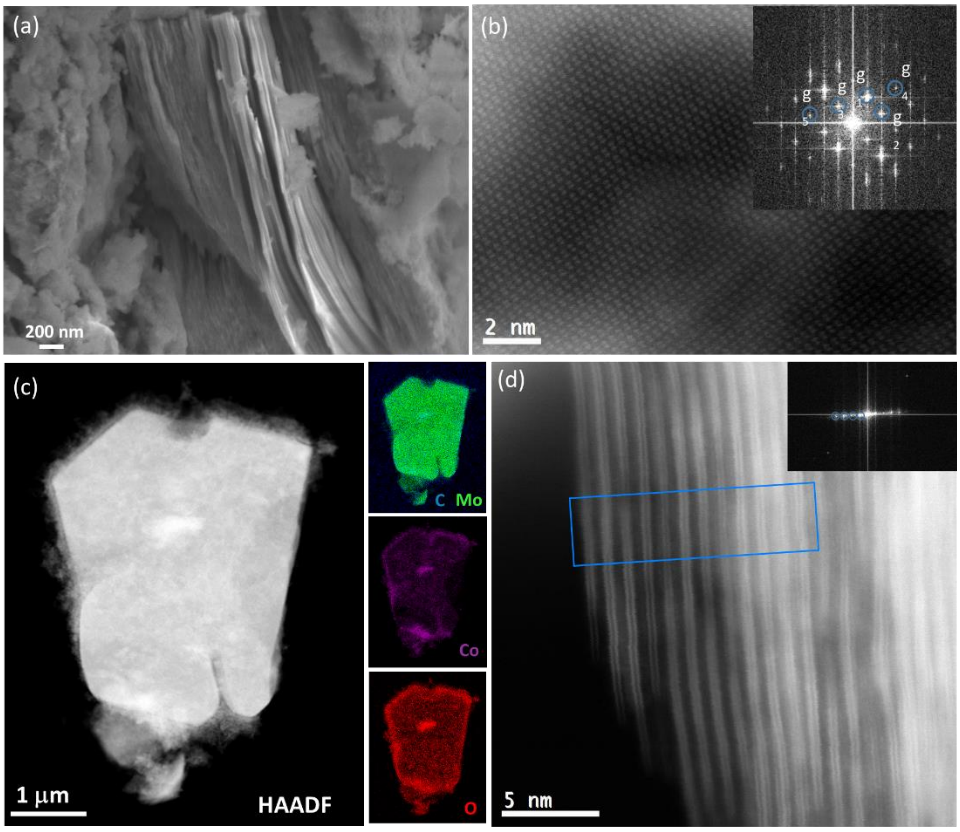

Figure 3 Microscopy characterisation of 5-Co_{Nit}-Mo_2CT_x catalyst**:** (a) SEM image of 5-Co_{Nit}-Mo_2CT_x displaying characteristics stacked layers with platelet morphology covered by external cobalt phase, (b) high-resolution HAADF-STEM displaying high-resolution HAADF-STEM of view along the [301] axis, Inset shows fast Fourier transform (FFT) pattern, (c) HAADF images and the corresponding STEM-EDS intensity maps for Mo-L_a edge at 2.292 keV (green), C-K at 0.277 keV (blue), Co-K_a at 6.926 keV (purple), O-K at 0.525 keV (red) of 5-Co_{Nit} -Mo_2CT_x, (d) HAADF-STEM image showing 5-Co_{Nit}-Mo_2CT_x MXene layers.

The evolution of the surface properties, *i.e.* chemical composition and oxidation states of Co and Mo in X-Co-Mo_2CT_x, were investigated using X-ray photoelectron spectroscopy (Figure 4, Table S2, Table S3). Upon Co impregnation, the concentration of functionalized C-Mo-T_x species decreased quasi-linearly with the weight percentage of Co. This observation suggests that these species may be involved in anchoring Co species to MXene surface [38, 39]. The introduction of 5 wt.% of Co, 5-Co_{Nit} -Mo_2CT_x, favoured the oxidation of Mo species resulting in an increase in the concentration of Mo^{4+} (Figure 4-d). The identity of Co species was also probed by XPS (Figure 4-e). In the high-resolution Co 2p spectra, the position of the major spectral line was found at 780.90 eV indicating an oxidation state of Co^{2+} in both 1-Co$_{Nit}$-Mo$_2$CT$_x$ and 5-Co$_{Nit}$ -Mo$_2$CT$_x$.

The effect of cobalt impregnation on the evolution of oxygen vacancies in 1-Co$_{Nit}$-Mo$_2$CT$_x$ and the concentration of Mo^{5+} was studied further using EPR (as shown in Figure 4-b and Figure 4-c). The 1-Co$_{Nit}$-Mo$_2$CT$_x$ material was found to exhibit a significantly higher concentration of oxygen vacancies compared to Mo$_2$CT$_x$ ($g \sim 2$) [37]. In the case of 5-Co$_{Nit}$-Mo$_2$CT$_x$, a similar EPR profile to Mo$_2$CT$_x$ was observed, with three signals attributed to Mo^{5+}, oxo species (O^{n-}) at the surface, and oxygen vacancies. However, the signals were weaker compared to Mo$_2$CT$_x$, with the concentration of Mo^{5+} species being three time less than for the parent MXene phase.

In summary, it has been demonstrated that upon incorporation of Co species, the MXene multilayer retained their initial morphology, with well dispersed Co^{2+} species within the MXene layers as seen in EDS and XPS

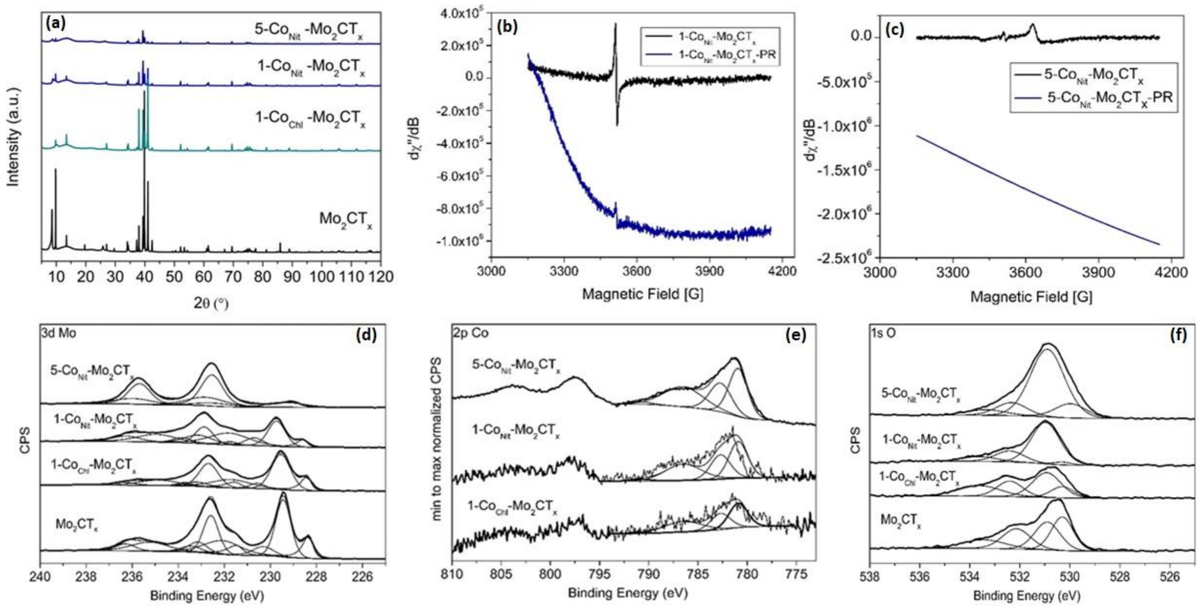

Figure 4 PXRD and spectroscopic characterizations of 1-Co$_{Nit}$-Mo$_2$CT$_x$ and 5-Co$_{Nit}$-Mo$_2$CT$_x$ catalysts**:** (a) PXRD pattern of 1-Co$_{Nit}$-Mo$_2$CT$_x$ and 5-Co$_{Nit}$-Mo$_2$CT$_x$ catalysts, (b) EPR spectra of 1-Co$_{Nit}$-Mo$_2$CT$_x$ recorded prior and after ammonia synthesis reaction, (c) EPR spectra of 5-Co$_{Nit}$-Mo$_2$CT$_x$ recorded prior and after ammonia synthesis reaction, (d) XPS spectra in the Mo 3d region of Mo$_2$CT$_x$ of 1-Co$_{Nit}$-Mo$_2$CT$_x$ and 5-Co$_{Nit}$-Mo$_2$CT$_x$ catalysts, (e) XPS spectra in the Co 2p region of Mo$_2$CT$_x$ of 1-Co$_{Nit}$-Mo$_2$CT$_x$ and 5-Co$_{Nit}$-Mo$_2$CT$_x$ catalysts, (f) XPS spectra in the O 1s region of Mo$_2$CT$_x$ of 1-Co$_{Nit}$-Mo$_2$CT$_x$ and 5-Co$_{Nit}$-Mo$_2$CT$_x$ catalysts.

VII.3.3 Catalytic activity in ammonia synthesis

The performance of MXene-based catalysts, namely Mo_2CT_x, 1-Co_{Nit}-Mo_2CT_x and 5-Co_{Nit}-Mo_2CT_x was evaluated for ammonia synthesis at ambient pressure. The reaction was conducted under the following conditions: a flow rate of 60 mL min^{-1} of 75 vol.% H_2:N_2 and a weight hourly space velocity (WHSV) of 9000 mL g^{-1} h^{-1}, with temperatures ranging from 250 to 400 °C without any pretreatment. To confirm catalytic stability over time, the reaction was carried out using all active catalysts for at least 15 days. The results are presented in Figure 5, Figure S2, and Table 1.

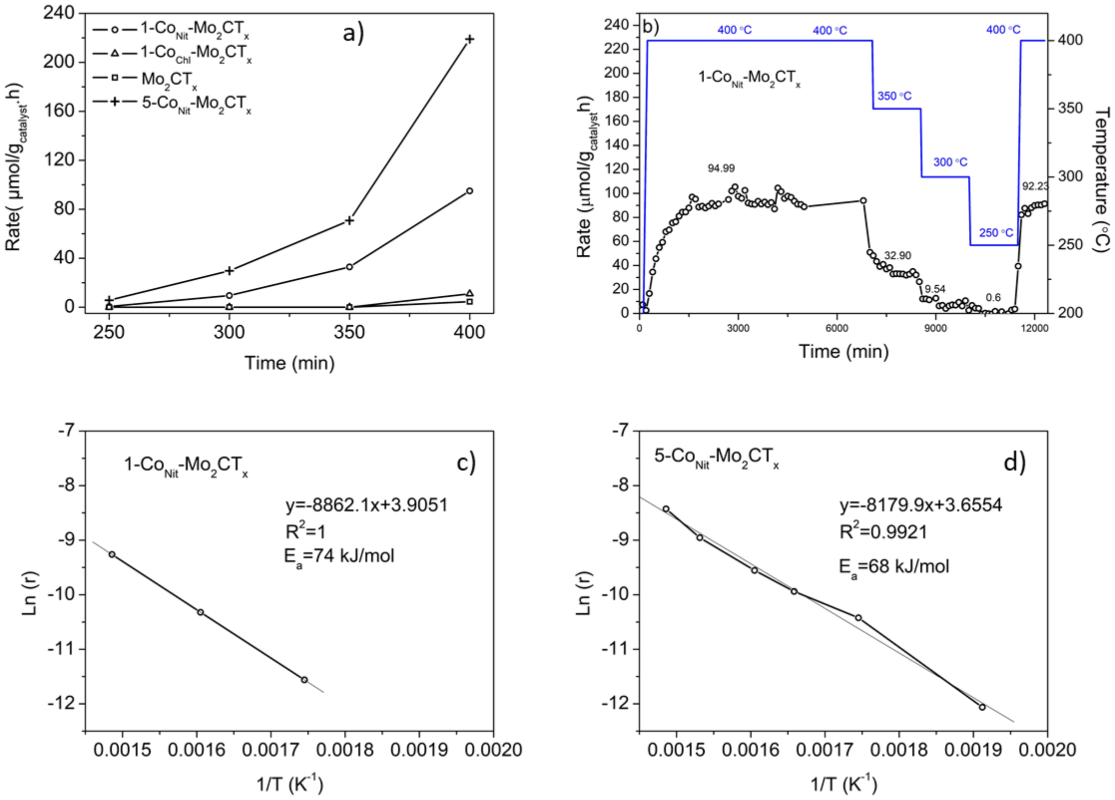

Figure 5 (a) Temperature dependence of catalytic activity of Mo_2CT_x, 1-Co_{Nit}-Mo_2CT_x and 5-Co_{Nit}-Mo_2CT_x in ammonia synthesis as function of temperatures, (b) Typical cumulative ammonia yield obtained of 1-Co_{Nit}-Mo_2CT_x catalyst, (c) Arrhenius plot obtained of 1-Co_{Nit}-Mo_2CT_x catalyst and (d) Arrhenius plot obtained of 5-Co_{Nit}-Mo_2CT_x catalyst. Reaction performed under 60 mL min^{-1} flow rate of 75 vol.% H_2/N_2 at 400 °C and ambient pressure.

Table 1. Summary of the catalytic activity of Mo_2CT_x, 1-Co_{Nit}-Mo_2CT_x, 1-Co_{Chl}-Mo_2CT_x, and 5-Co_{Nit}-Mo_2CT_x in ammonia synthesis

	Ammonia Synthesis reaction*								**Ea**
	Rate (µmol. g_{cata}^{-1} . h^{-1})				**Rate (µmol. g_{Co}^{-1} . h^{-1})**				**kJ/mol**
	400 °C	350 °C	300 °C	250 °C	400 °C	350 °C	300 °C	250°C	
Mo_2CT_x	4.5	ND	ND	ND		ND	ND	ND	-
1-Co_{Chl} -Mo_2CT_x	11.02	ND	ND	ND	1102	ND	ND	ND	-
1-Co_{Nit}-Mo_2CT_x	94.99	32.90	9.54	0.6	9499	3290	954	60	74
5-Co_{Nit}-Mo_2CT_x	219.01	70.85	29.75	5.78	4380	1417	595	115.6	68

* ammonia synthesis reaction under 60 mL min^{-1} of 75% H_2 in N_2 (BOC, 99.98 %) at 400 °C and atmospheric pressure.

The catalytic activity of the non-doped multilayer Mo_2CT_x was studied at 400 °C (Figure 5-a, Table 1). The undecorated MXene phase demonstrated a limited catalytic activity over time. Initially, the production of ammonia began at a slow rate and increased gradually, eventually reaching a maximum rate of approximately 32.66 µmol $g_{cat.}^{-1}h^{-1}$ However, it was observed that the material lacked stability, and the catalytic activity decreased gradually over time. After being on stream for 100 hours at 400 °C, the catalytic activity was found to have decreased to 4.5 µmol $g_{cat.}^{-1}h^{-1}$ which might be related to changes in the surface composition over time. Upon cobalt doping, and under the same catalytic conditions, 1-Co_{Nit}-Mo_2CT_x, displayed a higher catalytic activity of ~ 94.99 µmol $g_{cat.}^{-1}h^{-1}$ with respect to Mo_2CT_x. However, steady state rate was only attained after 25 h of reaction. Notably, once at steady state conditions, no sign of deactivation was observed even after 200 h of reaction. Remarkably, 1-Co_{Nit}-Mo_2CT_x displayed catalytic activity at temperatures lower than 400°C. The ammonia synthesis rate at temperatures of 350 and 300 °C was calculated to be ~32.90, and ~9.54 µmol $g_{cat.}^{-1}h^{-1}$ respectively. While decreasing the reaction temperature resulted in a decline in the catalytic activity, initial performance was restored upon increasing the temperature to 400°C with no induction time observed (Figure 1-b). Astonishingly, the use of cobalt chloride as a precursor for the preparation 1-Co_{Chl}-Mo_2CT_x led to poor catalytic activity (~ 11 µmol $g_{cat.}^{-1}h^{-1}$ at 400 °C, (WHSV 9000 mL g^{-1} h^{-1}). The loss of catalytic activity might be related to chlorine poisoning.

Increasing the loading of Co to 5 wt.% resulted in further increases in the catalytic activity (5-Co_{Nit}-Mo_2CT_x : ~ 219 µmol $g_{cat.}^{-1}h^{-1}$ at 400 °C (WHSV 9000 mL g^{-1} h^{-1}). In a similar manner to 1-Co_{Nit}-Mo_2CT_x, the steady state rate was only attained after an important induction time. Despite its very low loading in Co, 5-Co_{Nit}-Mo_2CT_x exhibits a close catalytic activity to the Co_3Mo_3N (248 µmol $g_{catalyst}^{-1}$ h^{-1}, WHSV 24 000 mL g^{-1} h^{-1}).[40] However, unlike Co_3Mo_3N, no ammonolysis step or pre-activation step is needed for 5-Co_{Nit}-Mo_2CT_x. Moreover, the increase in the cobalt load ameliorated significantly the performance of 5-Co_{Nit}-Mo_2CT_x allowing it to remain active at temperatures as low as 250°C. The ammonia synthesis rate at temperatures of 250, 300 and 350 °C was calculated to be approximately 5.78, 29.75, 70.85 µmol $g_{cat.}^{-1}h^{-1}$ respectively. 5-Co_{Nit}-Mo_2CT_x showed no sign of deactivation even after 360 h under stream.

The effect of MXenes on significantly ameliorating the performance of Co in ammonia synthesis at low temperature and its stability is evident, as Co on its own does not display any good catalytic activity. This effect becomes more apparent when ammonia synthesis rate is normalized with respect to the active phase loading (wt.% of Co). For instance, at steady state conditions a rate of 9499, 3290 and 945 µmol$g^{-1}_{\text{active phase}}$ h^{-1} is obtained over the 1-Co_{Nit}-Mo_2CT_x at 400, 350, and 300 °C respectively. A gradual decrease is however observed while increasing the cobalt loading to 5 wt.%. Thus, the ammonia synthesis rate decreased to 4380, 1417 and 595 µmol$g^{-1}_{\text{active phase}}$ h^{-1} at 400, 350 and 300 °C. However, 5-Co_{Nit}-Mo_2CT_x displayed ameliorated catalytic activity at lower temperature ~ 250°C when compared against the 1-Co_{Nit}-Mo_2CT_x. It was also observed that excess cobalt did not result in a linear increase in catalytic activity and actually had a negative impact on the normalized rate per gram of active phase. From these results, it can be inferred that not all of the introduced cobalt is active, and only a portion of cobalt is in direct interaction with MXene layers, contributing to the catalytic activity in ammonia synthesis.

The apparent activation energy (Ea) derived from Arrhenius plot was calculated to be approximately 74 and 68 kJ mol^{-1} for 1-Co_{Nit}-Mo_2CT_x and 5-Co_{Nit}-Mo_2CT_x respectively. These values are in par with the activation energies reported for some of the highest active catalyst such Li-MT, Mn_4N-BaH_2, Ru/C12A7:e^-, $BaTiO_{2.5}H_{0.5}$ [23, 41] [42, 43] which are in the range of 40 – 70 kJ mol^{-1} which is generally considered low for ammonia synthesis. In comparison, standard Ru-based catalysts have activation energies in the range of 80 – 130 kJ mol^{-1}, indicating that cobalt decorated MXene displays reasonably low activation energy [44].

However, caution should be exercised when comparing Ea of different catalysts, as reaction condition can vary and affect the observed activation energies.

In summary, cobalt decorated MXene could be a promising candidate for the development of a novel generation of catalysts capable of operating at low temperature while coping with intermittent reactions conditions.

VII.3.4 Investigation of Co-decorated MXene Phase and Structure Evolution during Ammonia Synthesis Conditions

The role of cobalt in inducing ammonia catalytic activity in MXene based support has been studied by comparing the performance of 1-Co_{Nit}-Mo_2CT_x, and 5-Co_{Nit}-Mo_2CT_x catalyst against the parent material Mo_2CT_x. It is quite evident that in absence of Co, the bare MXene phase displayed poor catalytic activity and stability in stream. However, the catalytic activity of Co-decorated MXenes displayed an induction time during which the activity gradually increases before stabilizing at a steady-state level. This induction time suggests that the material undergoes structural and/or surface changes, resulting in the formation of the active phase. This aspect was investigated further to gain a better understanding of the nature of the active phase. Figure 6 displays selected microscopic observations of post-reaction catalysts, namely 1-Co_{Nit}-Mo_2CT_x-PR and 5-Co_{Nit}-Mo_2CT_x-PR using SEM and HAADF-STEM. These catalysts were subjected to high reaction temperatures of up to 400 °C for extended periods (Figure 5-b and Figure S2). Interestingly, all the catalyst, including the parent material Mo_2CT_x, exhibited stable multilayers that retained their accordion-like structure despite the presence of some fractures. (Figure 6-a and Figure 6-c). Furthermore, STEM-EDS showed that both catalysts maintained a high dispersion of Co species within Mo_2CT_x (Figure 6-b and Figure 6-d). Upon reaction, the gross morphology is similar for all the materials tested. Therefore, there is compelling evidence suggesting that the differences in catalytic performance cannot be attributed to differences in morphology, and instead, it may be due to the variation in composition/surface composition during reaction. In fact, careful analysis of STEM-EDS analysis revealed that the surface is now populated with N adatoms upon reaction (Figure 6) in the case of 1-Co_{Nit} -Mo_2CT_x–PR and 5-Co_{Nit} -Mo_2CT_x–PR. The inclusion of nitrogen in post-reaction sample, Table S4, was further confirmed by elemental analysis (0.48 wt.% in 1-Co_{Nit} -Mo_2CT_x–PR and 0.84 wt.% in 5-Co_{Nit}-Mo_2CT_x –PR). Interestingly, no significant amount of N was detected in 1-Co_{Chl}-Mo_2CT_x–PR and Mo_2CT_x-PR which are both inactive in ammonia synthesis.

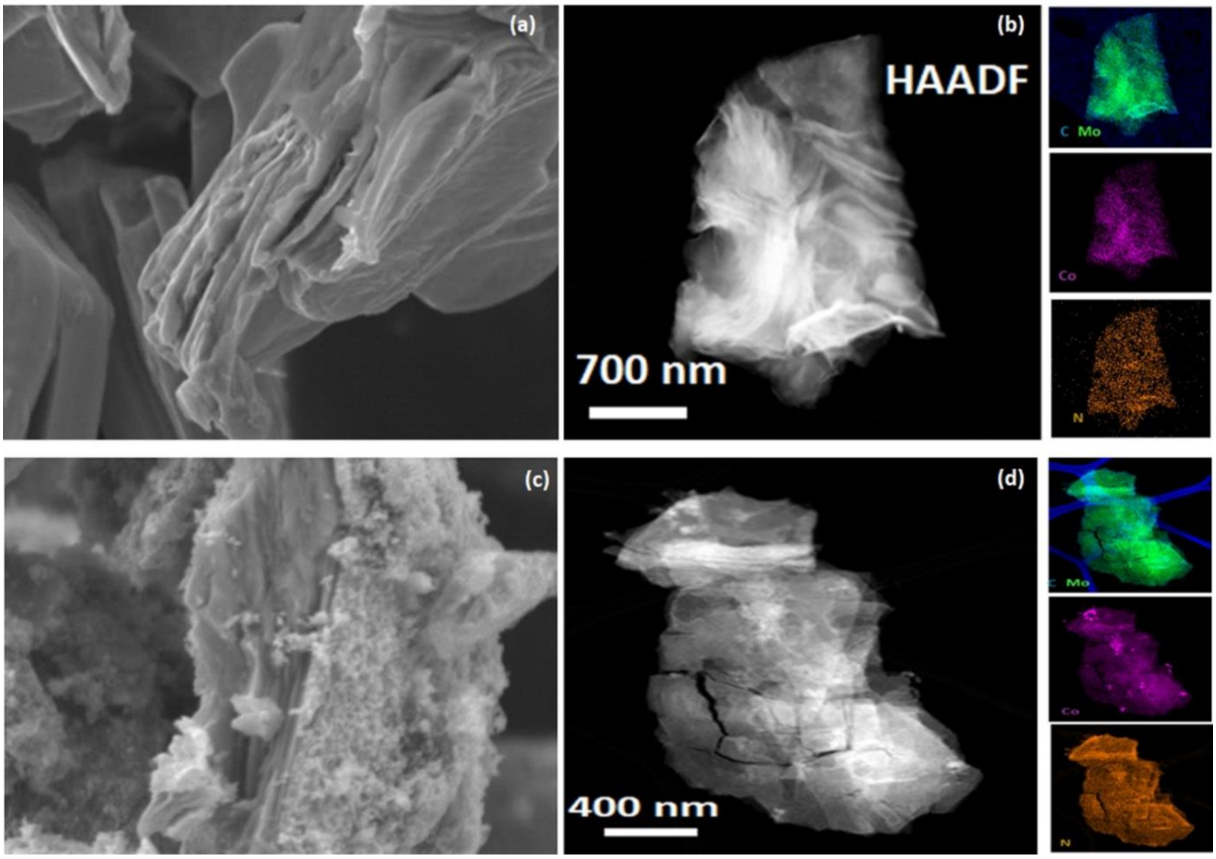

Figure 6 Microscopy characterisations of 1-Co_{Nit} -Mo_2CT_x-PR and 5-Co_{Nit} -Mo_2CT_x-PR post-reaction catalyst. (a) SEM image of 1-Co_{Nit} -Mo_2CT_x-PR, (b) Characteristic HAADF images and the corresponding STEM-EDS of 5-Co_{Nit} -Mo_2CT_x-PR. (c) SEM image of 5-Co_{Nit} -Mo_2CT_x-PR and (d) Characteristic HAADF images and the corresponding STEM-EDS of 1-Co_{Nit} -Mo_2CT_x-PR.

To gain insight on the evolution of the surface chemical composition during the reaction, XPS and EPR analysis were performed for the post reaction catalysts (Figure 7 and Table S1 and S2).

Upon reaction, the Mo 3d XPS spectrum features strong variation of the concentration of Mo oxidation state when compared to the as-prepared materials. In the Mo_2CT_x, most of Mo^{6+} and Mo^{5+} species were reduced to Mo^{4+} upon reaction which was the predominant surface species (73.34 wt.%). A decrease in C-Mo-T_x species, under reducing conditions, from 41.48 to 14.10 %.wt was also observed. Upon addition of cobalt, the distribution of Mo species in post reaction catalysts 1-Co_{Nit} -Mo_2CT_x-PR and 5-Co_{Nit} -Mo_2CT_x-PR was found to be largely different than Mo_2CT_x-PR. Remarkably, the addition of Co, stabilizes the fraction of C-Mo-T_x species in 1-Co_{Nit} -Mo_2CT_x-PR which even slightly increased from 30.81 to 58.90 wt.%. The effect of cobalt on the concentration of C-Mo-T_x was more pronounced in 5-Co_{Nit} -Mo_2CT_x-PR resulting in an increase from 2.33 to 60.33 wt.% (Table S1). To elucidate this behaviour, further insights can be obtained from the high-resolution Mo 3p spectra, which also allows the observation of N 1s (Figure 7-a). The deconvolution of 1-Co_{Nit} -Mo_2CT_x-PR and 5-Co_{Nit} -Mo_2CT_x-PR high resolution Mo 3p spectra show the presence of an additional peak observed at ~ 397.6± 0.1eV which corresponds to N 1s peak. The position of the peak is very comparable to N 1s observed in molybdenum nitride phases such as in Co_3Mo_3N (397,9 eV) and in Mo_2N and MoN bulk (397.8 eV) [45, 46] while NHx species possess binding energy at values close to ~ 400 eV [47]. This would be consistent with partial replacement of carbon with nitrogen in the MXene phase under ammonia synthesis conditions. The nature of cobalt species in the post-reaction catalysts was also probed using XPS. Upon reaction, a radical change in Co 2p XPS profiles was observed. The spectral decomposition of Co 2p profiles showed a partial reduction of Co^{2+} into a more metallic state Co^0. The position of the additional peak, related to the presence of a second phase, was observed at 779.05 eV and at 778.16 eV in 1-Co_{Nit} -Mo_2CT_x-PR and 5-Co_{Nit} -Mo_2CT_x-PR respectively. However, metallic cobalt is usually reported at 778.1 eV, while the observed BE in 1-Co_{Nit} -Mo_2CT_x-PR is slightly higher which might be due to strong interaction of Co with MXene surface. It might also imply that the extra-cobalt present in the amorphous layer enveloping the 5-Co_{Nit} -Mo_2CT_x-PR phase is more prone to reduction under ammonia synthesis conditions.

For more information regarding cobalt, EPR spectra of post-reaction catalysts were recorded on a wider magnetic field range (Figure 7-c and Figure 7-d). As expected, under highly reducing conditions, signals related to Mo^{5+} and O^{n-} species, present initially in Mo_2CT_x, disappeared. Whereas a signal with a g factor of 2,0024 attributed oxygen has been detected in Mo_2CT_x. The EPR spectra of 5-Co_{Nit} -Mo_2CT_x-PR (Figure 7-d) was characterized by a very broad line indicating ferromagnetic behaviour. The magnetic property of the catalyst, upon reaction, reveals the presence of $Co^{2+/}Co^0$ redox couple. The EPR spectra of the 1-Co_{Nit} -Mo_2CT_x-PR (Figure 7-c) was characterized by a broad line with a g factor of 2,15 can be attributed to low spin Co^{2+}.

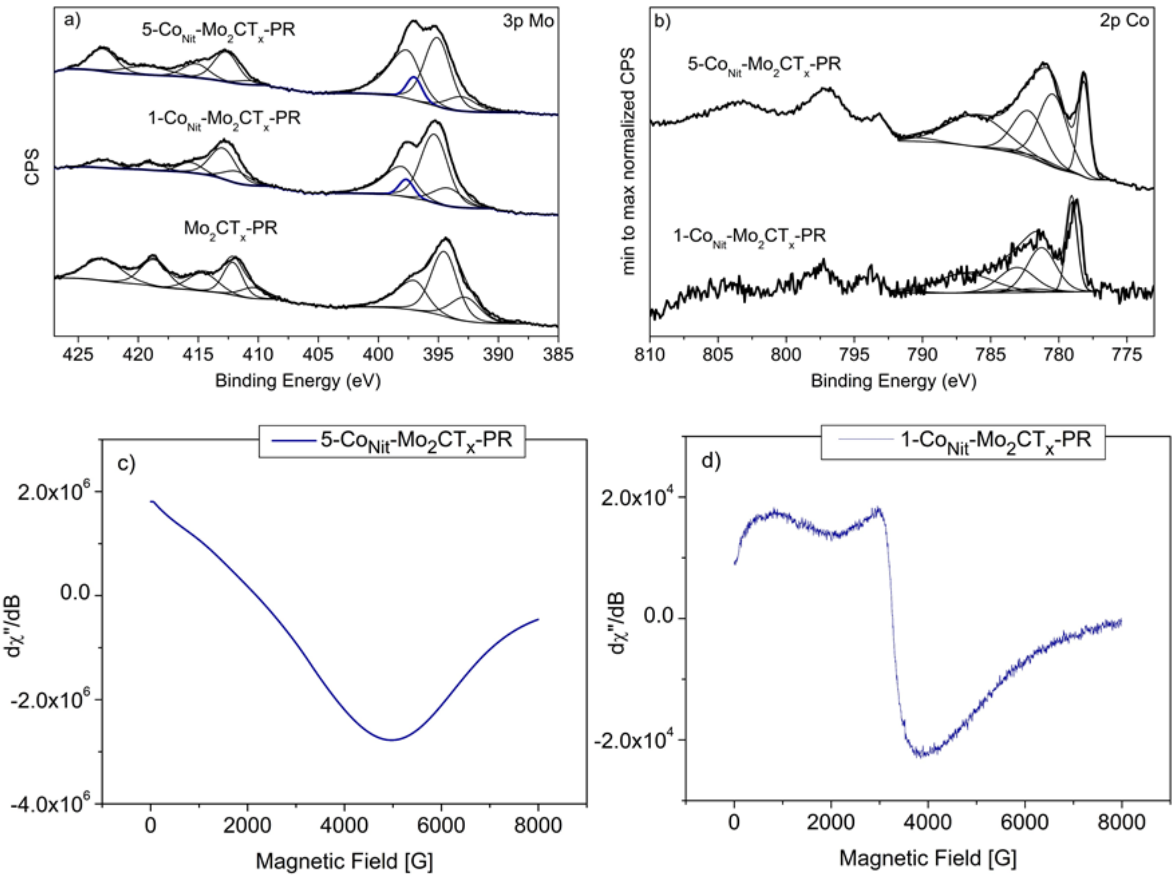

Figure 7 Spectroscopic characterizations of post-reaction catalysts Mo_2CT_x-PR, 1-Co_{Nit}-Mo_2CT_x-PR and 5-Co_{Nit}-Mo_2CT_x-PR catalysts: (a) XPS spectra in the Mo 3d region of post-reaction catalysts, (b) XPS spectra in the Co 2p region, (c) EPR spectra of 1-Co_{Nit}-Mo_2CT_x-PR and (d) EPR 5-Co_{Nit}-Mo_2CT_x-PR catalysts

VII.4 Conclusion

In this work, we introduce cobalt decorated MXenes as suitable heterogeneous catalysts for ammonia synthesis at mild conditions. The results of thorough characterization demonstrate a high dispersion of Co species within the 2D MXene (Mo_2CT_x) multilayers and pinpoint its stability during the reaction process. X-Co-Mo_2CT_x catalysts were found to be highly active for ammonia synthesis, where at steady state conditions a rate of 9499 and 4380 µmol $g^{-1}_{\text{active phase}}$ h^{-1} is obtained over the 5-Co_{Nit}-Mo_2CT_x and 1-Co_{Nit}-Mo_2CT_x at 400 °C respectively. Furthermore, these catalysts demonstrated catalytic activity in ammonia synthesis at temperature as low as 250°C. Remarkably, no ammonolysis step and/or pre-treatment step were required to activate X-Co-Mo_2CT_x catalysts. However, an induction time, in which the activity increased slowly, was observed. Post-reaction analysis revealed partial substitution of lattice carbon nitrogen as well as partial reduction of Co^{2+} during ammonia synthesis. However, the carbon substitution by nitrogen is rather limited (Up to 0.84 wt.%. 5-Co_{Nit} -Mo_2CT_x) Interestingly, replacement of C- by N- was only observed in the case of active materials for ammonia synthesis and not in the case of non-decorated MXene (Mo_2CT_x). The catalytic activity profiles, supported with post-reaction characterizations results, hint that the active site is generated upon reaction and might be a cobalt decorated carbonitrides Co- $Mo_2C_{1-\delta}N_{\delta}T_x$. Once reaching the steady state, activity was found to be stable upon recycling between low- and high- temperature conditions with no induction time. The results reported in this work demonstrate that Mo_2CT_x, upon appropriate modification resulted in a high-performance ammonia synthesis catalyst capable of operating under mild reaction conditions and under intermittent regime.

VII.5 References

[1] J.W. Erisman, M.A. Sutton, J. Galloway, Z. Klimont, W. Winiwarter, How a century of ammonia synthesis changed the world, Nature Geoscience, 1 (2008) 636-639.

[2] B. Stolz, M. Held, G. Georges, K. Boulouchos, Techno-economic analysis of renewable fuels for ships carrying bulk cargo in Europe, Nature Energy, 7 (2022) 203-212.

[3] C. Smith, A.K. Hill, L. Torrente-Murciano, Current and future role of Haber–Bosch ammonia in a carbon-free energy landscape, Energy & Environmental Science, 13 (2020) 331-344.

[4] L.J. Christiansen, Thermodynamic Properties in Ammonia Synthesis, in: A. Nielsen (Ed.) Ammonia: Catalysis and Manufacture, Springer Berlin Heidelberg, Berlin, Heidelberg, 1995, pp. 1-15.

[5] C.J.H. Jacobsen, S. Dahl, B.S. Clausen, S. Bahn, A. Logadottir, J.K. Nørskov, Catalyst Design by Interpolation in the Periodic Table: Bimetallic Ammonia Synthesis Catalysts, Journal of the American Chemical Society, 123 (2001) 8404-8405.

[6] G. Ertl, Surface Science and Catalysis—Studies on the Mechanism of Ammonia Synthesis: The P. H. Emmett Award Address, Catalysis Reviews, 21 (1980) 201-223.

[7] M.S. Spencer, On the rate-determining step and the role of potassium in the catalytic synthesis of ammonia, Catalysis Letters, 13 (1992) 45-53.

[8] A.J. Medford, A. Vojvodic, J.S. Hummelshøj, J. Voss, F. Abild-Pedersen, F. Studt, T. Bligaard, A. Nilsson, J.K. Nørskov, From the Sabatier principle to a predictive theory of transition-metal heterogeneous catalysis, Journal of Catalysis, 328 (2015) 36-42.

[9] A. Vojvodic, A.J. Medford, F. Studt, F. Abild-Pedersen, T.S. Khan, T. Bligaard, J.K. Nørskov, Exploring the limits: A low-pressure, low-temperature Haber–Bosch process, Chemical Physics Letters, 598 (2014) 108-112.

[10] K. McAulay, J.S.J. Hargreaves, A.R. McFarlane, D.J. Price, N.A. Spencer, N. Bion, F. Can, M. Richard, H.F. Greer, W.Z. Zhou, The influence of pre-treatment gas mixture upon the ammonia synthesis activity of Co–Re catalysts, Catalysis Communications, 68 (2015) 53-57.

[11] R.K. Rai, W. Al Maksoud, N. Morlanés, M. Harb, R. Ahmad, A. Genovese, M.N. Hedhili, L. Cavallo, J.-M. Basset, Iron–Cobalt-Based Materials: An Efficient Bimetallic Catalyst for Ammonia Synthesis at Low Temperatures, ACS Catalysis, 12 (2022) 587-599.

[12] R. Kojima, K.-i. Aika, Cobalt molybdenum bimetallic nitride catalysts for ammonia synthesis: Part 2. Kinetic study, Applied Catalysis A: General, 218 (2001) 121-128.

[13] R. Kojima, K.-i. Aika, Cobalt molybdenum bimetallic nitride catalysts for ammonia synthesis: Part 1. Preparation and characterization, Applied Catalysis A: General, 215 (2001) 149-160.

[14] D. McKay, J.S.J. Hargreaves, J.L. Rico, J.L. Rivera, X.L. Sun, The influence of phase and morphology of molybdenum nitrides on ammonia synthesis activity and reduction characteristics, Journal of Solid State Chemistry, 181 (2008) 325-333.

[15] R. Kojima, K.-i. Aika, Cobalt Molybdenum Bimetallic Nitride Catalysts for Ammonia Synthesis, Chemistry Letters, 29 (2000) 514-515.

[16] C.D. Zeinalipour-Yazdi, J.S.J. Hargreaves, C.R.A. Catlow, Nitrogen Activation in a Mars–van Krevelen Mechanism for Ammonia Synthesis on Co3Mo3N, The Journal of Physical Chemistry C, 119 (2015) 28368-28376.

[17] S.M. Hunter, D.H. Gregory, J.S.J. Hargreaves, M. Richard, D. Duprez, N. Bion, A Study of 15N/14N Isotopic Exchange over Cobalt Molybdenum Nitrides, ACS Catalysis, 3 (2013) 1719-1725.

[18] A. Daisley, L. Costley-Wood, J.S.J. Hargreaves, The Role of Composition and Phase upon the Lattice Nitrogen Reactivity of Ternary Molybdenum Nitrides, Topics in Catalysis, 64 (2021) 1021-1029.

[19] S. Hagen, R. Barfod, R. Fehrmann, C.J.H. Jacobsen, H.T. Teunissen, K. Ståhl, I. Chorkendorff, New efficient catalyst for ammonia synthesis: barium-promoted cobalt on carbon, Chemical Communications, (2002) 1206-1207.

[20] W. Raróg-Pilecka, E. Miśkiewicz, M. Matyszek, Z. Kaszkur, L. Kępiński, Z. Kowalczyk, Carbon-supported cobalt catalyst for ammonia synthesis: Effect of preparation procedure, Journal of Catalysis, 237 (2006) 207-210.

[21] K. Sato, S.-i. Miyahara, K. Tsujimaru, Y. Wada, T. Toriyama, T. Yamamoto, S. Matsumura, K. Inazu, H. Mohri, T. Iwasa, T. Taketsugu, K. Nagaoka, Barium Oxide Encapsulating Cobalt Nanoparticles Supported on Magnesium Oxide: Active Non-Noble Metal Catalysts for Ammonia Synthesis under Mild Reaction Conditions, ACS Catalysis, 11 (2021) 13050-13061.

[22] W. Gao, P. Wang, J. Guo, F. Chang, T. He, Q. Wang, G. Wu, P. Chen, Barium Hydride-Mediated Nitrogen Transfer and Hydrogenation for Ammonia Synthesis: A Case Study of Cobalt, ACS Catalysis, 7 (2017) 3654-3661.

[23] P. Wang, F. Chang, W. Gao, J. Guo, G. Wu, T. He, P. Chen, Breaking scaling relations to achieve low-temperature ammonia synthesis through LiH-mediated nitrogen transfer and hydrogenation, Nature Chemistry, 9 (2017) 64-70.

[24] Y. Inoue, M. Kitano, M. Tokunari, T. Taniguchi, K. Ooya, H. Abe, Y. Niwa, M. Sasase, M. Hara, H. Hosono, Direct Activation of Cobalt Catalyst by 12CaO·7Al2O3 Electride for Ammonia Synthesis, ACS Catalysis, 9 (2019) 1670-1679.

[25] M. Kitano, J. Kujirai, K. Ogasawara, S. Matsuishi, T. Tada, H. Abe, Y. Niwa, H. Hosono, Low-Temperature Synthesis of Perovskite Oxynitride-Hydrides as Ammonia Synthesis Catalysts, Journal of the American Chemical Society, 141 (2019) 20344-20353.

[26] Y. Tang, Y. Kobayashi, N. Masuda, Y. Uchida, H. Okamoto, T. Kageyama, S. Hosokawa, F. Loyer, K. Mitsuhara, K. Yamanaka, Y. Tamenori, C. Tassel, T. Yamamoto, T. Tanaka, H. Kageyama, Metal-Dependent Support Effects of Oxyhydride-Supported Ru, Fe, Co Catalysts for Ammonia Synthesis, Advanced Energy Materials, 8 (2018) 1801772.

[27] M. Kitano, Y. Inoue, M. Sasase, K. Kishida, Y. Kobayashi, K. Nishiyama, T. Tada, S. Kawamura, T. Yokoyama, M. Hara, H. Hosono, Self-organized Ruthenium–Barium Core–Shell Nanoparticles on a Mesoporous Calcium Amide Matrix for Efficient Low-Temperature Ammonia Synthesis, Angewandte Chemie International Edition, 57 (2018) 2648-2652.

[28] O. Mashtalir, M. Naguib, V.N. Mochalin, Y. Dall'Agnese, M. Heon, M.W. Barsoum, Y. Gogotsi, Intercalation and delamination of layered carbides and carbonitrides, Nature Communications, 4 (2013) 1716.

[29] M.R. Lukatskaya, O. Mashtalir, C.E. Ren, Y. Dall'Agnese, P. Rozier, P.L. Taberna, M. Naguib, P. Simon, M.W. Barsoum, Y. Gogotsi, Cation Intercalation and High Volumetric Capacitance of Two-Dimensional Titanium Carbide, Science, 341 (2013) 1502-1505.

[30] T. Hu, Z. Li, M. Hu, J. Wang, Q. Hu, Q. Li, X. Wang, Chemical Origin of Termination-Functionalized MXenes: Ti3C2T2 as a Case Study, The Journal of Physical Chemistry C, 121 (2017) 19254-19261.

[31] Y. Liu, H. Xiao, W.A. Goddard, III, Schottky-Barrier-Free Contacts with Two-Dimensional Semiconductors by Surface-Engineered MXenes, Journal of the American Chemical Society, 138 (2016) 15853-15856.

[32] C.E. Shuck, A. Sarycheva, M. Anayee, A. Levitt, Y. Zhu, S. Uzun, V. Balitskiy, V. Zahorodna, O. Gogotsi, Y. Gogotsi, Scalable Synthesis of Ti3C2Tx MXene, Advanced Engineering Materials, 22 (2020) 1901241.

[33] C. Hu, C.C. Lai, Q. Tao, J. Lu, J. Halim, L. Sun, J. Zhang, J. Yang, B. Anasori, J. Wang, Y. Sakka, L. Hultman, P. Eklund, J. Rosen, M.W. Barsoum, Mo2Ga2C: a new ternary nanolaminated carbide, Chemical Communications, 51 (2015) 6560-6563.

[34] E.B. Deeva, A. Kurlov, P.M. Abdala, D. Lebedev, S.M. Kim, C.P. Gordon, A. Tsoukalou, A. Fedorov, C.R. Müller, In Situ XANES/XRD Study of the Structural Stability of Two-Dimensional Molybdenum Carbide Mo2CTx: Implications for the Catalytic Activity in the Water–Gas Shift Reaction, Chemistry of Materials, 31 (2019) 4505-4513.

[35] C.C. Lai, R. Meshkian, M. Dahlqvist, J. Lu, L.Å. Näslund, O. Rivin, E.N. Caspi, O. Ozeri, L. Hultman, P. Eklund, M.W. Barsoum, J. Rosen, Structural and chemical determination of the new nanolaminated carbide Mo2Ga2C from first principles and materials analysis, Acta Materialia, 99 (2015) 157-164.

[36] Y. Ma, G. Guan, X. Hao, Z. Zuo, W. Huang, P. Phanthong, X. Li, K. Kusakabe, A. Abudula, Embedded structure catalyst: a new perspective from noble metal supported on molybdenum carbide, RSC Advances, 5 (2015) 15002-15005.

[37] C. Drouilly, J.-M. Krafft, F. Averseng, S. Casale, D. Bazer-Bachi, C. Chizallet, V. Lecocq, H. Vezin, H. Lauron-Pernot, G. Costentin, ZnO Oxygen Vacancies Formation and Filling Followed by in Situ Photoluminescence and in Situ EPR, The Journal of Physical Chemistry C, 116 (2012) 21297-21307.

[38] Y. Cui, Z. Cao, Y. Zhang, H. Chen, J. Gu, Z. Du, Y. Shi, B. Li, S. Yang, Single-Atom Sites on MXenes for Energy Conversion and Storage, Small Science, 1 (2021) 2100017.

[39] P. Rajput, P. Devi, In-situ synthesized gold nanoparticles modified Mo2C MXene for surface enhanced Raman scattering, Graphene and 2D Materials, 7 (2022) 107-117.

[40] A. Sfeir, C.A. Teles, C. Ciotonea, G.N.M. Reddy, M. Marinova, J. Dhainaut, A. Löfberg, J.-P. Dacquin, S. Royer, S. Laassiri, Enhancing ammonia catalytic production over spatially confined cobalt molybdenum nitride nanoparticles in SBA-15, Applied Catalysis B: Environmental, 325 (2023) 122319.

[41] F. Chang, Y. Guan, X. Chang, J. Guo, P. Wang, W. Gao, G. Wu, J. Zheng, X. Li, P. Chen, Alkali and Alkaline Earth Hydrides-Driven N2 Activation and Transformation over Mn Nitride Catalyst, Journal of the American Chemical Society, 140 (2018) 14799-14806.

[42] M. Kitano, Y. Inoue, Y. Yamazaki, F. Hayashi, S. Kanbara, S. Matsuishi, T. Yokoyama, S.-W. Kim, M. Hara, H. Hosono, Ammonia synthesis using a stable electride as an electron donor and reversible hydrogen store, Nature Chemistry, 4 (2012) 934-940.

[43] Y. Kobayashi, Y. Tang, T. Kageyama, H. Yamashita, N. Masuda, S. Hosokawa, H. Kageyama, Titanium-Based Hydrides as Heterogeneous Catalysts for Ammonia Synthesis, Journal of the American Chemical Society, 139 (2017) 18240-18246.

[44] F. Rosowski, A. Hornung, O. Hinrichsen, D. Herein, M. Muhler, G. Ertl, Ruthenium catalysts for ammonia synthesis at high pressures: Preparation, characterization, and power-law kinetics, Applied Catalysis A: General, 151 (1997) 443-460.

[45] Y. Tsuji, K. Ogasawara, M. Kitano, K. Kishida, H. Abe, Y. Niwa, T. Yokoyama, M. Hara, H. Hosono, Control of Nitrogen Activation Ability by Co-Mo Bimetallic Nanoparticle Catalysts Prepared via Sodium Naphthalenide-Reduction, J. Catal., 364 (2018) 31.

[46] L. Wang, S. Zhao, Y. Liu, D. Liu, J.M. Razal, W. Lei, Interfacial Engineering of 3D Hollow Mo-Based Carbide/Nitride Nanostructures, ACS Applied Materials & Interfaces, 13 (2021) 50524-50530.

[47] R.J.J. Jansen, H. van Bekkum, XPS of nitrogen-containing functional groups on activated carbon, Carbon, 33 (1995) 1021-1027.

VII.6 Supplementary Information

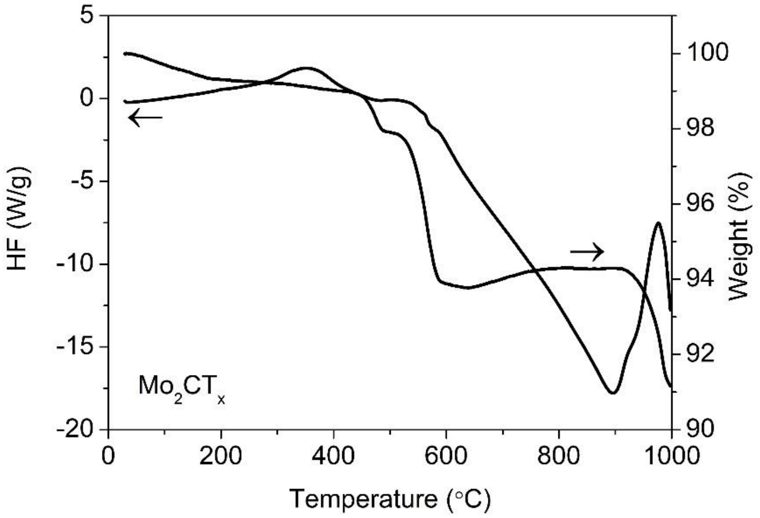

Figure S1: Thermogravimetric analysis of Mo_2CT_x

Table 1: Position of 3d Mo peaks of catalysts before and post reaction

	Mo Peaks										Surface Composition				
	Mo^{6+}		**Mo^{5+}**		**Mo^{4+}**		**T_x-Mo-C**		**Mo-C**		**Mo^{6+}**	**Mo^{5+}**	**Mo^{4+}**	**T_x-Mo-C**	**Mo-C**
	$3d_{5/2}$	$3d_{3/2}$	$3d_{5/2}$	$3d_{3/2}$	$3d_{5/2}$	$3d_{3/2}$	$3d_{5/2}$	$3d_{3/2}$	$3d_{5/2}$	$3d_{3/2}$	(%)	(%)	(%)	(%)	(%)
Mo_2CT_x	233.2	236.3	232.1	235.2	230.3	233.4	229.4	232.6	228.3	231.5	9.84	25.29	9.5	41.48	13.9
Mo_2CT_x-PR	233.0	236.1	231.7	234.8	230.7	233.8	228.7	231.9	228.0	231.2	0.88	2.39	73.34	14.1	9.29
1-Co_{Chl} -Mo_2CT_x	233.2	236.4	231.7	234.9	230.6	233.7	229.5	232.7	228.4	231.6	7.72	25.02	6.1	48.1	13.04
1-Co_{Chl} -Mo_2CT_x -PR	233.3	236.4	231.7	234.8	229.7	232.8	229.3	232.5	228.4	231.5	4.47	14.89	2.43	61.27	16.94
1-Co_{Nit} -Mo_2CT_x	233.1	236.6	231.8	235.0	230.7	233.8	229.7	232.9	228.6	231.7	17.52	34.46	10.44	30.81	6.77
1-Co_{Nit} -Mo_2CT_x -PR	233.1	236.2	231.7	234.8	230.7	233.8	229.3	232.5	228.6	231.7	9.32	12.7	4.85	58.90	14.22
5-Co_{Nit} -Mo_2CT_x	232.8	235.9	232.5	235.7	230.7	233.8	229.3	232.5	-	-	4.72	9.71	83.24	2.33	-
5-Co_{Nit} -Mo_2CT_x -PR	-	-	232.3	235.5	230.7	233.9	229.12	232.3	228.6	231.7	-	27.46	10.55	60.33	1.65

Table S2: Position of 2p Co peaks of catalysts before and post reaction

	Co peaks							**Surface composition**	
	Co^{2+}	**Co^{2+}**	**Co^{2+}**	**Co^{2+}**	**Co^{0}**	**Co^{0}**	**Co^{0}**	**Co^{2+}**	**Co^{0}**
	$2p_{3/2}$	$2p_{3/2}$	$2p_{3/2}$	$2p_{3/2}$	$2p_{3/2}$	$2p_{3/2}$	$2p_{3/2}$	(%)	(%)
1-Co_{Nit} -Mo_2CT_x	780.90	782.70	786.49	790.89	-	-	-	100	-
1-Co_{Nit} -Mo_2CT_x -PR	781.28	783.08	786.87	791.27	779.05	782.05	784.05	73.60	26.40
5-Co_{Nit} -Mo_2CT_x	780.90	782.70	786.49	790.89	-	-	-	100	-
5-Co_{Nit} -Mo_2CT_x -PR	780.42	782.22	786.01	790.41	778.16	781.16	783.16	81.05	18.95

Table S3: Position of 1s O peaks of catalysts before and post reaction

	O Peaks				**Surface Composition**			
	M-O 1s	**Mo_2CO_x** 1s	**$Mo_2C(OH)_x$** 1s	**H_2O_{ads}** 1s	**M-O** (%)	**Mo_2CO_x** (%)	**$Mo_2C(OH)_x$** (%)	**H_2O_{ads}** (%)
Mo_2CT_x	530.30	530.90	532.12	533.44	30.85	29.64	23.96	15.56
Mo_2CT_x-PR	530.19	531.08	532.19	533.60	17.72	35.61	14.22	32.45
1-Co_{Chl}-Mo_2CT_x	530.30	530.93	532.40	533.60	14.01	39.05	22.06	24.87
1-Co_{Chl}-Mo_2CT_x-PR	530.30	531.03	532.40	533.60	14.58	37.37	15.82	32.23
1-Co_{Nit}-Mo_2CT_x	530.30	530.97	532.40	533.60	3.06	69.02	18.37	9.55
1-Co_{Nit}-Mo_2CT_x-PR	530.30	530.94	532.00	533.45	4.89	57.21	26.98	10.95
5-Co_{Nit}-Mo_2CT_x	529.97	530.90	533.35	532.33	13.08	68.77	11.77	6.38
5-Co_{Nit}-Mo_2CT_x-PR	530.11	530.90	533.60	532.00	20.88	49.12	21.15	8.86

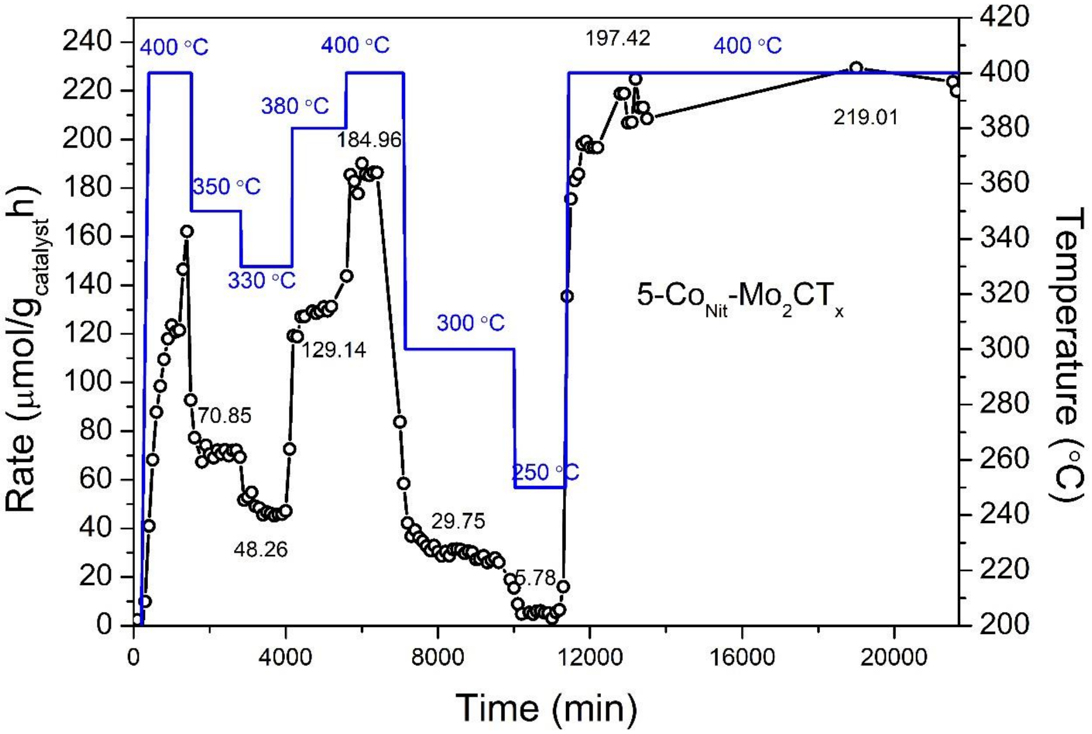

Figure S2: Typical cumulative ammonia yield obtained of 5-Co$_{Nit}$-Mo$_2$CT$_x$ catalyst.

Table S4: Elemental Analysis (CHNS) on catalysts before and after reaction

(wt.%)	**%C**	**%H**	**%N**
Mo_2CT_x	3.89	0.105	0
Mo_2CT_x-PR	4.86	0.026	0.04
1-Co_{Chl} -Mo_2CT_x	5.2	0.039	0.02
1-Co_{Chl} -Mo_2CT_x -PR	5.17	0.029	0.04
1-Co_{Nit} -Mo_2CT_x	5.09	0.023	0.03
1-Co_{Nit} -Mo_2CT_x -PR	4.68	0.028	0.48
5-Co_{Nit} -Mo_2CT_x	3.72	0.03	0.06
5-Co_{Nit} -Mo_2CT_x -PR	3.43	0.036	0.84

VIII. Conclusion

In this thesis, the development of novel Mo based catalysts for ammonia synthesis has been investigated. After a high-level overview of the state of the art on the Haber-Bosch process and the emerging alternative processes currently studied in scientific realm, the experimental work of the PhD focused on molybdenum-based catalysts for heterogeneous catalyst processes, discussed in a total of four chapters. In the first experimental section (Chapter III and IV), the effect of the support and the particle size of the active phase were investigated for Mo-N nanoparticles on ceria, titania, alumina, silica, and mesoporous silica. In the following section (Chapter V), the work progressed into ternary nitrides, namely Co_3Mo_3N NPs, encapsulated in mesoporous silica support. These more complex nitrides were stabilized on the channel-type porosity of the silica, and they are shown to display high activity for ammonia synthesis associated to an improved reactivity of nitrogen from the nitride. Finally, the last section (Chapter VI) describes the synthesis, characterization, and activity of new Co decorated molybdenum-based MXene multilayers. The results collected show the great potential of this family of catalysts in heterogeneous catalysis, being able to work under mild conditions. Below are the highlights concluded from the developments performed during the PhD:

- Applying dispersion strategy in Chapter III, small molybdenum nanoparticles were formed in both 10-Mo-N/SBA-15 (an amorphous mesostructured silica) and 10-Mo-N/TiO_2 catalysts. Although both samples exhibited ameliorated structural properties (reduced crystal size) when compared to the bulk material, β-Mo_2N, only 10-Mo-N/SBA-15 was found to be active in ammonia synthesis (1208 µmol $g_{\text{active phase}}^{-1}$ h^{-1}) while 10-Mo-N/TiO_2 only displayed a poor catalytic activity before completely deactivating over time. The origin of Mo species deactivation in ammonia synthesis when supported in TiO_2 probably is associated to the strong interaction between surface Mo species and the support. EPR results inform on the difference in reduction/nitridation process between the two catalysts, that occurs through the formation of Mo^{5+} species when MoO_x is supported over titania which is not the case in MoO_x supported SBA-15 suggesting the formation of different Mo nitrides species.
- Always with the objective to understand the role of the support nature, the dispersion of molybdenum nitrides was generalized over commercial silica, ceria and alumina supports in Chapter IV. It has been experimentally demonstrated that the identity of Mo

species generated during the activation process is significantly influenced by the type of support utilized, leading to important variations in Mo species formed (Mo-N, Mo^{6+}, Mo^{5+}, Mo^{4+}, Mo), and in turn in activity for the final material. In the case of 10-Mo-N/CeO_2 the nitridation of molybdenum nanoparticles through the pretreatment at 700 °C under 3:1 H_2:N_2 was rendered impossible due to high interaction between Mo surface species and the support surface, and the support reducibility and its oxygen transfer capability thus stabilizing MoO_x species. In the case of 10-Mo-N/Al_2O_3, as determined by XPS, this sample displayed the highest concentration of Mo-N species but displayed lower catalytic activity and poor stability as function of time, transpiring in a complete deactivation after 10 h of reaction. The progressive formation of $Al_2(MoO_4)_3$ might be also responsible of the deactivation of the catalyst (EPR). The activity of Mo-N species is dependent on crystallographic phases formed (i.e. β-Mo_2N and δ-MoN) and degree of nitridation (δ-MoN) hinting that different Mo-N species can lead to different catalytic activity.

From these first two experimental chapters, it was clearly demonstrated the important of the support surface nature in generating balanced interaction with the Mo surface species leading to an efficient Mo nitridation mechanism and final nitrides with different structural characteristics (surface composition, and probably different surface termination, vacancies concentrations). Also, it was clearly evidenced that the efficiency of the confining strategy to control nitride crystal growth during activation treatment. Indeed, when compared to the unsupported β-Mo_2N (initial rate of 76 µmol $g_{catalyst}^{-1}$ h^{-1}), 10-Mo-N/SBA-15 catalyst (initial rate of ~ 84,6 µmol $g_{catalyst}^{-1}$ h^{-1}) displayed a high catalytic activity while containing only 10 wt% of Mo. Under the same activation and catalytic conditions, 10-Mo-N/SiO_2 (initial rate of ~ 33.7 µmol $g_{catalyst}^{-1}$ h^{-1}) exhibited lower catalytic activity. When normalized against the active phase loading, initial rates of ~ 1208 µmol $g_{active\ phase}^{-1}$ h^{-1} and ~ 481 µmol $g_{active\ phase}^{-1}$ h^{-1} are obtained over 10-Mo-N/SBA-15 and 10-Mo-N/SiO_2.

- The next step, Chapter V, provided original results on the robustness of SBA-15 silica support. Globally, SBA-15 support displays good thermal and chemical stability under ammonolysis and ammonia synthesis reaction conditions. Although, changes in the local Si environment due to the formation of silyl-amine sites were evidenced by ^{29}Si and ^{1}H NMR upon ammonolysis, SBA-15 was found to be stable enough to maintain an ordered porous structure and high surface area ~504 m^2 g^{-1} for nitride phase immobilization. Thereafter, CoMo-N/SBA-15, with different loadings, was successfully prepared by consecutive impregnation steps (Mo -> Co). The results of characterization demonstrate a high dispersion of oxides, and thereafter metal nitrides within SBA-15. Analysis revealed that the surface composition of CoMo-N phase, when supported, retains comparable characteristic than non-supported Co_3Mo_3N which is a paramount condition to develop high catalytic activity. However, because of reduced crystal size associated to a high level of dispersion, supported CoMo-N displayed enhanced catalytic activity (up to 1714 µmol $g_{active\ phase}^{-1}$ h^{-1}) with respect to the Co_3Mo_3N catalyst (298 µmol $g_{catalyst}^{-1}$ h^{-1}). The excellent properties of supported catalysts are associated to the enhanced lattice nitrogen mobility and reactivity towards hydrogen in the supported materials, which is also indicative of ammonia synthesis occurring through a mechanism akin to MvK. Therefore, these results pave the way to the further development of N-chemical looping project.

- A final study, Chapter VI, we studied the capability of using MXenes type materials in ammonia synthesis. These materials, evidenced to be particularly efficient in several types of applications including electrocatalysis; where to date, only a handful of works have used MXenes for heterogeneous thermocatalytic reactions. Then, in the frame of collaboration, I spent 7 months at Drexel University (U.S.) in Prof. Yury Gogotsi's lab (DNI) to study the preparation of cobalt-doped Mo_2CT_x MXene multilayers (Co loading 1 wt.% and 5 wt.%). Characterization confirmed the diffusion of cobalt species in the interlayer spacing that resulted in single site to cluster type Co morphology. Interesting, with no ammonolysis or pretreatment, and at temperatures as low as 250 °C, some Co-doped Mo_2CT_x showed activity for ammonia synthesis. During reaction, the material transforms. Co(II) reduced into Co(0) and carbonitride MXene formed. Therefore, considering the preliminary results collected, an important margin of progress could be expected for the use of this family of material for ammonia synthesis.

Therefore, on the basis of this PhD contribution and to reach optimal catalysts, important future research steps are needed:

- A big pressure gap exists between our research laboratory scale, and real-life process scale. A step towards the right direction would be the testing of these catalysts at high pressure (~ 10-50 bars for delocalized ammonia synthesis applications).

- Several developments are feasible on the nitride phase in order to promote N-reactivity from the solid phase. The Addition of suitable promoters (Cs, K, Li, Nb), or the preparation of composites hydride-nitrite, can lead to promoted activity.
- Finally, moving past the conventional metals and nitrides, and exploring the properties of less known structures such as MXenes is a way to discover breakthrough catalysts overpassing the known catalysts and allowing to decrease the operating temperature and pressure of the ammonia process that is mandatory to consider the development of decentralized production units other than on a sheet of paper.

As Albert Einstein once said, *"To raise new questions, new possibilities, to regard old problems from a new angle, requires creative imagination and marks real advance in science."*

Finally, from this fundamental work are issued the following valorization :

- Scientific publications

A. Sfeir et al., **"Switching On/Off molybdenum nitride catalytic activity in ammonia synthesis through modulating metal support interaction,"** Faraday Discuss., p., 2023, doi: 10.1039/D2FD00154C.

A. Sfeir et al., **"Enhancing ammonia catalytic production over spatially confined cobalt molybdenum nitride nanoparticles in SBA-15,"** Appl. Catal. B Environ., vol. 325, no. August 2022, 2023, doi: 10.1016/j.apcatb.2022.122319.

- Presentation in international and national symposium and congresses

YOURHETCAT2022: Oral Presentation entitled

"The effect of support nature on the nitridation of MoO_3 and its catalytic activity for ammonia synthesis"

ROMCAT2022 : Oral Presentation entitled

"Ammonia synthesis through confined cobalt molybdenum nitrides nanoparticles in SBA-15"

MATERIAUX2022: Oral Presentation entitled: "

"Enhanced performance of CoMo-N/SBA-15 for Ammonia Synthesis"